

Copper Catalyzed Sun Fuel Generation by CO₂ and H₂O Reduction

Kumulative Dissertation

zur

Erlangung des akademischen Grades

doctor rerum naturalium (Dr. rer. nat.)

der Mathematisch-Naturwissenschaftlichen Fakultät

der Universität Rostock

vorgelegt von

M. Sc. Stefanie Kreft

geb. am 29.08.1985 in Neubrandenburg

aus Rostock

Rostock, 21. Juni 2019

Die vorliegende Arbeit entstand in der Zeit von Oktober 2015 bis Juni 2019 unter der Leitung von Prof. Dr. Matthias Beller am Leibniz-Institut für Katalyse e.V. an der Universität Rostock.

Gutachter 1: Prof. Matthias Beller, Leibniz-Institut für Katalyse e.V.

Gutachter 2: Prof. Ralf Ludwig, Universität Rostock

Datum der Einreichung: 21.06.2019

Datum der Verteidigung: 19.11.2019

ERKLÄRUNG

Ich versichere hiermit an Eides statt, dass ich die vorliegende Arbeit selbstständig angefertigt und ohne fremde Hilfe verfasst habe. Dazu habe ich keine außer den von mir angegebenen Hilfsmitteln und Quellen verwendet und die den benutzten Werken inhaltlich und wörtlich entnommenen Stellen habe ich als solche kenntlich gemacht.

I hereby affirm that I have written the present work by myself without outside assistance. No other resources were utilized than stated. All references as well as verbatim extracts were quoted and all sources of information were specifically acknowledged.

Rostock, 21. Juni 2019

.....

Stefanie Kreft

Acknowledgements - Danksagung

Zunächst gilt mein herzlichster Dank Herrn *Prof. Dr. Matthias Beller* für die Aufnahme in seinen Arbeitskreis. Ich danke dir für die zahlreichen stets produktiven und motivierenden Diskussionen, die perfekten Arbeitsbedingungen und den mir gewährten wissenschaftlichen Freiraum. Zudem möchte ich mich für die Möglichkeit des Auslandsaufenthaltes in der Gruppe von Prof. Dr. Kim Daasbjerg an der Universität Aarhus sowie für die finanzielle Unterstützung der Teilnahme nationaler und internationaler Konferenzen bedanken.

Dr. Henrik Junge gilt mein Dank für die freundliche Aufnahme in die Themengruppe „Katalyse für Energietechnologien“, den hilfreichen Anregungen sowie der Unterstützung bei offenen Fragestellungen. Ich habe es immer geschätzt, dass ich mit Problemen jeglicher Art zu dir kommen konnte. Zudem möchte ich mich für das stets entgegengebrachte Vertrauen bedanken.

Allen aktuellen und ehemaligen Mitarbeitern der *Arbeitsgruppe „Katalyse für Energietechnologien“* danke ich für die Zusammenarbeit und das gute Arbeitsklima. Hierbei möchte ich speziell *Dr. Annette-Enrica Surkus* für die stets hilfreichen Diskussionen danken und dass du immer ein offenes Ohr hattest. *Anja Kammer* gilt mein besonderer Dank für die hervorragende Unterstützung in all den Jahren sei es innerhalb oder außerhalb des Laborbetriebes. Auch *Petra Bartels* sei für die Hilfestellungen im Labor gedankt. Allerdings viel mehr möchte ich ihr und Frau *Dr. Elisabetta Alberico* für die ausgesprochen angenehme, herzliche und heitere Atmosphäre im Büro sowie Labor danken.

Weiterhin möchte ich mich herzlich bei Herrn *Dr. Sebastian Wohlrab* für die zahlreichen konstruktiven und offenen Diskussionen bedanken. Es war nicht selbstverständlich, dass du jederzeit beratend zur Verfügung standst und dadurch einen erheblichen Anteil an der Qualität dieser Arbeit hast. Zudem möchte ich der Arbeitsgruppe „*Anorganische Funktionsmaterialien*“, hierbei speziell *Dominik Seeburg*, *Marion Stöhr*, *Gabriele Georgi* sowie *Monika Heyken*, für die Unterstützung etwaiger Problemlösungen sowie der überaus freundlichen Atmosphäre außerhalb des Laborbetriebes danken.

Wissenschaftliche Kooperationen waren vor allem für die mechanistischen Untersuchungen von entscheidender Bedeutung. Dabei möchte ich vor allem *Dr. Jabor Rabeah* und *PD Dr. Evgenii Kondratenko* danken. Ohne die vielen gemeinsamen und sehr hilfreichen Diskussionen hätten einige wichtige Aspekte nicht aufgeklärt werden können. Weiterhin

möchte ich *Prof. Dr. Matthias Bauer* und *Dr. Roland Schoch*, *Dr. Jörg Radnik* sowie *Dr. Armin Hoell* für die sehr guten Zusammenarbeiten danken.

Many thanks to *Prof. Dr. Kim Daasbjerg* for giving me the opportunity to work in his group at the University of Aarhus and to get some insights of a different research project. It was a pleasure for me to be a part of your pleasant group. I learned a lot, it was a great time for me and probably, I will never eat so much different and delicious cakes within 1 hour again ;)

Stellvertretend für den gesamten Service-Bereich Analytik möchte ich mich vor allem bei *Dr. Marga-Martina Pohl* und *Dr. Carsten Kreyenschulte* für die vielen TEM-Untersuchungen, bei *Dr. Henrik Lund* für die schnelle Bearbeitung der XRD-Analysen sowie bei Frau *Anja Simmula* für die Durchführung der ICP-AES Messungen bedanken. Zudem seien Frau *Karin Struve* sowie Herrn *Reinhard Eckelt* für die N₂-sorption Messungen gedankt.

Für die finanzielle Unterstützung danke ich dem *BMBF*. Durch die Mitarbeit an dem Kopernikus-Projekt - P2X war es mir zudem möglich, Erfahrungen bezüglich der Zusammenarbeit mit Vertretern der Industrie sowie anderen Forschungsinstitutionen zu sammeln. Außerdem gilt mein Dank der *Danish National Research Foundation* (CADIAC-Projekt).

Weiterhin gilt mein besonderer Dank meinen Freunden für die stete Unterstützung, auch wenn es nicht immer einfach war und ich häufig wenig Zeit für Besuche hatte. Meinen Studienkollegen danke ich für die unglaublich schöne Zeit, die ich nie vergessen werde. Speziell möchte ich dabei *Max Schaller*, *Felix Anke*, *Julita Opalach*, *Hanna Busch* und *Sören Hancker* erwähnen. Denn auch wenn wir mittlerweile teilweise große Entfernungen überwinden müssen, sind innerhalb der letzten 8 ½ Jahre tolle Freundschaften entstanden, die ich nicht mehr missen möchte.

Schließlich gebührt mein herzlichster Dank meinen Eltern, nicht nur für die finanzielle Unterstützung, sondern vor allem für den bedingungslosen Rückhalt. Danke, dass ihr mir immer unterstützend zur Seite standet.

Abstract - Zusammenfassung

This thesis deals with the development of heterogeneous copper-based catalysts for the photocatalytic H_2O and CO_2 reduction. Initially, the conditions of an already known homogeneous system for the photocatalytic proton reduction have been applied on *ex situ* synthesized heterogeneous copper catalysts supported on inert silica. These materials have been characterized in detail by standard methods such as XRD, TEM and N_2 sorption and further by magnetic resonance and X-ray methods such as EPR, SAXS and XAS. Further, *in situ* investigations have been used as well to understand the ongoing process. The best supported photocatalyst achieved a significantly higher activity compared to the initial homogeneous precursor. The knowledge earned by these studies led to the development of various *in situ* prepared supported copper catalysts under different conditions which revealed a further enhancement of the photocatalytic performance.

In a second project highly porous photocatalysts (TiO_2 aerogels) have been synthesized, applied in aqueous CO_2 reduction and characterized, *inter alia*, by *in situ* XAS, EPR and UV-vis measurements. For the first time, an improved catalytic performance was observed by the addition of oxygen. Moreover, indications for the challenging oxidation counter reaction have been found.

Diese Arbeit beschäftigt sich mit der Entwicklung heterogener Kupfer-basierter Katalysatoren für die photokatalytische H_2O - und CO_2 -Reduktion. Dabei wurden die Bedingungen eines bereits vorhandenen ursprünglich homogenen Systems für die photokatalytische Protonenreduktion auf SiO_2 geträgerte *ex situ* synthetisierte Kupfer Katalysatoren angewandt. Diese Materialien wurden detailliert mittels XRD, TEM und N_2 -sorption sowie den Magnetresonanz- und Röntgen-Methoden EPR, SAXS und XAS charakterisiert. Um Einblicke in den ablaufenden Prozess zu erhalten, wurden zudem *in situ* Untersuchungen durchgeführt. Mit dem besten geträgerten Katalysator wurde eine signifikant höhere Aktivität im Vergleich zum ursprünglich homogenen System erzielt. Die gewonnenen Erkenntnisse wurden dann dazu genutzt, verschiedene geträgerte Kupfer-Katalysatoren *in situ* zu synthetisieren, wodurch eine weitere Erhöhung der Aktivität erreicht wurde.

In einem zweiten Projekt wurden verschiedene Photokatalysatoren mit einer hohen Porosität (TiO_2 Aerogele) synthetisiert, für die wässrige CO_2 Reduktion getestet und unter anderem mittels *in situ* XAS, EPR und UV-vis Untersuchungen charakterisiert. Zum ersten Mal wurde dabei eine verbesserte katalytische Aktivität in Anwesenheit von Sauerstoff beobachtet. Außerdem wurden Hinweise für die bisher kaum aufgeklärte Oxidationsreaktion gefunden.

Table of Contents

1	Introduction.....	1
1.1	Photocatalytic Water Splitting.....	3
1.1.1	Photocatalytic Hydrogen Generation – the three component system	4
1.1.2	CuI/Ir-PS system – State of the Art.....	6
1.2	Photocatalytic CO ₂ Reduction	7
1.2.1	Photocatalytic Processes on Semiconductors.....	7
1.2.2	Photocatalytic CO ₂ Reduction Reaction.....	11
1.2.3	Photocatalysis on TiO ₂	15
1.2.4	Investigation and influence of co-catalysts	17
1.2.5	Photocatalytic CO ₂ reduction with semiconductors – State of the Art	19
1.2.6	Oxidation reaction and the influence of oxygen	22
2	Objectives of this work.....	26
3	Summary.....	27
4	References.....	41
5	Selected Publications	49
5.1	Dye Activation of Heterogeneous Copper(II)-Species for Visible Light Driven Hydrogen Generation.....	49
5.2	Light-Driven Proton Reduction with <i>in situ</i> Supported Copper Nanoparticles.....	73
5.3	Improving Selectivity and Activity of CO ₂ Reduction Photocatalysts with O ₂	103
6	Appendix.....	141
6.1	Results for the photocatalytic CO ₂ reduction reaction since 2015	141
6.2	List of publications	146
6.3	Conference participations	147
6.3.1	Talks	147
6.3.2	Poster contributions.....	147

Abbreviations

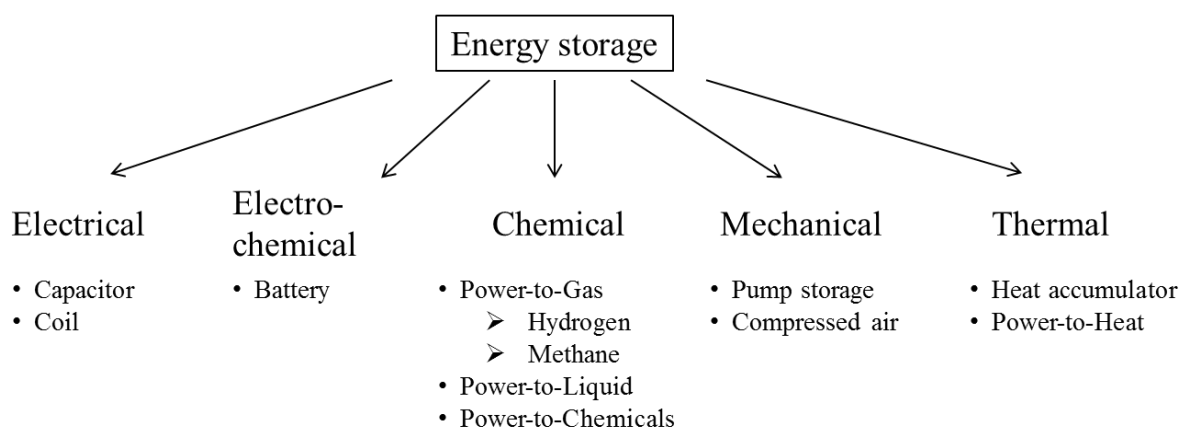
ASAXS	Anomalous Small Angle X-ray Scattering
bpy	2,2-bipyridine
CCU	Carbon capture and utilization
CB	Conduction band
DFT	Density functional theory
e ⁻	Electron
E _g	Band gap energy/potential
E _{CB}	Potential of conduction band
E _{VB}	Potential of valence band
EDXS	Energy dispersive X-ray spectroscopy
EPR	Electron paramagnetic resonance
EXAFS	Extended x-ray absorption fine structure
h ⁺	Hole
HAADF	High angle annular dark field-scanning transmission electron microscopy
HOMO	Highest occupied molecular orbital
LDH	Layered double hydroxides
LUMO	Lowest unoccupied molecular orbital
HER	Hydrogen evolution reaction
NHE	Normal hydrogen electrode
ICP-OES	Inductively coupled plasma optical emission spectrometry
IR	Infrared
OER	Oxygen evolution reaction
P25	TiO ₂ from Evonik, AEROXIDE P-25
ppy	2-Phenylpyridine
PS	Photosensitizer
SD	Sacrificial donor
TCS	Three component system
TEA	Triethylamine
TEM-BF	Transmission electron microscopy-bright field
TEM-HAADF	Transmission electron microscopy- high-angle annular dark field
TEOA	Triethanolamine
UV	Ultraviolet
VB	Valence band
Vis	Visible
WRC	Water reduction catalyst
XANES	X-ray absorption near edge structure
XAS	X-ray absorption spectroscopy
XPS	X-ray photoelectron spectroscopy
XRD	Powder X-ray diffraction

1 Introduction

From the beginning humans always exploited energy rich materials for a more comfortable life situation. Thereby, the photosynthesis stores solar radiation energy by water splitting and the reduction of carbon dioxide to form biomass which is subsequently converted to fossil fuels. Due to this energy storage device based on chemical compounds, it is denoted as a chemical one. Even though the efficiency of photosynthesis is very low, the energy supply of mankind was completely covered by renewable energy for thousands of years. Since the industrial revolution, humans resorted to this old “stored solar energy” in terms of fossil fuels like natural coal, oil or natural gas. The use of these sources increased exponentially in the last two centuries which led to an enormous increase of emission of the greenhouse gas carbon dioxide. Today these fuels dominate the global primary energy supply, but the resources are limited and will be used up resulting in the necessity for their replacement by renewable energy sources and storage systems. Thereby, the storage of energy in chemical form will continue to play a key role but the energy should be generated on the basis of renewable sources. Thus, for the long term it is essential to develop and apply new technologies for energy storage which are as sustainable as nature’s biomass generation.

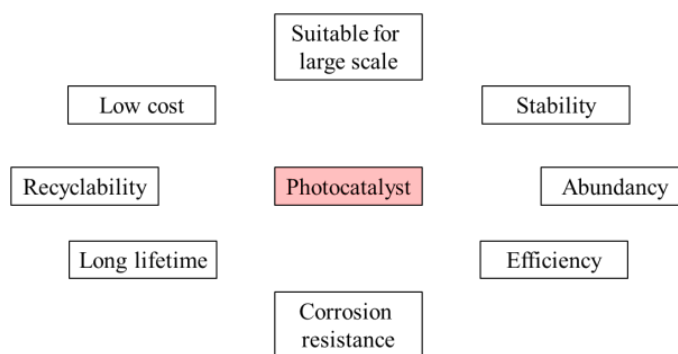
While the adjustment to renewable energy sources was extremely encouraged and furthered in the last decades, the area of storage technologies was less considered and developed. In particular due to its fluctuating availability (e.g. sun and wind power), it is absolutely necessary to find efficient ways to store such power. In other words, solar energy might be converted into chemical energy sources at places where it is abundantly available, locally not required and can be transported to where consumers need it.

Energy storage systems are classified by a number of ways. Scheme 1.1 demonstrates the categorization depending on physical properties.¹ For a better overview only the most representatives are listed.



Scheme 1.1 Classification of energy storage systems depending on their physical properties.¹

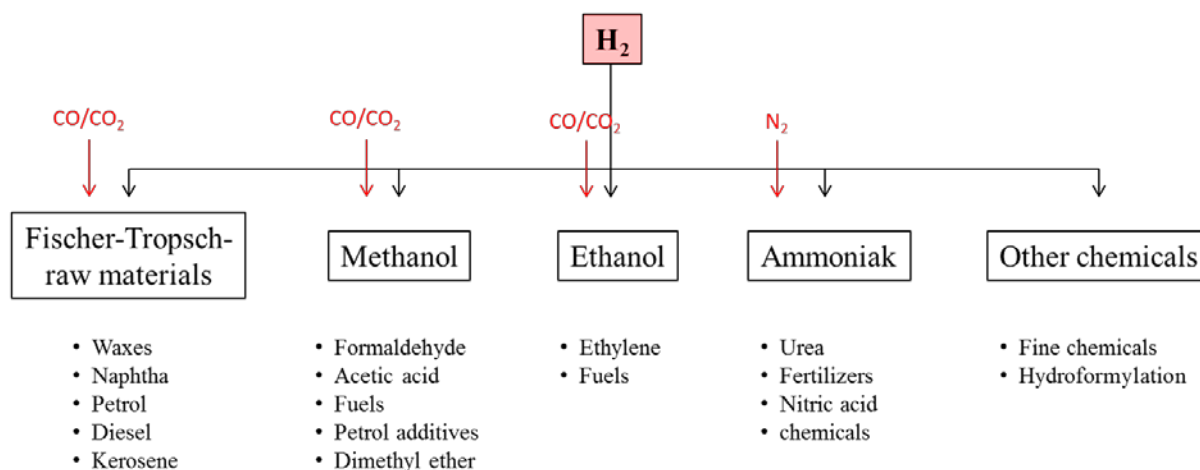
Several of these methods are already deployed. In the context of this thesis, particular attention should be given to chemical systems, namely Power-to-X. Thereby, hydrogen distinguishes itself as one of the most promising options to store energy.^{2,3} Furthermore, due to its outstanding attributes, hydrogen is particularly suitable for the use as fuel. Its high heating gravimetric value is more than double in comparison to methane, its fuel consumption is very low because of a very wide flammability limit and a high air to fuel ratio during the combustion process.³ Today, hydrogen is generated to a small amount from water electrolysis, renewable resources like biomass, and mainly from fossil fuels like natural gas or coal.⁴ Thereby, steam reforming of natural gas represents the most important process with 48 %.⁵ 60 Mio.t hydrogen are produced every year which matches up to 1 % of today's global primary energy input and about 330 Mio.t CO₂ emission. Even if hydrogen generation via electrolysis is a promising alternative, the required electricity is often linked with CO₂ formation due to low plant sizes and high investment costs for the generation *via* renewable resources.⁶ Alternatively, solar driven chemical processes offer the opportunity to produce hydrogen only by means of sunlight. It is a smart way to store surplus energy and to generate alternative fuels. Potential advantages are a considerably simpler technology, combined with lower costs and a longer life time due to non-corrosive electrolytes. However, currently known photocatalysts show either a low efficiency or a significantly poor stability, so far preventing an economical use. There are many requirements a photocatalyst has to fulfil (Scheme 1.2). Therefore,



Scheme 1.2 Required properties of a photocatalyst with respect to an economical hydrogen production.⁷

basic research is important and can assist to make photocatalytic water splitting processes more economically due to an improved catalyst productivity and stability.⁷

Besides functioning as an energy storage system and fuel, hydrogen is used in industry as a raw material for the synthesis of basic chemicals, whereby CO₂ often is a potential reaction partner (Scheme 1.3).



Scheme 1.3 Hydrogen as feedstock for industrially relevant raw materials.⁸

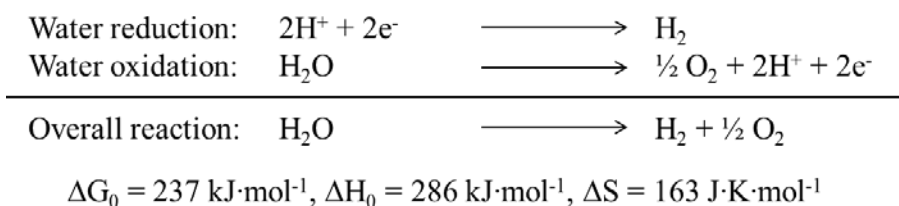
Thus, hydrogen may support to build up a CO₂-neutral carbon cycle by utilization of CO₂ *e.g.* from cement production⁹, steel industry¹⁰ to produce basic chemicals or new energy carriers. Nowadays, the intelligent use of CO₂ as feedstock is known as *carbon capture and utilization (CCU)* which implies the CO₂-separation, -compression for transportation and the -utilization to valuable carbon based materials.¹¹ However, CO₂ is chemically inert and a high energy input is needed for its conversion. Thus, basic research, especially in the field of catalysis, takes an important role to make this process more efficient. Apart from the electro¹²- and bio-catalytic^{13, 14} CO₂ utilization, there's a growing interest by activating CO₂ in the presence of sunlight (photocatalysis)¹⁵⁻¹⁷. If it will be possible to combine the water reduction simultaneously, it would correlate to the technical implementation of nature's photosynthesis and thereby, so-called *sun fuels* could be generated by renewable energy sources.

In general, the development of new catalysts, especially copper based materials, for the photocatalytic hydrogen generation and (coupled) CO₂ reduction are objects of this thesis. Thereby, mechanistic investigations of the overall photocatalytic CO₂ utilization process were intensively performed.

1.1 Photocatalytic Water Splitting

The first impression of the water splitting reaction is relatively simple and is also regarded as an artificial photosynthesis. It involves two half-reactions: the reduction of protons to hydrogen and the oxidation of water to form oxygen (Scheme 1.4). A closer look reveals a multi-electron process and most notably, a thermodynamically highly endergonic reaction.¹⁸

¹⁹ Thus, the reaction can only take place by the supply of energy.



Scheme 1.4 Water reduction and oxidation reaction as well as thermodynamics of the overall process.

Thermally, >1800 K are necessary to promote water splitting.¹⁹ Another way for providing this required energy is simply using light energy. It is thermodynamically feasible to split water with light in the solar spectrum with wavelengths around 500 nm.¹⁹ Due to the fact that about $500 \text{ kJ}\cdot\text{mol}^{-1}$ (correlates with a wavelength of <250 nm) are needed for breaking the O-H bond, the reaction is mainly kinetically inhibited. In combination with suitable photocatalysts, this activation barrier will be lowered and a water splitting reaction should be possible. So the prime challenge is to design a catalyst which is active for the overall reaction, which unfortunately would also be very active for the exothermic back reaction at the same time. Thus, it tends to be easier to carry out water splitting indirectly by separating the two half reactions which can be achieved by the addition of sacrificial reductants or oxidants.²⁰ Here, in particular alcohols²¹ and amines²² were used for the reduction half reaction and will be the focus of this thesis.

1.1.1 Photocatalytic Hydrogen Generation – the three component system

A three component system (TCS), which is comparable to the natural processes of photosynthesis²³, was already developed in the late seventies.²⁴⁻²⁶ The absorption of energy (photons) by a dye is the basis of all photosynthetic processes. The natural photosynthesis pigment chlorophyll consists of a tetrapyrrole ring system with magnesium as central ion and characteristic substituents. The π -electrons, delocalized in the porphyrins, are raised to higher energy levels by the absorption of photons related to the visible light spectrum (around 680 nm) whereby the molecule is to be found in the excited state. Due to this, thermal energy or fluorescence is emitted. First, to understand the energy transfer during the photosynthesis, the structure of photosystems has to be clarified. A photosystem is a light-harvesting complex which is built up of various proteins and chlorophyll molecules. Furthermore, there is a reaction centre consisting of only two chlorophyll molecules. The most important step of the photosynthesis is the energy transfer from the molecules of the light-harvesting complex to the reaction centre by the conversion of light into chemical energy. Reduction equivalents are generated by electron transfer chains in these centres which are then available for subsequent

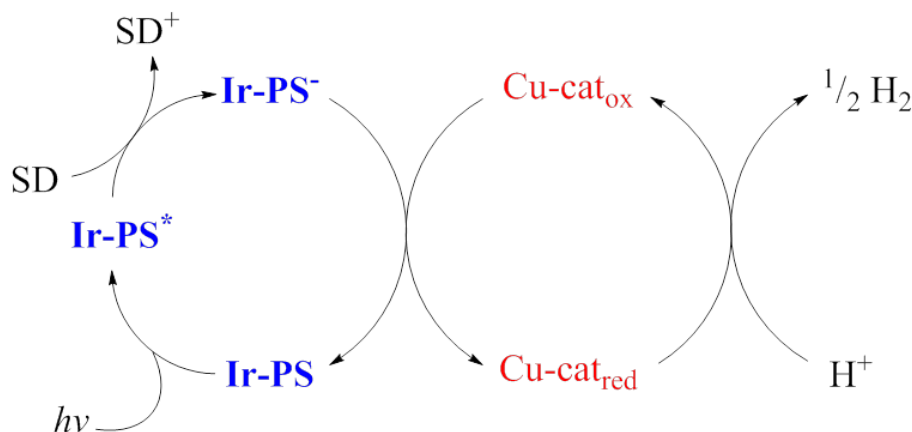
reduction processes. Inspired by this natural design, a number of artificial systems have been developed. The TCS contains (i) a dye or photosensitizer (PS) which harvests light, (ii) the sacrificial e^- donor (SD) which provides electrons to the photo-excited PS and (iii) the water reduction catalyst (WRC) which makes use of the electrons in a chemical reaction. The approach of the TCS is the following²²: due to light absorption the PS is promoted to the excited state (PS^*) and followed by an oxidative or reductive quenching. The latter one occurs if the PS^* is quenched by an electron of the SD to form PS^- . Alternatively, PS^* transfers an electron to the WRC, whereby the formed PS^+ is subsequently regenerated by the SD (oxidative quenching). Which pathway occurs, depends on the nature of all compounds of the TCS and the reaction conditions (solvent, pH).

The earliest works dealt with Ru complexes as PS (e.g. tris(bipyridine)ruthenium(II) chloride), triethanolamine (TEOA) or cysteine as SD and PtO_2 or colloid Pt as WRC. The issue was to develop catalysts which are cheaper, less toxic and available in large amounts compared to the hitherto used noble metal catalysts in order to make this process more economical and efficient. Thus, metal compounds consisting of a d^0 and d^{10} configuration got into the focus of research.^{27, 28} Above all, Fe-, Ni- and Co-catalysts showed promising results concerning proton reduction.²⁹⁻³⁵ However, their untimely deactivation already after a few hours and/or the necessity of adding a huge excess of ligand for an enhanced stability were disadvantages of these homogeneous catalysts. In 2014 our group developed a system containing copper-based WRCs, $[Ir(ppy)_2(bpy)]PF_6$ as photosensitizer (Ir-PS) and triethylamine (TEA) as SD.³⁶ Among different investigated copper(I)- and copper(II)-precursors, CuI showed the highest activity towards hydrogen generation. In comparison to the hitherto best catalyst, $Fe(CO)_5$ ³², the stability of the system was significantly improved applying CuI. In general, also heterogeneous copper catalysts, especially Cu_xO on TiO_2 , are well known for photocatalytic proton reduction, whereby copper(I)-species are proved as the active ones.³⁷⁻⁴⁴ However, the generated hydrogen amount is extremely low. Furthermore, Cu_2O coated photocathodes are applied for the photoelectrochemical water reduction.⁴⁵⁻⁴⁷ Nonetheless, the disadvantage of using Cu_2O for water reduction is its instability in aqueous media due to the potential oxidation to CuO which leads to a deactivation of the catalyst.^{48, 49}

The objective of this work was the improvement of the CuI/Ir-PS system by the investigation of classic supported as well as *in situ* formed copper catalysts for the photocatalytic hydrogen generation. In a first approach, MCM-41 was impregnated with $Cu(NO_3)_2$ and $CuCl_2$, respectively and the resulted materials were treated under various conditions. The second way

included the addition of different SiO₂ supports to the initial homogeneous CuI precursor to obtain active copper catalysts.

1.1.2 CuI/Ir-PS system – State of the Art



Scheme 1.5 Basic concept of the photocatalytic hydrogen generation in the presence of an Ir-PS and copper-WRC.³⁶

Inspired by the natural process of photosynthesis, our group developed the photocatalytic hydrogen generation based on an Ir-PS, a copper-based WRC and TEA as SD (Scheme 1.5).³⁶ Here, [Ir(ppy)₂(bpy)]PF₆ as PS is excited by photon absorption from the visible light spectrum (>385 nm). This generated triplet state PS* was characterized in detail via DFT calculations⁵⁰ and time-resolved photoluminescence spectroscopy⁵¹. The highest occupied molecular orbital (HOMO) is located in the 2,2-bipyridine ligand, whereby the lowest unoccupied molecular orbital (LUMO) includes the d-orbitals of the central ions as well as the π -orbitals of the 2-phenylpyridine ligands (ppy). These properties of the excited state ensure a reductive quenching in the presence of a SD. However, if the LUMO was only located in the orbital of the central ion this quenching would not have been possible.^{50, 52} TEA was found to be particularly suitable as SD. This formed reduced Ir-PS⁻-species transfers an electron to the copper-WRC which is able to reduce protons to hydrogen.

Previous investigations showed the activity of various Cu(I)- and Cu(II)-compounds towards hydrogen generation in the mentioned system.³⁶ No direct influence of the initial copper oxidation state on the activity could be observed. CuI was identified as the best precursor after 3 h (13 ml H₂, 280 mmol_{H₂}·g_{Cu}⁻¹·h⁻¹) and 20 h (24 ml H₂, 79 mmol_{H₂}·g_{Cu}⁻¹·h⁻¹), respectively. Noteworthy, some of the investigated substances, like Cu(OTf)₂, [Cu(CH₃CN)₄][PF₆], CuOAc or Cu@CuO, deactivated already after 6-8 h. All materials achieved the highest productivity within the first hours. The stability of the system could be improved by the addition of organic N-containing ligands, whereby especially bpy enhanced the hydrogen generation over longer

reaction times (30 ml H₂ after 20 h and 58 ml H₂ after 96 h). Other tested PS didn't show a positive influence.

Notably, during the photocatalytic reaction a black precipitate was observed which was analyzed by high angle annular dark field-scanning transmission electron microscopy (HAADF-STEM) and energy dispersive X-ray spectroscopy (EDXS). These methods revealed that copper particles of 5-10 nm were formed and decorated with iridium nanoparticles with a size of 1-2 nm. These copper particles grew during the reaction and formed agglomerates which functioned as support for a higher number of iridium particles. In the absence of the nitrogen ligand bpy significantly larger copper particles were generated. In conclusion, bpy prevents the growth of the nanoparticles and in addition, stabilizes the Ir-PS which led to the higher productivity. Furthermore, x-ray absorption spectroscopy (XAS) was performed before, during and after the photocatalytic reaction to earn more information about the nature of the formed copper nanoparticles. Interestingly, no Cu-I bonds were observed before the reaction started. Instead, Cu-O ones were analyzed by EXAFS which slightly differed from the Cu₂O and CuO structure, respectively. This concludes that CuI was hydrolyzed in the reaction mixture THF/TEA/H₂O and partly oxidized before the reaction started. Within the first minutes of the reaction the copper species were already partly reduced and the analysis after 120 min reaction time revealed a complete reduction to metallic copper nanoparticles.

Due to this knowledge, there was an interest in how *ex situ* synthesized supported catalysts will work in this reaction and if there will be a stabilizing effect of supporting materials onto the formed copper nanoparticles.

1.2 Photocatalytic CO₂ Reduction

1.2.1 Photocatalytic Processes on Semiconductors

Besides the dye-sensitizing methods for hydrogen generation, the application of semiconductors has been intensively studied for photocatalytic reactions. Nowadays, hundreds of heterogeneous catalysts are known for water reduction processes^{28, 53, 54} and additionally, in the last decade there has also been a great and growing interest for their use in CO₂ reduction⁵⁵⁻⁵⁷. First studies of a semiconductor (TiO₂) in photocatalytic water splitting reaction⁵⁸ and CO₂ reduction⁵⁹, respectively, have already been published by Honda *et al.* in the 70's. First, their pioneering work⁵⁸ showed the suitable properties of a semiconductor for the application as an anode in a photoelectrolysis cell to produce oxygen from water. Due to further improvements of the system, the group succeeded in the utilization of carbon dioxide

to small amounts of formic acid, formaldehyde, methanol and methane by the investigation of various semiconductors, such as TiO_2 , ZnO , CdS , GaP and SiC , in photoelectrocatalytic reactions.⁵⁹ Since these studies, many heterogeneous semiconductor materials, including metal oxides, sulfides, phosphides and oxynitrides, have been developed and intensively examined.^{7, 15, 53, 60} As a result, the number of publications for materials with respect to the photocatalytic CO_2 reduction increased exponentially in the last few years.⁵⁷

In the following section, the principal processes of photocatalysis on semiconductors will be described in detail (Scheme 1.6a). In general, the whole reaction involves three steps: (i) light absorption by the semiconductor to create electron-hole pairs (e^-h^+ pairs), (ii) separation of these pairs and transfer to the surface of the semiconductor and (iii) surface reactions for the $\text{H}_2\text{O}/\text{CO}_2$ reduction and H_2O oxidation. The first step (i) includes the generation of excited charges (e^- , h^+) in the semiconductor particles. Thereby, electrons of the valence band (VB) are transferred to the conduction band (CB) by light absorption. It has to be mentioned that the effective use of solar energy strongly depends on the band gap energy (E_g) of the semiconductor. Thus, the energy of the photons has to be larger than E_g for a successful excitation of the material (equation (1)). This requirement is especially fulfilled by irradiation with smaller wavelength light.

$$E_{\text{photon}} \geq E_g \quad (1)$$

$$E_{\text{photon}} = \frac{hc}{\lambda_{\text{photon}}} \quad (2)$$

$$\frac{hc}{\lambda_{\text{photon}}} \geq E_g \quad (3)$$

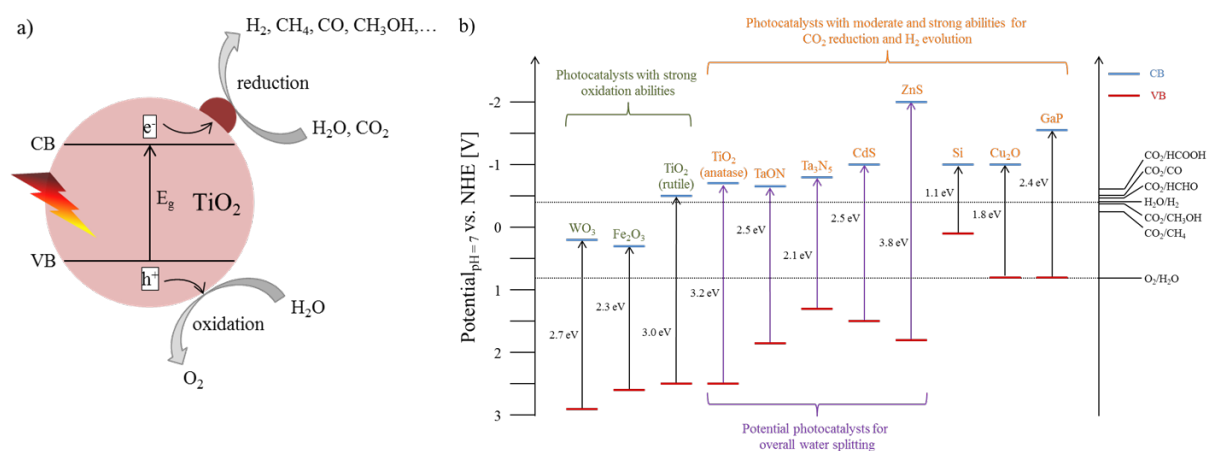
$$\frac{1240 \text{ eV nm}}{\lambda_{\text{photon}}} \geq E_g \quad (4)$$

$$\lambda_{\text{photon}} \leq \frac{1240 \text{ eV nm}}{E_g} \quad (5)$$

Based on the equations (2)-(5), by using *e.g.* TiO_2 as the photocatalyst with a E_g of about 3.2 eV⁶¹ the wavelength of incident light should be smaller than 387 nm which means that primarily UV light would be worth considering. Consequently, E_g has to be less than 3.1 eV for absorbing light from the visible spectrum. Scheme 1.6b shows an overview of some selected semiconductors regarding their E_g , the position of the related valence and conduction bands⁶²⁻⁶⁴ and the potential reactions due to $\text{H}_2\text{O}/\text{CO}_2$ reduction as well as H_2O oxidation⁶⁵ ([V] vs. normal hydrogen electrode (NHE) at pH 7). Thereby, the potential (E) of the band

levels are essentially important for each occurring reaction. Thus, E_{VB} has to be more positive than E_{ox} of O_2/H_2O (0.82 V vs. NHE, pH 7) while E_{CB} has to be more negative than the potential of the respective reduction reaction (E_{red}). There are photocatalysts which are either attractive for the oxidation or reduction reactions and some possess strong abilities for the overall process (Scheme 1.6b).

Furthermore, the illustration of different E_g for the two TiO_2 materials, anatase and rutile, indicates that its characteristics not only depend on the composition of the semiconductor but also on the modification and moreover on the particle size. This might also be the reason why the values of E_g , E_{VB} and E_{CB} for some semiconductors slightly differ in literature.



Scheme 1.6 a) Schematic illustration of the photocatalytic H_2O and CO_2 reduction process as well as the related oxidation reaction on the semiconductor TiO_2 and b) band gap positions of various semiconductors due to references ⁶²⁻⁶⁴ and redox potentials vs. NHE at pH 7 of the H_2O and CO_2 reduction as well as the H_2O oxidation reactions due to reference ⁶⁵.

If the above discussed conditions for a potential light absorption are fulfilled, step (ii) of the photocatalytic process implies the separation of the generated electron-hole pairs and their transfer to the surface of the semiconductor. Notably, the charge recombination process is usually much faster than the H_2O and/or CO_2 reduction process itself which means that the acceleration of the electron-hole separation step remarkably affects the efficiency of the process.⁶⁵ Thereby, the charges can recombine with their counterparts on the surface and/or in the bulk of the material. This can be influenced, *inter alia*, by the mobility and trapping of charge carriers and by the defect density in the semiconductor lattice.⁶⁶⁻⁶⁸ The practically more feasible way is the addition of “catching” molecules or by using a second catalyst. In previous studies photocatalytic reductions were often carried out in the presence of a large excess of electron donors such as alcohols or amines.^{55, 69, 70} The purpose is to scavenge the generated holes in the valence band diminishing the recombination rate. Nowadays, the aim is to perform the reaction without these agents as far as possible. Furthermore, the addition of a secondary material, typically, narrow-band semiconductors^{71, 72} ($E_g \ll 3$ eV, absorption light

in visible range) or visible-light-active molecules (dyes)^{73, 74} is more favorable. Coupling semiconductors, like CdS and TiO₂⁷⁵ or CdSe and ZnO⁷⁶, enhanced the efficiency by extending the absorption range and in particular by improving the charge separation. When the band gap edges of the two semiconductors are suitable, an electron is preferentially transferred to the semiconductor with the lower CB and the hole moves to the VB with the higher level resulting in a smaller recombination rate. Apart from these strategies, employing so called *co-catalysts* on the semiconductor's surface is widely common to improve this complex sub-process. Due to its improved properties regarding the enhancement of the photocatalytic process, the investigation of co-catalysts will be discussed in a separate chapter (1.2.4).

The final step (iii) of the photocatalytic process on semiconductors implies the actual chemical reaction. The migrated electrons and holes will interact with the active sites on the surface *via* multiple intermediates to produce hydrogen/C-compounds (reduction) and oxygen (oxidation). Even if the charges are well separated and transferred to the material's surface, the reaction cannot, or only poorly, proceed without suitable and sufficient active sites. Thus, the position of the CB and VB, respectively, becomes the critical factor whether a reaction will take place or not. More specifically, it is assumed that the band edges are nearly located to the redox potentials of the relevant chemical reaction, which is in approximation to n-type semiconductors, such as TiO₂. Therefore, the CB edge has to be located above the LUMO of the adsorbed acceptor molecule. Analogously, the transfer of a hole to an adsorbed molecule requires the energy level of its HOMO which has to be above the VB edge of the semiconductor. These thermodynamic aspects show that the choice of a suitable photocatalyst has to fulfil two requirements which are contradictory: (i) it is beneficial to absorb light in the visible spectrum which means the semiconductor has to exhibit a comparable small band gap but on the other hand, (ii) the band gap also has to provide a huge range for the necessary reduction and oxidation potentials of the relevant reaction. However, co-catalysts act as a promoter as well. Additionally, high surface areas can offer more accessible active sites and also the crystallinity and particle size influence this process step.⁷⁷⁻⁸⁰ These characteristics are also important for the adsorption and desorption processes of the reactants and products which will be discussed in chapter 1.2.2.

Summarising, many factors, such as crystal structure, crystallinity, particle size, surface structure and area, morphology and the addition of co-catalysts affect the described steps for the photocatalytic process on semiconductors.

1.2.2 Photocatalytic CO₂ Reduction Reaction

The combination of water splitting and CO₂ reduction is an extremely challenging task due to mutually incompatible conditions for the CO₂ reduction and water oxidation, especially performing CO₂ reduction without using any sacrificial reductant.⁸¹ Furthermore, if only CO₂ shall be reduced in aqueous media, the redox potentials for the CO₂ conversion reactions are close to that one for the reduction of H₂O to H₂ (Scheme 1.6b) which means, the photocatalyst which catalyzes the CO₂ utilisation may most probably lead to H₂ evolution. Moreover, the activation of H₂O is kinetically and partly thermodynamically much easier than that one of CO₂. Due to the complexity of the CO₂ reduction reactions, this will be explained in more detail below.

CO₂ molecules are stable and chemically inert due to their closed-shell electronic configuration, linear geometry and D_{∞h} symmetry.⁸² Thermodynamically, most transformations to reduced products are endothermic processes. So, it requires a significant input of energy which can be supplied by solar or electrical energy. Table 1 shows various reactions to the reduction of CO₂ in H₂O and the corresponding electrochemical redox potentials vs. NHE at pH 7.^{83, 84} The one-electron reduction of CO₂, the kinetically most favoured reaction, to the anion radical CO₂^{•-} (eq 1) requires a strongly negative electrochemical potential of -1.85 V vs. NHE⁸⁴ making this step highly improbable. The transfer of one electron leads to a bending of the linear geometry resulting in the loss of the symmetry and an increased repulsion between the free electron pairs in the bent structure. This contributes to the high energy level of the LUMO of CO₂ and thus to its extremely low electron affinity. CO₂ reduction by multiple proton-coupled electron transfers proceeds much easier due to the significantly lower redox potentials (eq 2-6). Thermodynamically, it becomes much easier by lowering the potential but in this case, however, CO₂ conversion to methanol (eq 5) and methane (eq 6) includes the transfer of 6 or 8 electrons, respectively, making these reactions kinetically very difficult. The redox potential for the H₂O reduction (eq 7) is comparable to the values of the multiple electron transfer reaction of CO₂ but this is a two-electron process which makes it much more feasible and demonstrates why CO₂ reduction in the presence of H₂O is such a difficult challenge.

Table 1. Electrochemical redox potentials (pH 7) for various CO₂ reduction reactions and related compounds in aqueous media.^{83, 84}

Equation	Reaction	E ⁰ vs NHE [V]
1	CO ₂ + e ⁻ → CO ₂ ^{•-}	-1.850
2	CO _{2(g)} + H ₂ O _(l) + 2e ⁻ → HCOO ⁻ _(aq) + OH ⁻ _(aq)	-0.665
3	CO _{2(g)} + H ₂ O _(l) + 2e ⁻ → CO _(g) + 2OH ⁻ _(aq)	-0.521
4	CO _{2(g)} + 3H ₂ O _(l) + 4e ⁻ → HCOH _(l) + 4OH ⁻ _(aq)	-0.485
5	CO _{2(g)} + 5H ₂ O _(l) + 6e ⁻ → CH ₃ OH _(l) + 6OH ⁻ _(aq)	-0.399
6	CO _{2(g)} + 6H ₂ O _(l) + 8e ⁻ → CH _{4(g)} + 8OH ⁻ _(aq)	-0.246
7	2H ₂ O _(l) + 2e ⁻ → H _{2(g)} + 2OH ⁻ _(aq)	-0.414

Besides the noted properties of semiconductors, their structural characteristics are also important especially for adsorption processes of the reductants and consequently for the dominating mechanistic procedures during the CO₂ reduction. However, many researchers have studied the photocatalytic mechanism of CO₂ reduction over several semiconductors.⁸⁵⁻⁹² Mostly, they are rather focused on the light absorption and electron transfer processes and thus, a comprehensive understanding of the overall process including the adsorption and activation of CO₂ molecules remains partly incomprehensible. Due to its importance and complexity for the photocatalytic CO₂ reduction, these essential reaction steps are clarified in the following.

As described above, CO₂ is an extremely stable and inert molecule due to its linear structure and the absence of a dipole moment. However, the semiconductor surface offers the opportunity to activate it by various adsorption configurations.⁹³⁻⁹⁵ Firstly, CO₂ can be physically, linearly adsorbed by weakly binding one oxygen of CO₂ or by its π -bonds to the metal site of the semiconductor. This is the most stable configuration for CO₂ adsorption due to the weak interaction and the still valid linear configuration of the molecule resulting in a high stability and low electron affinity. If CO₂ is chemically bound to the surface, the structure of the molecule is bent. Three modes of coordination to the semiconductor are possible: (i) a pure carbon, (ii) a pure oxygen bidentate or (iii) a mixed carbon-oxygen coordination.⁹⁴ This leads to the formation of the partially charged species CO₂^{δ-} through the interaction with the surface atoms. Due to the bending of these adsorbates, the energy of the LUMO level decreases and the barrier for accepting an electron is lowered compared to the free and stable CO₂ molecules. A computational study on different semiconductor surfaces revealed that the bent CO₂ adsorption only occurs on some surfaces, especially on TiO₂ (001), MgO (100), CeO₂ (111) and CeO₂ (110).⁹¹ This corresponds to the high activity of TiO₂ and

the positive effect of the addition of MgO on the photocatalytic CO₂ reduction.^{96, 97} The chemisorption of CO₂ can be promoted by several factors such as increased surface area or surface defects, basic sites and the addition of co-catalysts.^{94, 95, 98, 99} Obviously, a higher surface area provides a larger number of active sites which enables a stronger adsorption.^{100, 101} Surface defects can promote the adsorption process since they change the geometrical and electronic structure of the photocatalysts. Tan *et al.* for example have shown that the interactions at oxygen vacancy sites are much stronger due to the ability of a foreign oxygen (oxygen atom of the CO₂ molecule) to fill this vacancy resulting in a dissociation of CO₂.¹⁰² Huygh *et al.* studied the adsorption and activation of CO₂ on a fully oxidized and reduced surface using density functional theory (DFT) calculations.¹⁰³ On the fully oxidized material four configurations for the CO₂ adsorption were identified: one strongly bent and three linear physisorbed configurations. By reducing this material and introducing different oxygen vacancies six new bent adsorption configurations have been found. Thus, due to a significant charge transfer to CO₂ and elongations of the C-O bonds, a substantial weakening of the bond arose. In addition to oxygen vacancies, surface sulfur vacancies on sulfide-based materials can also function as adsorptive sites for CO₂ molecules and obtain a higher photocatalytic activity.^{104, 105} It is clearly comprehensible that CO₂ can act as an electron acceptor when the electrophilic C atom interacts with the surface's electron center or Lewis basic sites. Therefore, by introducing functional basic sites to the surface of the photocatalyst, CO₂ adsorption can be improved. Additives might be basic hydroxides or oxides such as NaOH, MgO, ZrO₂, CaO or Ga₂O₃.^{96, 106-108} As mentioned before, the application of co-catalysts has not only a positive influence on the prevention of the electron-hole recombination and on providing active sites for the relevant reaction but also on modifying the electron structure of the material to enhance the CO₂ adsorption (Chapter 1.2.4).

As discussed above, there are three kinds of chemical CO₂ adsorption and each mode may lead to a different reaction mechanism and thus various product distributions. Due to the presence of water in the reaction, protons play an essential role in the respective pathways. After the activation of CO₂ and the generation of the surface-bound CO₂^{•-} the reduction process undergoes several elementary steps, *inter alia* the transfer of an electron and/or a proton for breaking C-O and creating new C-H bonds. Some of the intermediates are highly reactive radicals, which makes mechanistic investigations much more complicated so that some steps are still to be clarified in detail. Nevertheless, three pathways of the multiple electron transfer reaction to CH₄ are proposed in literature. The first pathway (carbene pathway) is based on the anchoring of CO₂^{•-} *via* the carbon atom to the surface of the

semiconductor (carbon or mixed coordination mode of CO₂ adsorption). Initially, a protonation of the adsorbed CO₂^{•-} species takes place at the oxygen atom position to form carboxyl radicals •COOH.¹⁰⁹ Then, by an electron transfer, CO and OH are released which might also be the most probable pathway for the CO generation. In consecutive reactions, CO can accept two additional electrons forming carbon radicals which react with up to four H• radicals to CH• radicals, carbene, methyl radicals and eventually methane.⁸⁵ The second (formaldehyde) and third (glyoxal) pathways start with the chemical CO₂ adsorption on the semiconductor *via* the pure oxygen coordination mode. Thereby, both oxygen atoms of formed CO₂^{•-} are bound bidentate to the metal of the semiconductor which results in the attachment of hydrogen atoms to the carbon generating a formate anion.¹⁰⁹ After a second proton transfer formic acid is formed. Subsequently the formaldehyde pathway involves the CH₄ generation *via* several hydrogen radical transfer reactions forming formaldehyde and methanol intermediates. This mechanistic pathway was never verified experimentally. The specific radical intermediates, dihydroxymethyl and hydroxymethyl radical, have not been detected.¹¹⁰ Shkrob *et al.* performed EPR investigations of CO₂ intermediates during the reaction.¹¹¹ They particularly focused on its respective formation towards reduction vs. oxidation processes in the presence of photogenerated electrons and holes. They pointed out, that also the partly strong oxidation ability of semiconductors is very important and often ignored for mechanistic studies. Up to the formic acid formation the glyoxal corresponds to the formaldehyde pathway. Shkrob *et al.* were able to indicate formyl radicals HC•O. The authors concluded an electron transfer from the CB of the semiconductor to formic acid which is coupled with a transfer of the oxygen from a hydroxyl group to the metal of the semiconductor by breaking the C-O bond. This leads to a release of HC•O and adsorbed OH groups on the semiconductor surface. These species were also observed as intermediates in the 6e⁻ transfer reaction to methanol.¹¹² Furthermore, the study of Shkrob *et al.* showed that formaldehyde and methanol were more readily oxidized than reduced indicated by the formation of formyl and hydroxymethyl radicals.¹¹³ Due to these results, the authors postulated an alternative mechanism involving the presence of C₂ intermediates. Therefore, the formyl radicals dimerize to glyoxal which can be easily be reduced due to its π conjunction. After several reduction steps *via* hydrogen radical transfer reactions acetaldehyde is generated. This species is further oxidized to an unstable acetyl radical. Under a decarbonylation reaction a methyl radical is formed and is finally transferred into methane by protonation. Furthermore, CO is achieved from the aldehyde which is often observed as a by-product in CO₂ photoreduction.¹¹⁴⁻¹¹⁶ The various and versatile mechanistic pathways for the

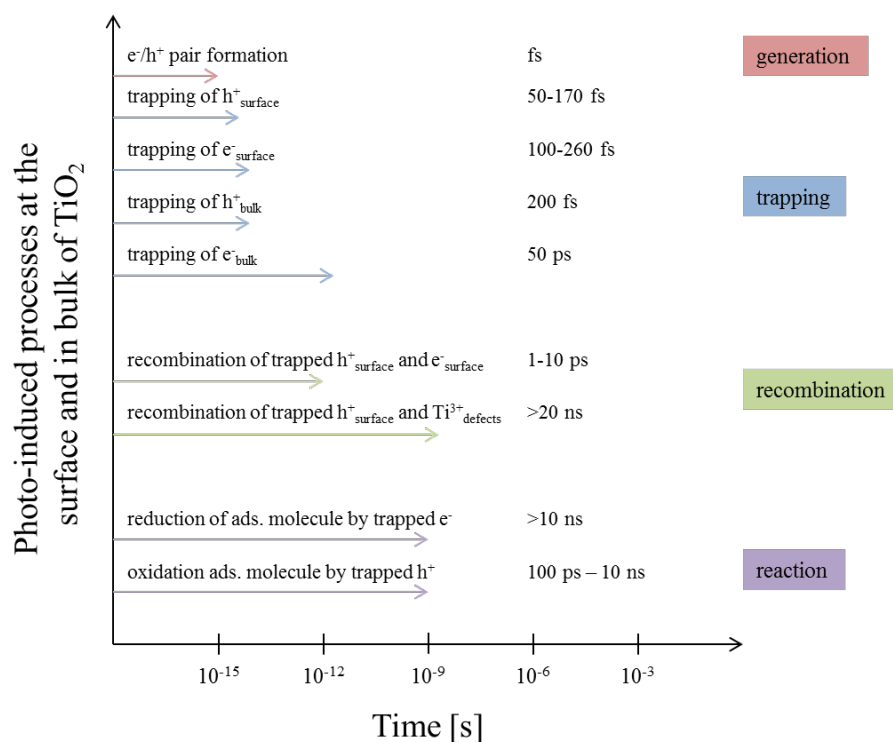
utilization of CO₂ in the presence of H₂O demonstrate the complexity and difficulty of the clarification of these multiple electron transfer reactions.

1.2.3 Photocatalysis on TiO₂

The first and most investigated semiconductor for photocatalytic reactions is TiO₂. As compared to others, it has shown its promising ability for fundamental and also practical applications due to its high photoactivity and its cheap, nontoxic, chemically and biologically inert and highly stable properties.¹¹⁷ Primarily, TiO₂ is used as pigment in paints, sunscreens, ointments and toothpaste. As a result of its high refractive index, it ensures a higher opacity than any other commercially available white pigments. Another important property of this inorganic solid is its photocatalytic activity in various applications like dye-sensitized solar cells¹¹⁸, environmental purifications^{119, 120}, antibacterial technologies¹²¹, C-C coupling reactions¹²² and notably the generation of sun fuels.^{123, 124}

TiO₂ has mainly four crystal phases, namely, anatase, rutile, brookite¹¹⁷ and TiO₂(B)¹²⁵ whereby the first three occur naturally. Thermodynamically, rutile is the most stable form in bulk titania whereby anatase shows the highest stability at sizes below 14 nm.^{126, 127} Brookite and TiO₂(B) are metastable and difficult to synthesize in pure form. Rutile can be obtained by the annealing of the other three polymorphs at higher temperatures. All types consist of TiO₆ octahedra, but the distortion of the units and the design of edges and corners differ.¹²⁷ Related to photocatalytic activity, especially anatase shows a superior performance due to the high electron mobility and affinity.^{82, 128, 129} It has been pointed out that the electrons of the anatase phase have a much longer lifetime (>1 ms) of the excited state compared to rutile TiO₂.¹³⁰ Brookite has been rarely studied due to the challenging pure phase synthesis.¹³¹ Furthermore, several studies showed that the synthesized TiO₂(B) phase achieved comparable photocatalytic activities to anatase probably due to the similar structure.^{132, 133} To improve the performance of TiO₂ as photocatalyst, it is crucial to understand the photo-induced processes on the surface and in the bulk of the semiconductor. Scheme 1.7 demonstrates the several steps and the corresponding duration process time.^{68, 134} Each time scale depends on the crystal phase, crystallinity, surface area and on the presence of bulk and/or surface defects. Thereby, the formation of the e⁻/h⁺ pairs by the photon absorption occurs within few femtoseconds, however, the recombination of these free charge carriers can easily happen in the bulk or on the surface. To prevent this recombination process, the free charges which migrate to the semiconductor surface, should be trapped by several possibilities (e.g. another semiconductor, co-catalyst, electron donor/acceptor, defects). Furthermore, before the transfer

of the charges to the adsorbed molecules is achieved, these trapped h^+ and e^- can also recombine at the surface or in the bulk of TiO_2 due to the lower process time. In conclusion, the overall photocatalytic efficiency is defined by the competition between the free charge carrier recombination and its trapping and also by the competition between the trapped charge carriers and its transfer to the adsorbed reactants.¹³⁵



Scheme 1.7 Photo-induced processes in TiO_2 photocatalysis and the required reaction time due to ref. ⁶⁸ and ¹³⁴.

Due to this knowledge, instead of investigating pure TiO_2 phase materials, the use of two phases (anatase and rutile or anatase and brookite) as a heterojunction can enhance the performance.¹³⁶⁻¹³⁸ This improvement occurs due to trapping of electrons and/or holes by one of the TiO_2 materials which hinder the recombination of the charge carriers in the other phase. Commercially available TiO_2 from Evonik, named AEROXIDE P-25 (sequentially only denoted as P25),¹³⁹ is a mixed-phase TiO_2 containing anatase (majority) and rutile (about 15-20 %) and is a benchmark material for photocatalytic studies. Various strategies have been developed to further improve the photocatalytic efficiency of TiO_2 .¹⁴⁰ In particular, these are morphological modifications, such as increasing surface area and porosity which will be obtained by a small crystallite size and titania nanostructures, respectively. Moreover, chemical modifications by the incorporation of additional components, such as nitrogen, carbon, sulfur or fluorine doping (non-metal dopants) and/or metal co-catalysts lead to an enhanced productivity.¹¹⁹ Thereby, the addition of the dopant can change the properties of the material including the structure and also narrow the band gap of the semiconductor. The

insertion of structure defects such as oxygen vacancies and Ti^{3+} centers influences the photocatalytic ability of TiO_2 positively.^{141, 142} The lifetime of photogenerated charge carriers in defect-rich materials is much longer than in defect-less ones.¹⁴³ Electrons and/or holes are trapped by the defects which leads to a low mobility and a reduced recombination rate.

1.2.4 Investigation and influence of co-catalysts

In addition to the above mentioned factors for the promotion of the electron-hole separation to improve the photocatalytic efficiency, co-catalysts, such as noble and non-noble metals or metal oxides, may also act on the surface of the semiconductor as charge carrier trapping centers. However, the synergetic enhancement of the surface reaction kinetics and the bulk charge separation in the presence of co-catalysts has rarely been reported so far. The interface between the photocatalyst and the co-catalyst is essential for the separation and transfer of the charge carriers. Chang *et al.* demonstrated that a high dispersion of the co-catalyst on the surface plays an important role to suppress the recombination and to improve the surface reaction kinetics.¹⁴⁴ Thereby, they achieved a charge separation efficiency of 77 % in the bulk and 47 % on the surface. A higher metal loading led to an agglomeration of the particles which hampered the surface reaction kinetics and the bulk charge separation.

In addition to the promotion of the charge carrier separation (i), the investigation of co-catalysts offers further advantages: (ii) lowering of the barrier or the overpotential for the CO_2 activation, (iii) providing active sites and improving selectivity towards desired products, (iv) modifying the electron structure of the photocatalyst to encourage the adsorption of reactants and (v) the inhibition of the side and/or back reaction of the products.

In general, co-catalysts can be classified into two categories due to their phases. One of them implies nanoparticles of metals or metal oxides which are deposited on the surface of the semiconductor. If the Fermi level of the co-catalyst lies below the CB edge and above the redox potential of the desired reaction, the co-catalyst can improve the reduction reaction.¹⁴⁵ Metal oxide co-catalysts can also act as trapping agent for holes and therefore as a promoter for the oxidation reaction. The major second class of co-catalysts comprises molecular species. Metal complexes of rhenium,¹⁴⁶ ruthenium,¹⁴⁷ iron¹⁴⁸ and copper¹⁴⁹ are the most investigated ones. These compounds are primarily used in electrolytes in photoelectrocatalytic reactions and were not considered in this thesis.

Ran *et al.*⁵⁶ and Li *et al.*¹⁵⁰ presented an overview of the most investigated co-catalysts for the photocatalytic CO_2 reduction in broad detail and discussed the functions and mechanism of various commonly used co-catalyst separately. Moreover, the ability of these promoters can

be influenced by different factors which are mostly related to their structural properties.⁵⁶ In particular, as mentioned before, the particle size and dispersion of the co-catalyst play an important role regarding the interaction with the semiconductor and this depends mostly on the loading of the species. If the loading is too high, larger nanoparticles or a thick layer are formed. Thus, the surface active sites of the semiconductor could be covered and/or the light absorption could be weakened. Furthermore, its structure, morphology and accessible crystal phase can affect the productivity of the whole photocatalyst. Apart from this, the valence state is also a crucial factor for an enhanced performance.

In literature, Pt, Pd, Ru, Rh, Ag and Au as noble and Cu- and Ni-species as non-noble metal-based co-catalysts are mainly listed to promote a selective, stable and enhanced CO₂ photocatalytic reduction.⁵⁶ Due to its lowest Fermi level and the high electron affinity, Pt strongly improves the electron-hole separation and migration. Thus, it is the most studied and best investigated noble metal-based co-catalyst. Ag- and Au-based promoters show specific properties due to their ability to stimulate surface plasmons by the absorption of light, particularly in the visible range.¹⁴⁵ Thereby, a strong electric field is generated by the plasmon resonance of the nanoparticles which ensures an enhanced charge carrier isolation and an increase in CO₂ reduction activity by several orders of magnitude.¹⁵¹ Even though these noble metal-based co-catalysts show excellent activities, selectivities and stabilities, they are rare and expensive thereby circumventing an application on large-scale. Hence, it is important to focus on noble metal-free promoters and especially copper-based systems raised great interest in the last few years which will be demonstrated in detail in chapter 1.2.5.

Furthermore, the presence of basic metal oxides, such as MgO, will also favour the photocatalytic CO₂ reduction. Xie *et al.* showed that the addition of MgO to an Pt/TiO₂ photocatalyst led to an increased activity and suppressed H₂ formation resulting in an enhanced CH₄ selectivity.⁹⁷ This effect is caused by the improved adsorption of CO₂ on the surface under the influence of the basic metal oxide which is explained in detail in chapter 1.2.2.

To give a complete summary, it is mentioned that natural enzymes¹⁵² and bacteria¹⁵³ are also investigated as co-catalysts for CO₂ reduction, nevertheless this will not be discussed in this thesis.

Various studies have shown that the combination of reduction and oxidation co-catalysts in only one material enhanced the water splitting reaction.¹⁵⁴ Therefore, RuO_x, CoO_x, IrO_x or MnO_x can act as promoters for the oxidation reaction. However, there are only few reports which are focused on the development of dual co-catalysts for the CO₂ reduction and H₂O

oxidation.¹⁵⁰ Hence, there is a need to study these reactions initially with two separated co-catalysts in order to get more information and to open new ways for combined systems to improve the photoactivity for simultaneous CO₂ reduction and water oxidation. A closer insight into the oxidation reaction is given in chapter 1.2.6.

1.2.5 Photocatalytic CO₂ reduction with semiconductors – State of the Art

Although researchers all over the world have intensively worked on the clarification and enhancement of the photocatalytic reduction of CO₂ for the past 40 years, there is still a long way to make this process efficient and commercially applicable. The highest, achieved rates of product formation were only one-digit values of μmol carbon product per hour irradiation and per gram photocatalyst ($[\mu\text{mol}\cdot\text{h}^{-1}\cdot\text{g}^{-1}]$). However, due to the rise in atmospheric CO₂ concentration and the need of renewable energy sources, the interest in this field grew exponentially during the last few years. Here, the focus is primarily on improved synthetic methods for defined supported nanostructure semiconductors and on a better mechanistic understanding by theoretical and computational studies (e.g. DFT calculations).

So far, as mentioned before, investigated semiconductors for the photocatalytic CO₂ reduction reaction include metal oxides, nitrides, sulfides and phosphides as well as layered double hydroxides (LDHs).^{57, 145} In principal, metal oxides consist of metal cations with a d^0 (Ti^{4+} , Zr^{4+} , Nb^{5+} , Ta^{5+} , V^{5+} , Mo^{6+} , W^{6+}) and d^{10} (In^{3+} , Ga^{3+} , Ge^{4+} , Sn^{4+} , Sb^{5+}) configuration. Examples for d^0 metal oxides are: titanates - TiO_2 , ATiO_3 ($A = \text{Sr}, \text{Ca}, \text{Ba}, \text{Pb}$), $\text{K}_2\text{Ti}_6\text{O}_{13}$, $\text{Ala}_4\text{Ti}_4\text{O}_{15}$ ($A = \text{Ca}, \text{Sr}, \text{Ba}$); ZrO_2 ; niobates - HNb_3O_8 , InNbO_4 , ANbO_3 ($A = \text{Li}, \text{Na}, \text{K}$); tantalates - Ta_2O_5 , InTaO_4 , ATaO_3 ($A = \text{Li}, \text{Na}, \text{K}$); vanadates - BiVO_4 , $\text{Fe}_2\text{V}_4\text{O}_{13}$, $\text{Na}_2\text{V}_6\text{O}_{16}$, $\text{Bi}_6\text{Mo}_2\text{O}_{15}$; and tungstates - WO_3 , $\text{W}_{18}\text{O}_{49}$, Bi_2WO_6 . Further, examples for d^{10} metal oxides and nitrides are the following materials: $\text{In}(\text{OH})_3$; gallates - Ga_2O_3 , ZnGa_2O_4 , CuGaO_2 ; germinates - Zn_2GeO_4 , $\text{In}_2\text{Ge}_2\text{O}_7$; stannates - Zn_2SnO_4 ; and nitrides – $(\text{Zn}_{1+x}\text{Ge})(\text{N}_2\text{O}_x)$, $(\text{Ga}_{1-x}\text{Zn}_x)(\text{N}_{1-x}\text{O}_x)$. Metal sulfides which have been already successfully applied are e.g. CdS , ZnS , MnS , $\text{Cu}_x\text{Ag}_y\text{In}_z\text{Zn}_k\text{S}$ and $\text{Cu}_2\text{ZnSnS}_4$. The p-type semiconductors silicon, InP and GaP were proven to be suitable photocathodes for the photo-electrocatalytic CO₂ reduction. LDHs are compounds with a layered structure of brucite ($\text{Mg}(\text{OH})_2$) with a cation replacement or cation oxidation and a hexagonal crystal structure.⁵⁷ The general type is $[\text{M}^{\text{II}}_{1-x}\text{M}^{\text{III}}_x(\text{OH})_2]^{x+}$ which means that some divalent cations are substituted by trivalent cations. Mg , Mn , Fe , Co , Ni , Cu and Zn have been investigated as M^{II} and Al , Cr , Mn , Fe and Ga as M^{III} components. The value of x usually varies between 0.17 – 0.33. Furthermore, water is present in-between the cationic layers with a total mass of about 50 %. Due to their excellent sorption capacity for

CO₂, LDHs are efficient materials for the desired reaction. Another class of photocatalysts includes metal-free materials such as graphene and its derivatives (graphene oxide and heteroatom-doped graphene) as well as carbon nanotubes, C₃N₄ and carbon-doped *h*-BN.^{57, 155} A more detailed overview of all investigated photocatalyst systems goes beyond the scope of this thesis and therefore the following part contains a closer view on the results obtained applying TiO₂ systems since 2015. This is the most widely used material in photocatalytic CO₂ reduction and besides the catalyst used in this study. The research work on TiO₂ photocatalysis until 2015 is presented in many excellent reviews.^{15, 55, 60, 82, 134, 145, 156}

In particular, studies for the CO₂ reduction have to ensure that the formed carbon product was generated from CO₂ and not from any impurities. Strunk and Co-workers have intensively focused on this problem and suggested three possible approaches:¹⁵⁷ (i) the stoichiometric formation and detection of oxygen which demonstrate the absence of a sacrificial reagent and a closed catalytic cycle, (ii) the investigation of ¹³C-labeling for CO₂ and a detection of ¹³C-labeled products or (iii) the evidence of the absence of carbon products during a blank experiment under similar conditions with the replacement of CO₂ by an inert gas. The last possibility is the easiest way to implement and should therefore be included in every reliable investigation.

Noteworthy, a direct comparison of active results of various photocatalytic systems and materials is hardly possible due to wide variety of experimental conditions, parameters and setups. In principal, reactions for the photocatalytic CO₂ reduction can be performed in liquid or gas phases.¹⁵⁶ Investigations in liquid phase are mostly done in a slurry reactor whereby the gas phase reactions are carried out in flow or batch reactors. Obviously, the disadvantage of a slurry reactor is the high amount of water which provides the liquid phase and the solvent for CO₂ but might also suppress the CO₂ reduction due to a favored proton reduction (chapter 1.2.2). Furthermore, scattering properties are strongly influenced by the reactor design and, in particular, by possible photocatalyst agglomeration phenomena which will affect the activity rates.¹⁵⁶ Nevertheless, most of the studies were performed in a batch and thereby often in a slurry reactor due to a less complicated experimental setup and especially due to higher detectable product concentration compared to a continuous-flow reactor. So far, the number of reports about the flow mode is rather limited¹⁵⁸ and these investigations have often been performed in the presence of a sacrificial reagent to increase the product rate.¹⁵⁹

The results of the most essential studies with pure and doped TiO₂ materials since 2015 are listed in Tables A1-A4. Thereby, the generated products and the related activities, the reaction

conditions and also some comments to the quality of the investigations (*e.g.* blank and/or labeled measurements, hints to the oxidation reaction) are mentioned.

The main products of the CO₂ conversion on pure TiO₂ are CH₄, CO and H₂ whereby the selectivity mostly depends on the reaction phase composition. Xie *et al.* showed the differences in selectivity regarding the reaction phase variation in the presence of pure TiO₂ and Pt-doped TiO₂.⁹⁷ In both cases the formation rate for H₂ was much higher in liquid phase, while the selectivity for CO₂ reduction was 3 to 4 times higher in gas phase reactions. The product formation is easily comprehensible because CH₄, CO and H₂ are stable molecules with only little tendency to adsorb or react on TiO₂ compared to methoxy species which are strongly bound on oxides like TiO₂.¹⁶⁰ Only some references report the formation of methanol or formaldehyde in liquid phase except when a base¹⁶¹ or hole scavenger¹⁶² was added. Furthermore, some studies revealed the direct comparison between pure and co-catalyzed TiO₂ investigations. Thereby, in any case the activity increased in the presence of the co-catalyst, *e.g.* Xiong *et al.* achieved a five times higher activity to CH₄ in the presence of Pt as co-catalyst (38 μmol_{CH₄}·g⁻¹·h⁻¹).^{114, 163-166} However, the amount of the co-catalyst should not be too high due to the formation of larger particles resulting in less active surfaces or a covering of the semiconductor's active sites.^{164, 167, 168} The most commonly investigated co-catalysts are still the noble metals Pt,^{163, 169-173} Ag,^{164, 174} Au,^{175, 176} Pd^{177, 178} and Rh¹⁷⁸ as well as the non-noble metals Ni,¹⁷⁹⁻¹⁸¹ Co^{182, 183} and to an increasing extent Cu^{114, 165-168, 184-188}. Notably, if the authors also considered the hydrogen evolution rate, which was often neglected, the use of Pt frequently led to a huge activity for this competing reaction.^{163, 169, 172} The major product of CO₂ reduction was primarily CH₄ due to the high ability of Pt to provide the large amount of electrons for this 8-e⁻-transfer process.^{163, 169-173} Xiong and co-workers demonstrated a possibility to prevent proton reduction by the addition of copper to the Pt/TiO₂ material with a simultaneous increase in CH₄ carbon-selectivity.¹⁸⁹ Unfortunately, such obvious trends in product formation were not gained by studying reactions in the presence of the mentioned noble metal co-catalysts Ag, Au, Pd or Rh. Here, the influence of the reaction conditions (*e.g.* gas or liquid phase, light source, temperature, additives or co-catalyst amount) was more crucial. The addition of a basic component such as NaOH or MgO led to a higher activity and to a suppression of hydrogen formation due to a lower amount of protons.^{161, 171} Furthermore, investigations of the same catalyst in both phases, gas and liquid, showed significant differences in product formation and the related activities.^{174, 176} Liquid products such as CH₃OH, C₂H₅OH, HCHO or HCOOH were mainly formed during CO₂ reduction in liquid phase due to a higher number of available protons.^{161, 162, 165, 174-176, 178, 190, 191} The

selection of the light source (UV or vis range) did not only affect the activity, which is mostly more than one order of magnitude smaller in the visible light, but also the product species.^{167, 176, 177, 192}

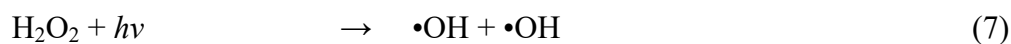
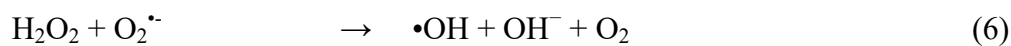
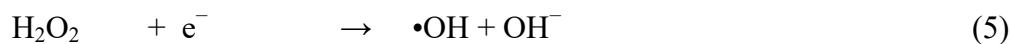
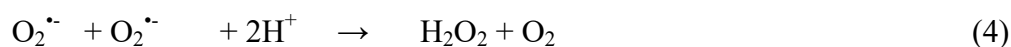
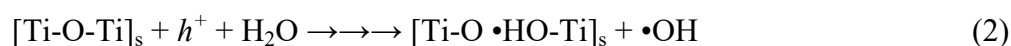
In investigations in the presence of the non-noble metal co-catalyst copper (Table A3), it was not possible to indicate a clear product formation of CO₂ reduction and in many cases CO was generated.^{166, 167, 193, 194} In addition, hydrogen was formed during aqueous CO₂ reaction.^{114, 186} Thereby, the highest activities for CO generation were 14 $\mu\text{mol}_{\text{CO}}\cdot\text{g}^{-1}\cdot\text{h}^{-1}$ in a liquid phase¹¹⁴ and 140 $\mu\text{mol}_{\text{CO}}\cdot\text{g}^{-1}\cdot\text{h}^{-1}$ in a gas phase reaction¹⁶⁷ in the presence of a Cu/TiO₂ catalyst. However, these investigations were performed under UV-light irradiation (254 nm). In general, copper exists in the oxidation states 0, +1 and +2, respectively. Most of the studies showed a presence of copper(I), more precise Cu₂O.^{167, 168, 185, 186, 189} Previous works have already shown the higher performance of copper(I)-species whereas the presence of copper(0) lowers the activity.¹⁹⁵⁻¹⁹⁷ An *in situ* formation of initial copper(II)- to active copper(I)-species might also be possible under photocatalytic conditions¹⁹³ and also the complete reduction to the deactivated copper(0)-species has been already observed.¹⁹⁷ Interestingly, copper(0) can easily be re-oxidized to active copper(I) in an air-containing environment which also means in the presence of additional or formed molecular oxygen.

1.2.6 Oxidation reaction and the influence of oxygen

Theoretically, the water oxidation is an important accompanying reaction for the photocatalytic CO₂ reduction due to the trapping of holes resulting in an improved charge carrier separation and enhanced activity for the CO₂ utilization. Unfortunately, the four-electron oxygen evolution reaction (OER) with its large overpotential is kinetically limited,¹⁹⁸ very complex and up to now not fully elucidated. Thus, it is recognized as the major challenge to ensure the solar fuel production (overall water splitting and CO₂ reduction).¹⁹⁹ Above all, the first one-electron oxidation step, the rate-limiting one, is still not identified and several models are proposed. The most disputed point concerning the nature of the hole trapping mechanism is which species is the most essential one. In comparison to many others, Paraneli *et al.* demonstrated that surface-trapped holes in TiO₂ only exist in the presence of adsorbed water.²⁰⁰ The amount of holes significantly increased if the TiO₂ surface is covered with hydroxyl groups and water molecules are physisorbed. In any other cases, only the presence of holes in the bulk was observed concluding holes on the surface recombined or were quickly trapped. To achieve the most effective trapping of holes and to avoid the complicated and slow water oxidation reaction sacrificial agents such as alcohols have been applied.¹³⁴

Thereby, the alcohol oxidation proceeds *via* a two-electron process to the respective aldehyde. Tamaki *et al.* studied the reaction dynamics in the presence of various alcohols and determined a lifetime of trapped holes in methanol, ethanol and 2-propanol of 300, 1000 and 3000 ps, respectively.²⁰¹ This means, the addition of methanol provides the fastest trapping of holes and therewith the best charge carrier separation occurs. In comparison, kinetic investigations of Yamakata *et al.* demonstrated a very slow hole capture within 2 μ s in the presence of only water vapor.²⁰² Nevertheless, this latter process is the most important one and the aim has to be the development of an active photocatalyst for this system without the addition of any external sacrificial reagents.

In theory, in the presence of H₂O (also as vapor) molecular oxygen should be generated due to thermodynamics if TiO₂ is used in an active photoreaction system. However, only a few researchers were able to quantify the amount of oxygen.^{163, 169, 189} In the presence of Pt/TiO₂ Xiong *et al.* analyzed an O₂ average production rate of 290 $\mu\text{mol}_{\text{O}_2}\cdot\text{g}^{-1}\cdot\text{h}^{-1}$ which is in conformity to the calculated production rate.¹⁶³ Others have identified traces of labelled ¹⁸O₂,^{184, 193} or detected a change in the N₂/O₂ ratio^{197, 203} but primarily the amount of O₂ couldn't be quantified or wasn't even mentioned (Tables A1-A4). Obviously, the small amounts of carbon-based products formed, would lead to a very small amount of oxygen, which can only be detected with huge standard deviations. Furthermore, oxygen can be adsorbed on the semiconductor's surface and surface oxidation might occur.^{158, 204} Other researchers assume a re-oxidation of generated products.^{166, 167, 205} Moreover, the formation of other partially oxidized products may be possible.^{68, 206} Substantially, these species might be •OH or O₂^{•-} radicals, ¹O₂ and/or H₂O₂ (*inter alia* Scheme 1.8). Therefore, •OH radicals are generally formed by the oxidation of surface hydroxyl groups and/or adsorbed water (Scheme 1.8, eq. (1) and (2)). The presence of •OH radicals is demonstrated by spin trap experiments with electron paramagnetic resonance (EPR) spectroscopy.²⁰⁷ Furthermore, there are several ways to generate these radicals from H₂O₂ (Scheme 1.8, eq. (5)-(7)) which is produced by the reduction of formed O₂ or the disproportionation reaction of superoxides (Scheme 1.8, eq. (3) and (4)). In case of eq. (5) only surface-bounded radicals might be formed, whereby also free •OH radicals can be produced in eq. (6) and (7) which are much easier to verify *via* the spin trap method.



Scheme 1.8 Possible oxidation reaction in aqueous media in the presence of the photocatalyst TiO_2 .⁶⁸

The detection of H_2O_2 should be the easiest among all possible oxidation products as it can be verified *via* a direct optical absorption in UV and IR regions, coloration methods, fluorescence probe and chemiluminescence methods.²⁰⁶ The formation of superoxide $\text{O}_2^{\bullet-}$ is less important and there's a small number of examples compared to the generation of $\bullet\text{OH}$ radicals. These $\text{O}_2^{\bullet-}$ radicals can be also analyzed by the spin trap experiment (EPR spectroscopy).²⁰⁶ However, the reaction rates are significantly smaller compared to the one with $\bullet\text{OH}$. The formation of $\text{O}_2^{\bullet-}$ is mainly discussed as photocatalytic oxidation process during the mineralization of organic substances, the production of H_2O_2 and anti-microbial activities.^{135, 208} The reaction between $\text{O}_2^{\bullet-}$ and a trapped hole might produce singlet oxygen $^1\text{O}_2$.²⁰⁶ This species can be detected *via* near-infrared phosphorescence at 1270 nm. The lifetime was determined to be 2 μs which is much shorter compared to those of $\bullet\text{OH}$ radicals (10 μs). All these reactions mainly occur on the surface of TiO_2 and/or by releasing the mentioned species.²⁰⁶ Thereby, also surface peroxo species, such as $[\text{Ti-O-O-Ti}]$ or $\text{Ti-OO}\bullet$, might be generated. These many various ways show the complexity of the oxidation reaction process and confirm why the overall mechanism has not been clearly elucidated yet. Obviously, this process is strongly influenced by the nature and properties of the photocatalysts' active sites and also by the reaction conditions.

In this context, another aspect is the influence of oxygen on the photocatalytic performance. Thus, the question arises, if oxygen, once formed, can even be detected. First, it is likely that released gas-phase oxygen promotes the reverse reaction back to CO_2 and/or H_2O as few researchers assumed.^{166, 167, 205} However, this requires the desorption of the oxygen species which might be challenging due to the energetically favored adsorption on the surface of TiO_2 compared to CO_2 and also the providing of a higher number of adsorption sites for O_2 by a defective surface.^{103, 209} Hence, CO_2 competes with O_2 for adsorption sites on TiO_2 which leads to a restricted CO_2 adsorption and thus to a lower product formation. Indeed, Strunk *et al.* have shown that in the presence of O_2 the photocatalytic formation of CH_4 over TiO_2 was

inhibited above a concentration of 5 ppm.¹⁵⁸ Moreover, O₂ is more readily reduced than CO₂. The one-electron transfer to form superoxide radicals is thermodynamically possible due to the less negative potential ($E_0 = -0.137$ V) compared to that of the conduction band of TiO₂ (Scheme 1.6). As mentioned before, the one-electron reduction of CO₂ ($E_0 = 1.85$ V) is highly improbable (chapter 1.2.2). So, the reduction of O₂ might reduce the number of photogenerated electrons which are available for the CO₂ reduction. Thus, these are further hints for the challenging analysis of generated O₂ and the whole oxidation reaction process.

2 Objectives of this work

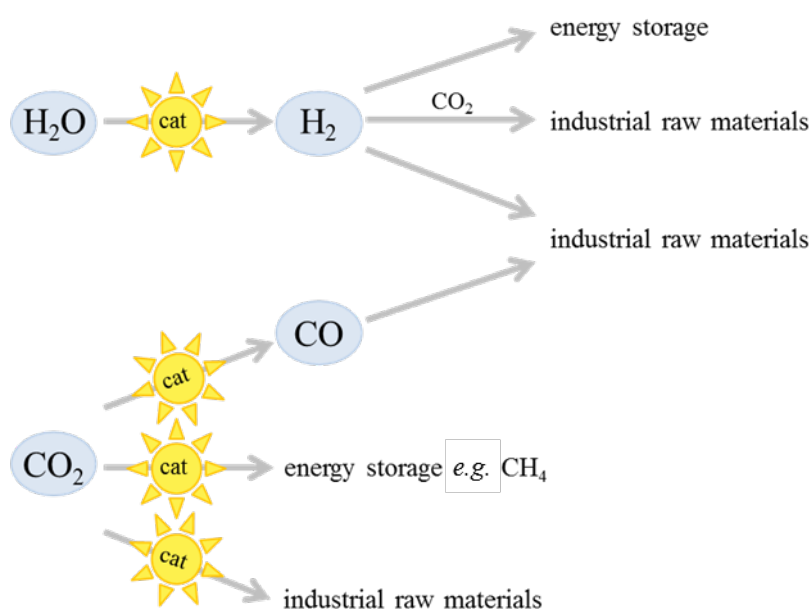
The sustainable and sufficient supply of energy remains one of the most important challenges nowadays. Therefore, the abundant sunlight shall be converted to chemical energy by the investigation of suitable photocatalysts. This might be feasible by the capture of the energy of light in the energy vector hydrogen and also by the photocatalytic utilization of the greenhouse gas CO₂. The intelligent use of CO₂ as a C₁-feedstock and its conversion to valuable carbon-based materials and sustainable energy sources can furthermore establish a closed-CO₂ cycle.

Hence, the major objective of this thesis was the development of catalysts for the light driven hydrogen generation and reduction of aqueous CO₂, respectively. The aim was to develop non-noble metal-based materials, such as copper species, to examine the ongoing processes and to improve the current catalytic performances. In case of the photocatalytic hydrogen generation the existing system containing a copper-based water reduction catalyst, an Ir-complex as photosensitizer and triethylamine as sacrificial reagent should be improved applying various supported copper catalysts which were prepared by different *ex situ* and *in situ* methods. Here, the understanding of the material's characteristics and properties was of significant importance.

Regarding the CO₂ utilization, the investigation with the most commonly used photocatalyst TiO₂ P25 was to be improved by *e.g.* the modification of the semiconductor, the addition of several co-catalysts and amounts or by the variation of the reaction conditions. Furthermore, the clarification of the process, including the reduction and also the challenging oxidation reaction, was a central issue. Therefore, mechanistic investigations by applying various *in situ* analytical methods such as XAS, EPR and UV-vis spectroscopy were carried out so that due to the findings the catalytic performance was enhanced.

3 Summary

The generation of hydrogen by reduction of protons in the presence of light and a photocatalyst offers an attractive way to store energy and form a sustainable energy vector. In a related way the energy of sunlight can also be utilized to convert the major greenhouse gas CO_2 *e.g.* to CH_4 which constitutes another type of storage media. Furthermore, in the presence of suitable photocatalysts CO_2 , as a potential carbon feedstock, leads to a number of industrially relevant raw materials and in particular, the generation of carbon monoxide might be an unusual but interesting conversion. CO , in addition with hydrogen, is an important reactant especially for many industrial processes performed on large-scale (*e.g.* Fischer Tropsch).



Scheme 3.1 Conversion of sunlight into chemical energy by the utilization of H_2O and CO_2 in the presence of a suitable catalyst.

In 2014, a system for the photocatalytic hydrogen generation was developed in our group (chapter 1.1.2).³⁶ Here, CuI proved to be the best copper precursor of all tested materials. However, during the photocatalytic reaction *in situ* copper nanoparticles were formed which also demonstrated an inherent activity towards proton reduction. Hence, in the present work heterogeneous copper catalysts were prepared by various synthesis methods and investigated under visible light irradiation.²¹⁰ The advantages compared to the initial previous system are the investigation of defined vs. random aggregated catalysts and the easier separation of the material after the reaction.

First, the heterogeneous copper catalysts were synthesized by an incipient wetness impregnation of inert SiO_2 . Therefore, mesoporous silica MCM-41 was impregnated with a

$\text{Cu}(\text{NO}_3)_2$ - and CuCl_2 -solution, respectively. After drying at 80 °C the nitrate sample was calcined at 400 °C in air ($\text{CuO}(\text{N,a})/\text{MCM-41}$ and N_2 ($\text{CuO}(\text{N,N})/\text{MCM-41}$). The chloride sample was further impregnated with NaOH after the drying step to precipitate $\text{Cu}(\text{OH})_2$ and to remove the chloride *via* a washing step. Afterwards, the material was dried again at 80 °C ($\text{CuO}(\text{Cl})/\text{SiO}_2$) and calcined at 400 °C under air ($\text{CuO}(\text{Cl,a})/\text{SiO}_2$). Table 3.1 shows the main preparation parameters, the copper content as well as the surface area and pore size of the samples.

Table 3.1 Preparation, copper content and structural properties of different Cu-based catalysts.²¹⁰

Sample	Precursor	Support	Precipitation	Calcination	Cu content [wt.%] ^a	Surface area [m ² g ⁻¹] ^b	Pore size [nm] ^b
$\text{CuO}(\text{N,a})/\text{MCM-41}$	$\text{Cu}(\text{NO}_3)_2$	MCM-41	-	400 °C (air)	6.5	434	3.7
$\text{CuO}(\text{N,N})/\text{MCM-41}$	$\text{Cu}(\text{NO}_3)_2$	MCM-41	-	400 °C (N_2)	6.5	498	3.9
$\text{CuO}(\text{Cl,a})/\text{SiO}_2$	CuCl_2	MCM-41	NaOH	400 °C (air)	6.2	163	8.7
$\text{CuO}(\text{Cl})/\text{SiO}_2$	CuCl_2	MCM-41	NaOH	-	6.6	185	11.4

^a Determined by inductively coupled plasma optical emission spectrometry.

^b Determined by nitrogen sorption.

ICP-OES analytics indicated a copper amount between 6.2 – 6.6 wt% for all materials. The surface area and pore size significantly depended on the applied copper precursor and in particular on the NaOH treatment. Additionally, the surface area was considerably smaller compared to the unloaded MCM-41 (surface area: 1214 m²/g, pore size: 4.1 nm) caused by pore-blocking. XRD patterns revealed the typical reflexes for the monoclinic phase of CuO except for sample $\text{CuO}(\text{Cl})/\text{SiO}_2$. In the related diffraction pattern of $\text{CuO}(\text{Cl})/\text{SiO}_2$ the reflexes of very low intensity were assigned to $\text{Cu}_2\text{Cl}(\text{OH})_3$. TEM analysis demonstrated definite and small copper particles with a narrow size distribution on the surface of the support (Fig. 3.1). If MCM-41 was impregnated with aqueous $\text{Cu}(\text{NO}_3)_2$ the achieved material obtained after calcination under air possessed slightly smaller particles (<2 nm, Fig. 3.1a) compared to the material calcined under N_2 (~3 nm, Fig. 3.1b). Incipient wetness impregnation of MCM-41 with aqueous CuCl_2 and a following NaOH treatment led to a destruction of the typical hexagonal pore structure of the silica. This observation also clarifies the significant decrease of the surface area and the unusual increase of the pore volume. The copper particles were not as finely and homogeneously dispersed as in the materials prepared by the nitrate precursor. EDX measurements confirmed the presence of Cl in $\text{CuO}(\text{Cl})/\text{SiO}_2$ which is in agreement to the XRD results. After calcination at 400 °C ($\text{CuO}(\text{Cl,a})/\text{SiO}_2$), no Cl was observed and the particles grew (Fig. 3.1c) compared to $\text{CuO}(\text{Cl})/\text{SiO}_2$ (Fig. 3.1d).

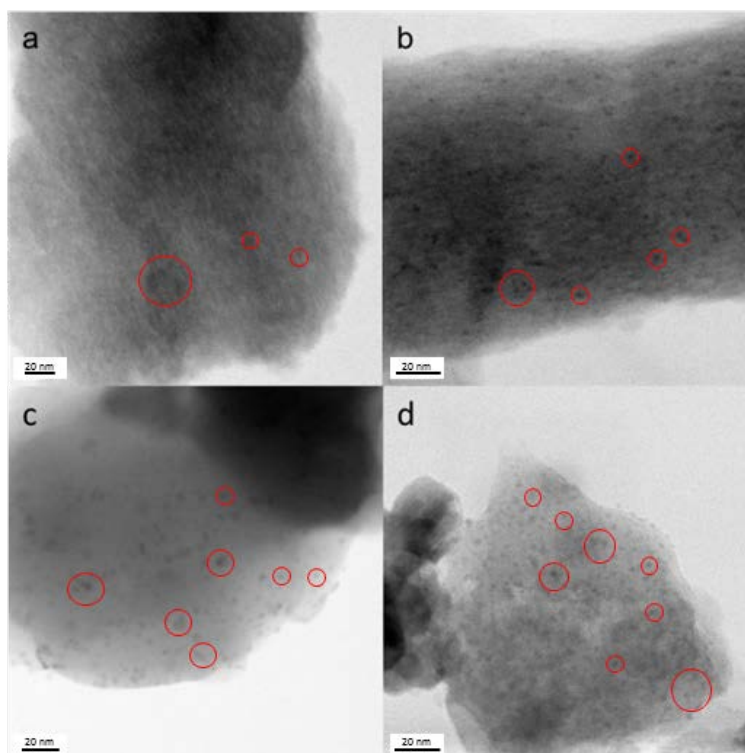


Figure 3.1 BF-TEM images of CuO(N,a)/MCM-41 (a), CuO(N,N)/MCM-41 (b), CuO(Cl)/SiO₂ (c) and CuO(Cl,a)/SiO₂ (d).²¹⁰

It has to be mentioned, that EDX data of CuO(Cl)/SiO₂ also presented copper particles not accompanied by any Cl. This demonstrated the presence of two different copper species in this material. Disadvantageously, TEM analysis records only a small part of the material. Instead, Anomalous Small Angle X-ray Scattering (ASAXS) offers information about a larger volume of the investigated sample. The four materials, in particular, CuO(Cl)/SiO₂ have been intensively analyzed by this latter method. First, ASAXS analysis confirmed the maintained hexagonal pore structure of MCM-41 in CuO(N,a)/MCM-41 and CuO(N,N)/MCM-41 and furthermore the destruction of the MCM-41 structure in the materials formed by CuCl₂ and NaOH impregnation. A deeper insight in the scattering curve of CuO(Cl)/SiO₂ actually revealed the presence of two copper species. Thereby, the major part consisted of homogeneously dispersed copper particles on the support. Their behaviour is comparable to the CuO(N,N)/MCM-41 sample. The second copper species appeared to be nanoparticles with a diameter of 1.4 ± 0.12 nm which were agglomerated in a network with a size of 11 nm. This minor part of the material presents the observed particles in the TEM investigations. Furthermore, to elucidate the oxidation state and the local structure of the copper species, X-ray absorption spectroscopic (XAS) measurements were performed. XANES determined a Cu(II)-species with a distorted octahedral symmetry in all investigated materials (Fig. 3.2a). Thereby, the spectra of the samples CuO(N,a)/MCM-41, CuO(N,N)/MCM-41 and CuO(Cl,a)/SiO₂ are comparable to the reference measurement of CuO with a less pronounced

distortion of the octahedral geometry. In contrast, the structure of CuO(Cl)/SiO₂ deviated considerably from CuO which was most notably observed in the derivative spectrum (Fig. 3.2b). These results were also substantiated by EXAFS and confirmed the different features of CuO(Cl)/SiO₂ compared to all the other materials.

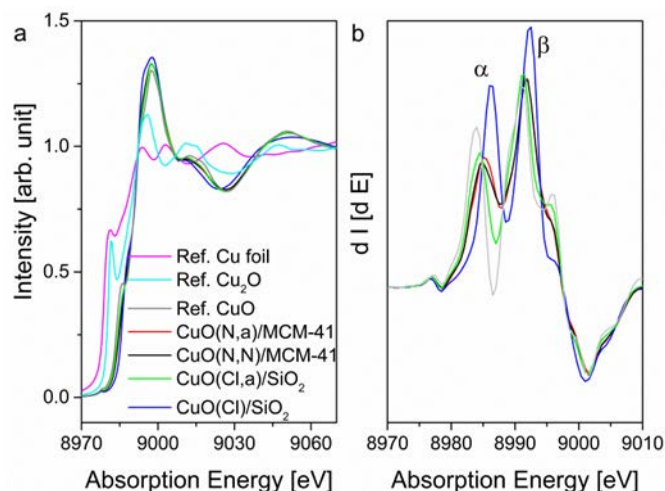


Figure 3.2 *Ex situ* XANES measurements (a) and first derivation (b) of supported copper materials in comparison to the reference materials Cu foil, Cu₂O and CuO.²¹⁰

Afterwards, all these synthesized supported copper materials were tested as WRC with [Ir(ppy)₂(bpy)]PF₆ as PS and TEA as sacrificial reagent compared to the previously mentioned system containing CuI as WRC precursor.³⁶ Table 3.2 summarizes the hydrogen evolution after 3 and 20 h illumination and the related catalyst activities which present the amount of hydrogen in mmol per hour and g of copper.

First, it has to be mentioned that in all investigations the activity of the systems decreased within the 20 h which is caused by the decomposition of the PS during the reaction.³⁶ After the first three hours, CuO(Cl)/SiO₂ showed the highest activity followed by CuO(Cl,a)/SiO₂ > CuO(N,N)/MCM-41 > CuO(N,a)/MCM-41. Applying these three structurally similar materials, nearly the same hydrogen formation was obtained after 20 h while CuO(Cl)/SiO₂ achieved the highest activity. This behaviour indicates a correlation between the significantly different CuO structure in the latter material and its improved productivity. As known from literature, by lowering the copper amount on the support the activity can be enhanced. Thus, a material equally prepared, but with a lower copper amount (1/10 compared to CuO(Cl)/SiO₂) was synthesized and investigated (CuO(Cl0.1)/SiO₂). Notably, after 3 h the activity was 10 times and after 20 h 8 times higher compared to CuO(Cl)/SiO₂.

Table 3.2 Photocatalytical hydrogen generation from THF/TEA/H₂O mixture with different Cu-based WRCs.²¹⁰

Sample	V(H ₂) [ml] / 3h	Activity [mmol·h ⁻¹ ·g ⁻¹] / 3h	V(H ₂) [ml] / 20h	Activity [mmol·h ⁻¹ ·g ⁻¹] / 20h
CuO(N,a)/MCM-41	5.3	113.7	12.4	39.9
CuO(N,N)/MCM-41	5.7	122.3	13.2	42.5
CuO(Cl,a)/SiO ₂	6.7	141.1	11.8	38.0
CuO(Cl)/SiO ₂	8.9	189.4	17.1	55.0
CuO(Cl0.1)/SiO ₂ ^a	8.0	1702	12.5	402

All experiments have been performed at least twice and the averages are shown. Experimental conditions: 15 μ mol Ir-PS, 10 μ mol [Cu], 10 mL THF:TEA:H₂O = 3:2:1, 1.5 W Xe-light irradiation, \geq 385 nm, 25 °C, gas volumes determined by automatic gas burettes and corrected by blank volume (0.5 ml after 3 h and 1.3 mL after 20 h), gases analyzed by GC, Activity = $n(\text{H}_2)/(t \cdot m(\text{Cu}))$.

H₂ evolution in the absence of any copper catalyst but in the presence of MCM-41: 1.6 ml after 20 h.

^a Experimental conditions: see above, with the exception of 1 μ mol [Cu] being used.

To indicate differences between these two catalysts, EPR measurements have been performed (Fig. 3.3). The spectra of CuO(Cl)/SiO₂ revealed a superimposition of two Cu(II) signals resulting from two isolated Cu(II) single sites (Fig. 3.3a). Furthermore, a weak magnetic interaction between the Cu(II)-ions was determined which confirmed the EXAFS results of this material. Instead, the EPR spectrum of CuO(Cl0.1)/SiO₂ presented only one signal indicating the existence of only one copper species and additionally, a homogeneous and fine dispersion on the silica support was achieved. Hence, the formation of the Cu₂Cl(OH)₃ agglomerates was prevented during the synthesis of the catalyst and the second copper species with the considerably deviated CuO structure effected the improved catalytic activity.

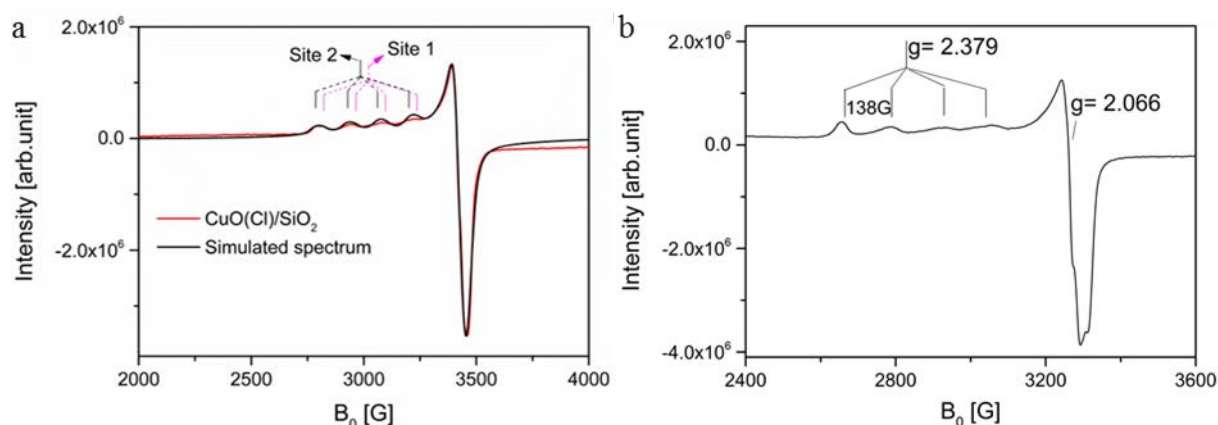


Figure 3.3 EPR spectrum of CuO(Cl)/SiO₂ (a) and CuO(Cl0.1)/SiO₂ (b) measured at RT with x-band frequencies 9.877 and 9.450 GHz, respectively.²¹⁰

Furthermore, EPR and *in situ* XANES measurements of the suspension were performed to determine the change of copper species during the photocatalytic reduction reaction. In the presence of the Ir-PS the EPR signal of the Cu(II)-species decreased rapidly indicating a reduction of Cu(II) to the EPR silent species Cu(I) or Cu(0). This was also confirmed by the time resolved XANES measurements. Thus, an *in situ* formed Cu(I)-species is proposed which is known from literature to be the most photocatalytically active copper species.

Unfortunately, due to the insolubility of CuI in water, it was not possible to prepare a catalyst in a similar way to CuO(Cl)/SiO₂ starting from CuI as copper precursor.³⁶ Therefore and also in order to stabilize the *in situ* formed copper particles in these investigations, the influence of the addition of various silica based materials to the CuI/Ir-PS system was examined.²¹¹ Figure 3.4a demonstrates the hydrogen generation in the presence of the mesoporous MCM-41 and SBA-15 as well as the nanoporous glass (npG, pore diameter 39 nm). The result of the photocatalytic reaction without the addition of any silica is added for comparison (without additive). Interestingly, during the first three hours, nearly the same production of hydrogen was achieved independent on the application and kind of silica. During the reaction process a higher gas evolution was observed in the presence of MCM-41 compared to the npG 39, in particular, which showed only a minimal rise of hydrogen after 20 h. Remarkably, after 48 h an enhanced productivity was identified by the addition of MCM-41 compared to the initial homogeneous CuI system. Moreover, the influence of the copper precursor was tested (CuI, CuCl₂, Cu(NO₃)₂) with the best additive. However, the application of CuCl₂ and Cu(NO₃)₂ led to a decrease of the ability to reduce protons compared to CuI as precursor. This effect is most pronounced for Cu(NO₃)₂ where the system even deactivated after 20 h. Previous studies presented an influence of the amount of the THF/TEA/H₂O mixture on the productivity. However, applying the non-supported CuI system, the best activity in 10 ml was obtained.³⁶ In the presence of MCM-41 an optimum of hydrogen generation was reached in 50 ml of THF/TEA/H₂O, whereby the reproducibility in 10 ml was poor.

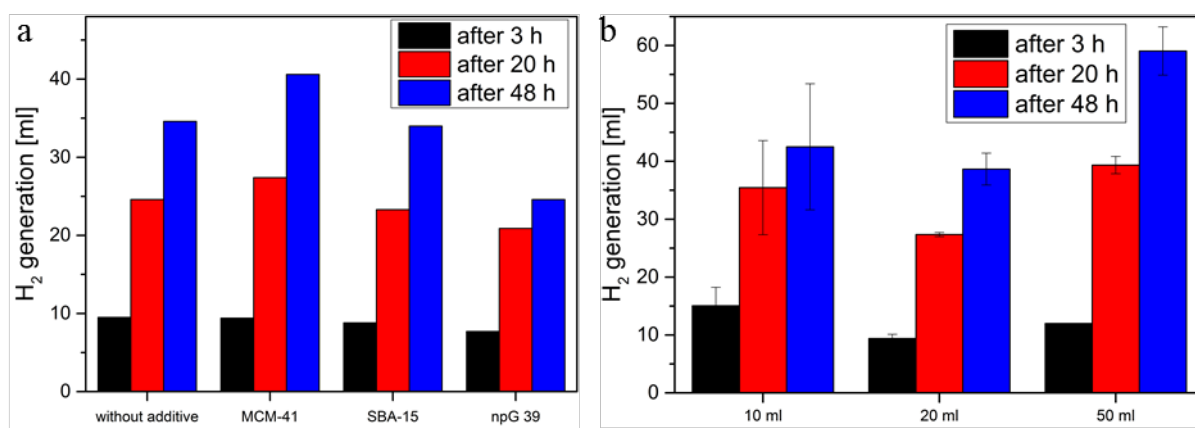


Figure 3.4 Investigation of the influence of the various silica additives (a) and the amount of THF/TEA/H₂O (3:2:1) (b) on the photocatalytic system. Experiments have been performed at least twice and the averages are shown. Differences between the measurements of Fig.3.4a were between 1 and 7%.

Experimental conditions: 10 μ mol CuI, 15 μ mol Ir-PS, 20 μ mol bpy, 11.4 mg additive, THF:TEA:H₂O = 3:2:1, 1.5 W Xe-light irradiation with >385 nm, 25 $^{\circ}$ C, gas volumes determined by automatic gas burettes and corrected by blank volume (2 mL).²¹¹

After defining the optimal conditions for the photocatalytic hydrogen generation by addition of a silica, the long-term stability was investigated applying CuI, Ir-PS, MCM-41 in 50 ml

THF/TEA/H₂O (3:2:1). Noteworthy, in the presence of the stabilizing ligand bpy, a hydrogen volume of about 90 ml after 160 h was obtained by the CuI/MCM-41 system and was still active at that time. In comparison, the non-supported system was already rarely active after 20 h illumination under the same conditions.

HAADF-TEM images of the catalyst, received after different reaction times during this long-term experiment, are shown in Figure 3.5. EDX analysis ensured a deposition of copper particles and/or agglomerates on the silica support. This copper deposition on the support was not observed in every experiment in 10 ml THF/TEA/H₂O which might explain the worse reproducibility of this system. In 50 ml reaction media, copper nanoparticles of 5-10 nm arose *in situ* during the first 48 h (Fig. 3.5b) and partially formed agglomerates (Fig. 3.5a). These copper species were decorated with iridium nanoparticles of about 2 nm. During the photocatalytic reaction the copper as well as the iridium particle sizes did not increase noticeably concluding a stabilization of the particles' growth during this long-term investigation.

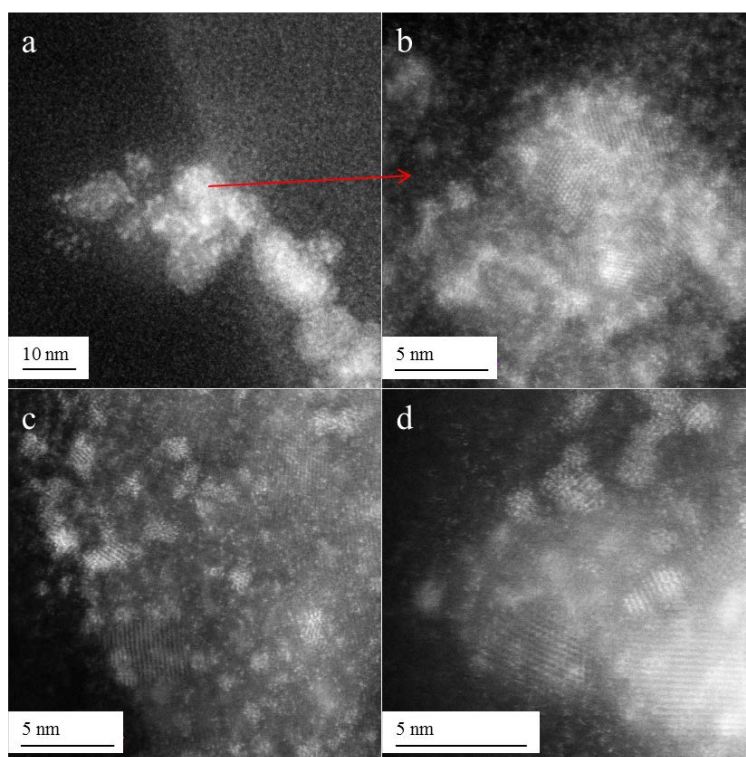


Figure 3.5 HAADF-TEM images of the IrPS/CuI/MCM-41 system in 50 ml THF:TEA:H₂O 3:2:1 (volume based) after proton reduction reaction after 48 h (a) and (b), after 96 h (c) and after 164 h (d).²¹¹

After determination of an active and stable catalyst, recycling experiments were performed to evaluate the catalysts' ability for separation and reuse (Figure 3.6). Therefore, the *in situ* generated catalyst was separated from the reaction mixture by centrifugation and decantation, washed and afterwards reused with fresh Ir-PS under the same conditions. Within the initial

and the consecutive 4 recycling steps only a small decrease in hydrogen generation was observed. Remarkably, the activity of the initial *in situ* formed material was partially slightly lower compared to the recycled ones, especially at the beginning of the respective reaction. This suggests the formed particles were mainly responsible for the hydrogen generation instead of the initial homogeneous CuI system. Finally, all recycling experiments resulted in a catalyst lifetime of more than 400 h.

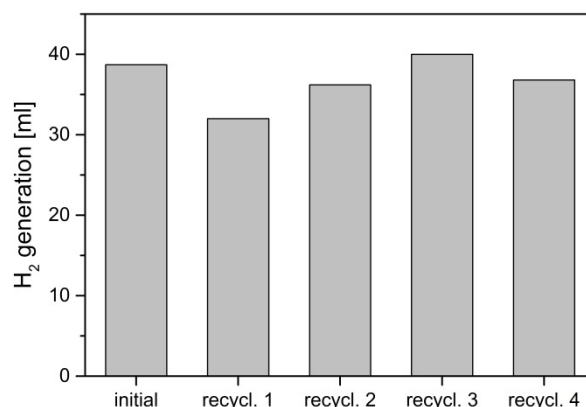


Figure 3.6 Recycling experiments: 10 μmol Cu from the prepared material; 15 μmol Ir-PS added after every run; 20 mL THF:TEA:H₂O (3:2:1, volume based); irradiation with 300 W Xe-lamp Lot Oriel 1.5W; ≥ 385 nm; manual burette.²¹¹

In conclusion, the previously developed system consisting of CuI as WRC precursor, [Ir(ppy)₂(bpy)]PF₆ as PS and TEA as the sacrificial reagent was improved regarding the photocatalytic hydrogen generation by the investigation of *ex situ* and *in situ* prepared silica supported copper catalysts. Thereby, a higher catalytic activity was achieved and an enhanced stability and recyclability of the system were reached by the addition of a supporting silica-based material. Especially the *ex situ* prepared catalysts were fully characterized in detail to ensure the identification of structural differences. Thus, structure-activity relations could be made.

Besides photocatalytic hydrogen generation, the second major aim of this thesis was the reduction of CO₂ to CO, which is of interest for the production of so-called sun fuels. Therefore, various metal-doped highly porous TiO₂ aerogels were synthesized, characterized in detail and investigated in aqueous CO₂ photoreduction.²¹²

Commonly, investigations of photocatalytic reduction reactions in the presence of the semiconductor TiO₂ are performed with the commercially available material P25 (Evonik industries). For this study highly porous TiO₂ aerogels (AG) with the addition of different co-catalysts were synthesized as previously described.^{213, 214} Thereby, co-catalysts based on Pt, Ru, Co, Cu and Mn were attached to the surface of TiO₂ AG. Standard methods such as N₂-sorption, XRD and TEM were used to identify the structural properties of the aerogels. N₂-

physisorption measurements revealed a specific surface area of the pure TiO₂-AG of about 480 m²/g which is almost 10 times higher compared to TiO₂-P25 (56 m²/g). The reasons for this huge difference are the larger particles and their random aggregation compared to the defined wire-like structure of the aerogel which was also observed in the TEM images. XRD analysis indicated nanosized crystallites of the anatase phase for the TiO₂ aerogel. Furthermore, FT-IR- and x-ray photoelectron spectroscopy (XPS) revealed a six times higher amount of hydroxyl groups on the surface of the aerogel compared to P25. Table 3.3 summarizes the results of the photocatalytic CO₂ reduction which have been performed in liquid phase at room temperature under UV-A/vis (320-500 nm) irradiation without the addition of an external sacrificial reductant. In all investigations no CH₄ or any other gaseous (except CO and H₂) or liquid products could be detected via GC/TCD, GC-MS and capillary electrophoresis. Blank measurements in the absence of CO₂ and light irradiation, respectively, showed no identification of any carbon products concluding that the produced CO was generated by reduction of CO₂ and not by any residuals of the catalyst. In contrast to commercially available TiO₂ (Table 3.3, entries 1 and 2) the synthesized TiO₂-AG showed some activity, albeit mainly for water reduction (entry 3). Then, 6 wt% of the co-catalysts Ru, Co and Cu respectively, were loaded on the TiO₂-AG: Co prevented both reduction reactions (entry 5), whereby Ru (entry 4) and Cu (entry 6) enhanced the activity towards H₂ and CO generation. When the copper loading was reduced from 6.3 to 0.3 wt% (entry 7), CO production was significantly increased due to a higher dispersion and smaller co-catalyst particles on the surface of the semiconductor. Adding the same amount of Pt (entry 8) or Mn (entry 9) as co-catalyst instead of Cu, lower amounts of CO were detected. H₂ generation increased in the presence of Pt/TiO₂-AG because Pt as co-catalyst promotes this competing reaction.^{163, 169, 172} Based on these results, further investigations as well as mechanistic studies were performed on the Cu/TiO₂ system. Although the best catalytic performance was achieved with 0.3_Cu/TiO₂-AG, the following photocatalytic and characteristic measurements were done in the presence of 6.3_Cu/TiO₂-AG due to a clearer and better interpretation of the analysis with respect to the higher copper content. As XRD, XPS and TEM analysis showed copper was already homogeneously and extremely finely dispersed on the surface of TiO₂-AG in the material 6.3_Cu/TiO₂-AG concluding a copper identification in the dispersion is very challenging.

Table 3.3 Photocatalytic reduction of CO₂ in H₂O with various TiO₂ and M/TiO₂ catalysts.

Entry	Catalyst	Reaction time [h]	Amount _{H₂} [μ l] (Activity [μ mol·g _{cat} ⁻¹ ·h ⁻¹])	Amount _{CO} [μ l] (Activity [μ mol·g _{cat} ⁻¹ ·h ⁻¹])
1	TiO ₂ -P25	4	n.d.	n.d.
2	TiO ₂ Anatase	4	n.d.	n.d.
3	TiO ₂ -AG	4	240 (200)	1.8 (1.5)
4	10_Ru/TiO ₂ -AG	4	650 (540)	6.7 (5.6)
5	10_Co/TiO ₂ -AG	4	n.d.	n.d.
6	6.3_Cu/TiO ₂ -AG	4	530 (430)	6.2 (5.1)
7	0.3_Cu/TiO ₂ -AG	4	600 (490)	13.2 (10.9)
8	0.4_Pt/TiO ₂ -AG	4	700 (580)	6.7 (6.7)
9	0.3_Mn/TiO ₂ -AG	4	540 (430)	4.6 (5.1)
10	6.3_Cu/TiO ₂ -AG	6	580 (320)	6.6 (3.6)
11	6.3_Cu/TiO ₂ -AG	20	750 (120)	7.5 (1.2)
12	6.3_Cu/TiO ₂ -AG	0.5	41 (290)	4.3 (28)
13	-	4	n.d.	n.d.
14	6.3_Cu/TiO ₂ -AG ^[a]	4	n.d.	n.d.
15	6.3_Cu/TiO ₂ -AG ^[b]	4	550 (450)	n.d.

All experiments have been performed at least twice and the averages are shown. Differences between the measurements are between 1 and 14%. Experimental conditions: 12.6 mg catalyst, 7.5 ml H₂O, 60 min flushing with CO₂, 20 °C, Lumatec lamp: 2.5 W output, Filter 320-500 nm, gases analyzed by GC, Activity = n(gas)/(m(catalyst)*t).

n.d.: not detectable.

[a] without irradiation.

[b] without CO₂.

After identification of Cu/TiO₂-AG as the most suitable catalyst, the reaction time was varied (entries 10-12). Here, only a small amount of additional reduction product was obtained after increased irradiation time. However, the activity was significantly higher performing the reaction only half an hour concluding the catalyst deactivated during the photoreduction.

In situ EPR and XANES investigations were used to determine the oxidation state of copper during the photocatalytic reduction (Fig. 3.7). Both analytics presented a Cu(II)-species in 6.3_Cu/TiO₂-AG before the irradiation which confirmed the XPS analysis of the solid material. During the first seconds of the reaction the intensity of the EPR signal for Cu(II) decreased rapidly indicating a reduction of Cu(II) to Cu(I) or Cu(0) (Fig. 3.7a). Which oxidation state was formed, cannot be identified *via* EPR because both species are EPR silent. Furthermore, a change of the typical absorption edge of Cu(II) (Fig. 3.7b, grey) was observed by XANES investigations of the catalyst in suspension during the reaction. After 4 h the spectra of Cu/TiO₂-AG corresponded to that of the reference Cu(0). In conclusion, the results of the EPR and XANES measurements revealed a reduction of Cu(II) to Cu(I) or Cu(0) within the first minutes of the photocatalytic reaction whereby after 4 h a complete reduction to Cu(0) was generated which might be the deactivating species.

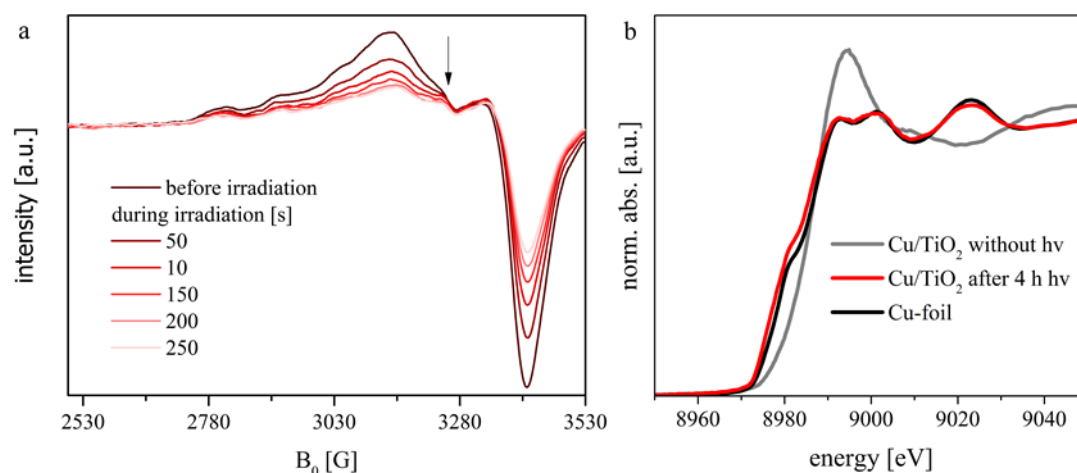


Figure 3.7 Following of the oxidation state of Cu in 6.3_Cu/TiO₂-AG in aqueous suspension under photocatalytic conditions via *in situ* EPR (a) and XANES (b).²¹²

Afterwards, investigations for the photocatalytic CO₂ reduction of this catalyst were performed in the presence of different amounts of oxygen to inhibit the formation of the potentially deactivating Cu(0) species (Fig. 3.8). Obviously, at first it might be irrational to perform CO₂ reduction in the presence of O₂ because the reducibility of latter molecule is much easier which is mentioned in detail in chapter 1.2.6.

Nevertheless, by the addition of 0.5 vol% O₂ to the CO₂ atmosphere a three times higher amount of produced CO could be obtained after 20 h irradiation in the presence of the 6.3_Cu/TiO₂-AG catalyst. Also, hydrogen was still generated under these conditions but the ratio of CO/H₂ strongly increased compared to O₂-free investigations. To the best of our knowledge this presents the first time that CO₂ photoreduction was improved in the presence of oxygen. The reason for the change in selectivity might be the re-oxidation of H₂ to H₂O by adding O₂. A further increase of the O₂ amount to the CO₂ atmosphere led to a deactivation of the catalyst and/or to a re-oxidation of CO to CO₂. Additionally, TiO₂-P25 and TiO₂-AG were also investigated under these conditions. TiO₂-P25 was still not active. Interestingly, TiO₂-AG indeed showed some activity towards H₂ and CO generation, but the amount of both compounds decreased in the presence of O₂ compared to the O₂-free test. This was in contrast to the investigations with 6.3_Cu/TiO₂-AG and demonstrated the importance of the copper co-catalyst and the influence of O₂ on the active copper species. Therefore, *operando* UV-vis measurements in the presence of various amounts of O₂ were performed to analyze the effect of O₂ on the copper species and thus on the photocatalytic CO₂ reduction.

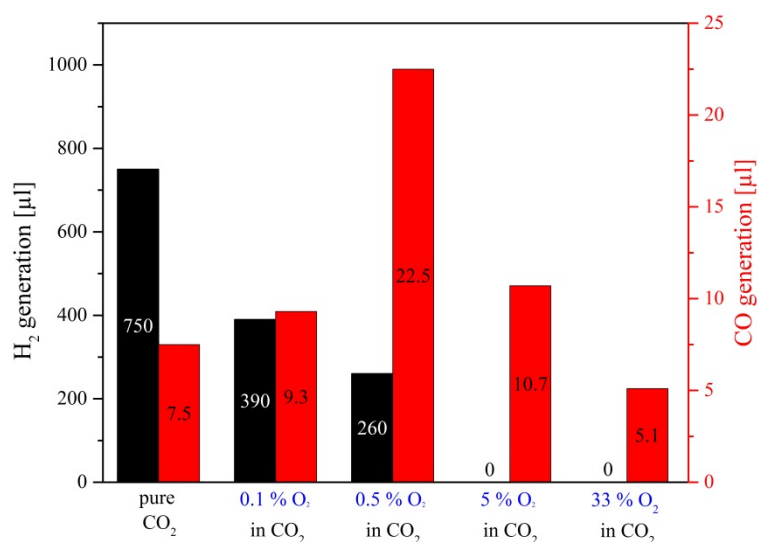


Figure 3.8 Photocatalytic CO₂ reduction with 6.3_Cu/TiO₂-AG catalyst by using different CO₂/O₂ mixtures. Conditions: catalyst: 12.6 mg 6.3_Cu/TiO₂-AG, medium 7.5 ml H₂O, 20 °C, 20 h, Lumatec lamp: 2.5 W output, Filter 320-500 nm.²¹²

First, the initial Cu(II) was reduced to Cu(I) within the first minutes under O₂-free atmosphere. However, also Cu(0) was rapidly generated but the intensity of the Cu(I) absorption band decreased almost immediately. In the presence of 0.5 vol% O₂ the reduction of Cu(II) to Cu(I) was also identified within the first minutes of the reaction. Indeed, the signal of Cu(I) was much longer present compared to the investigation in pure CO₂. By adding a higher amount of O₂ (>5 vol%) Cu(II) was identified as the main oxidation state during the whole reaction. Plausibly, higher amounts of O₂ led to a slower and inhibited reduction of Cu(II) to Cu(I) and Cu(0) concluding Cu(I) was the active species in this investigations. These findings were also confirmed by the product analysis at the beginning and at the end of the photocatalytic reaction. Within the first 10 minutes the amount of CO was higher in pure CO₂ and still lower in the presence of 0.5 vol% O₂. However, after 30 min the CO generation nearly stagnated in 100% CO₂ but was still in progress in the presence of O₂. Thus, there was also a significantly higher CO amount after 20 h due to the higher stability of this active Cu(I) species.

As mentioned in chapter 1.2.6 (oxidation reaction), the back reaction of this photocatalytic progress is still a challenging task. In fact, without the presence of any sacrificial reductant in the aqueous system, an oxidation of H₂O would have been expected. Unfortunately, it was not possible to detect any O₂ in the gas phase using GC/TCD or an optical O₂ detection set-up. Furthermore, H₂O₂ as an alternative oxidation product could also not be identified *via* a typical H₂O₂ detection test. Of course, generated O₂ might also prevent the premature formation of the deactivated Cu(0) species in the presence of the Cu/TiO₂-AG catalyst but then also the less active TiO₂-AG might show some traces of O₂. Furthermore, as other

researchers had proposed previously, a re-oxidation of the products CO and H₂ might also be possible. Hence, investigations in the presence of 0.5 vol% O₂ in the CO₂ atmosphere were performed with an oxygen sensor (Clark electrode) to get more information on the generated oxygen. Figure 3.9 shows the trends of the O₂ concentration during the photocatalytic reaction in the presence of various TiO₂ and Cu/TiO₂-AG, respectively. In all investigations a light-induced O₂ uptake was observed. TiO₂-P25 demonstrated the lowest consumption of O₂ which was less pronounced if the material was calcined at 500 °C. TiO₂-AG and Cu/TiO₂-AG captured a much higher amount of O₂ without any different behavior which indicated an O₂ photoadsorption primarily by the aerogel. As mentioned in the section of the aerogel structural characteristics, this material possessed a significantly higher number of hydroxyl groups and the trend in O₂ uptake correlates with that property. Undoubtedly, calcination of a TiO₂ lowers the amount of the hydroxyl surface groups resulting in a lower O₂ consumption. Consequently, this distinctive structural feature of the TiO₂ aerogel led to the increased O₂ photoadsorption.

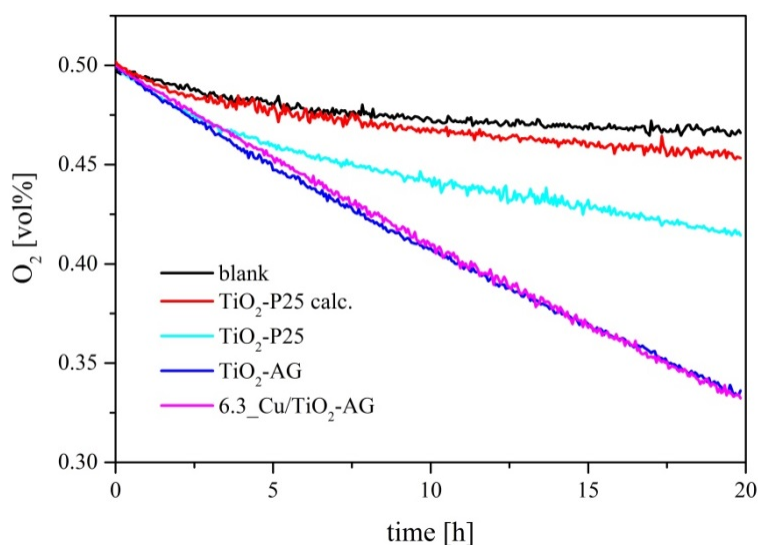


Figure 3.9 Following the O₂ amount with an oxygen sensor during the photocatalytic reduction in 0.5 vol% O₂/CO₂ in the presence of various materials.²¹²

It is known from literature that hydroxyl groups can be released and converted to super- and peroxo species by photoadsorption of O₂ on the TiO₂.²¹⁵⁻²¹⁷ Titration investigations before and after a long-term photoreaction (5 d reaction time, 6.3_Cu/TiO₂-AG, 0.5 vol% O₂/CO₂ atmosphere) were performed to compare the number of hydroxyl groups on the aerogel surface. Indeed, the amount of these groups was reduced by roughly one half. Furthermore, *in situ* EPR measurements in the presence of TiO₂-AG revealed the generation of released •OH radicals during the irradiation. Finally, analyzing the suspension after the long-term photoreaction peroxide was determined *via* a colouring enzymatic reaction in the suspension

and to a significantly lower amount in the isolated liquid phase. This indicated that most of the peroxo species were bound on the TiO_2 surface. Moreover, this was also observed after a standard photoreaction with $\text{Cu/TiO}_2\text{-AG}$ in pure CO_2 . Thus, the consumption of hydroxyl groups, the detection of $\bullet\text{OH}$ radicals and the formation of peroxo species on the semiconductor's surface evidenced the surface hydroxyl groups to be photo-oxidized and thus to be the electron source for the reduction counter reaction. Obviously, the regeneration of these hydroxyl groups has to be solved to generate a real photocatalytic overall process.

Due to all these photocatalytic investigations under different conditions and the interaction of various standard, *in situ* and *operando* analytical methods it was possible to propose the following mechanism for the photocatalytic process of aqueous CO_2 :

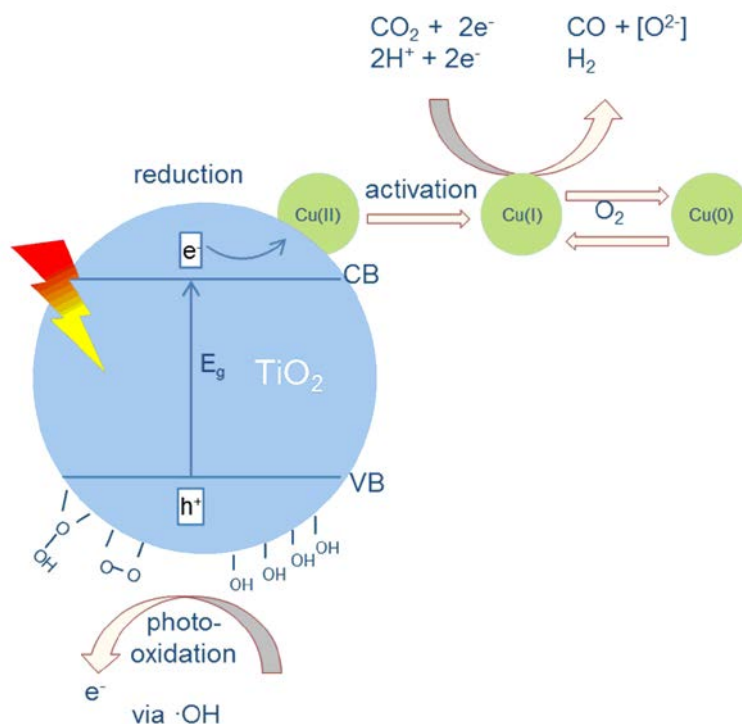


Figure 3.10 Proposed reaction scheme for photocatalytic reduction of CO_2 with H_2O on $\text{Cu/TiO}_2\text{-AG}$. (Photooxidation: $\bullet\text{OH}$ radical intermediate (via $\bullet\text{OH}$), e^- product)

Thereby, electrons from the valence band are excited to the conduction band by light absorption. These electrons are trapped by the co-catalyst copper to prevent the electron-hole recombination. The initial Cu(II) -species is activated to Cu(I) to catalyze the CO_2 to CO reduction. In the presence of small amounts of oxygen the reduction to the deactivating Cu(0) species is inhibited and Cu(I) is stabilized. The electrons for this reduction process are provided by the photo-oxidation of the TiO_2 surface hydroxyl groups.

4 References

1. M. Sterner and I. Stadler, in *Energiespeicher - Bedarf, Technologien, Integration*, Springer Vieweg, Berlin, Heidelberg, **2014**, pp. 161-574.
2. F. Zhang, P. Zhao, M. Niu and J. Maddy, *Int. J. Hydrogen Energ.*, **2016**, *41*, 14535-14552.
3. R. Amirante, E. Cassone, E. Distaso and P. Tamburrano, *Energy Convers. Manage.*, **2017**, *132*, 372-387.
4. S. E. Hosseini and M. A. Wahid, *Renew. Sust. Energ. Rev.*, **2016**, *57*, 850-866.
5. L. Bertuccioli, A. Chan, D. Hart, F. Lehner, B. Madden and E. Standen, *Elem. Energ.*, **2014**.
6. O. Machhammer, A. Bode and W. Hormuth, *Chem. Eng. Technol.*, **2016**, *39*, 1185-1193.
7. C. Acar, I. Dincer and G. F. Naterer, *Int. J. Energ. Res.*, **2016**, *40*, 1449-1473.
8. A. Bazzanella and D. Krämer, in *Technologien für Nachhaltigkeit und Klimaschutz - Chemische Prozesse und stoffliche Nutzung von CO₂*, Dechema Gesellschaft für Chemische Technik und Biotechnologie e.V., **2017**, p. 124.
9. M. Schneider, M. Romer, M. Tschudin and H. Bolio, *Cem. Concr. Res.*, **2011**, *41*, 642-650.
10. V. G. Lisienko, A. V. Lapteva, Y. N. Chesnokov and V. V. Lugovkin, *Steel Transl.*, **2015**, *45*, 623-626.
11. A. Al-Mamoori, A. Krishnamurthy, A. A. Rownaghi and F. Rezaei, *Energy Technol.*, **2017**, *5*, 834-849.
12. W. Zhang, Y. Hu, L. Ma, G. Zhu, Y. Wang, X. Xue, R. Chen, S. Yang and Z. Jin, *Adv. Sci.*, **2018**, *5*, 1700275.
13. Y. Amao, *Sustainable Energy Fuels*, **2018**, *2*, 1928-1950.
14. A. Alissandratos and C. J. Easton, *Beilstein J. Org. Chem.*, **2015**, *11*, 2370-2387.
15. S. N. Habisreutinger, L. Schmidt-Mende and J. K. Stolarczyk, *Angew. Chem. Int. Ed.*, **2013**, *52*, 7372-7408.
16. H. Takeda, C. Cometto, O. Ishitani and M. Robert, *ACS Catal.*, **2017**, *7*, 70-88.
17. S. Nahar, M. F. M. Zain, A. A. H. Kadhum, H. A. Hasan and M. R. Hasan, *Materials*, **2017**, *10*, 629-654.
18. N. Fajrina and M. Tahir, *Int. J. Hydrogen Energ.*, **2019**, *44*, 540-577.
19. M. Bowker, *Green Chem.*, **2011**, *13*, 2235-2246.
20. J. Schneider and D. W. Bahnemann, *J. Phys. Chem. Lett.*, **2013**, *4*, 3479-3483.
21. H. Bahruji, M. Bowker, P. R. Davies and F. Pedrono, *Appl. Catal., B*, **2011**, *107*, 205-209.
22. Y. Pellegri and F. Odobel, *C. R. Chim.*, **2017**, *20*, 283-295.
23. P. Sitte, E. W. Weiler, J. W. Kadereit, A. Beresinsky and C. Körner, *Lehrbuch der Botanik*, Spektrum Akademischer Verlag Heidelberg Berlin, **2002**.
24. K. Kalyanasundaram, J. Kiwi and M. Grätzel, *Helv. Chim. Acta*, **1978**, *61*, 2720-2730.
25. M. Kirch, J.-M. Lehn and J.-P. Sauvage, *Helv. Chim. Acta*, **1979**, *62*, 1345-1384.
26. C. V. Krishnan and N. Sutin, *J. Am. Chem. Soc.*, **1981**, *103*, 2141-2142.
27. A. Kudo and Y. Miseki, *Chem. Soc. Rev.*, **2009**, *38*, 253-278.
28. X. Chen, S. Shen, L. Guo and S. S. Mao, *Chem. Rev.*, **2010**, *110*, 6503-6570.
29. V. Artero, M. Chavarot-Kerlidou and M. Fontecave, *Angew. Chem.*, **2011**, *123*, 7376-7405.

30. P. Du and R. Eisenberg, *Energy Environ. Sci.*, **2012**, 5, 6012-6021.
31. W. T. Eckenhoff and R. Eisenberg, *Dalton T.*, **2012**, 41, 13004-13021.
32. F. Gärtner, B. Sundararaju, A.-E. Surkus, A. Boddien, B. Loges, H. Junge, P. H. Dixneuf and M. Beller, *Angew. Chem. Int. Ed.*, **2009**, 48, 9962-9965.
33. F. Gärtner, B. Sundararaju, A.-E. Surkus, A. Boddien, B. Loges, H. Junge, P. H. Dixneuf and M. Beller, *Angew. Chem.*, **2009**, 121, 10147-10150.
34. O. R. Luca, J. D. Blakemore, S. J. Konezny, J. M. Praetorius, T. J. Schmeier, G. B. Hunsinger, V. S. Batista, G. W. Brudvig, N. Hazari and R. H. Crabtree, *Inorg. Chem.*, **2012**, 51, 8704-8709.
35. M. Wang and L. Sun *ChemSusChem*, **2010**, 3, 551-554.
36. H. Junge, Z. Codolà, A. Kammer, N. Rockstroh, M. Karnahl, S.-P. Luo, M.-M. Pohl, J. Radnik, S. Gatla, S. Wohlrab, J. Lloret, M. Costas and M. Beller, *J. Mol. Catal. A: Chem.*, **2014**, 395, 449-456.
37. M. Jung, J. N. Hart, J. Scott, Y. H. Ng, Y. Jiang and R. Amal, *Appl. Catal., A*, **2016**, 521, 190-201.
38. M. Jung, J. Scott, Y. H. Ng, Y. Jiang and R. Amal, *Int. J. Hydrogen Energ.*, **2014**, 39, 12499-12506.
39. K. Lalitha, G. Sadanandam, V. D. Kumari, M. Subrahmanyam, B. Sreedhar and N. Y. Hebalkar, *J. Phys. Chem. C*, **2010**, 114, 22181-22189.
40. Y. Liu, Z. Wang and W. Huang, *Appl. Surf. Sci.*, **2016**, 389, 760-767.
41. I. Tamiolakis, I. T. Papadas, K. C. Spyridopoulos and G. S. Armatas, *RSC Adv.*, **2016**, 6, 54848-54855.
42. Z. Wang, Y. Liu, D. J. Martin, W. Wang, J. Tang and W. Huang, *Phys. Chem. Chem. Phys.*, **2013**, 15, 14956-14960.
43. Y. Wu, G. Lu and S. Li, *Catal. Lett.*, **2009**, 133, 97.
44. V. V. Pham, D. P. Bui, H. H. Tran, M. T. Cao, T. K. Nguyen, Y. S. Kim and V. H. Le, *RSC Adv.*, **2018**, 8, 12420-12427.
45. L. Pan, J. H. Kim, M. T. Mayer, M.-K. Son, A. Ummadisingu, J. S. Lee, A. Hagfeldt, J. Luo and M. Grätzel, *Nat. Cat.*, **2018**, 1, 412-420.
46. Y. Ghayeb, M. M. Momeni and M. Menati, *J. Mater. Sci. Mater. El.*, **2017**, 28, 7650-7659.
47. J. Han, X. Zong, X. Zhou and C. Li, *RSC Adv.*, **2015**, 5, 10790-10794.
48. P. E. de Jongh, D. Vanmaekelbergh and J. J. Kelly, *Chem. Commun.*, **1999**, 1069-1070.
49. Y. Kwon, A. Soon, H. Han and H. Lee, *J. Mater. Chem. A*, **2015**, 3, 156-162.
50. L. L. Tinker, N. D. McDaniel, P. N. Curtin, C. K. Smith, M. J. Ireland and S. Bernhard, *Chem. Eur. J.*, **2007**, 13, 8726-8732.
51. A. Neubauer, G. Grell, A. Friedrich, S. I. Bokarev, P. Schwarzbach, F. Gärtner, A.-E. Surkus, H. Junge, M. Beller, O. Kühn and S. Lochbrunner, *J. Phys. Chem. Lett.*, **2014**, 5, 1355-1360.
52. E. D. Cline, S. E. Adamson and S. Bernhard, *Inorg. Chem.*, **2008**, 47, 10378-10388.
53. X. Li, J. Yu, J. Low, Y. Fang, J. Xiao and X. Chen, *J. Mater. Chem. A*, **2015**, 3, 2485-2534.
54. L. Clarizia, D. Russo, I. Di Somma, R. Andreozzi and R. Marotta, *Energies*, **2017**, 10, 1624.
55. Y. Izumi, in *Advances in CO₂ Capture, Sequestration, and Conversion*, ACS Symposium Series, **2015**, vol. 1194, pp. 1-46.
56. J. Ran, M. Jaroniec and S.-Z. Qiao, *Adv. Mat.*, **2018**, 30, 1704649.

-
57. A. Nikokavoura and C. Trapalis, *Appl. Surf. Sci.*, **2017**, *391*, 149-174.
58. A. Fujishima and K. Honda, *Nature*, **1972**, *238*, 37-38.
59. T. Inoue, A. Fujishima, S. Konishi and K. Honda, *Nature*, **1979**, *277*, 637-638.
60. Y. Izumi, *Coord. Chem. Rev.*, **2013**, *257*, 171-186.
61. A. Hagfeldt and M. Graetzel, *Chem. Rev.*, **1995**, *95*, 49-68.
62. S. Chen and L.-W. Wang, *Chem. Mater.*, **2012**, *24*, 3659-3666.
63. S. Kohtani, E. Yoshioka and H. Miyabe, *Hydrogenation*, IntechOpen, **2012**.
64. X. Li, R. Shen, S. Ma, X. Chen and J. Xie, *Appl. Surf. Sci.*, **2018**, *430*, 53-107.
65. S. Xie, Q. Zhang, G. Liu and Y. Wang, *Chem. Commun.*, **2016**, *52*, 35-59.
66. M. A. Henderson, *Surf. Sci. Rep.*, **2011**, *66*, 185-297.
67. S. H. Szczepankiewicz, A. J. Colussi and M. R. Hoffmann, *J. Phys. Chem. B*, **2000**, *104*, 9842-9850.
68. A. Fujishima, X. Zhang and D. A. Tryk, *Surf. Sci. Rep.*, **2008**, *63*, 515-582.
69. A. Mills and N. Wells, *Chem. Soc. Rev.*, **2015**, *44*, 2849-2864.
70. A. Mills and S. K. Lee, *Platinum Met. Rev.*, **2003**, *47*, 2-12.
71. H. Zhang, G. Chen and D. W. Bahnemann, *J. Mater. Chem.*, **2009**, *19*, 5089-5121.
72. J. Theerthagiri, S. Chandrasekaran, S. Salla, V. Elakkiya, R. A. Senthil, P. Nithyadharseni, T. Maiyalagan, K. Micheal, A. Ayeshamariam, M. V. Arasu, N. A. Al-Dhabi and H.-S. Kim, *J. Solid State Chem.*, **2018**, *267*, 35-52.
73. A. Hagfeldt, G. Boschloo, L. Sun, L. Kloo and H. Pettersson, *Chem. Rev.*, **2010**, *110*, 6595-6663.
74. P. Chowdhury, H. Gomaa and A. K. Ray, in *Sustainable Nanotechnology and the Environment: Advances and Achievements*, American Chemical Society, **2013**, vol. 1124, pp. 231-266.
75. P. A. Sant and P. V. Kamat, *Phys. Chem. Chem. Phys.*, **2002**, *4*, 198-203.
76. F. Liao, Z. Zeng, C. Eley, Q. Lu, X. Hong and S. C. E. Tsang, *Angew. Chem. Int. Ed.*, **2012**, *51*, 5832-5836.
77. J. R. McKone, E. L. Warren, M. J. Bierman, S. W. Boettcher, B. S. Brunschwig, N. S. Lewis and H. B. Gray, *Energy Environ. Sci.*, **2011**, *4*, 3573-3583.
78. S. W. Boettcher, E. L. Warren, M. C. Putnam, E. A. Santori, D. Turner-Evans, M. D. Kelzenberg, M. G. Walter, J. R. McKone, B. S. Brunschwig, H. A. Atwater and N. S. Lewis, *J. Am. Chem. Soc.*, **2011**, *133*, 1216-1219.
79. A. Zhygotsky, E. Rynda, V. Kochkodan, M. Zagorny, T. Lobunets, L. Kuzmenko and A. Ragulya, *J. Chem. Chem. Eng.*, **2013**, *7*, 949-957.
80. K. Kočí, L. Obalová, L. Matějová, D. Plachá, Z. Lacný, J. Jirkovský and O. Šolcová, *Appl. Catal., B*, **2009**, *89*, 494-502.
81. R. D. Richardson, E. J. Holland and B. K. Carpenter, *Nat. Chem.*, **2011**, *3*, 301-303.
82. V. P. Indrakanti, J. D. Kubicki and H. H. Schobert, *Energy Environ. Sci.*, **2009**, *2*, 745-758.
83. J. Qiao, Y. Liu, F. Hong and J. Zhang, *Chem. Soc. Rev.*, **2014**, *43*, 631-675.
84. P. S. Surdhar, S. P. Mezyk and D. A. Armstrong, *J. Phys. Chem.*, **1989**, *93*, 3360-3363.
85. M. Anpo, H. Yamashita, Y. Ichihashi and S. Ehara, *J. Electroanal. Chem.*, **1995**, *396*, 21-26.

-
86. K. Iizuka, T. Wato, Y. Miseki, K. Saito and A. Kudo, *J. Am. Chem. Soc.*, **2011**, *133*, 20863-20868.
87. L. Liu, Z. Liu, H. Sun and X. Zhao, *Appl. Surf. Sci.*, **2017**, *399*, 469-479.
88. Y. J. Jang, J.-W. Jang, J. Lee, J. H. Kim, H. Kumagai, J. Lee, T. Minegishi, J. Kubota, K. Domen and J. S. Lee, *Energy Environ. Sci.*, **2015**, *8*, 3597-3604.
89. H. Shi, G. Chen, C. Zhang and Z. Zou, *ACS Catal.*, **2014**, *4*, 3637-3643.
90. J. Lin, Z. Pan and X. Wang, *ACS Sustain. Chem. Eng.*, **2014**, *2*, 353-358.
91. S. Zhu, L. Guo, P. Li, B. Zhang, G. Zhao and T. He, *Catal. Today*, **2019**.
92. Q. Shi, Z. Li, L. Chen, X. Zhang, W. Han, M. Xie, J. Yang and L. Jing, *Appl. Catal., B*, **2019**, *244*, 641-649.
93. H. J. Freund and R. P. Messmer, *Surf. Sci.*, **1986**, *172*, 1-30.
94. H. J. Freund and M. W. Roberts, *Surf. Sci. Rep.*, **1996**, *25*, 225-273.
95. C. Peng, G. Reid, H. Wang and P. Hu, *J. Chem. Phys.*, **2017**, *147*, 030901.
96. S. Xie, Y. Wang, Q. Zhang, W. Fan, W. Deng and Y. Wang, *Chem. Commun.*, **2013**, *49*, 2451-2453.
97. S. Xie, Y. Wang, Q. Zhang, W. Deng and Y. Wang, *ACS Catal.*, **2014**, *4*, 3644-3653.
98. J. Lee, D. C. Sorescu and X. Deng, *J. Am. Chem. Soc.*, **2011**, *133*, 10066-10069.
99. C.-T. Yang, B. C. Wood, V. R. Bhethanabotla and B. Joseph, *Phys. Chem. Chem. Phys.*, **2015**, *17*, 25379-25392.
100. J. Mao, T. Peng, X. Zhang, K. Li, L. Ye and L. Zan, *Catal. Sci. Technol.*, **2013**, *3*, 1253-1260.
101. Q. Liu, D. Wu, Y. Zhou, H. Su, R. Wang, C. Zhang, S. Yan, M. Xiao and Z. Zou, *ACS Appl. Mater. Inter.*, **2014**, *6*, 2356-2361.
102. S. Tan, Y. Zhao, J. Zhao, Z. Wang, C. Ma, A. Zhao, B. Wang, Y. Luo, J. Yang and J. Hou, *Phys. Rev. B*, **2011**, *84*, 155418.
103. S. Huygh, A. Bogaerts and E. C. Neyts, *J. Phys. Chem. C*, **2016**, *120*, 21659-21669.
104. M. Kanemoto, H. Hosokawa, Y. Wada, K. Murakoshi, S. Yanagida, T. Sakata, H. Mori, M. Ishikawa and H. Kobayashi, *J. Chem. Soc., Faraday Trans.*, **1996**, *92*, 2401-2411.
105. H. Fujiwara, H. Hosokawa, K. Murakoshi, Y. Wada, S. Yanagida, T. Okada and H. Kobayashi, *J. Phys. Chem. B*, **1997**, *101*, 8270-8278.
106. X. Meng, S. Ouyang, T. Kako, P. Li, Q. Yu, T. Wang and J. Ye, *Chem. Commun.*, **2014**, *50*, 11517-11519.
107. Y. Kohno, T. Tanaka, T. Funabiki and S. Yoshida, *Phys. Chem. Chem. Phys.*, **2000**, *2*, 5302-5307.
108. H. Tsuneoka, K. Teramura, T. Shishido and T. Tanaka, *J. Phys. Chem. C*, **2010**, *114*, 8892-8898.
109. H. He, P. Zapol and L. A. Curtiss, *Energy Environ. Sci.*, **2012**, *5*, 6196-6205.
110. K. Kočí, L. Obalová and O. Šolcová, *Chem. Process Eng.*, **2010**, *31*, 395-407.
111. I. A. Shkrob, N. M. Dimitrijevic, T. W. Marin, H. He and P. Zapol, *J. Phys. Chem. C*, **2012**, *116*, 9461-9471.
112. E. Barton Cole, P. S. Lakkaraju, D. M. Rampulla, A. J. Morris, E. Abelev and A. B. Bocarsly, *J. Am. Chem. Soc.*, **2010**, *132*, 11539-11551.
113. I. A. Shkrob, T. W. Marin, H. He and P. Zapol, *J. Phys. Chem. C*, **2012**, *116*, 9450-9460.

114. B. Fang, Y. Xing, A. Bonakdarpour, S. Zhang and D. P. Wilkinson, *ACS Sustain. Chem. Eng.*, **2015**, *3*, 2381-2388.
115. S. Jeong, W. D. Kim, S. Lee, K. Lee, S. Lee, D. Lee and D. C. Lee, *ChemCatChem*, **2016**, *8*, 1641-1645.
116. L. Liu, F. Gao, H. Zhao and Y. Li, *Appl. Catal., B*, **2013**, *134-135*, 349-358.
117. A. R. Khataee and M. B. Kasiri, *J. Mol. Catal. A: Chem.*, **2010**, *328*, 8-26.
118. D. M. Kannan and D. Sreenivasan, *Review of TiO₂ nanowires in dye sensitized solar cell*, **2015**.
119. C. Byrne, G. Subramanian and S. C. Pillai, *J. Environ. Chem. Eng.*, **2018**, *6*, 3531-3555.
120. F. Han, V. S. R. Kambala, M. Srinivasan, D. Rajarathnam and R. Naidu, *Appl. Catal., A*, **2009**, *359*, 25-40.
121. Z. Zhu, H. Cai and D.-W. Sun, *Trends Food Sci. Tech.*, **2018**, *75*, 23-35.
122. Y. Wang, A. Liu, D. Ma, S. Li, C. Lu, T. Li and C. Chen, *Catalysts*, **2018**, *8*, 355-379.
123. Y. Ma, X. Wang, Y. Jia, X. Chen, H. Han and C. Li, *Chem. Rev.*, **2014**, *114*, 9987-10043.
124. J. Cai, J. Shen, X. Zhang, Y. H. Ng, J. Huang, W. Guo, C. Lin and Y. Lai, *Small Methods*, **2019**, *3*, 1800184.
125. R. Marchand, L. Brohan and M. Tournoux, *Mater. Res. Bull.*, **1980**, *15*, 1129-1133.
126. H. Zhang and J. F. Banfield, *J. Mater. Chem.*, **1998**, *8*, 2073-2076.
127. M. Cargnello, T. R. Gordon and C. B. Murray, *Chem. Rev.*, **2014**, *114*, 9319-9345.
128. D. O. Scanlon, C. W. Dunnill, J. Buckeridge, S. A. Shevlin, A. J. Logsdail, S. M. Woodley, C. R. A. Catlow, M. J. Powell, R. G. Palgrave, I. P. Parkin, G. W. Watson, T. W. Keal, P. Sherwood, A. Walsh and A. A. Sokol, *Nat. Mater.*, **2013**, *12*, 798-801.
129. P. Bouras, E. Stathatos and P. Lianos, *Appl. Catal., B*, **2007**, *73*, 51-59.
130. A. Yamakata, J. J. M. Vequizo and H. Matsunaga, *J. Phys. Chem. C*, **2015**, *119*, 24538-24545.
131. X. Chen and S. S. Mao, *Chem. Rev.*, **2007**, *107*, 2891-2959.
132. S. Liu, H. Jia, L. Han, J. Wang, P. Gao, D. Xu, J. Yang and S. Che, *Adv. Mat.*, **2012**, *24*, 3201-3204.
133. H. Liu, Z. Bi, X.-G. Sun, R. R. Unocic, M. P. Paranthaman, S. Dai and G. M. Brown, *Adv. Mat.*, **2011**, *23*, 3450-3454.
134. J. Schneider, M. Matsuoka, M. Takeuchi, J. Zhang, Y. Horiuchi, M. Anpo and D. W. Bahnemann, *Chem. Rev.*, **2014**, *114*, 9919-9986.
135. M. R. Hoffmann, S. T. Martin, W. Choi and D. W. Bahnemann, *Chem. Rev.*, **1995**, *95*, 69-96.
136. D. S. Muggli and L. Ding, *Appl. Catal., B*, **2001**, *32*, 181-194.
137. R. R. Bacsá and J. Kiwi, *Appl. Catal., B*, **1998**, *16*, 19-29.
138. T. Ohno, K. Tokieda, S. Higashida and M. Matsumura, *Appl. Catal., A*, **2003**, *244*, 383-391.
139. X. Jiang, M. Manawan, T. Feng, R. Qian, T. Zhao, G. Zhou, F. Kong, Q. Wang, S. Dai and J. H. Pan, *Catal. Today*, **2018**, *300*, 12-17.
140. M. Pelaez, N. T. Nolan, S. C. Pillai, M. K. Seery, P. Falaras, A. G. Kontos, P. S. M. Dunlop, J. W. J. Hamilton, J. A. Byrne, K. O'Shea, M. H. Entezari and D. D. Dionysiou, *Appl. Catal., B*, **2012**, *125*, 331-349.
141. F. Zuo, L. Wang, T. Wu, Z. Zhang, D. Borchardt and P. Feng, *J. Am. Chem. Soc.*, **2010**, *132*, 11856-11857.

142. M. Xing, W. Fang, M. Nasir, Y. Ma, J. Zhang and M. Anpo, *J. Catal.*, **2013**, 297, 236-243.
143. A. Yamakata, J. J. M. Vequizo and M. Kawaguchi, *J. Phys. Chem. C*, **2015**, 119, 1880-1885.
144. X. Chang, T. Wang, P. Zhang, J. Zhang, A. Li and J. Gong, *J. Am. Chem. Soc.*, **2015**, 137, 8356-8359.
145. W. Tu, Y. Zhou and Z. Zou, *Adv. Mat.*, **2014**, 26, 4607-4626.
146. B. Kumar, J. M. Smieja, A. F. Sasayama and C. P. Kubiak, *Chem. Commun.*, **2012**, 48, 272-274.
147. S. Sato, T. Arai, T. Morikawa, K. Uemura, T. M. Suzuki, H. Tanaka and T. Kajino, *J. Am. Chem. Soc.*, **2011**, 133, 15240-15243.
148. K. Alenezi, S. K. Ibrahim, P. Li and C. J. Pickett, *Chem. Eur. J.*, **2013**, 19, 13522-13527.
149. Y. Liu, Y. Yang, Q. Sun, Z. Wang, B. Huang, Y. Dai, X. Qin and X. Zhang, *ACS Appl. Mater. Inter.*, **2013**, 5, 7654-7658.
150. X. Li, J. Yu, M. Jaroniec and X. Chen, *Chem. Rev.*, **2019**, 119, 3962-4179.
151. W. Hou, W. H. Hung, P. Pavaskar, A. Goeppert, M. Aykol and S. B. Cronin, *ACS Catal.*, **2011**, 1, 929-936.
152. A. Bachmeier and F. Armstrong, *Curr. Opin. Chem. Biol.*, **2015**, 25, 141-151.
153. K. K. Sakimoto, S. J. Zhang and P. Yang, *Nano Lett.*, **2016**, 16, 5883-5887.
154. J. Yang, D. Wang, H. Han and C. Li, *Acc. Chem. Res.*, **2013**, 46, 1900-1909.
155. Z. Sun, N. Talreja, H. Tao, J. Texter, M. Muhler, J. Strunk and J. Chen, *Angew. Chem. Int. Ed.*, **2018**, 57, 7610-7627.
156. E. V. Kondratenko, G. Mul, J. Baltrusaitis, G. O. Larrazábal and J. Pérez-Ramírez, *Energy Environ. Sci.*, **2013**, 6, 3112-3135.
157. N. G. Moustakas and J. Strunk, *Chem. Eur. J.*, **2018**, 24, 12739-12746.
158. M. Dilla, R. Schlögl and J. Strunk, *ChemCatChem*, **2017**, 9, 696-704.
159. C. Zhao, A. Krall, H. Zhao, Q. Zhang and Y. Li, *Int. J. Hydrogen Energ.*, **2012**, 37, 9967-9976.
160. M. Badlani and I. E. Wachs, *Catal. Lett.*, **2001**, 75, 137-149.
161. Z. Xiong, Y. Zhao, J. Zhang and C. Zheng, *Fuel Process. Technol.*, **2015**, 135, 6-13.
162. F. Galli, M. Compagnoni, D. Vitali, C. Pirola, C. L. Bianchi, A. Villa, L. Prati and I. Rossetti, *Appl. Catal., B*, **2017**, 200, 386-391.
163. Z. Xiong, H. Wang, N. Xu, H. Li, B. Fang, Y. Zhao, J. Zhang and C. Zheng, *Int. J. Hydrogen Energ.*, **2015**, 40, 10049-10062.
164. K. Li, T. Peng, Z. Ying, S. Song and J. Zhang, *Appl. Catal., B*, **2016**, 180, 130-138.
165. E. Liu, L. Qi, J. Bian, Y. Chen, X. Hu, J. Fan, H. Liu, C. Zhu and Q. Wang, *Mater. Res. Bull.*, **2015**, 68, 203-209.
166. M. Tahir and B. Tahir, *Appl. Surf. Sci.*, **2016**, 377, 244-252.
167. N. Singhal, A. Ali, A. Vorontsov, C. Pendem and U. Kumar, *Appl. Catal., A*, **2016**, 523, 107-117.
168. S. Zhu, S. Liang, Y. Tong, X. An, J. Long, X. Fu and X. Wang, *Phys. Chem. Chem. Phys.*, **2015**, 17, 9761-9770.
169. J. Jiao, Y. Wei, K. Chi, Z. Zhao, A. Duan, J. Liu, G. Jiang, Y. Wang, X. Wang, C. Han and P. Zheng, *Energy Technol.*, **2017**, 5, 877-883.

-
170. S. Sorcar, Y. Hwang, C. A. Grimes and S.-I. In, *Mater. Today*, **2017**, *20*, 507-515.
171. F. Wang, Y. Zhou, P. Li, L. Kuai and Z. Zou, *Chinese J. Catal.*, **2016**, *37*, 863-868.
172. Z. Xiong, Z. Lei, X. Chen, B. Gong, Y. Zhao, J. Zhang, C. Zheng and J. C. S. Wu, *Catal. Commun.*, **2017**, *96*, 1-5.
173. X. Zhang, G. Zuo, X. Lu, C. Tang, S. Cao and M. Yu, *J. Colloid Interface Sci.*, **2017**, *490*, 774-782.
174. B. Yu, Y. Zhou, P. Li, W. Tu, P. Li, L. Tang, J. Ye and Z. Zou, *Nanoscale*, **2016**, *8*, 11870-11874.
175. I. Rossetti, A. Villa, M. Compagnoni, L. Prati, G. Ramis, C. Pirola, C. L. Bianchi, W. Wang and D. Wang, *Catal. Sci. Technol.*, **2015**, *5*, 4481-4487.
176. M. Wang, Q. Han, Y. Zhou, P. Li, W. Tu, L. Tang and Z. Zou, *RSC Adv.*, **2016**, *6*, 81510-81516.
177. Y. Zhu, Z. Xu, W. Jiang, S. Zhong, L. Zhao and S. Bai, *J. Mater. Chem. A*, **2017**, *5*, 2619-2628.
178. Y. Zhu, Z. Xu, Q. Lang, W. Jiang, Q. Yin, S. Zhong and S. Bai, *Appl. Catal., B*, **2017**, *206*, 282-292.
179. T. Billo, F.-Y. Fu, P. Raghunath, I. Shown, W.-F. Chen, H.-T. Lien, T.-H. Shen, J.-F. Lee, T.-S. Chan, K.-Y. Huang, C.-I. Wu, M. C. Lin, J.-S. Hwang, C.-H. Lee, L.-C. Chen and K.-H. Chen, *Small*, **2018**, *14*, 1870008.
180. A. Meng, S. Wu, B. Cheng, J. Yu and J. Xu, *J. Mater. Chem. A*, **2018**, *6*, 4729-4736.
181. M. Tahir, B. Tahir, N. A. S. Amin and A. Muhammad, *Energy Convers. Manage.*, **2016**, *119*, 368-378.
182. O. Ola and M. M. Maroto-Valer, *Appl. Catal., A*, **2015**, *502*, 114-121.
183. S. Yan, S. Ouyang, H. Xu, M. Zhao, X. Zhang and J. Ye, *J. Mater. Chem. A*, **2016**, *4*, 15126-15133.
184. S. Shoji, G. Yin, M. Nishikawa, D. Atarashi, E. Sakai and M. Miyauchi, *Chem. Phys. Lett.*, **2016**, *658*, 309-314.
185. M. Alves Melo Júnior, A. Morais and A. F. Nogueira, *Microporous Mesoporous Mater.*, **2016**, *234*, 1-11.
186. N. Ambrožová, M. Reli, M. Šihor, P. Kuśtrowski, J. C. S. Wu and K. Kočí, *Appl. Surf. Sci.*, **2018**, *430*, 475-487.
187. T. Zhang, J. Low, X. Huang, J. F. Al-Sharab, J. Yu and T. Asefa, *ChemCatChem*, **2017**, *9*, 3054-3062.
188. H. Lee, B. S. Kwak, N.-K. Park, J.-I. Baek, H.-J. Ryu and M. Kang, *Appl. Surf. Sci.*, **2017**, *393*, 385-396.
189. Z. Xiong, Z. Lei, C.-C. Kuang, X. Chen, B. Gong, Y. Zhao, J. Zhang, C. Zheng and J. C. S. Wu, *Appl. Catal., B*, **2017**, *202*, 695-703.
190. S. Qamar, F. Lei, L. Liang, S. Gao, K. Liu, Y. Sun, W. Ni and Y. Xie, *Nano Energy*, **2016**, *26*, 692-698.
191. D. O. Adekoya, M. Tahir and N. A. S. Amin, *J. CO2 Util.*, **2017**, *18*, 261-274.
192. Y. Li, W. Zhang, X. Shen, P. Peng, L. Xiong and Y. Yu, *Chinese J. Catal.*, **2015**, *36*, 2229-2236.
193. G. Yin, M. Nishikawa, Y. Nosaka, N. Srinivasan, D. Atarashi, E. Sakai and M. Miyauchi, *ACS Nano*, **2015**, *9*, 2111-2119.

-
194. Y. Yan, Y. Yu, C. Cao, S. Huang, Y. Yang, X. Yang and Y. Cao, *CrystEngComm*, **2016**, *18*, 2956-2964.
195. I. H. Tseng and J. C. S. Wu, *Catal. Today*, **2004**, *97*, 113-119.
196. I. H. Tseng, J. C. S. Wu and H.-Y. Chou, *J. Catal.*, **2004**, *221*, 432-440.
197. Y. Li, W.-N. Wang, Z. Zhan, M.-H. Woo, C.-Y. Wu and P. Biswas, *Appl. Catal., B*, **2010**, *100*, 386-392.
198. Y.-F. Li, Z.-P. Liu, L. Liu and W. Gao, *J. Am. Chem. Soc.*, **2010**, *132*, 13008-13015.
199. M. Muuronen, S. M. Parker, E. Berardo, A. Le, M. A. Zwijnenburg and F. Furche, *Chemical Science*, **2017**, *8*, 2179-2183.
200. E. G. Panarelli, S. Livraghi, S. Maurelli, V. Polliotto, M. Chiesa and E. Giamello, *J. Photochem. Photobiol., A*, **2016**, *322-323*, 27-34.
201. Y. Tamaki, A. Furube, M. Murai, K. Hara, R. Katoh and M. Tachiya, *J. Am. Chem. Soc.*, **2006**, *128*, 416-417.
202. A. Yamakata, T.-a. Ishibashi and H. Onishi, *J. Mol. Catal. A: Chem.*, **2003**, *199*, 85-94.
203. Z. He, J. Tang, J. Shen, J. Chen and S. Song, *Appl. Surf. Sci.*, **2016**, *364*, 416-427.
204. J. Nowotny, T. Bak, M. K. Nowotny and L. R. Sheppard, *Int. J. Hydrogen Energ.*, **2007**, *32*, 2630-2643.
205. P. Akhter, M. Hussain, G. Saracco and N. Russo, *Fuel*, **2015**, *149*, 55-65.
206. Y. Nosaka and A. Y. Nosaka, *Chem. Rev.*, **2017**, *117*, 11302-11336.
207. G. M. Rosen and E. J. Rauckman, *Methods Enzymol.*, **1984**, *105*, 198-209.
208. A. Fujishima, T. N. Rao and D. A. Tryk, *J. Photochem. Photobiol., C*, **2000**, *1*, 1-21.
209. E. Carter, A. F. Carley and D. M. Murphy, *J. Phys. Chem. C*, **2007**, *111*, 10630-10638.
210. S. Kreft, J. Radnik, J. Rabeah, G. Agostini, M.-M. Pohl, E. Gericke, A. Hoell, M. Beller, H. Junge and S. Wohlrab, *Int. J. Hydrogen Energ.*, **2019**, DOI: 10.1016/j.ijhydene.2019.1004.1006.
211. S. Kreft, M. Sonneck, H. Junge, A. Pöpcke, A. Kammer, C. Kreyenschulte, S. Lochbrunner, S. Wohlrab and M. Beller, *Int. J. Hydrogen Energ.*, **2019**, submitted.
212. S. Kreft, R. Schoch, J. Schneidewind, J. Rabeah, E. V. Kondratenko, V. A. Kondratenko, H. Junge, M. Bauer, S. Wohlrab and M. Beller, *Chem*, **2019**, DOI:10.1016/j.chempr.2019.1004.1006.
213. R. O. da Silva, F. J. Heiligt, M. Karnahl, H. Junge, M. Niederberger and S. Wohlrab, *Catal. Today*, **2015**, *246*, 101-107.
214. F. J. Heiligt, M. D. Rossell, M. J. Suess and M. Niederberger, *J. Mater. Chem.*, **2011**, *21*, 16893-16899.
215. T. Berger, M. Sterrer, O. Diwald and E. Knözinger, *ChemPhysChem*, **2005**, *6*, 2104-2112.
216. A. H. Boonstra and C. A. H. A. Mutsaers, *J. Phys. Chem.*, **1975**, *79*, 1694-1698.
217. J. R. Harbour, J. Tromp and M. L. Hair, *Can. J. Chem.*, **1985**, *63*, 204-208.

5 Selected Publications

5.1 Dye Activation of Heterogeneous Copper(II)-Species for Visible Light Driven Hydrogen Generation

Stefanie Kreft, Jörg Radnik, Jabor Rabeah, Giovani Agostini, Marga-Martina Pohl, Eike Gericke, Armin Hoell, Matthias Beller, Henrik Junge, Sebastian Wohlrab

Int. J. Hydrogen Energ. **2019**, DOI: 10.1016/j.ijhydene.2019.04.006.

© 2019 Hydrogen Energy Publications LLC. Published by Elsevier Ltd.

Electronic Supporting Information for this article is available under <https://doi.org/10.1016/j.ijhydene.2019.04.006>.

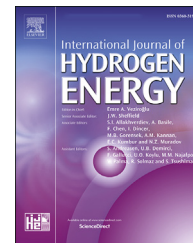
Contribution: S. K. designed and synthesized all catalytic materials. She analyzed the data of the standard characteristic methods (XRD, TEM, N₂-sorption) and the catalytic performance. Furthermore, she performed the *ex situ* and *in situ* XAS experiments at the ESRF and was involved in the EPR measurements. She wrote the draft for the manuscript and prepared the supporting information. Her overall contribution is about 65 %.



ELSEVIER

Available online at www.sciencedirect.com

ScienceDirect

journal homepage: www.elsevier.com/locate/he

Dye activation of heterogeneous Copper(II)-Species for visible light driven hydrogen generation

Stefanie Kreft ^a, Jörg Radnik ^b, Jabor Rabeah ^a, Giovanni Agostini ^{a,c,1},
Marga-Martina Pohl ^a, Eike Gericke ^{d,e}, Armin Hoell ^d, Matthias Beller ^a,
Henrik Junge ^{a,*}, Sebastian Wohlrab ^{a,**}

^a Leibniz Institute for Catalysis at the University of Rostock, Albert-Einstein-Straße 29a, 18059 Rostock, Germany

^b Federal Institute of Material Research and Testing (BAM), Unter den Eichen 44-46, 12203 Berlin, Germany

^c European Synchrotron Radiation Facility (ESRF), Grenoble, France

^d Helmholtz-Zentrum Berlin für Materialien und Energie, Hahn-Meitner Platz 1, 14109 Berlin, Germany

^e Humboldt-Universität zu Berlin, Institut für Chemie, Brook-Taylor Straße 2, 12489 Berlin, Germany

ARTICLE INFO

Article history:

Received 29 January 2019

Received in revised form

28 March 2019

Accepted 1 April 2019

Available online xxx

Dedicated to Prof. Gabor Laurenczy
on the occasion of his 65th birthday.

ABSTRACT

Heterogeneous Cu catalysts are widely used in photocatalytic hydrogen generation. The typical working mode includes the transfer of photo-induced charges from a semiconductor to CuO which itself is reduced to Cu₂O to initiate the catalytic cycle. In this contribution a photosensitizer (dye), excited by visible light absorption, was used to transfer an electron to the CuO which after reduction catalyzes the water reduction to hydrogen. Several copper(II)-catalysts on high surface silica were prepared by impregnation or precipitation and applied in photocatalytic water reduction. The best catalyst CuO(ClO₄)/SiO₂, synthesized via incipient wetness impregnation of CuCl₂ in MCM-41 and a following precipitation with NaOH, achieved a 6 times higher activity (1702 mmol h⁻¹ g⁻¹) compared to a previously investigated copper system (280 mmol h⁻¹ g⁻¹ for CuI) under the same reaction conditions. All materials were fully characterized by XRD, TEM and N₂ sorption and further by magnetic resonance and X-ray methods EPR, SAXS and XAS. *In situ* measurements evidenced a reduction of the initial Cu(II)-species, which confirms the (proposed) photocatalytic mechanism.

© 2019 Hydrogen Energy Publications LLC. Published by Elsevier Ltd. All rights reserved.

Introduction

In the context of alternative energy technologies the transformation of sun light energy into the inherent chemical energy of a hydrogen molecule is of actual interest. For this purpose numerous approaches are currently

developed [1–3], whereas one of the more basic ones is the photocatalytic splitting of water into hydrogen and oxygen. Because of their availability and lower toxicity compared to noble metals, oxides consisting of metal cations with d⁰ and d¹⁰ configurations are intensively investigated as water reduction catalysts (WRC's) [4–8]. Among these, different

* Corresponding author.

** Corresponding author.

E-mail addresses: henrik.junge@catalysis.de (H. Junge), sebastian.wohrlab@catalysis.de (S. Wohlrab).

¹ Actual address: Alba Synchrotron, Carrer de la Llum 2-26, 08290 Cerdanyola del Vallés, Spain.

<https://doi.org/10.1016/j.ijhydene.2019.04.006>

0360-3199/© 2019 Hydrogen Energy Publications LLC. Published by Elsevier Ltd. All rights reserved.

copper species on various semiconductors have been explored for the photocatalytic hydrogen generation [9–36]. These photocatalytic reactions mainly take place in a water/alcohol mixture and require UV-light activation due to the large band gap of the preferred semiconductor TiO_2 (Table S1). It was shown that photo-induced charges from the TiO_2 are transferred to CuO which itself is reduced to Cu_2O in the activation period before the photocatalytic hydrogen generation starts [14]. Indeed, several examples demonstrate the high activity of copper(I)-species in hydrogen generation [9–11,14,17,29,30]. Furthermore, DFT calculations support a formation mechanism including the reduction of CuO to Cu_2O by photogenerated electrons [9].

The apparent disadvantage of using Cu_2O for photocatalytic water splitting is its sensitivity towards oxidation back to CuO in aqueous solutions and, thus its low stability and ease of deactivation [37,38]. Whereas Cu_2O alone as photocatalyst for overall water splitting was discussed since the 90's of the last century [38,39], it is nowadays mainly applied in photoelectrochemical water reduction using photocathodes consisting of Cu_2O [40,41]. This actual dominance is so to say an inevitable consequence of the nature of the currently available Cu(II)-catalysts, as CuO has to be activated by a semiconductor (SC) whereby activation occurs at the CuO –SC interface which is, however, rarely accessible for the reactants.

Dye sensitizing is a feasible approach to overcome spectral limitations of wide bandgap semiconductors [42]. This photocatalytic process can be separated in four single steps, namely 1) photo excitation of the dye, 2) electron transfer from the lowest unoccupied molecular orbital (LUMO) of the dye to the conduction band of the semiconductor, 3) migration of the electron to the surface and proton reduction to form H_2 and 4) closing the catalytic cycle by regeneration of the dye with a sacrificial reductant. Commonly, co-catalysts on the semiconductor serve as active sites, as Schottky barrier for electron trapping and charge separation as well as to reduce the overpotential for H_2 evolution [43]. Jin et al. worked on a system consisting of i) dye-sensitized CuO incorporated TiO_2 catalyst and ii) various sacrificial reductants under visible light irradiation [19]. Thereby, the excited electrons from the LUMO of the Eosin Y are trapped efficiently into the conduction band of the TiO_2 and are transferred to CuO which then reduce protons to hydrogen. Herein, we present a method for direct dye activation of Cu(II)-oxo species at easily accessible surface sites that makes catalysis more efficient.

Recently, some of us developed a system containing copper(I) and copper (II) compounds as water reduction catalysts (WRC), $[\text{Ir}(\text{ppy})_2(\text{bpy})]\text{PF}_6$ as a photosensitizer (PS) and triethylamine as the sacrificial electron donor (SR) in a THF/ H_2O mixture [44]. Following this homogeneous approach, using CuI as dissolved WRC catalyst, the Ir-PS^* transfers one electron to the Cu species which itself reduces protons to form H_2 . CuI as the WRC was found to be the most active compound in proton reduction and through the addition of nitrogen ligands such as 2,2'-bipyridine (bpy) a significantly improved stability and productivity in hydrogen generation was achieved. However, in situ formed heterogeneous Cu species were identified which also possess an inherent catalytic activity for hydrogen

generation according to Scheme 1. Consequently, in this work heterogeneous copper catalysts, prepared on photocatalytically inactive high surface silica as support by various synthesis methods, were examined in the hydrogen reduction under visible light.

Experimental

Materials preparation

Chemicals

The mesoporous silica MCM-41 was purchased from Süd-Chemie AG. The copper-precursors were delivered by the following companies: $\text{Cu}(\text{NO}_3)_2 \cdot 3\text{H}_2\text{O}$ ($\geq 99.0\%$) from Fluka and $\text{CuCl}_2 \cdot 2\text{H}_2\text{O}$ ($\geq 99.0\%$) from Laborchemie Apolda. The precipitating agent NaOH ($\geq 98.0\%$) was purchased from J.T. Baker. The synthesis of the Ir-PS , $[\text{Ir}(\text{ppy})_2(\text{bpy})][\text{PF}_6]$, used in this work, was prepared in two steps according to previous reports [45,46].

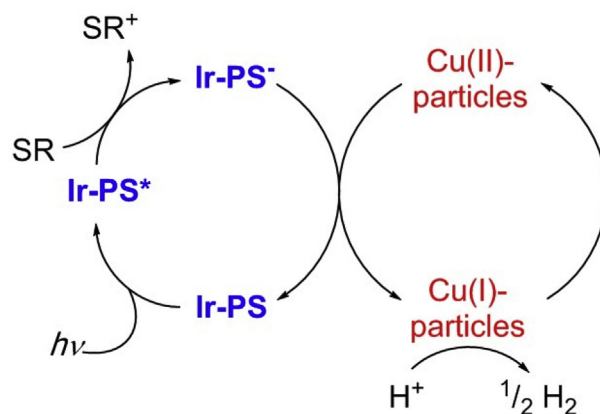
Impregnation with $\text{Cu}(\text{NO}_3)_2 \cdot 3\text{H}_2\text{O}$ -precursor

1 g of the mesoporous silica MCM-41 was used as received and impregnated with 2 ml of 0.63 M aqueous $\text{Cu}(\text{NO}_3)_2$ to achieve a completely incipient wetness impregnation. After drying at 80°C for 2 h, the material was calcined at 400°C at a heating ramp of 5 K/min for 1 h under air ($\text{CuO}(\text{N,a})/\text{MCM-41}$) or under N_2 ($\text{CuO}(\text{N,N})/\text{MCM-41}$).

Impregnation with $\text{CuCl}_2 \cdot 2\text{H}_2\text{O}$ -precursor

1 g of the mesoporous silica MCM-41 was impregnated with 2 ml of 0.63 M aqueous CuCl_2 until complete impregnation was achieved and further dried at 80°C for 2 h. Then the material was impregnated with 1.9 ml of 2 M aqueous NaOH . After drying at 80°C for 2 h the material was washed three times with distilled water and dried again at 80°C for 2 h ($\text{CuO}(\text{Cl})/\text{SiO}_2$).

These impregnation and precipitation processes were performed once more, however afterwards the material was calcined at 400°C under air applying a heating ramp of 5 K/min for 2 h ($\text{CuO}(\text{Cl,a})/\text{SiO}_2$).



Scheme 1 – Mechanism for the hydrogen generation using a photosensitizer and Cu-particles.

Analytical methods

The obtained materials were characterized by the following methods:

Inductively coupled plasma optical emission spectrometry (ICP-OES) using a Varian 715-ES ICP-emission spectrometer was carried out, in order to quantify the amount of copper in the material. Specific surface area and pore size distribution were determined from N_2 -physisorption data obtained using a NOVA 4200e instrument (Quantachrome). As a pre-treatment, samples were outgassed and dried for 2 h at 220 °C under vacuum. Data analysis of isotherm data was carried out according to methods described by Brunauer, Emmett, Teller (BET) [47] and Barrett, Joyner, Halenda (BJH) [48]. Powder X-ray diffraction (XRD) was carried out on a STADI P automated transmission diffractometer from STOE (Darmstadt, Germany) with an incident beam curved germanium monochromator selecting $CuK\alpha_1$ radiation ($\lambda = 1.5406 \text{ \AA}$, 40 kV, 40 mA) and a 6° linear position sensitive detector (PSD). The alignment was checked by use of a silicon standard. The data were collected in the 2θ range from 5 to 60° with a step size of 0.5° and a measurement time of 50 s per step. The TEM measurements were performed at 200 kV with an aberration-corrected JEMARM200F (JEOL, Corrector: CEOS). The microscope is equipped with a JED-2300 (JEOL) energy-dispersive x-ray-spectrometer (EDXS) for chemical analysis. The samples were prepared from freshly made reaction mixtures. After certain hours of light irradiation a droplet of the reaction mixture was placed on a holey carbon supported Ni-grid mesh 300, dried and transferred to the microscope. The ASAXS experiments were performed at the K edge of Cu (8979 eV) at the FCM beamline of the Physikalisch Technische Bundesanstalt (PTB) [49] at the Synchrotron Radiation Facility BESSY II using the HZB-SAXS-Instrument [50]. The monochromatic X-ray beam was obtained from the white beam by using a Si(111) four crystal monochromator combined with two platinum coated mirrors for focusing requirements and to reject higher harmonics. The scattering was detected using an area sensitive hybrid pixel in-vacuum detector (Pilatus 1 M) [51]. The incident monochromatic beam intensities were monitored using a $7 \mu\text{m}$ thin transmission photo diode. An X-ray photo diode behind the sample on a moveable stage was used for measuring the transmitted beam intensity between taking the scattering patterns. The photon energy was calibrated by using a Cu foil placed in the white beam in front of the monochromator. The powder samples were mounted between two week scattering polymer films, only weak

compacted, and having a final thickness of some hundred micrometers. The X-ray beam transmitted the samples perpendicular while all samples are mounted on a sample changer that is moveable inside a vacuum sample chamber ($<10^{-5}$ mbar). For each measurement sequence a sample of Ag-behenate powder was measured as a standard for the q -axis calibration. Additionally, a glassy carbon standard was measured for all samples to convert the measured intensities to absolute scattering units. For data processing [52], the acquired 2D small-angle scattering patterns were radial integrated and normalized with the incoming photon flux. Subsequently, the scattering curves were normalized to their X-ray transmission and subtracted by the respective background scattering (two layers of polymer film for the samples). Total scattering cross sections can be derived by dividing the sample thickness and normalizing to the glassy carbon scattering). For the normalization, a MatLab[®] routine was used. The EXAFS experiments were performed at the Cu K edge (8979 eV) at the BM23 beamline at the European Synchrotron Radiation Facility (ESRF, Grenoble). Monochromatic X-ray beam was obtained from the white beam by using Si(111) double crystal; a harmonic rejection has been performed using Si coated mirrors. Both the incident (I0) and transmitted (I1) monochromatic beam intensities were measured by using ionic chambers filled with 1.7 bar N_2 and 0.3 bar Ar, respectively, and eventually the chambers filled up to 2 bar with He. The photon energy was calibrated with the edge energy obtained from the maxima first derivative of the Cu K-edge in the Cu foil (8984 eV). The reference samples (Cu foil, Cu_2O and CuO) were measured in transmission mode. For the liquid samples (Cu-species before, during and after the radiation with visible light) the EXAFS measurements were performed in fluorescence mode with a 13-element Ge detector (Canberra Industries). EXAFS signals were extracted and analyzed using IFEFFIT package [53]. In situ XANES experiments were recorded in dispersive mode at the EDXAS_L branch of ID24 beamline [54]. The X-ray source consisted of one undulator U27 whose gap was optimized to tune the first harmonic at energies covering the Cu K edge. The beam was focused horizontally by an elliptical polychromator (Si(111)) crystal in Bragg configuration and a Hamamatsu CCD camera as a detector for time-resolved studies was utilized. A spectrum every 7.5 s was collected. XANES data of in situ experiments were normalized by XAS plug-in implemented in PyMca allowing data treatment in batch. The evolution of reduction process was followed by the "ROI imaging" tool implemented in PyMca package [55] integrating the first derivative of normalized XANES spectra between 8986 and

Table 1 – Preparation, copper content and structural properties of different Cu-based catalysts.

Sample	Precursor	Support	Precipitation	Calcination	Cu content [wt.%] ^a	Surface area [$\text{m}^2 \text{g}^{-1}$] ^b	Pore size [nm] ^b
CuO(N,a)/MCM-41	$\text{Cu}(\text{NO}_3)_2$	MCM-41	–	400 °C (air)	6.5	434	3.7
CuO(N,N)/MCM-41	$\text{Cu}(\text{NO}_3)_2$	MCM-41	–	400 °C (N_2)	6.5	498	3.9
CuO(Cl,a)/ SiO_2	CuCl_2	MCM-41	NaOH	400 °C (air)	6.2	163	8.7
CuO(Cl)/ SiO_2	CuCl_2	MCM-41	NaOH	–	6.6	185	11.4

^a From inductively coupled plasma optical emission spectrometry.

^b From nitrogen sorption.

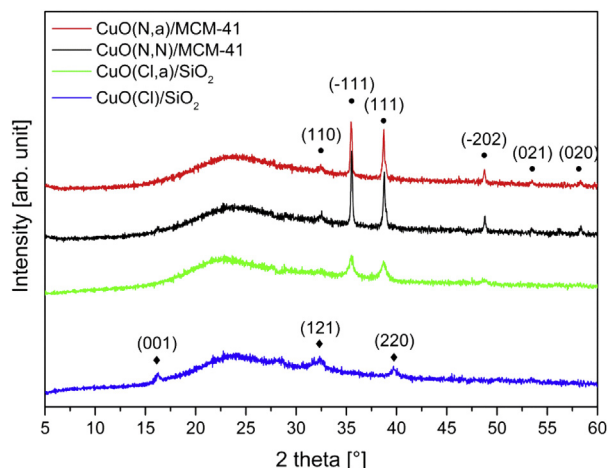


Fig. 1 – XRD patterns of the samples and of CuO (•) according to ICDD file No. 01-080-1916 and $\text{Cu}_2\text{Cl}(\text{OH})_3$ (♦) according to ICDD file No. 01-080-9252.

8990.5 eV (see vertical lines in inset Fig. 8). X-band EPR spectra were recorded on a Bruker EMX CW-micro spectrometer at 20 °C with a microwave power of 6.3 mW, a

modulation frequency of 100 kHz and modulation amplitude up to 5 G.

Photocatalytic measurements

The catalytic experiments were carried out in an inert gas atmosphere. A double walled reaction vessel was evacuated and purged with argon several times. The catalyst (10 μmol Cu) and the iridium-photosensitizer (15 μmol) were added in a Teflon crucible. Then a degassed solution of THF/TEA/ H_2O (3:2:1, 10 ml) was added to the vessel. After tempering to 25 °C for 8 min the reaction was started by switching on the light source (300 W Xe lamp from LOT, irradiation output 1.5 W, filter: ≥ 385 nm). The evolved gas was collected by an automatic gas burette and additionally analyzed by gas chromatography (HP6890 N, carboxen 1000).

Results and discussion

Materials characterization

At the start of this project, four silica supported CuO catalysts (6.2–6.6 wt% Cu) were prepared via incipient wetness

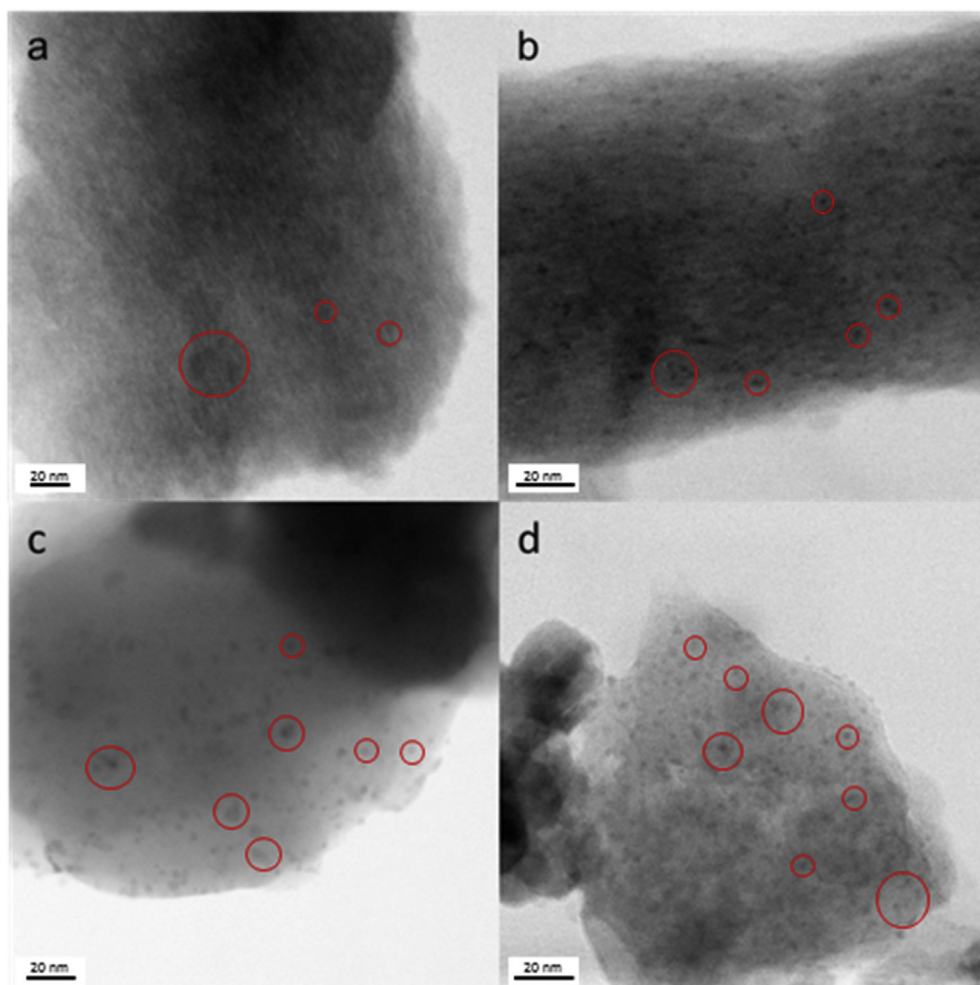


Fig. 2 – BF-TEM images of CuO(N,a)/MCM-41 (a), CuO(N,N)/MCM-41 (b) and CuO(Cl)/SiO₂ (c) and CuO(Cl,a)/SiO₂ (d). The red circles indicate the copper particles within the porous support.

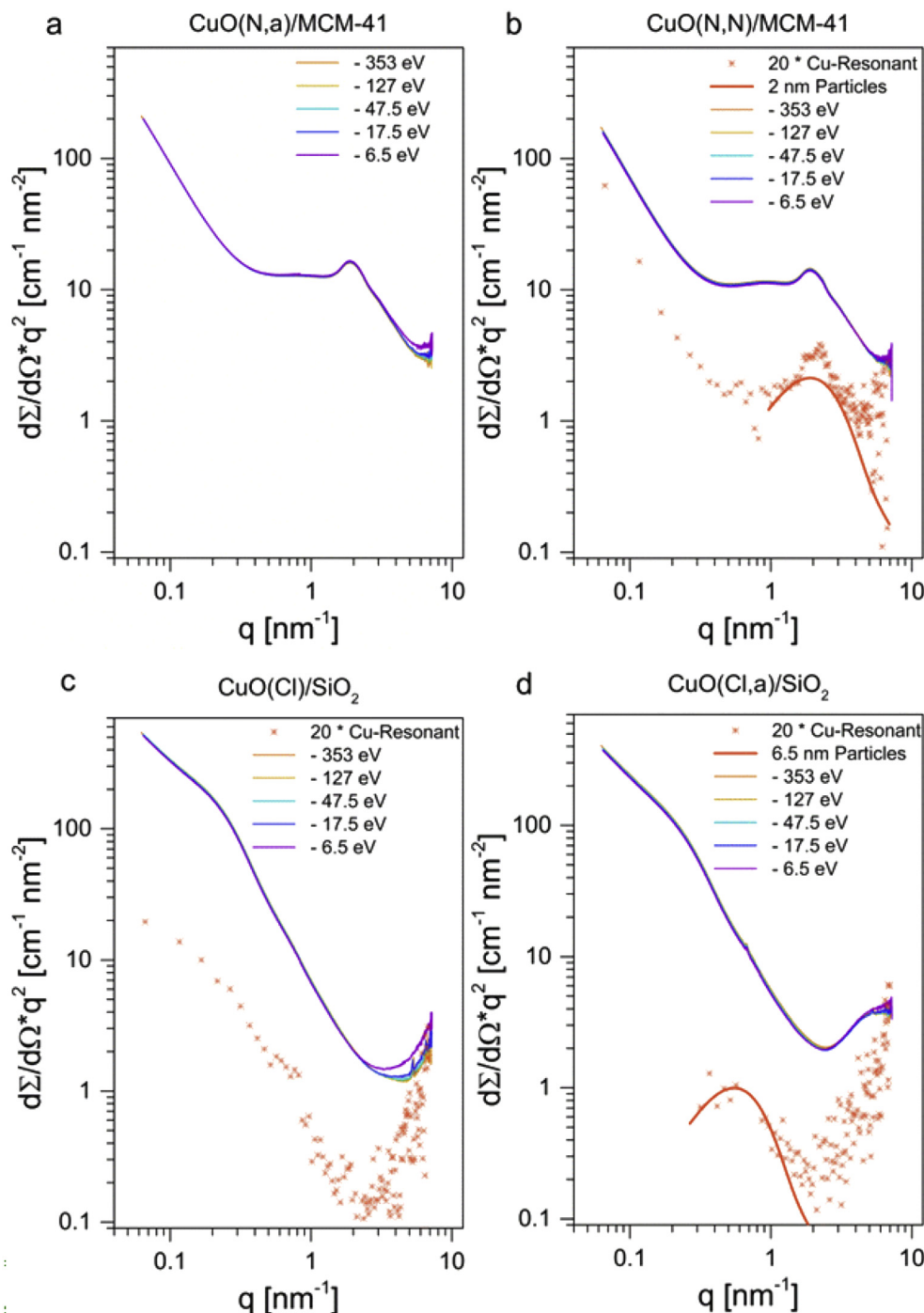


Fig. 3 – Scattering curves measured 353 eV, 127 eV, 47.5 eV, 17.5 eV and 6.5 eV below the Cu K-edge, found at 8986.5 eV. Energy calibrated to a copper reference sample. All scattering curves are merged from scattering experiments at two different sample to detector distances and plotted as lines. The calculated resonant Cu-scattering is given as orange stars scaled with a factor 20.

impregnation of MCM-41 (surface area of 1214 m²/g, pore size of 4.1 nm). Table 1 summarizes the main preparation parameters for each of these catalysts as well as their copper content, surface area and pore size. The catalysts possess reduced surface areas compared to the unloaded MCM-41

which could be caused by pore-blocking and the NaOH treatment.

X-ray powder diffraction patterns in the range of 5–60° 2 theta-scale reveal crystalline species being present in all catalysts (Fig. 1). The obtained reflections can be indexed to the

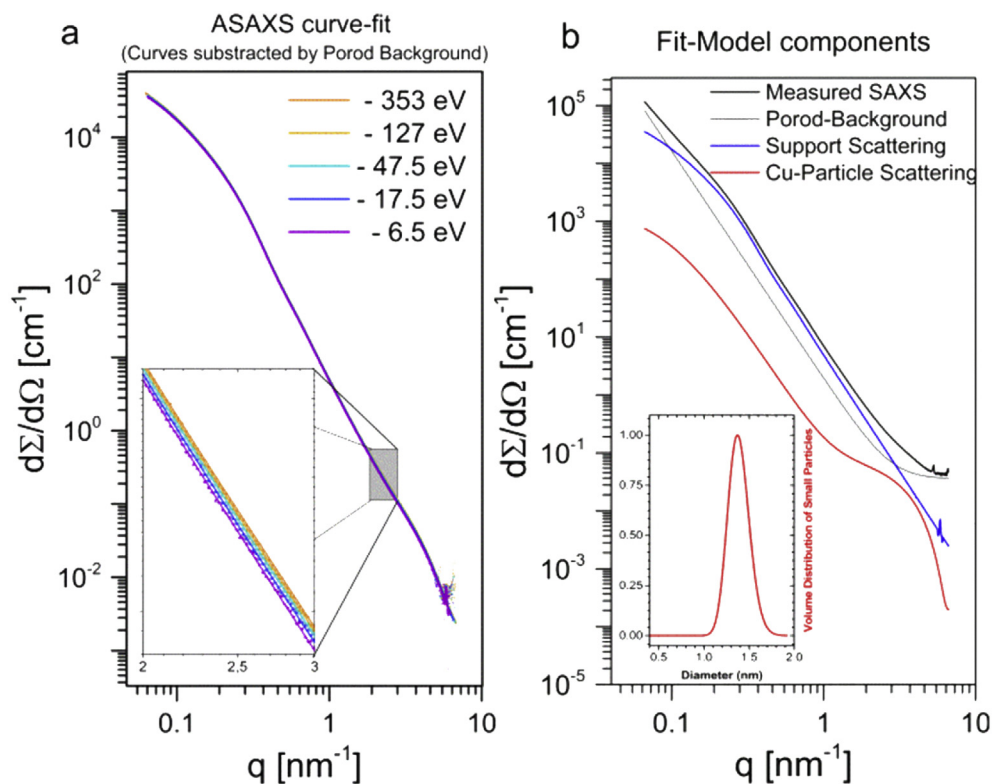


Fig. 4 – Scattering curves of CuO(Cl)/SiO₂ subtracted with a Porod scattering background with magnification inset, labeled by the energy difference of the used photons and the position of the Cu K_α absorption edge can be seen in the left figure (a). Measured data are represented by stars and crosses, and overlaid by the fit results displayed as line. On the right side the scattering curve measured 127 eV below the Cu-edge (black) with its three model components Porod (gray), support scattering (blue) and nanoparticle scattering (red) is displayed (b). The size distribution found for the small particles is shown in the inset.

monoclinic phase of CuO (ICDD file No. 01-080-1916) except for sample CuO(Cl)/SiO₂. In CuO(Cl)/SiO₂ the appearing low intense reflections can be ascribed to Cu₂Cl(OH)₃ (ICDD file No. 01-080-9252). The reflections of CuO(N,N)/MCM-41 and CuO(N,N)/MCM-41 are much sharper and narrower as those of the materials achieved by the CuCl₂ precursor pointing to larger particles of the former.

Transmission electron microscopy (TEM) and recorded bright-field (BF) images (Fig. 2, S1, S2a, S2b, S3) as well as high-angle annular dark field (HAADF) images (Fig. S2c, S4) provide a visual overview of the Cu species on the (inner) surfaces of the supports. Focusing on the particles it is observed, that incipient wetness impregnation produces definite particles with a narrow size distribution and leads to a fine catalyst dispersion over the silica surface. The well dispersed CuO particles (dark spots distributed over the support) in CuO(N,N)/MCM-41 are slightly larger (~3 nm, Fig. 2b, S2c) than those in CuO(N,a)/MCM-41 (<2 nm, Fig. 2a).

Incipient wetness impregnation of MCM-41 followed by precipitation with NaOH as in case of CuO(Cl)/SiO₂ and CuO(Cl,a)/SiO₂ leads to the destruction of the hexagonal pore structure of the mesoporous silica. After calcination at 400 °C larger and smaller CuO particles are formed in CuO(Cl,a)/SiO₂ (Fig. 2d, S4). In case of CuO(Cl)/SiO₂ (Fig. 2c) a rearrangement of the silica to a glassy material with larger pores occurs and

some not evenly dispersed Cu₂Cl(OH)₃ agglomerates get visible (Fig. S3). Respective EDX measurements confirm the presence of Cl in accordance to the XRD results which designate the Cu phase in CuO(Cl)/SiO₂ as Cu₂Cl(OH)₃. It is important to mention, that areas with Cu without Cl-signals are observed, interpreting the formation of small copper oxide particles. These structures play an important role in catalysis and were deeply investigated via Anomalous Small Angle X-ray Scattering (ASAXS), XANES (X-ray Absorption Near Edge Structure) and EXAFS (Extended X-ray Absorption Fine Structure) and identified as major part of the Cu species as discussed in the following paragraph.

Deeper insights into the Cu particle morphology, size, and the spatial distribution of the Cu-atoms within nanostructures were gained with ASAXS [56] measurements which were performed at 5 different photon energies below the Cu K-edge. While the Cu K-edge has an energy of 8979 eV, the edge of the catalysts is found to be at 8986.5 eV due to the chemical shift. ASAXS probes an anomalous contrast behavior close to the X-ray absorption edge of an element contained in the sample. This anomalous behavior of any element can be predicted from Cromer-Lieberman calculations to be used to extract resonant-curves for the scattering contribution of e.g. Cu only, by using the Stuhrmann approximation [57,58]. Thus, the investigated sample volume by ASAXS is much bigger

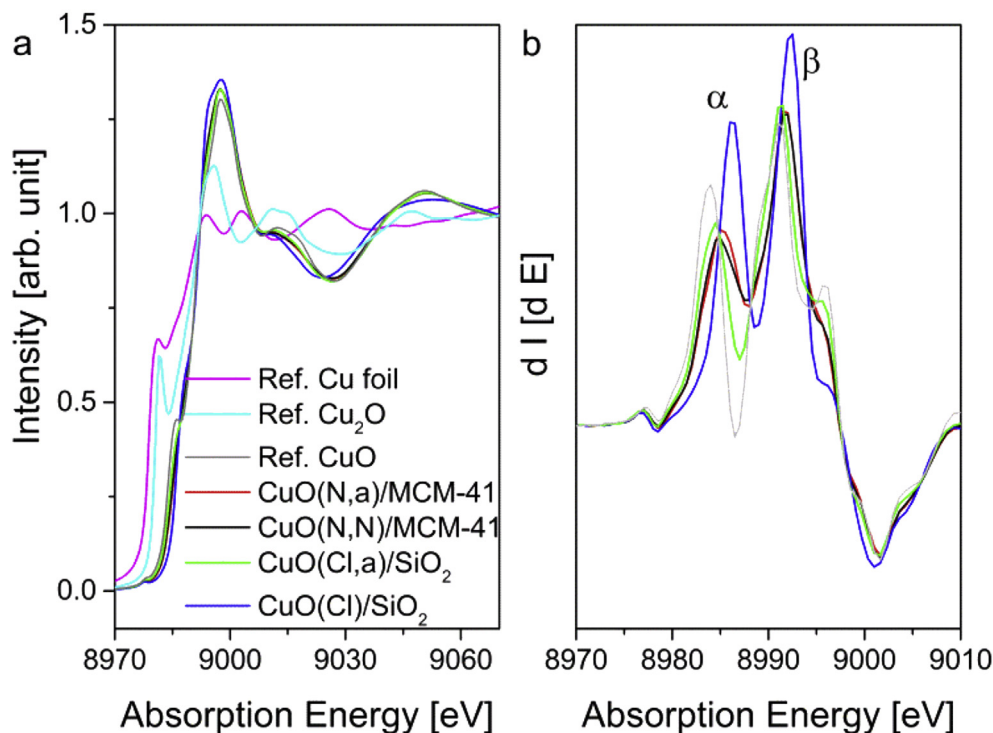


Fig. 5 – Ex situ XANES measurements (a) and first derivation (b) of supported copper materials in comparison to the reference materials Cu foil, Cu_2O and CuO.

than for TEM which provides statistically more relevant information about the samples. Therefore, this experimental approach is complimentary to the XRD and TEM investigations. For complex systems like the Cu catalysts described in this study the element-sensitivity of ASAXS is crucial for the understanding of the results.

The results are shown as scattering curves in terms of the total scattering cross sections multiplied by the square of the magnitude of the scattering vector q as a function of q (Fig. 3a–d). The contributions of the Cu containing particles alone are represented by the calculated resonant copper scattering curve (Fig. 4a).

First of all, for the samples $\text{CuO}(\text{N,a})/\text{MCM-41}$ and $\text{CuO}(\text{N,N})/\text{MCM-41}$, a broad peak at 2 nm^{-1} is observed (Fig. 3a and b), which can be correlated with the MCM-41 channel structure. This observation corresponds to the TEM results showing the MCM-41 structure for these samples. Surprisingly, no statistically significant resonant scattering contribution is found for the $\text{CuO}(\text{N,a})/\text{MCM-41}$. This result seems to contrast with TEM showing small Cu particles for this sample, but it is in accordance to the sharp XRD reflections correlated to CuO for this sample. It seems that the major part of the Cu atoms is located in the large CuO particles leading to the described sharp XRD reflections. Interestingly, the ASAXS results differ for the $\text{CuO}(\text{N,N})/\text{MCM-41}$ sample, although the observations obtained with TEM and XRD are very similar to the one for $\text{CuO}(\text{N,a})/\text{MCM-41}$. In case of $\text{CuO}(\text{N,N})/\text{MCM-41}$ a significant Cu scattering contribution is observed (Fig. 3b), which shape is similar to the total scattering curves. That indicates the morphology of the Cu containing parts of the

samples to be similar to the MCM-41 structure. Obviously, a part of the Cu atoms is located in particles those sizes are determined by the pores of the MCM-41 structure, another part of Cu could be atomically distributed in the substrate. It must be noted, that the atmosphere used during the calcination seems to influence the distribution of the Cu atoms. These structural details are only observed with ASAXS.

For $\text{CuO}(\text{Cl})/\text{SiO}_2$ and $\text{CuO}(\text{Cl,a})/\text{SiO}_2$ (Fig. 3c and d) the SAXS-term does not show the typical shape of MCM-41. This indicates that the ordered structure of the MCM-41 is almost destroyed during the preparation process which is also confirmed by TEM. The ASAXS effect is illustrated in Fig. 4a for sample $\text{CuO}(\text{Cl})/\text{SiO}_2$. This sample shows a complex scattering curve, which can be explained with three different contributions which are shown in Fig. 4b for one scattering curve at 127 eV below the Cu edge. The first contribution is the Porod region at large q -values and the angularly independent incoherent scattering used as background, which shows no resonant effect. This background was subtracted from the scattering curves showing in Fig. 4a. The Porod-law describes the scattering related to all inner surfaces, in this case the surface of the support material. The second contribution can be explained with the nano-structure of the support. This was modeled with spherical objects with a broad size distribution. Thereby, the contrast of this feature decays slightly while approaching the Cu edge. This indicated a resonant effect and can be explained with a major part of homogeneously dispersed Cu species in the support behaving comparable to the $\text{CuO}(\text{N,N})/\text{MCM-41}$ sample. The third component can be correlated with Cu nanoparticles with a logarithmic size

distribution and a diameter of 1.4 ± 0.12 nm. These particles are agglomerated in a loosely network with a size of 11 nm. This latter result corresponds to the TEM investigations described before.

For CuO(Cl,a)/SiO₂, the resonant scattering curve shows the typical shape of particles scattering. By a spherical model a volume weighted particle diameter of 6.5 ± 1 nm was found for the Cu particles. An additional feature between 2 nm^{-1} and 7 nm^{-1} was observed which refers to particles below 1 nm diameter. Unfortunately, it is not possible to determine surely, if these particles contain Cu, or not. Both different kinds of particles were discussed in the TEM paragraph before.

XAS measurements were performed to elucidate the valence state and the local structure of the Cu species. The XANES exhibits clearly, that Cu is bivalent in all samples before their application in the photocatalysis (Fig. 5a). No hint of any reduced Cu species is found. The coordination geometry was further concluded. For CuO next to the main absorption peak at 8991 eV a significant shoulder at lower energies can be observed that lead to a splitting in the derivative spectrum (Fig. 5b), the so-called α - β splitting. A splitting of about 6 eV indicates a large tetragonal distortion from octahedral symmetry typical for CuO [59]. For all the measured samples such a splitting between 5.5 and 7 eV is observed confirming distorted octahedral symmetry for Cu(II). Additionally, a weak pre-edge feature due to the $1s \rightarrow 3d$ transition is observed at 8978 eV. Besides the similarities between the spectra also some differences are found: The spectra of the CuO samples (CuO(N,a)/MCM-41, CuO(N,N)/MCM-41 and CuO(Cl,a)/SiO₂) are comparable to the CuO reference but show broader peaks and a slightly smaller splitting indicating a less pronounced distortion of the octahedral geometry. Contrary, the differences between CuO(Cl)/SiO₂ and the reference CuO are most pronounced. Like for the other supported Cu species the splitting is slightly smaller, but

the peaks in the derivative spectrum (Fig. 5b) are very sharp. Furthermore, a shift of the absorption edge of about 2 eV is observed. This result indicates that the structure of this species differs significantly from the CuO structure.

To gain insight into the coordination of the Cu species EXAFS patterns were investigated, too (see Fig. 6). The first Cu–O shells are very similar for all 4 samples according to the same valence state of (II). However, differences are found for the Cu–Cu shells. The spectra of the calcined materials CuO(N,a)/MCM-41, CuO(N,N)/MCM-41 and CuO(Cl,a)/SiO₂ are more or less in accordance with the one of the ref. CuO, only at longer distances (Cu–Cu₃) the coordination number (CN) is much lower indicating smaller CuO particles. Instead of this, for CuO(Cl)/SiO₂ notable differences are observed. Compared to all other samples, for CuO(Cl)/SiO₂ the coordination number of Cu–Cu interactions is much lower and the distances between the Cu atoms seems to be higher hinting to a weak interaction between the Cu atoms.

Catalytic performance

All the heterogeneous copper catalysts were tested as WRC with [Ir(ppy)₂(bpy)]PF₆ as visible light active photosensitizer (PS) and trimethylamine (TEA) as the sacrificial reagent (SR) under previously optimized conditions in a mixture of THF/H₂O [44,60]. UV–Vis absorption of the PS (dissolved in acetonitrile) is shown in Fig. S5 [61]. A strong absorption in the UV can be attributed to π - π^* transitions whereas in the visible range of the spectrum ($\lambda > 390$ nm) the PS absorptions above 500 nm are neglectable. The performance of the heterogeneous catalysts is summarized in Table 2. The hydrogen evolution curves of the respective testes are depicted in Fig. S7a.

In the absence of WRC the Ir–PS produced 0.5 ml H₂ after 3 h reaction time and 1.3 ml after 20 h. The gas volumes of the experiments with WRC were corrected by this blank value in order to get the productivity of the Cu-based catalysts. To identify the influence of the SiO₂ support, only MCM-41 and the Ir–PS were added to the mixture THF:TEA:H₂O = 3:2:1 without any copper catalyst. After 20 h only 1.6 ml H₂ were formed which is comparable to the blank value. During the ongoing photocatalytic reaction the activity of the catalyst decreased for all tested materials which is a consequence of the decomposition of the PS during the reaction [44]. Within the first 3 h, the activity of catalysts with approx. 6.5 wt % Cu is increasing in the following order: CuO(N,a)/MCM-41 < CuO(N,N)/MCM-41 < CuO(Cl,a)/SiO₂ < CuO(Cl)/SiO₂. Here, CuO(Cl)/SiO₂ showed the highest activity with $189.4 \text{ mmol h}^{-1} \text{ g}^{-1}$. After 20 h, again CuO(Cl)/SiO₂ significantly outperformed the other catalysts. Due to the higher activity and the divergent structural properties of CuO(Cl)/SiO₂ compared to the other investigated catalysts we decided to prepare a similar material with less copper amount (CuO(Cl0.1)/SiO₂). It is known from literature decreasing the copper amount may have a positive effect on the productivity [10,16,30]. Thereby, by lowering the copper amount to 1/10 (CuO(Cl0.1)/SiO₂) the activity was almost 10 times higher after 3 h and 8 times after 20 h, respectively, compared to (CuO(Cl)/SiO₂). Exemplary, the calculation of the quantum yield was determined for the catalyst with the highest activity

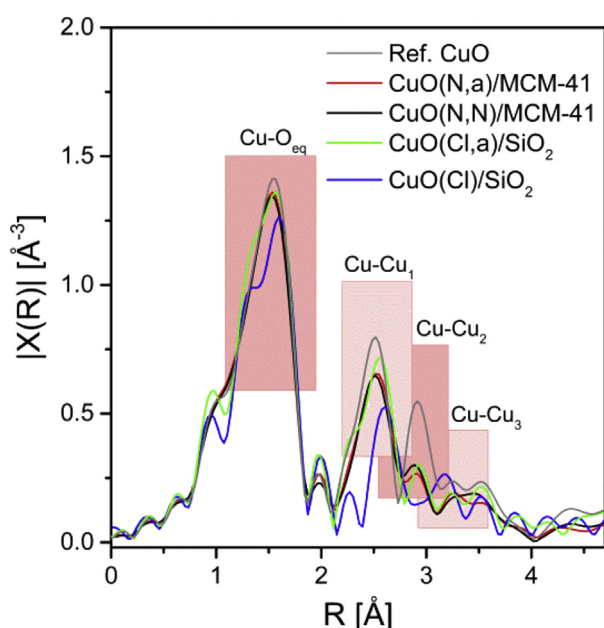


Fig. 6 – FT of the EXAFS oscillations. The corresponding atomic pairs are highlighted.

Table 2 – Photocatalytical hydrogen generation from THF/TEA/H₂O mixture with different Cu-based WRCs.

Sample	V(H ₂) [ml]/3 h	Activity [mmol·h ⁻¹ ·g ⁻¹]/3 h	V(H ₂) [ml]/20 h	Activity [mmol·h ⁻¹ ·g ⁻¹]/20 h
CuO(N,a)/MCM-41	5.3	113.7	12.4	39.9
CuO(N,N)/MCM-41	5.7	122.3	13.2	42.5
CuO(Cl,a)/SiO ₂	6.7	141.1	11.8	38.0
CuO(Cl)/SiO ₂	8.9	189.4	17.1	55.0
CuO(Cl0.1)/SiO ₂ ^a	8.0	1702	12.5	402

All experiments have been performed at least twice and the averages are shown. Experimental conditions: 15 μmol Ir-PS, 10 μmol [Cu], 10 ml THF:TEA:H₂O = 3:2:1, Xe-light irradiation: 1.5 W ≥ 385 nm, 25 °C, gas volumes determined by automatic gas burettes and corrected by blank volume (0.5 ml after 3 h and 1.3 mL after 20 h), gases analyzed by GC, Activity = n(H₂)/(t·m(Cu)).

H₂ evolution in the absence of any copper catalyst but in the presence of MCM-41: 1.6 ml after 20.

^a Experimental conditions: see above, with the exception of 1 μmol [Cu] being used.

(CuO(Cl0.1)/SiO₂) and revealed in 1.2% (Table S1, SI section quantum yield calculation). EPR measurements showed the differences between the CuO(Cl)/SiO₂ (Fig. 7, "fresh" and Fig. S8a) and CuO(Cl0.1)/SiO₂ (Fig. S8b) catalysts. Both materials exhibit EPR signals due to the presence of isolated Cu(II) ions ($S = 1/2$, d^9) in tetragonally distorted symmetry [62]. However, the EPR signal of CuO(Cl)/SiO₂ catalyst can be elucidated as the superposition of two Cu(II) signals arising from different isolated Cu(II) single sites (Fig. S8a). Both sites exhibit well resolved and slightly broad quartet hfs arising from the coupling of the unpaired electron (d^9 , $S = 1/2$) with the nuclear spin of copper ($^{63,65}\text{Cu}$ $I = 3/2$) while the perpendicular component shows only a broad line due to unresolved hfs coupling (Fig. 7, red line). The spin Hamiltonian parameters deduced from the simulated spectrum (Fig. S8a) [63] (Site 1: $g_{\parallel} = 2.332$, $g_{\perp} = 2.060$, $A_{\parallel} = 161$ G and site 2: $g_{\parallel} = 2.358$, $g_{\perp} = 2.062$, $A_{\parallel} = 164$ G) indicate that both Cu(II) sites have in an axial geometry with elongation along the tetragonal axis since $g_{\parallel} > g_{\perp}$ i.e. the ground state of the unpaired electron is $d_{x^2-y^2}^2$ [62]. The proper resolution of the parallel component of the hyperfine structure indicates the existence of only weak magnetic interaction between the Cu(II) ions on the surface of the catalyst. The EPR spectrum of CuO(Cl0.1)/SiO₂ shows only one axial signal at $g_{\parallel} = 2.379$ and $g_{\perp} = 2.066$ with $A_{\parallel} = 138$ and $A_{\perp} = 22$ G (Fig. S8b) indicating a well dispersion of Cu(II) ions on the surface of the support and exclude the generation of

less active Cu₂Cl(OH)₃ agglomerates which are characterized by broad EPR signals.

Furthermore, the influence of chloride ions on the catalytic performance was also studied in case of CuO(N,N)/MCM-41. The addition of NaCl led to a significant decrease of hydrogen generation, almost independently of the chloride concentration (Fig. S7b). This points out that chloride ions negatively affect the catalytic activity and their presence has to be avoided.

Further, we were interested in the changes of the catalyst during the photocatalytic reactions. Thus, EPR measurements as well as in situ XANES investigations were performed before and after the hydrogen evolution experiments. The EPR spectrum (Fig. 7) of CuO(Cl)/SiO₂ catalyst after 20 h irradiation (without Ir-PS) is similar to the fresh catalyst, however with low signal intensity indicating that only small part of Cu(II) is converted to EPR silent species during the catalytic test, more probably, Cu(I) species as evident from XAS measurements. However, presence of [Ir(ppy)₂(bpy)]PF₆ as photosensitizer in the photocatalytic reaction obviously decreases the EPR signal intensity of Cu(II) ions of the CuO(Cl)/SiO₂ catalyst (Fig. 7) indicating that the reducibility of Cu(II) to Cu(I) is enhanced by the PS. This reduction is evidenced by XAS measurements.

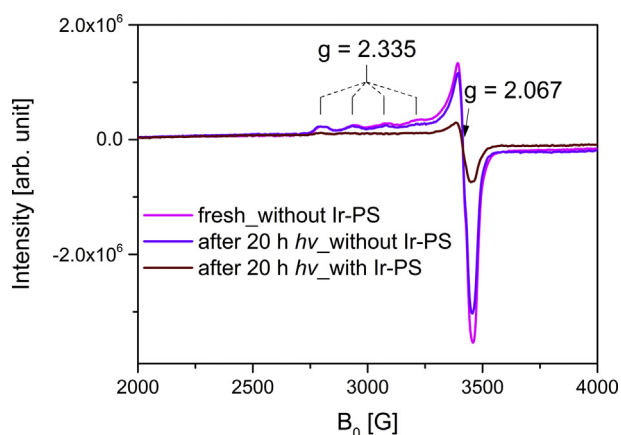


Fig. 7 – EPR spectra of fresh and used CuO(Cl)/SiO₂ catalyst measured at RT.

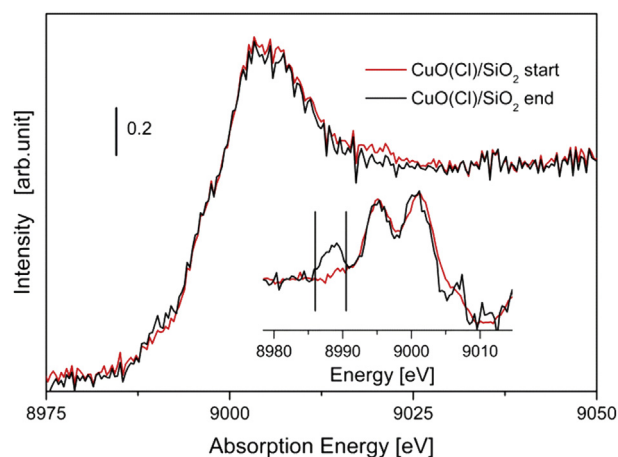


Fig. 8 – XANES spectra of CuO(Cl)/SiO₂ before (red) and after (black) the photocatalytic process. In the inset the first derivative of normalized XANES spectra between 8986 and 8990.5 eV (see vertical lines) is reported.

Time resolved measurements of CuO(Cl)/SiO₂ in the XANES region during the reduction process show an intensity increment of the feature at 8989.9 eV. At the same time in the first derivative a peak centred at 8987.8 eV grows up, testifying the reduction of Cu atoms which confirms the EPR results. The evolution of the integrated area of this peak during the in situ experiment is reported, see inset Fig. 8. The kinetics of the corresponding process is shown in the SI (Fig. S9).

In summary, EPR and XANES investigations show the reduction of the copper(II) species during the photocatalytic proton reduction which is in accordance with the studies of the previously investigated copper system [44].

Conclusions

Five silica supported copper catalysts were synthesized and successfully applied for visible light driven hydrogen generation by dye sensitizing. The catalyst derived from mesoporous silica MCM-41 impregnated with aqueous CuCl₂, dried and impregnated with 2 M aqueous NaOH yielded the best catalyst CuO(Cl)/SiO₂. TEM and SAXS measurements revealed particle sizes of about 1.4 nm of CuO in these materials, which is lower in comparison to the other tested catalysts. Furthermore, the CuO structure in CuO(Cl)/SiO₂ significantly differed from the standard CuO and all investigated other materials, respectively, which was analyzed by EXAFS. Cu₂Cl(OH)₃ particles were detected as second copper species determined via XRD, TEM and EPR. The formation of Cu₂Cl(OH)₃ agglomerates was completely suppressed by decreasing the copper amount to about 0.6 wt% in (CuO(Cl0.1)/SiO₂) which indicates that Cu₂Cl(OH)₃ only contributes to a minor extent to the catalytic activity. Accordingly, the activity under visible light increased to 1702 mmol h⁻¹ g⁻¹ which is 6 times higher compared to the previously investigated Cu/[Ir(ppy)₂(bpy)]PF₆ system.

Acknowledgements

This work has been supported by the State of Mecklenburg-Vorpommern and the Bundesministerium für Bildung und Forschung (BMBF). The authors thank Anja Kammer for her work in the hydrogen generation measurements and Dr. Matthias Schneider (XRD), Anja Simmulla (ICP) and Karin Struve (BET) for their analytical support. Furthermore, we thank the staff of the BM23 and ID24 beamline of the ESRF, especially Dr. Sakura Pascarelli and Dr. Olivier Mathon, for their assistance and the ESRF for providing the beam time. The authors are grateful to Michael Krumrey from the PTB (National Metrology Institute of Germany) for using the FCM beamline and the in vacuum Pilatus detector of the PTB at the Synchrotron BESSY II/HZB.

Appendix A. Supplementary data

Supplementary data to this article can be found online at <https://doi.org/10.1016/j.ijhydene.2019.04.006>.

REFERENCES

- [1] Blankenship RE, Tiede DM, Barber J, Brudvig GW, Fleming G, Ghirardi M, et al. Comparing photosynthetic and photovoltaic efficiencies and recognizing the potential for improvement. *Science* 2011;332:805–9.
- [2] Balzani V, Credi A, Venturi M. Photochemical conversion of solar energy. *ChemSusChem* 2008;1:26–58.
- [3] Esswein AJ, Nocera DG. Hydrogen production by molecular photocatalysis. *Chem Rev* 2007;107:4022–47.
- [4] Kudo A, Miseki Y. Heterogeneous photocatalyst materials for water splitting. *Chem Soc Rev* 2009;38:253–78.
- [5] Navarro Yerga RM, Álvarez Galván MC, del Valle F, Villoria de la Mano JA, Fierro JLG. Water splitting on semiconductor catalysts under visible-light irradiation. *ChemSusChem* 2009;2:471–85.
- [6] Chen X, Shen S, Guo L, Mao SS. Semiconductor-based photocatalytic hydrogen generation. *Chem Rev* 2010;110:6503–70.
- [7] Tee SY, Win KY, Teo WS, Koh L-D, Liu S, Teng CP, et al. Recent Progress in energy-driven water splitting. *Adv Sci* 2017;4:1600337.
- [8] Takayama T, Tsuji I, Aono N, Harada M, Okuda T, Iwase A, et al. Development of various metal Sulfide photocatalysts consisting of d⁰, d⁵, and d¹⁰ metal ions for sacrificial H₂ evolution under visible light irradiation. *Chem Lett* 2017;46:616–9.
- [9] Jung M, Hart JN, Scott J, Ng YH, Jiang Y, Amal R. Exploring Cu oxidation state on TiO₂ and its transformation during photocatalytic hydrogen evolution. *Appl Catal, A* 2016;521:190–201.
- [10] Jung M, Scott J, Ng YH, Jiang Y, Amal R. CuO_x dispersion and reducibility on TiO₂ and its impact on photocatalytic hydrogen evolution. *Int J Hydrogen Energy* 2014;39:12499–506.
- [11] Liu Y, Wang Z, Huang W. Influences of TiO₂ phase structures on the structures and photocatalytic hydrogen production of CuO_x/TiO₂ photocatalysts. *Appl Surf Sci* 2016;389:760–7.
- [12] Praveen Kumar D, Shankar MV, Mamatha Kumari M, Sadanandam G, Srinivas B, Durgakumari V. Nano-size effects on CuO/TiO₂ catalysts for highly efficient H₂ production under solar light irradiation. *Chem Commun* 2013;49:9443–5.
- [13] Wang A, Che LK, Dong R, Zhao G. Preparation of CuO-decorated core-shell montmorillonite-TiO₂ colloids and their photocatalytic activity for hydrogen evolution from water. *Adv Mat Res* 2013;724–725:740–3.
- [14] Wang Z, Liu Y, Martin DJ, Wang W, Tang J, Huang W. CuO_x-TiO₂ junction: what is the active component for photocatalytic H₂ production? *Phys Chem Chem Phys* 2013;15:14956–60.
- [15] Yoong LS, Chong FK, Dutta BK. Development of copper-doped TiO₂ photocatalyst for hydrogen production under visible light. *Energy* 2009;34:1652–61.
- [16] Yu Y-H, Chen Y-P, Cheng Z. Microwave-assisted synthesis of rod-like CuO/TiO₂ for high-efficiency photocatalytic hydrogen evolution. *Int J Hydrogen Energy* 2015;40:15994–6000.
- [17] Tamiolakis I, Papadas IT, Spyridopoulos KC, Armatas GS. Mesoporous assembled structures of Cu₂O and TiO₂ nanoparticles for highly efficient photocatalytic hydrogen generation from water. *RSC Adv* 2016;6:54848–55.
- [18] Hu Q, Huang J, Li G, Jiang Y, Lan H, Guo W, et al. Origin of the improved photocatalytic activity of Cu incorporated TiO₂ for hydrogen generation from water. *Appl Surf Sci* 2016;382:170–7.
- [19] Jin Z, Zhang X, Li Y, Li S, Lu G. 5.1% Apparent quantum efficiency for stable hydrogen generation over eosin-

- sensitized CuO/TiO₂ photocatalyst under visible light irradiation. *Catal Commun* 2007;8:1267–73.
- [20] Xu S, Sun DD. Significant improvement of photocatalytic hydrogen generation rate over TiO₂ with deposited CuO. *Int J Hydrogen Energy* 2009;34:6096–104.
- [21] Bandara J, Udawatta CPK, Rajapakse CSK. Highly stable CuO incorporated TiO₂ catalyst for photocatalytic hydrogen production from H₂O. *Photochem Photobiol Sci* 2005;4:857–61.
- [22] Sreethawong T, Yoshikawa S. Comparative investigation on photocatalytic hydrogen evolution over Cu-, Pd-, and Au-loaded mesoporous TiO₂ photocatalysts. *Catal Commun* 2005;6:661–8.
- [23] Choi H-J, Kang M. Hydrogen production from methanol/water decomposition in a liquid photosystem using the anatase structure of Cu loaded. *Int J Hydrogen Energy* 2007;32:3841–8.
- [24] Gombac V, Sordelli L, Montini T, Delgado JJ, Adamski A, Adami G, et al. CuO_x-TiO₂ photocatalysts for H₂ production from Ethanol and glycerol solutions. *J Phys Chem A* 2010;114:3916–25.
- [25] Sakata Y, Yamamoto T, Okazaki T, Imamura H, Tsuchiya S. Generation of visible light response on the photocatalyst of a copper ion containing TiO₂. *Chem Lett* 1998;27:1253–4.
- [26] Lee SS, Bai H, Liu Z, Sun DD. Optimization and an insightful properties—activity study of electrospun TiO₂/CuO composite nanofibers for efficient photocatalytic H₂ generation. *Appl Catal, B* 2013;140–141:68–81.
- [27] Wu N-L, Lee M-S. Enhanced TiO₂ photocatalysis by Cu in hydrogen production from aqueous methanol solution. *Int J Hydrogen Energy* 2004;29:1601–5.
- [28] Yu J, Ran J. Facile preparation and enhanced photocatalytic H₂-production activity of Cu(OH)₂ cluster modified TiO₂. *Energy Environ Sci* 2011;4:1364–71.
- [29] Wu Y, Lu G, Li S. The role of Cu(I) species for photocatalytic hydrogen generation over CuO_x/TiO₂. *Catal Lett* 2009;133:97.
- [30] Lalitha K, Sadanandam G, Kumari VD, Subrahmanyam M, Sreedhar B, Hebalkar NY. Highly stabilized and finely dispersed Cu₂O/TiO₂: a promising visible sensitive photocatalyst for continuous production of hydrogen from glycerol:water mixtures. *J Phys Chem C* 2010;114:22181–9.
- [31] Foo WJ, Zhang C, Ho GW. Non-noble metal Cu-loaded TiO₂ for enhanced photocatalytic H₂ production. *Nanoscale* 2013;5:759–64.
- [32] Ibrahim S, Cheng Y, Zhao D, Nadeem MA. A new insight for photocatalytic hydrogen production by a Cu/Ni based cyanide bridged polymer as a co-catalyst on titania support in glycerol water mixture. *Int J Hydrogen Energy* 2019;44:2508–18.
- [33] Guerrero-Araque D, Acevedo-Peña P, Ramírez-Ortega D, Calderon HA, Gómez R. Charge transfer processes involved in photocatalytic hydrogen production over CuO/ZrO₂-TiO₂ materials. *Int J Hydrogen Energy* 2017;42:9744–53.
- [34] Liu Z, Bai H, Xu S, Sun DD. Hierarchical CuO/ZnO “corn-like” architecture for photocatalytic hydrogen generation. *Int J Hydrogen Energy* 2011;36:13473–80.
- [35] Shaislamov U, Krishnamoorthy K, Kim SJ, Abidov A, Allabergenov B, Kim S, et al. Highly stable hierarchical p-CuO/ZnO nanorod/nanobranched photoelectrode for efficient solar energy conversion. *Int J Hydrogen Energy* 2016;41:2253–62.
- [36] Wu F, Wang X, Hu S, Hao C, Gao H, Zhou S. Solid-state preparation of CuO/ZnO nanocomposites for functional supercapacitor electrodes and photocatalysts with enhanced photocatalytic properties. *Int J Hydrogen Energy* 2017;42:30098–108.
- [37] Kwon Y, Soon A, Han H, Lee H. Shape effects of cuprous oxide particles on stability in water and photocatalytic water splitting. *J Mater Chem* 2015;3:156–62.
- [38] de Jongh PE, Vanmaekelbergh D, Kelly JJ. Cu₂O: a catalyst for the photochemical decomposition of water? *Chem Commun* 1999:1069–70.
- [39] Hara M, Kondo T, Komoda M, Ikeda S, Kondo JN, Domen K, et al. Cu₂O as a photocatalyst for overall water splitting under visible light irradiation. *Chem Commun* 1998:357–8.
- [40] Paracchino A, Laporte V, Sivula K, Grätzel M, Thimsen E. Highly active oxide photocathode for photoelectrochemical water reduction. *Nat Mater* 2011;10:456–61.
- [41] Somasundaram S, Raman Nair Chenthamarakshan C, de Tacconi NR, Rajeshwar K. Photocatalytic production of hydrogen from electrodeposited film and sacrificial electron donors. *Int J Hydrogen Energy* 2007;32:4661–9.
- [42] Zhang X, Peng T, Song S. Recent advances in dye-sensitized semiconductor systems for photocatalytic hydrogen production. *J Mater Chem* 2016;4:2365–402.
- [43] Maeda K, Eguchi M, Youngblood WJ, Mallouk TE. Niobium oxide nanoscrolls as building blocks for dye-sensitized hydrogen production from water under visible light irradiation. *Chem Mater* 2008;20:6770–8.
- [44] Junge H, Codolà Z, Kammer A, Rockstroh N, Karnahl M, Luo S-P, et al. Copper-based water reduction catalysts for efficient light-driven hydrogen generation. *J Mol Catal A Chem* 2014;395:449–56.
- [45] Sprouse S, King KA, Spellane PJ, Watts RJ. Photophysical effects of metal-carbon .sigma. bonds in ortho-metalated complexes of iridium(III) and rhodium(III). *J Am Chem Soc* 1984;106:6647–53.
- [46] Schwartz KR, Chitta R, Bohnsack JN, Ceckanowicz DJ, Miró P, Cramer CJ, et al. Effect of axially projected oligothiophene pendants and nitro-functionalized diimine ligands on the lowest excited state in cationic Ir(III) bis-cyclometalates. *Inorg Chem* 2012;51:5082–94.
- [47] Brunauer S, Emmett PH, Teller E. Adsorption of gases in multimolecular layers. *J Am Chem Soc* 1938;60:309–19.
- [48] Barrett EP, Joyner LG, Halenda PP. The determination of pore volume and area distributions in porous substances. I. Computations from nitrogen isotherms. *J Am Chem Soc* 1951;73:373–80.
- [49] Krumrey M. Design of a four-crystal monochromator beamline for radiometry at BESSY II. *J Synchrotron Radiat* 1998;5:6–9.
- [50] Hoell A, Zizak I, Bieder H, Mokrani L. DE 10 2006 029 449 patent specification. 2006.
- [51] Wernecke J, Gollwitzer C, Muller P, Krumrey M. Characterization of an in-vacuum PILATUS 1M detector. *J Synchrotron Radiat* 2014;21:529–36.
- [52] Breßler I, Kohlbrecher J, Thünemann AF. SASfit: a tool for small-angle scattering data analysis using a library of analytical expressions. *J Appl Crystallogr* 2015;48:1587–98.
- [53] Newville M. EXAFS analysis using FEFF and FEFFIT. *J Synchrotron Radiat* 2001;8:96–100.
- [54] Pascarelli S, Mathon O, Mairs T, Kantor I, Agostini G, Strohm C, et al. The time-resolved and extreme-conditions XAS (Texas) facility at the european Synchrotron radiation facility: the energy-dispersive X-ray absorption spectroscopy beamline ID24. *J Synchrotron Radiat* 2016;23:353–68.
- [55] Cotte M, Fabris T, Agostini G, Motta Meira D, De Viguierie L, Solé VA. Watching kinetic studies as chemical maps using open-source software. *Anal Chem* 2016;88:6154–60.
- [56] Haas S, Zehl G, Dorbandt I, Manke I, Bogdanoff P, Fiechter S, et al. Direct accessing the nanostructure of carbon supported Ru–Se based catalysts by ASAXS. *J Phys Chem C* 2010;114:22375–84.
- [57] Stuhrmann HB. Resonance scattering in macromolecular structure research. Berlin, Heidelberg: Springer Berlin Heidelberg; 1985. p. 123–63.

- [58] Cromer DT, Liberman D. Relativistic calculation of anomalous scattering factors for X rays. *J Chem Phys* 1970;53:1891–8.
- [59] Lytle FW, Greegor RB, Panson AJ. Discussion of x-ray-absorption near-edge structure: application to Cu in the high- T_c superconductors $\text{La}_{1.8}\text{Sr}_{0.2}\text{CuO}_4$ and $\text{YBa}_2\text{Cu}_3\text{O}_7$. *Phys Rev B* 1988;37:1550–62.
- [60] Gärtner F, Boddien A, Barsch E, Fumino K, Losse S, Junge H, et al. Photocatalytic hydrogen generation from water with iron carbonyl phosphine complexes: improved water reduction catalysts and mechanistic insights. *Chem Eur J* 2011;17:6425–36.
- [61] Gärtner F, Cozzula D, Losse S, Boddien A, Anilkumar G, Junge H, et al. Synthesis, characterisation and application of iridium(III) photosensitisers for catalytic water reduction. *Chem Eur J* 2011;17:6998–7006.
- [62] Hathaway BJ, Billing DE. The electronic properties and stereochemistry of mono-nuclear complexes of the copper(II) ion. *Coord Chem Rev* 1970;5:143–207.
- [63] Stoll S, Schweiger A. EasySpin, a comprehensive software package for spectral simulation and analysis in EPR. *J Magn Reson* 2006;178:42–55.

Supporting Information

Dye Activation of Heterogeneous Copper(II)-Species for Visible Light Driven Hydrogen Generation

*Stefanie Kreft,^a Jörg Radnik,^b Jabor Rabeah,^a Giovanni Agostini,^c Marga-Martina Pohl,^a Eike
Gericke,^{d,e} Armin Hoell,^d Matthias Beller,^a Henrik Junge^{*a} and Sebastian Wohlrab ^{*a}*

^a. Leibniz Institute for Catalysis at the University of Rostock, Albert-Einstein-Straße 29a, 18059 Rostock, Germany.

^b. Federal Institute of Material Research and Testing (BAM), Unter den Eichen 44-46, 12203 Berlin, Germany.

^c. Alba Synchrotron, Carrer de la Llum 2-26, 08290 Cerdanyola del Valle's, Spain.

^d. Helmholtz-Zentrum Berlin für Materialien und Energie, Hahn-Meitner Platz 1, 14109 Berlin, Germany.

^e. Humboldt-Universität zu Berlin, Institut für Chemie, Brook-Taylor Straße 2, 12489 Berlin, Germany.

* Corresponding authors: mail: henrik.junge@catalysis.de, sebastian.wohrlab@catalysis.de.

Dedicated to Prof. Gabor Laurenczy on the occasion of his 65th birthday.

Table S1: Results from literature for the photocatalytic proton reduction with CuO_x/TiO₂ catalysts

No.	Active System	Amount of Cu	Irradiation	Activity [mmol·g ⁻¹ ·h ⁻¹]	Quantum yield	Conditions	Ref. in manuscript
1	Cu/TiO ₂	1 wt%	> 400 nm	5.8	n.d.	10 vol% glycerol in water	9
2	CuO _x /TiO ₂	0.5 wt%	Xe lamp	1.1	n.d.	10 vol% methanol in water	10
3	Cu ₂ O/TiO ₂	1 wt%	> 300 nm	3.2	n.d.	20 vol% methanol in water	11
4	CuO/TiO ₂ ^[a]	1.5 wt%	solar irradiation	99.8	n.d.	5 vol% glycerol in water	12
5	CuO/TiO ₂ ^[a]	5 wt%	Xe lamp	0.2	n.d.	6 vol% methanol in water	13
6	Cu ₂ O/TiO ₂	42 wt%	Xe lamp	0.1	n.d.	20 vol% methanol in water	14
7	CuO/TiO ₂ ^[a]	10 wt%	Halogen lamp	8.5	n.d.	6 vol% methanol in water	15
8	CuO/TiO ₂ ^[a]	1 wt%	Xe lamp	3.5	n.d.	20 vol% methanol in water	16
9	Cu ₂ O/TiO ₂	1.5 wt%	360-780 nm	36.1	13.5 % at 365 nm	20 vol% methanol in water	17
10	Cu ₂ O/TiO ₂	2.7 wt%	Xe lamp	2.8 ^[b]	n.d.	10 vol% methanol in water	18
11	CuO/TiO ₂ ^[c]	1 wt%	> 420 nm	0.5	5.1 % at 420 nm	15 vol% DEA in water ^[d]	19
12	CuO/TiO ₂ ^[e]	9 mol%	Xe lamp	18.5	n.d.	10 vol% methanol in water	20
13	CuO/TiO ₂ ^[e]	7 wt%	Hg lamp	4.2	n.d.	5 vol% methanol in water	21
14	CuO/TiO ₂ ^[a]	1.5 wt%	Hg lamp	1.8	n.d.	10 vol% methanol in water	22
15	CuO/TiO ₂ ^[e]	10 mol%	365 nm	0.7	n.d.	50 vol% methanol in water	23
16	CuO/TiO ₂ ^[e]	2.5 wt%	Hg lamp	1.3	29 % at 365 nm	50 vol% ethanol in 1 M aqueous glycerol	24
17	Cu ₂ O/TiO ₂	1 wt%	Xe lamp	5 · 10 ⁻³	n.d.	50 vol% methanol in water	25
18	CuO _x /TiO ₂ ^[a]	6 mol%	Hg lamp	10	n.d.	10 vol% methanol in water	26
19	Cu ₂ O/TiO ₂	1.2 wt%	UV-light	3	n.d.	40 vol% methanol in water	27
20	Cu(OH) ₂ /TiO ₂ ^[e]	0.3 mol%	365 nm	3.4	13.9 % at 365 nm	0.5 vol% ethylene glycol in water	28
21	Cu ₂ O/TiO ₂	1 wt%	Hg lamp	5	n.d.	20 vol% ethanol in water	29
22	Cu ₂ O/TiO ₂	2 wt%	Hg lamp	3	n.d.	water	30
23	Cu ₂ O/TiO ₂	0.5 wt%	Hg lamp	200	n.d.	5 vol% glycerol in water	30
24	Cu-Cu ₂ O/TiO ₂	9 wt%	Xe lamp	13	n.d.	10 vol% methanol in water	31
25	Cu/Ni/TiO ₂	n.d.	UV-light	9.2	n.d.	5 vol% glycerol in water	32
26	Cu ₂ O ^[f]		Xe lamp	1.6 · 10 ⁻³	n.d.	water	33
27	Cu ₂ O		> 460 nm	1 · 10 ⁻³	0.3 % at 550 nm	water	35
28	CuO(ClO ₄)/SiO ₂	0.6 wt%	> 385 nm	1702 ^[h]	1.2 % at 415 nm	THF/TEA/H ₂ O = 3:2:1	

^[a] active Cu-species was not analyzed.

^[b] unit: [μmol·cm⁻²·h⁻¹], catalyst: Cu incorporated TiO₂ thin films deposited on quartz glass.

^[c] Reaction was performed in the presence of a dye (Eosin Y).

^[d] DEA: Diethanolamine

^[e] Observation of a reduction of Cu(II) during the reaction.

^[f] Oxidation of Cu(I) in water during the reaction.

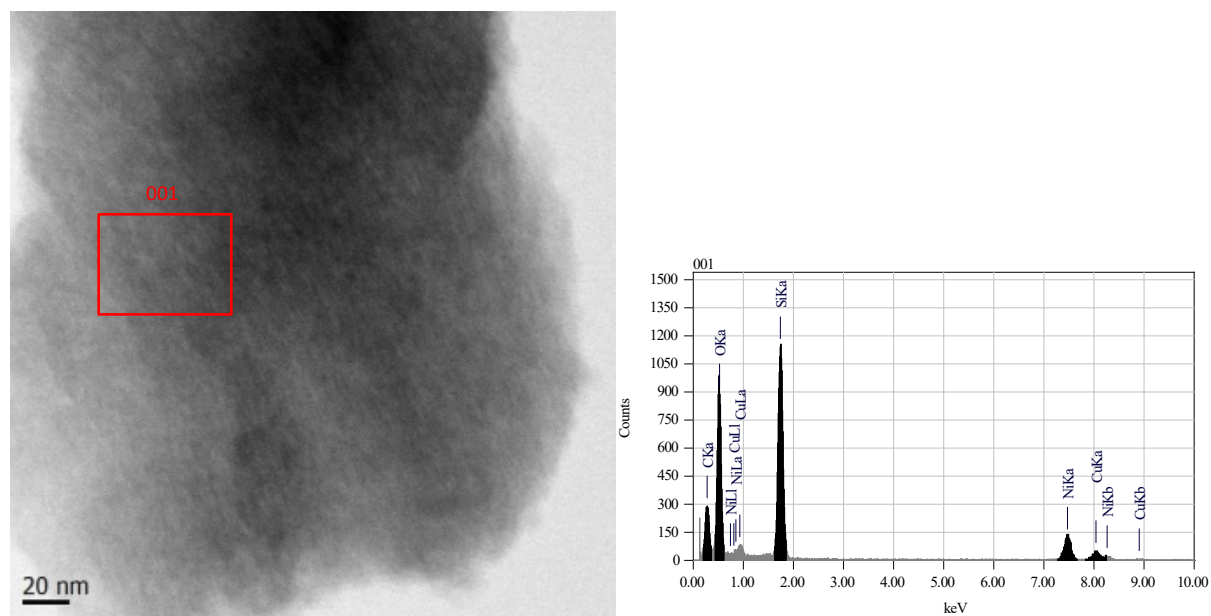
^[g] TEOA: Triethanolamine

^[h] activity correlated to copper amount [mmol·g⁻¹·h⁻¹]

n.d. not declared.

TEM images and EDXS measurements of Cu/SiO₂ materials

a)



b)

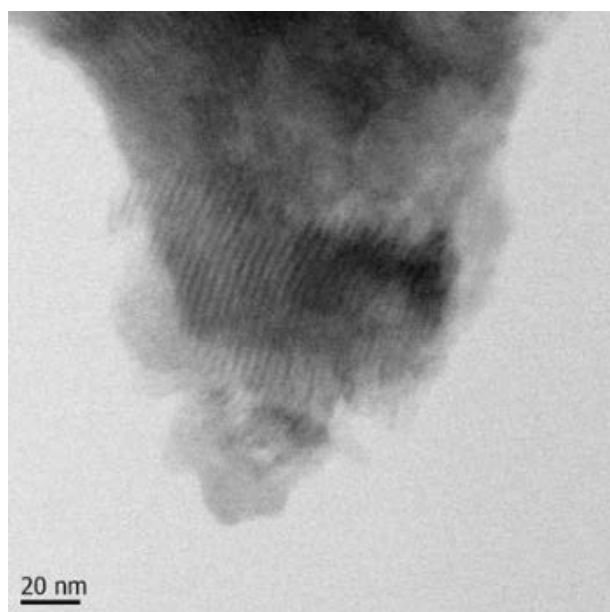
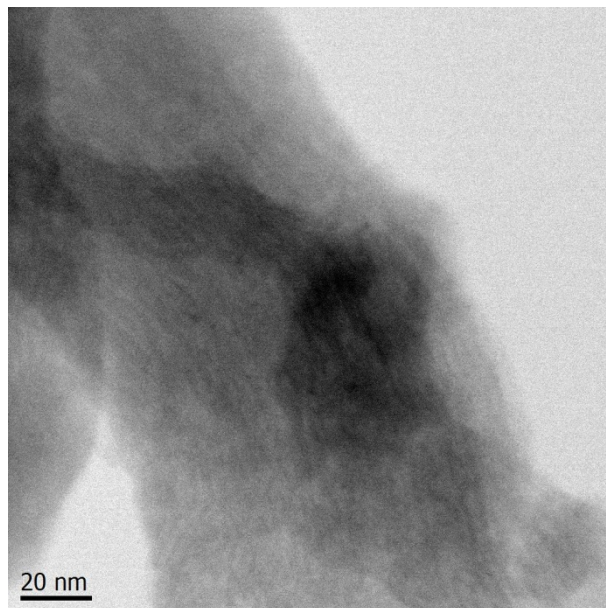
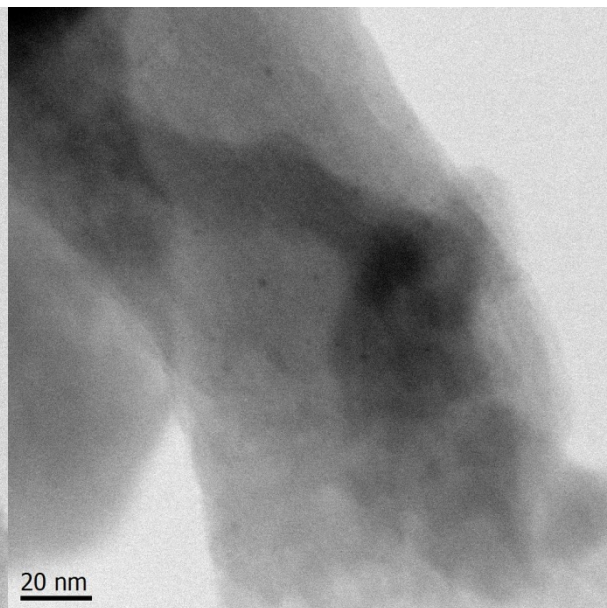


Figure S1 BF-TEM image and EDX measurement of CuO(N,a)/MCM-41, focus on the particles (a) and the MCM-41 hexagonal pore structure.

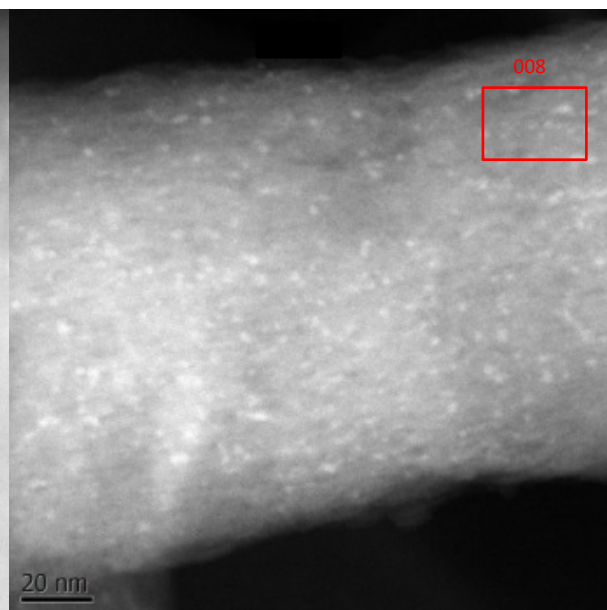
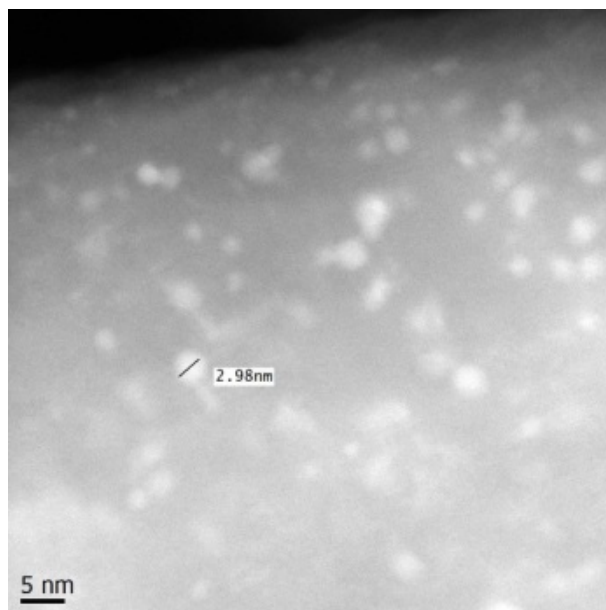
a)



b)



c)



d)

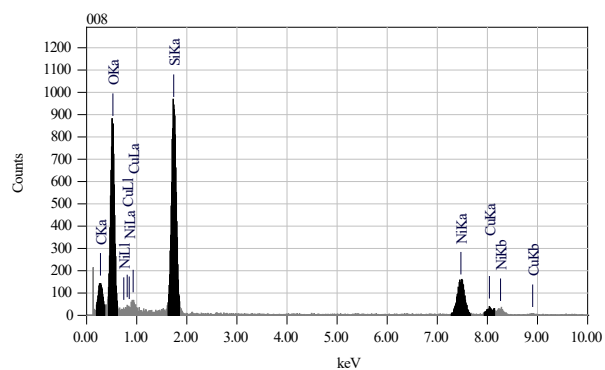


Figure S2 CuO(N,N)/MCM-4: BF-TEM, focus on pore structure (a) and particles (b); HAADF-TEM images (c) and EDX measurement (d).

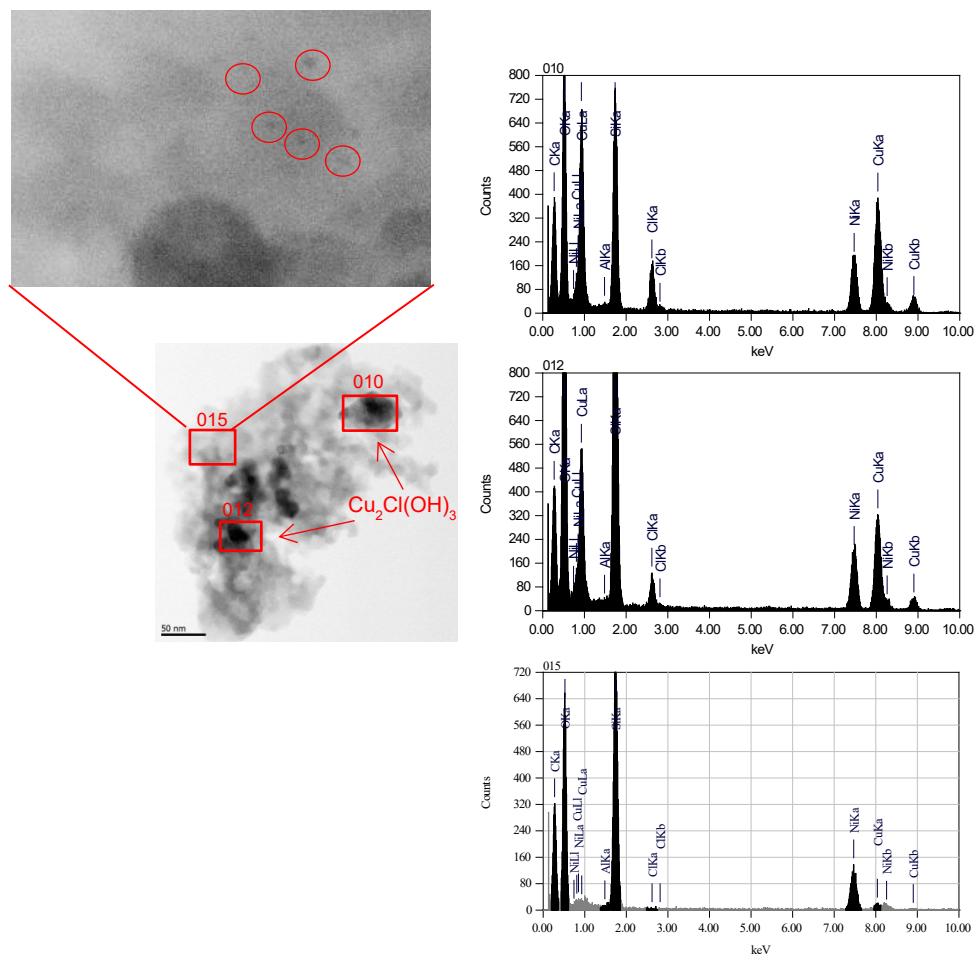
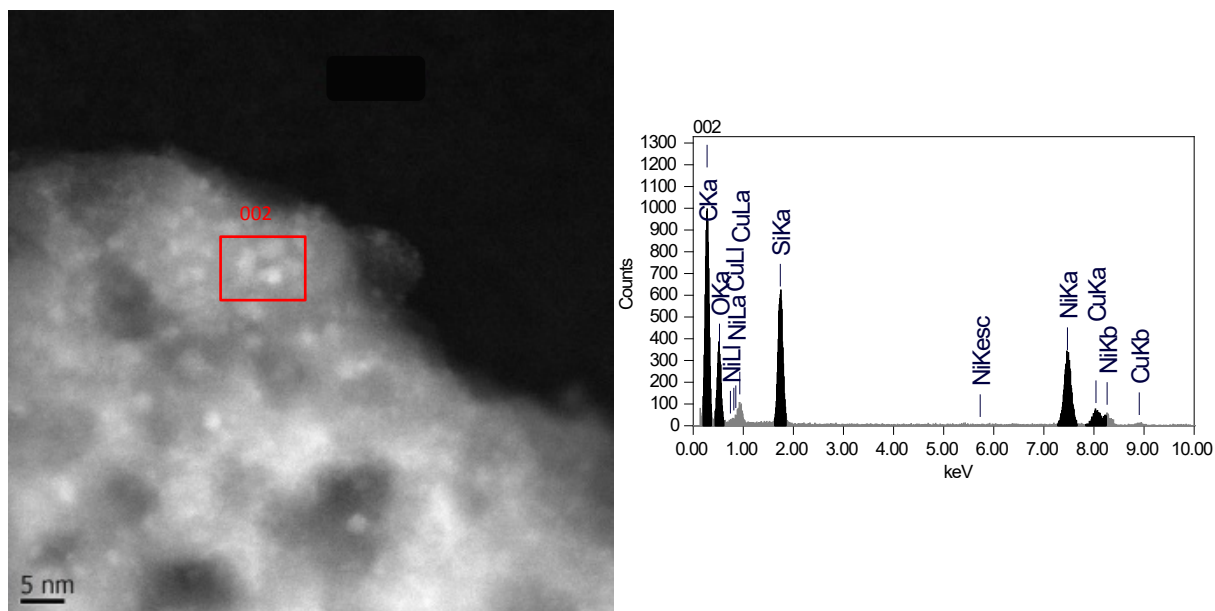


Figure S3 BF-TEM image and EDX measurements of CuO(Cl)/SiO₂.

a)



b)

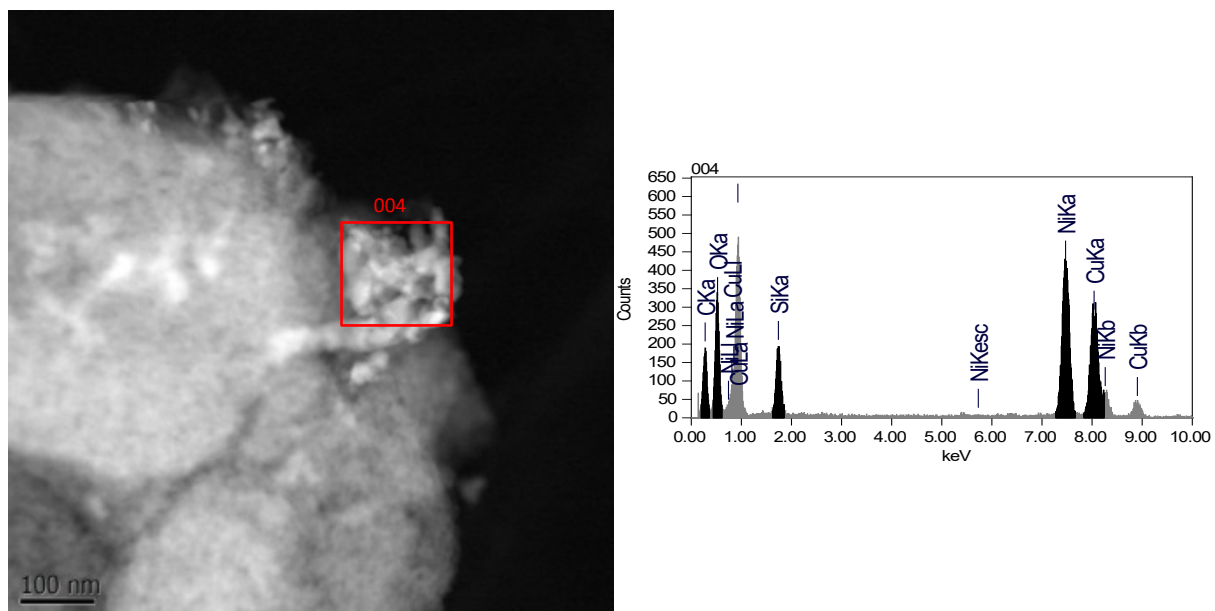


Figure S4 HAADF-TEM images and EDX measurements of CuO(Cl,a)/SiO₂, focus on small particles (a) and agglomerates (b).

UV/Vis spectra of the Ir-PS

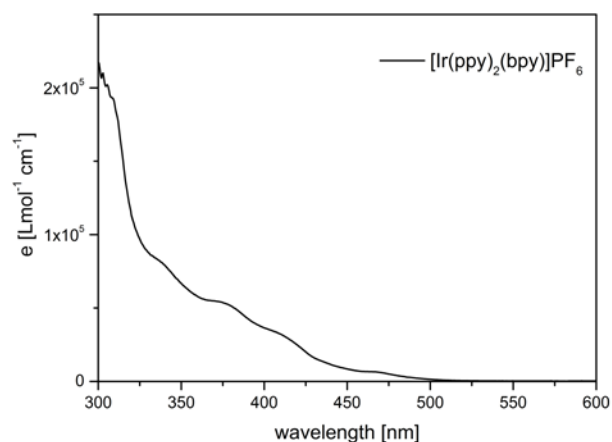


Figure S5 UV/Vis spectra of catalytically active iridium photosensitizer ($[\text{Ir}(\text{ppy})_2(\text{bpy})]\text{PF}_6$). Conditions: $0.1 \text{ mmol} \cdot \text{L}^{-1}$ degassed solutions in acetonitrile.[1]

Experimental hydrogen evolution measurements

General information about the experimental set up

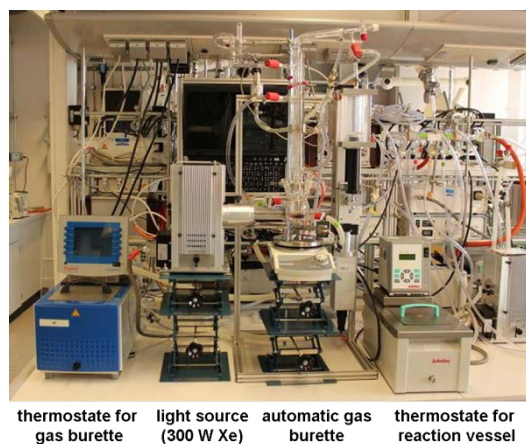
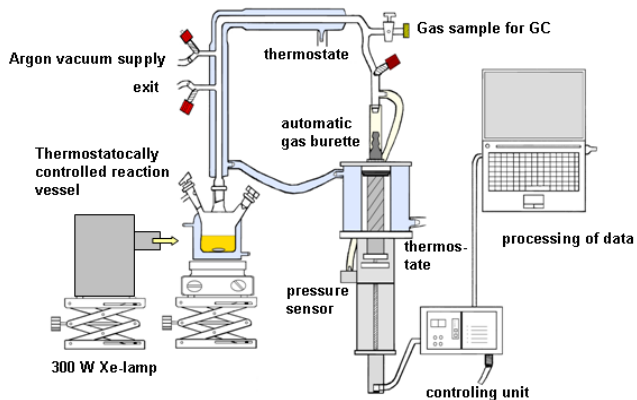


Figure S6a Experimental set-up for automatic quantification of evolved gases (adjusted output of the Xe-lamp was 1.5 W, wavelength $\geq 385 \text{ nm}$).

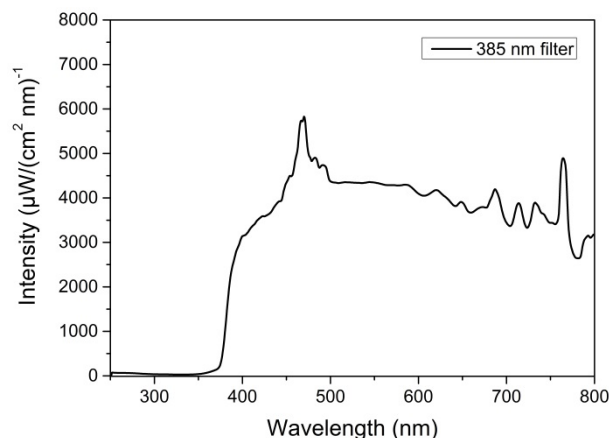


Figure S6b Absorption spectrum of the Xe lamp with 385 nm cut off filter.

General principle of quantitative gas measurements:

A double walled thermostatically controlled reaction vessel (temperature kept constant at 25.0°C during the reactions) is connected via a condenser to an automatic gas burette (temperature kept constant at 25 °C during measurements). The gas burette is equipped with a pressure sensor. Evolving gas during the reaction causes a pressure increase in the closed system, which is compensated by volume increase of the burette syringe by an automatic controlling unit. The gas evolution curves are collected by a PC.

Details on GC measurements:

A GC sample is taken from the collected gas in the burette after each reaction. GCs were calibrated with certified commercially available gas mixtures. GC measurements were carried out on one of two available systems:

GC a): HP Plot Q / FID – hydrocarbons, Carboxen / TCD - permanent gases, He carrier gas.

GC b): Carboxen / TCD / Methanizer / FID - permanent gases, He carrier gas.

The systems allow for the determination of H₂, Ar, CO, CH₄ and CO₂ within the ranges:

H₂ ≥ 0.5 vol% - 100 vol%

CO ≥ 10 ppm (system a), CO down to 1 ppm (system b)

CO₂ 1 - 100 vol%.

The collected gas volumes were corrected by a blank value (average 2.0 mL gas), which was measured in an experiment without any catalysts present in the mixture. With respect to the reproducibility of our method (1-14%) the traces of CO and CO₂ are neglected for calculation of the activity for a standard experiment. The activity was calculated by equation 1 ($V_{obs.}$: measured gas volume from automatic gas burette; V_{blank} : blank volume):

$$activity = \frac{\frac{V_{obs.} - V_{blank}}{V_{m, H_2, 25^\circ C}}}{t \cdot m_{Cu}} \quad (1)$$

The calculation of $V_{m, H_2, 25^\circ C}$ was carried out using van der Waals equation (eq. 2):

$$V_{m, H_2, 25^\circ C} = \frac{RT}{p} + b - \frac{a}{RT} = 24.48 \frac{ml}{mmol} \quad (2)$$

with:

R: 8.3145 x 10⁶ cm³ Pa mol⁻¹ K⁻¹

T: 298.15 K

p: 101325 Pa

b: 26.6 cm³ mol⁻¹

a: 24.7 x 10⁹ cm⁶ Pa mol⁻²

Quantum Yield calculation

The quantum yield for the photocatalytic proton reduction reaction was determined using the following equation:

$$\Phi(\%) = \frac{2 \times \text{H}_2 \text{ molecules}}{\text{incident photons}} \times 100\%$$

Where the H₂ molecules were quantified using a calibrated GC (see below) and the incident photons were measured using K₃Fe(C₂O₄)₃[2] as chemical actinometer. Therefore, 3 mL (V₁) of an aqueous solution containing the iron actinometer (0.15 M) and H₂SO₄ (0.05 M) were irradiated with a high pressure Hg-lamp (Lumatec Superlite 400, 120 W) equipped with built-in band pass filters. The time of the irradiation was kept as short as possible to avoid more than 10 % decomposition of the actinometer. Before each measurement, the power output of the Hg-lamp was measured using a thermopile (Fa. LOT Quantum Design). After irradiation, an aliquot of 0.180 mL (V₂) was taken and 2 mL of a buffered solution of phenanthroline (0.015 M / 0.5 M H₂SO₄) were added together with distilled H₂O to give a final volume of 25 mL (V₃). The absorbance of the solution at 510 nm was recorded and the value was used to calculate the number of Fe²⁺ ions (nFe²⁺) generated during the irradiation process through the following equation:

$$nFe^{2+} = \frac{V_1 \cdot V_3 \cdot (A - A_0)}{1000 \cdot V_2 \cdot \epsilon_0}$$

where V₁ = volume of actinometer solution irradiated (mL)

V₂ = volume of aliquot taken for analysis (mL)

V₃ = final volume to which the aliquot V₂ is diluted (mL)

A = measured optical density at 510 nm

A₀ = measured optical density at 510 nm of a non-irradiated sample

ε₀ = experimental value of the molar extinction coefficient of the Fe²⁺ complex (11100 L mol⁻¹ cm⁻¹)

Finally, the number of incident photons per second (# photons) is calculated using the following equation:

$$\# \text{ photons } (s^{-1}) = \frac{6.022 \cdot 10^{23} \cdot nFe^{2+}}{\Phi_{\lambda} \cdot t}$$

Where Φ_λ = quantum yield of Fe²⁺ formation

t = time of irradiation (s)

The numbers of incident photons were determined at 415 nm using 4 different power outputs (0.15 W, 0.5 W, 1.0 W and 1.50 W) as shown in Figure S6c.

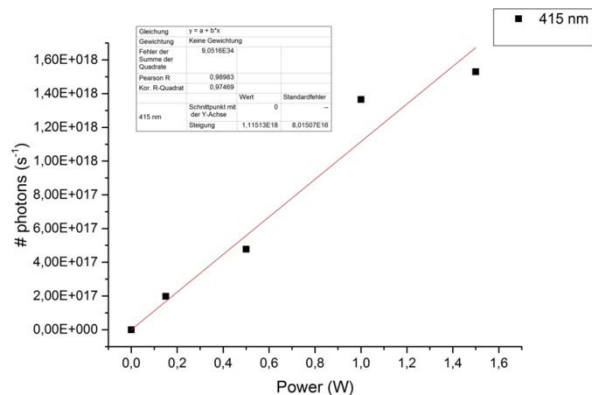


Figure S6c Numbers of photons vs. power output.

Then, the experiment for the determination of the quantum yield in the presence of $\text{CuO}(\text{ClO}_4)/\text{SiO}_2$ was performed under the following conditions: 15 μmol Ir-PS, 11.4 mg $\text{CuO}(\text{ClO}_4)/\text{SiO}_2$, 10 mL THF:TEA:H₂O = 3:2:1, 1.5 W Hg-light irradiation, 415 nm, 25 °C.

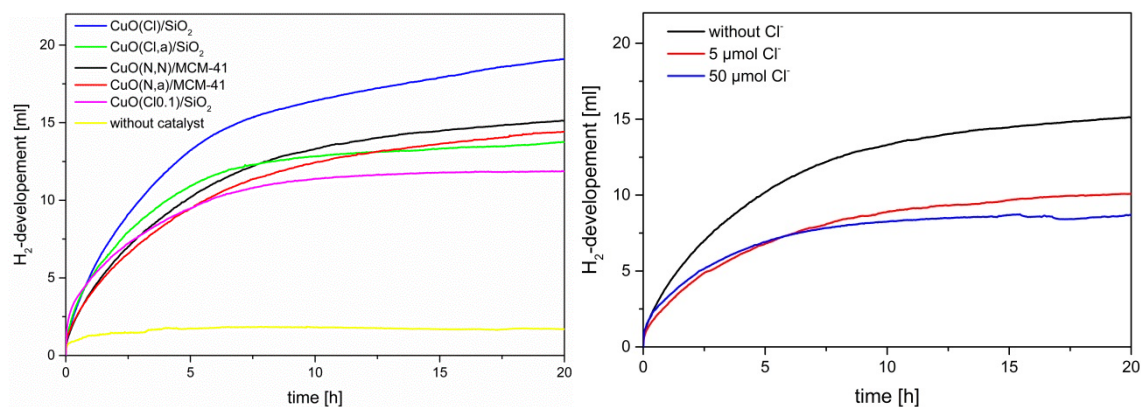
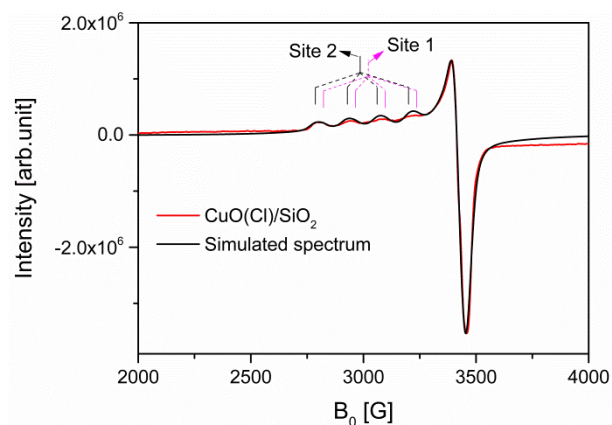


Figure S7 Experimental conditions: a) 15 μmol $[\text{Ir}(\text{ppy})_2(\text{bpy})]\text{PF}_6$, 10 μmol $[\text{Cu}]$ (1 μmol $[\text{Cu}]$ for $\text{CuO}(\text{ClO}_4)/\text{SiO}_2$), 10 mL THF:NEt₃:H₂O 3:2:1 (volume based), 1.5 W Xe-light irradiation, ≥ 385 nm cut-off filter, 25 °C, gas volumes determined by automatic gas burette and corrected by blank volume (2 mL). b) 15 μmol $[\text{Ir}(\text{ppy})_2(\text{bpy})]\text{PF}_6$, 10 μmol $\text{CuO}(\text{N,N})/\text{MCM}-41$, addition of various amounts of NaCl, 10 mL THF:NEt₃:H₂O 3:2:1 (volume based), 1.5 W Xe-light irradiation, ≥ 385 nm cut-off filter, 25 °C, gas volumes determined by automatic gas burette and corrected by blank volume (2 mL).

EPR spectrum of $\text{CuO}(\text{Cl})/\text{SiO}_2$ and $\text{CuO}(\text{ClO}_4)$

a)



b)

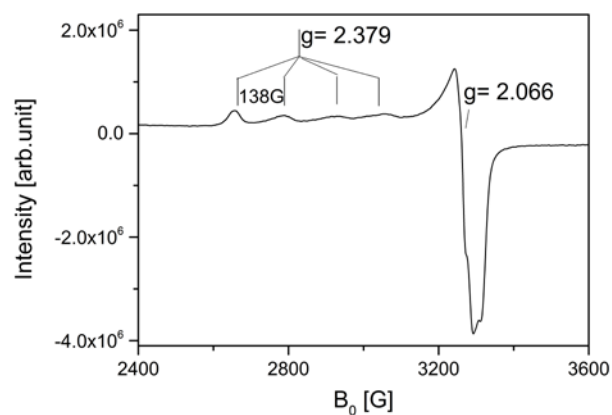


Figure S8 EPR spectrum of CuO(Cl)/SiO₂ (a) and CuO(Cl0.1)/SiO₂ (b) measured at RT with x-band frequencies 9.877 and 9.450 Ghz, respectively.

Kinetics of the process by analysis of the *in situ* XANES measurements

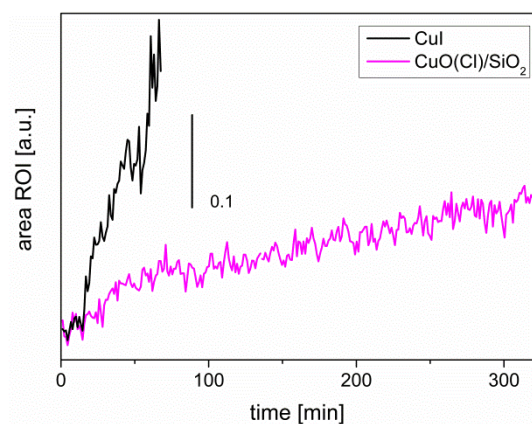


Figure S9 Kinetics of the photocatalytic process by analyzing the integrated area of the first derivate of normalized XANES spectra between 8986 and 8990.5 eV (see Manuscript Fig. 8 inset, vertical lines)

References

- [1] Gärtner F, Cozzula D, Losse S, Boddien A, Anilkumar G, Junge H, et al. Synthesis, Characterisation and Application of Iridium(III) Photosensitisers for Catalytic Water Reduction. *Chem Eur J* 2011;17:6998-7006.
- [2] Alsabeh PG, Rosas-Hernandez A, Barsch E, Junge H, Ludwig R, Beller M. Iron-catalyzed photoreduction of carbon dioxide to synthesis gas. *Catal Sci Technol* 2016;6:3623-30.

5.2 Light-Driven Proton Reduction with *in situ* Supported Copper Nanoparticles

Stefanie Kreft*, Marcel Sonneck*, Henrik Junge*, Ayla Pöpcke, Anja Kammer, Carsten Kreyenschulte, Stefan Lochbrunner, Sebastian Wohlrab, Matthias Beller

* These authors contributed equally to this work.

Int. J. Hydrogen Energ. **2019**, submitted.

Contribution: S. K. analyzed the data of the characteristic methods. She wrote the main part of the manuscript and prepared the supporting information. She has contributed significantly in the development and arrangement of the publications' concept. Her overall contribution is about 25 to 30 %.

Light-Driven Proton Reduction with *in situ* Supported Copper Nanoparticles

Stefanie Kreft^{‡, a}, Marcel Sonneck^{‡, a}, Henrik Junge^{‡, a}, Ayla Pöpcke,^b Anja Kammer,^a Carsten
Kreyenschulte,^a Stefan Lochbrunner,^b Sebastian Wohlrab^{a*} and Matthias Beller^{a*}

^aLeibniz Institute for Catalysis at the University of Rostock, Albert-Einstein-Straße 29a, 18059
Rostock, Germany

^bInstitute of Physics and Department of Life, Light & Matter, University of Rostock, 18051
Rostock, Germany

* Corresponding Author: Dr. Sebastian Wohlrab, E-mail: sebastian.wohlrab@catalysis.de, Prof. Dr.
Matthias Beller, E-Mail: matthias.beller@catalysis.de;
FAX: (+49) 381 1281 5000

[‡] These authors contributed equally to this work.

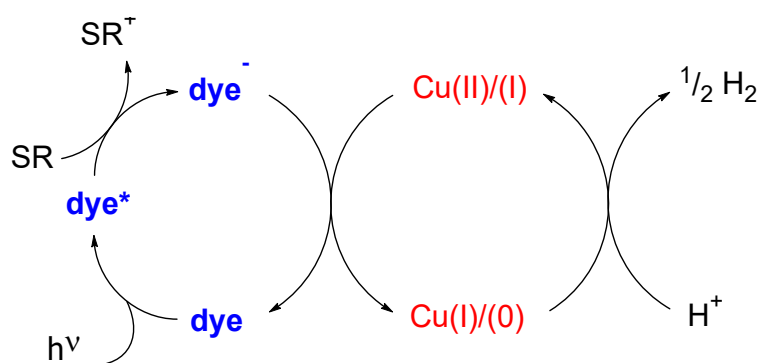
Abstract. Heterogeneous copper particles have been widely investigated in photocatalytic reduction processes to produce hydrogen. In this contribution heterogeneous copper catalysts, *i.e.* supported copper nanoparticles, were generated *in situ* in the presence of an iridium photosensitizer (PS) which itself was activated by visible light absorption. Thereby, the influence of different C- and SiO₂-based additives on the formation of the active species and their performance were studied. The additives ensure heterogeneous nucleation leading to lower sizes of the formed copper particles and prevent their further growth during the reaction which was verified by TEM analysis. Consequently, the hydrogen productivity in the presence of the supports was enhanced and the best carbon material rGO(H₂) revealed a 3 times higher activity compared to the non-supported system after 20 h. Photoluminescence measurements confirmed the proposed reductive quenching mechanism in this system and suggested that rGO(H₂) mediates reoxidation of the PS. However, in the presence of the ligand 2,2'-bipyridine (bpy) the application of the silica MCM-41 showed a fourfold increase of hydrogen evolution compared to the non-supported system, which was still active after 160 h and could be successfully reused in recycling experiments.

Introduction

With the transformation of a mainly fossil fuel-based energy system towards a more sustainable one, hydrogen attracts increasing attention as a secondary energy carrier.^{1,2} Nowadays, it is mostly produced by steam reforming of methane³⁻⁵ and coal gasification^{6,7} involving water gas shift reaction.

In contrast to these traditional processes, biomass gasification⁸ as well as electrolysis of water^{9, 10} using renewable energy offer potentially greener solutions.^{11, 12} In addition, there's a strong scientific interest in direct photocatalytic hydrogen generation.^{13, 14} In fact, in the last decade, numerous photocatalytic homogeneous and heterogeneous water reduction catalysts (WRC's) have been developed.¹⁵⁻²⁰ Clearly, all these processes are still far away from practical, large scale applications, but from the viewpoint of basic science it is important to understand the elementary processes in these proton reduction reactions. In this regard, the use of sacrificial reagents such as amines and alcohols for proton reduction facilitates the study of potential catalytic materials.

Due to their availability, lower costs and toxicity compared to noble metals, oxides consisting of metal cations with d^0 and d^{10} configurations supported on photoactive semi-conductors are particularly interesting as water reduction catalysts.²¹⁻²⁵ Among these, copper catalysts, especially Cu_xO nanoparticles on TiO_2 , are intensively investigated for proton reduction, although the generated hydrogen amount is extremely low (Table S1, entries 1-24).²⁶⁻⁴⁸ Apart from well-known semi-conductors, dye-sensitized copper materials constitute an alternative class of catalysts, which have been successfully applied in previous investigations (Table S1, entries 25, 26).⁴⁹⁻⁵² Here, the photocatalytic process starts with photo excitation of the dye and a subsequent reductive quenching by a sacrificial reductant. The reduced dye is then able to transfer an electron to the Cu-based WRC to catalyze the proton reduction and to form H_2 (Scheme 1).



Scheme 1. Proton reduction using supported copper nanoparticles on dye-sensitized materials.

Previously, we have reported CuI as an appropriate precursor for the WRC and a homogeneous iridium complex as photosensitizer⁴⁹ (Ir-PS). In the course of the catalytic reaction the Cu undergoes heterogenization to copper oxo species. In terms of catalytic properties these species also follow the catalytic cycle of Scheme 1. Interestingly, improved long-term stability and activity were obtained in the presence of 2,2'-bipyridine (bpy) which could be traced back to the stabilization of smaller copper oxo particles preventing further growth.⁴⁹ On the other hand, according to the classical theory of heterogeneous nucleation, the energy barrier required for the formation of solid particles is reduced in the presence of foreign surfaces.⁵³ Hence, solid additives should also yield smaller copper oxo particles by reducing the supersaturation of their precursors. In this respect, we started to exploit the *in situ* formation of stabilized Cu-nanoparticles on porous silica and graphene derivatives for hydrogen generation in order to obtain active, but more stable systems, which can be easily separated and reused, too.

Results and discussion

Photocatalytic studies

In initial attempts copper oxide was *in situ* deposited on three types of silica-based supports which showed enhanced activity towards hydrogen compared to the hitherto best Cu₂O/TiO₂ catalyst.³¹ Also different carbon materials were tested in the presence of dye-sensitizers in order to understand the potential role of electron-conducting properties of the support material. Following previous work⁴⁹, CuI was tested as precursor for the active WRC with [Ir(ppy)₂(bpy)]PF₆ as photosensitizer (PS) in a mixture of 20 ml THF/TEA/H₂O (3:2:1) whereby triethylamine (TEA) acts as the sacrificial reagent (SR). By adding different SiO₂ and carbon additives, the *in situ* generated copper particles should be stabilized. Table 1 shows the results for the photocatalytic hydrogen generation with and without applying SiO₂ additives like MCM-41, SBA-15 and nanoporous glass (pores 39 nm, npG 39) and the carbon additives graphene oxide (GO), hydrogen reduced graphene oxide (rGO(H₂)), activated carbon, and graphite, respectively. Thereby, the volume of generated hydrogen [ml] and the related activities [mmol·h⁻¹·g⁻¹] after 3, 10 and 20 h are listed. First, we investigated the SiO₂-based materials MCM-41, SBA-15 and npG39 (Table 1, Entries 1-3) and the carbon-based rGO(H₂) (Entry 4). Obviously, there is an activity loss for all investigated systems with ongoing duration of the photocatalytic reaction which is in part explained by the decomposition of the photosensitizer.^{49, 50} Among the different additives, the addition of MCM-41 led to the best hydrogen generation after 20 h (Entry 1), which is also higher compared to the non-supported system (Entry 5). Similar WRC activity compared to the non-supported system (Entry 5) was achieved by using the silica SBA-15 (Entry 2). In contrast, the addition of nanoporous glass led to a significant loss of hydrogen generation during the reaction, while at the beginning only a slightly lower activity was observed (Entry 3). Adding rGO (Entry 4) showed after 3 h a slightly higher activity compared to the best SiO₂ material, but a more rapid decrease.

Table 1 Photocatalytic hydrogen generation from THF/TEA/H₂O in the presence of CuI/IrPS/bpy and various additives.

Entry	Additives	V _(THF:TEA:H₂O) [ml]	V [ml] 3h	Activity [mmol·h ⁻¹ ·g ⁻¹] 3h	V [ml] 10h	Activity [mmol·h ⁻¹ ·g ⁻¹] 10h	V [ml] 20h	Activity [mmol·h ⁻¹ ·g ⁻¹] 20h
1	MCM-41	20	9.4	197.7	19.6	123.4	27.4	86.4
2	SBA-15		8.8	187.7	17.5	112.3	23.3	74.8
3	npG 39		7.7	162.7	16.0	101.4	20.9	66.0
4	rGO(H ₂)		10.2	217.0	17.4	110.5	21.8	69.4
5	-		9.5	183.6	18.4	106.8	24.6	70.4
6	rGO(H ₂)	50	11.0	232.6	23.9	151.5	34.4	109.6
7	-		10.2	220.5	15.9	99.6	19.6	61.6
8 ^a	-		8.3	175.4	12.6	79.9	14.9	46.9
9 ^a	rGO(H ₂)		12.2	257.9	26.9	170.6	37.1	117.7
10 ^a	GO		8.1	173.9	17.3	111.4	23.5	75.7
11 ^a	activated carbon ^b		8.5	179.7	16.4	104.0	21.1	66.9
12 ^a	graphite (3-4nm)		8.3	175.4	18.5	117.3	25.5	80.9

All experiments have been performed at least twice and the averages are shown. Differences between the measurements are between 1 and 11%.

Experimental conditions: 10 μmol [Cu], 15 μmol Ir-PS, 20 μmol bpy, 12 mg additive, THF:TEA:H₂O = 3:2:1, 1.5 W Xe-light irradiation with 385 nm cut-off filter, 25 °C, gas volumes determined by automatic gas burettes and corrected by blank volume (2 mL), gases analyzed by GC, Activity = n(H₂)/(t·m(Cu)).

^ameasurements were performed without bpy.

^bDarco G60

Next, (rGO(H₂)) was investigated applying 50 mL of the solvent mixture to improve light absorption (Entry 6). Indeed, with ongoing reaction time the activity of the supported system was nearly

doubled (20 h) compared to the unsupported system (Entry 7). As known from our previous work, the presence of the ligand 2,2'-bipyridine (bpy) prevents the growth of the formed particles and stabilizes the photosensitizer.⁴⁹ Hence, in the absence of bpy the hydrogen generation for the non-supported system decreased (Entry 8). However, in the presence of the conductive rGO no significant influence of bpy on the activity was revealed (Entries 6 and 9). The same observations were made in 20 ml solvent mixture (Table 1, Entry 4 and Table S4, Entry 6). Therefore, further investigations applying rGO were performed in the absence of bpy. Variation of the carbon additive (GO, activated carbon and graphite) gave almost the same hydrogen productivity, whereby, the loss of activity was the highest in the presence of activated carbon (Entries 10-12). Other investigated carbon materials, namely graphite and activated carbon, showed lower activities (Table S4, Entries 7-9). Blank experiments without CuI and Ir-PS, respectively, resulted in nearly the same amount of hydrogen (2 mL) as the experiments without any PS, catalyst and additive (Table S4, Entries 1-4).

Due to the positive effect of MCM-41 and rGO(H₂) in the reaction, the influences of the amount of solvent, additive and Cu precursors onto the catalyst performance were investigated in more detail. The application of CuCl₂ and Cu(NO₃)₂ in the presence of MCM-41 led to a decrease of productivity compared to CuI as copper source (Fig. 1a). This effect is most pronounced for Cu(NO₃)₂ which is also deactivated after 20 h. In agreement with previous investigations, there is a general influence of the amount of THF/TEA/H₂O on the activity (Fig. 1b). Although recent experiments with the non-supported CuI system revealed an optimum in 10 ml of the mixture THF/TEA/H₂O,⁴⁹ with MCM-41 we observed a better hydrogen evolution under more diluted conditions (50 mL) (Figure 1b).

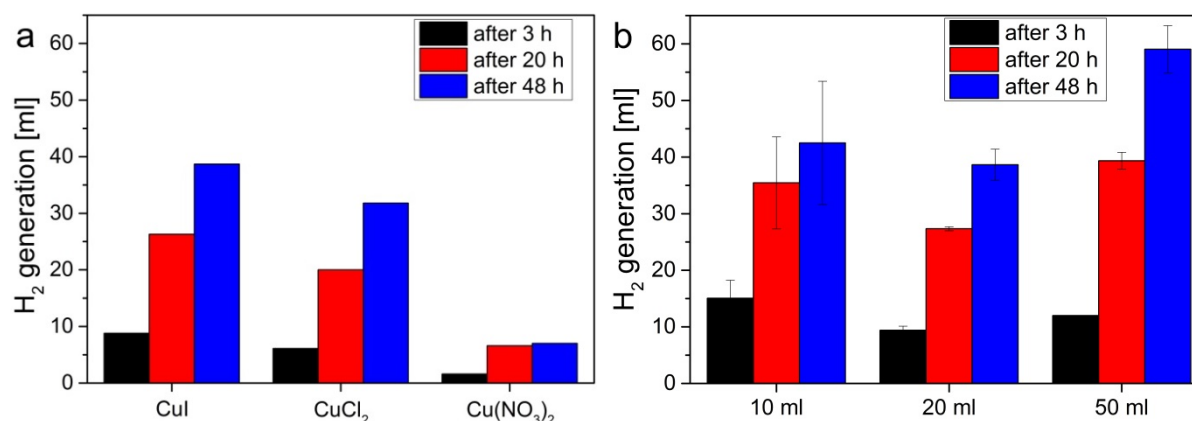


Figure 1. Investigation of the influence of the Cu precursor and amount of THF/TEA/H₂O (3:2:1) on the photocatalytic system using MCM-41 as additive: a) using different Cu-precursors in 20 ml and b) using different amounts of the solvent mixture. Experiments have been performed at least twice and the averages are shown. Differences between the measurements of Fig. 1a are between 1 and 7%. Experimental conditions: 10 μ mol [Cu], 15 μ mol Ir-PS, 20 μ mol bpy, 12 mg MCM-41, THF:TEA:H₂O = 3:2:1, 1.5 W Xe-light irradiation with 385 nm cut-off filter, 25 °C, gas volumes determined by automatic gas burettes and corrected by blank volume (2 mL).

Apart from MCM-41, also the rGO system was further investigated. As shown in Table S5, different commercially available as well as freshly prepared samples using hydrogen, hydroiodic acid or hydrazine as reductants were active under the optimized reaction conditions. It became clear that applying rGO(H₂) the highest amount of H₂ within 20 h reaction time was obtained.

Finally, different amounts of the best material (rGO(H₂)) were tested for 48 h in 50 ml reaction media (Fig. 2, gas evolution curves: Fig. S4). With increasing amount of additive, hydrogen generation is improved until reaching a critical amount of rGO(H₂). The maximum gas evolution is achieved applying 12 mg rGO(H₂), and more additive led to declined hydrogen productivities. The latter might be caused by the increased light absorption of the black rGO(H₂) material. As demonstrated in Figure

S4, using higher amounts (8-20 mg) of rGO(H₂) also led to increased stability of the catalyst system even after 48 h.

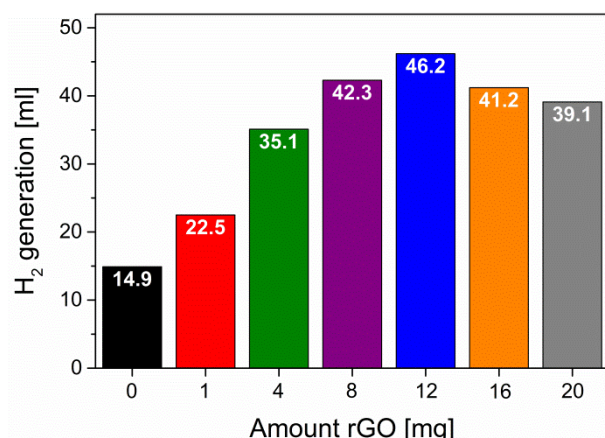


Figure 2. Influence of different rGO(H₂) amounts on the photocatalytic hydrogen evolution.

Experiments have been performed at least twice and the averages are shown. Differences between the measurements are between 1 and 10 %. Experimental conditions: 10 μ mol [Cu], 15 μ mol Ir-PS, 50 mL THF:TEA:H₂O = 3:2:1, 1.5 W Xe-light irradiation with 385 nm cut-off filter, 25 °C, 48 h, gas volumes determined by automatic gas burettes and corrected by blank volume (2 mL).

Long-term stability and recycle experiments

After identifying the optimized conditions for both systems, the long-term stability was tested applying the Ir-PS, CuI, and MCM-41 or rGO(H₂) (Fig. 3) in 50 mL THF/TEA/H₂O (3:2:1). For comparison, the photocatalytic reactions were performed in the absence of any additives and bpy (Fig. 3a, black line), as well as in the presence of bpy (Fig. 3a, orange line). After 20 h the unsupported systems (CuI) were not active anymore or showed only little activity (CuI/bpy), respectively. Noteworthy, the addition of bpy led to a slower growth of copper particles, which explains the improved hydrogen evolution.⁴⁹ When MCM-41 is used in the absence of bpy (Fig. 3a, blue line) the activity is enhanced to 30 mL hydrogen after 20 h, which is comparable to the non-supported system with bpy. Apparently, the small copper nanoparticles are stabilized in the presence of both bpy and MCM-41, as well. However, also the MCM-41 containing system is deactivated after 20 hours. The addition of rGO(H₂) significantly improved the activity for the first 20 hours, but not the overall stability of the system at longer times (Fig. 3a, purple line). Interestingly, applying either MCM-41 or rGO(H₂) together with bpy more stable WRC systems were obtained (Fig. 3b). Indeed, both systems were still active after 96 h. Besides the stability also the activity could be significantly improved under these conditions. Applying MCM-41 resulted in a slightly better catalytic performance (Fig. 3b, red line) compared to rGO(H₂) (Fig. 3b, green line), although the application of both additives resulted in nearly the same size distribution of formed copper nanoparticles. Finally, combining MCM-41 and bpy a more than three times higher amount of hydrogen was achieved after 160 h compared to the non-supported system with bpy (Figure S6). Thereby, the addition of both the ligand bpy and the additive are essentially necessary to achieve long term stability.

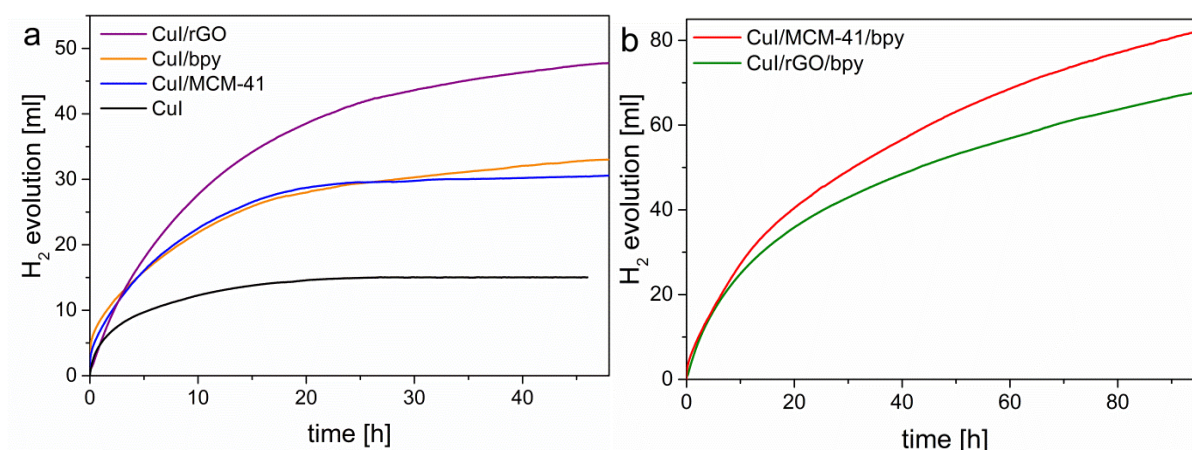


Figure 3. Reaction conditions: 15 μmol Ir-PS, 10 μmol CuI, 20 μmol bpy (if mentioned in the legend), 11.4 mg MCM-41 or 12 mg rGO, 50 mL THF:TEA:H₂O=3:2:1, 1.5 W Xe-light, ≥ 385 nm.

Having an optimal and stable WRC in hand (*i.e.* CuI, bpy, MCM-41), we were interested in the separation and reuse of this system (Fig. 4, S7). For catalyst recycling, the generated material was separated from six reaction runs and washed with THF/H₂O (3:1). The collected material was reused in the presence of Ir-PS (Fig. 4, initial experiment). In order to investigate the reuse in dispersion the reaction was restarted by addition of Ir-PS when the catalytic hydrogen production stopped (Fig. 4, restarts 1-4). Along the five consecutive runs only a slight decrease in hydrogen generation was observed. Interestingly, the activity of the material, which was formed *in situ*, was lower than that of the recycled one at the beginning of the reaction. This reveals that the main contribution to the hydrogen generation from water is provided by the formed nanoparticles and not by the homogeneous CuI system. Figure S7 shows the hydrogen evolution curves of all recycling experiments, where a catalyst lifetime of $\Sigma > 400$ h was observed.

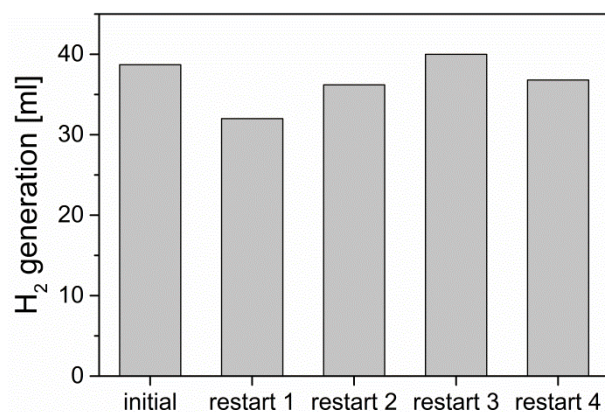
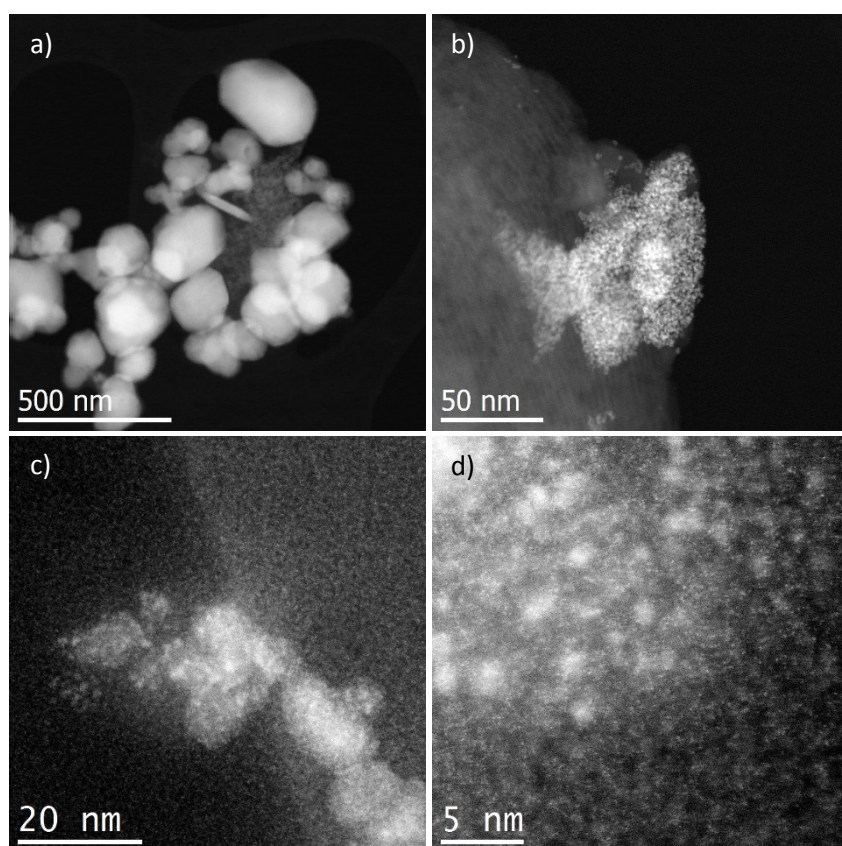


Figure 4. Recycle experiments: 10 μmol Cu from the prepared material; 15 μmol Ir-PS added after every run; 20 mL THF:TEA:H₂O (3:2:1, volume based); irradiation with 300 W Xe-lamp Lot Oriel 1.5W; ≥ 385 nm; manual burette.

Catalyst characterization and mechanism

Table S8 shows the surface area of the SiO₂ and rGO starting materials which were determined by N₂-physisorption or given by the manufacturer. For silica-based materials also the pore diameter and pore volume are given. In order to understand the structure of the catalysts, based on MCM-41 and rGO(H₂) formed during the photocatalytic reduction, material samples were isolated from the reaction mixture and analyzed by aberration corrected high angle annular dark field (HAADF) scanning transmission electron microscopy (STEM) and energy dispersive X-ray spectroscopy (EDXS).

Figures 5a, b and S10, S11, respectively, show the HAADF-STEM images and corresponding EDX analysis of materials obtained from MCM-41 added to a reaction performed in 10 ml THF:TEA:H₂O. Unfortunately, under these conditions a fine dispersion as well as a complete deposition of the copper species on the MCM-41 couldn't be achieved (Fig. 5a, S10). Besides, unsupported copper nanoparticles were observed but no supported ones (Fig. 5a, S10a). Interestingly, the catalytic performance of this material was lower than that of the second experiment performed under the same conditions (Fig. S9 reactions CuI/MCM-41 [2] and CuI/MCM-41 [1]). For the latter material, Figures 5b and S11 show agglomerates containing Cu with deposited Ir particles which were formed on the outer surface of MCM-41 while the characteristic pore structure of the support remained unchanged. It might be concluded, if copper is precipitated on the silica the activity of the system is slightly better than that of the non-supported catalyst. An improved reproducibility of the catalyst performance was obtained applying 20 mL THF:TEA:H₂O (Fig. 1b, S12). In this case, the resulting catalyst material consisted of small isolated iridium particles (about 4 nm) (Fig. S12a) additionally huge copper agglomerates similar to the unsupported material formed in 10 ml (Fig. S12b). This finding might be the reason for the lack of increase in activity compared to the non-supported system (Table 1, Entries 1 and 5). By further increasing the solvent amount to 50 ml (Fig. 5c,d, S13a,b) small and bigger copper particles (20 nm) supported on the silica are recorded. We assume the generation of these smaller supported nanoparticles led to the increased photocatalytic activity. Additionally, smaller iridium nanoparticles (< 2 nm) are deposited on the copper ones (Fig. S13a).



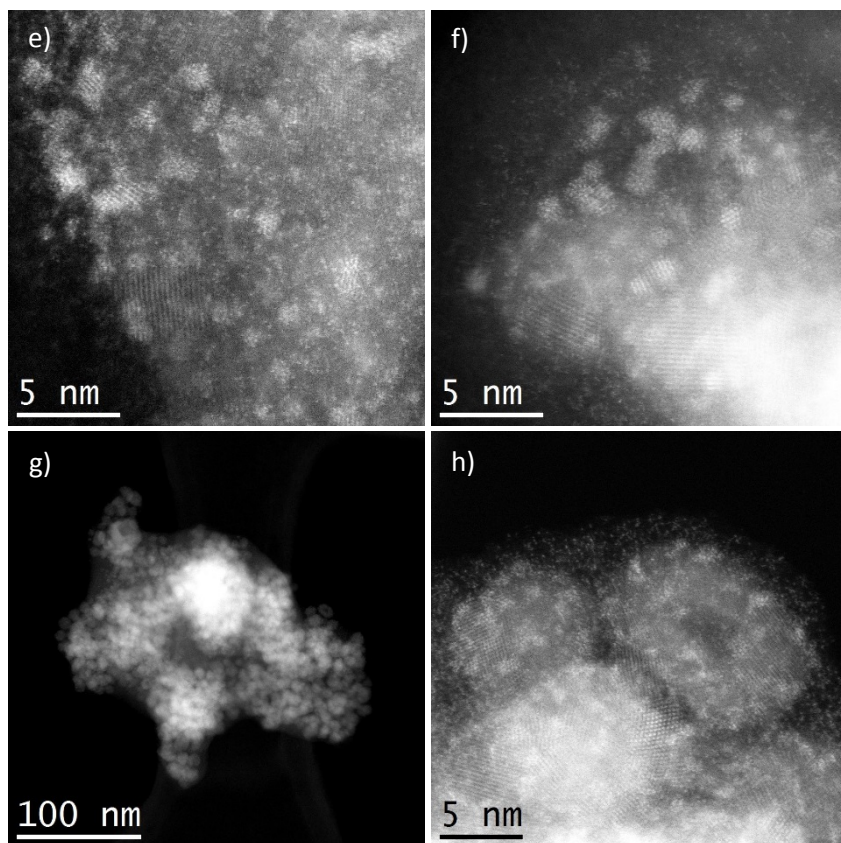


Figure 5. HAADF-STEM images of the IrPS/CuI/MCM-41 system in THF:TEA:H₂O 3:2:1 (volume based) after proton reduction reaction (a) and (b) after 48 h with bpy in 10 ml, (c) and (d) after 48 h with bpy in 50 ml, (e) after 96 h with bpy in 50 ml, (f) after 164 h with bpy in 50 ml and (g) and (h) after 48 h without bpy in 50 ml.

As shown by our HAADF-STEM investigation on materials isolated after different reaction times in 50 ml (Fig. 5c-f and S13a,b), the size of the copper particles in the presence of bpy was nearly stable during the reaction (Fig. 5d-f). In the absence of the ligand bpy (Fig. 5g,h and S13c) the obtained particles are nearly in the same size concluding no influence of bpy on the copper particle size was observed. Furthermore, regardless of the presence of bpy, these copper particles support smaller iridium nanoparticles (< 2 nm).

For the rGO(H₂)-based WRC, copper particles with similar size are formed on the surface of the carbonaceous material. In Figure 6, HAADF-STEM images are displayed and show the heterogenization of smaller copper particles in the absence of bpy after 48 h reaction time. Apparently, as in the case of MCM-41 graphene also ensures the formation of small, stable copper particles, which otherwise can be formed in the presence of the bpy ligand. In general, the copper particle sizes are independent on the amount of additive and significantly smaller compared to particles obtained without solid additive (Fig. S14). The copper particles are homogeneously precipitated on the support and also decorated with iridium particles.

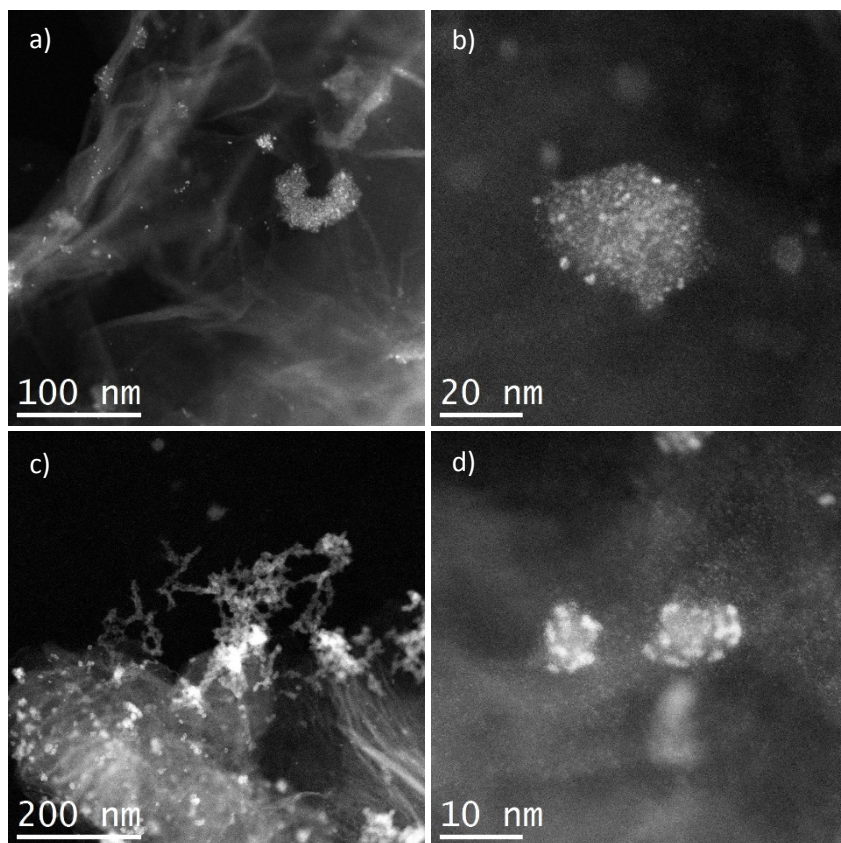


Figure 6. HAADF-STEM images of the IrPS/Cu-System without bpy in 50 mL THF:TEA:H₂O 3:2:1 (volume based) after proton reduction reaction (a) and (b) with 4 mg and (c) and (d) with 16 mg rGO after 48 h.

However, from the HAADF-STEM investigations it became not clear why in the absence of bpy the rGO(H₂)-system is preferred over the MCM-41 one (Fig. 3a). Hence, photoluminescence experiments were performed in order to examine the influence of rGO(H₂) on the photocatalytic mechanism.

For this purpose, the photoluminescence lifetime of the Ir-PS ($c = 4.2 \cdot 10^{-5}$ M) in THF was measured with a streak camera (Streakscope C10627, Hamamatsu Photonics) in dependence on different compositions. The obtained decay times are listed for all time-resolved luminescence measurements in Table S15. Excited Ir-PS in THF showed a lifetime of ca. 320 ns. Recent publications showed the possible uptake of electrons from (covalently attached) photosensitizers.⁵⁴⁻⁵⁷ Surprisingly, by adding CuI or rGO(H₂) or both components, no change in the lifetime was observed. Instead, on addition of TEA (THF/TEA 4:2) strong quenching of the luminescence lifetime took place and the lifetime decreased to only 8 ns (Fig. 7).

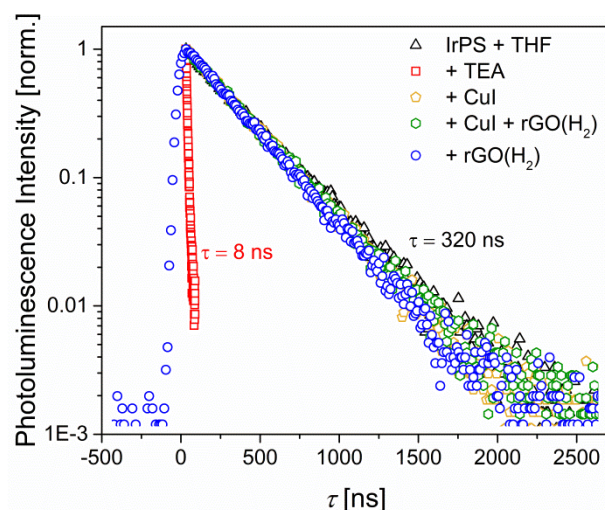
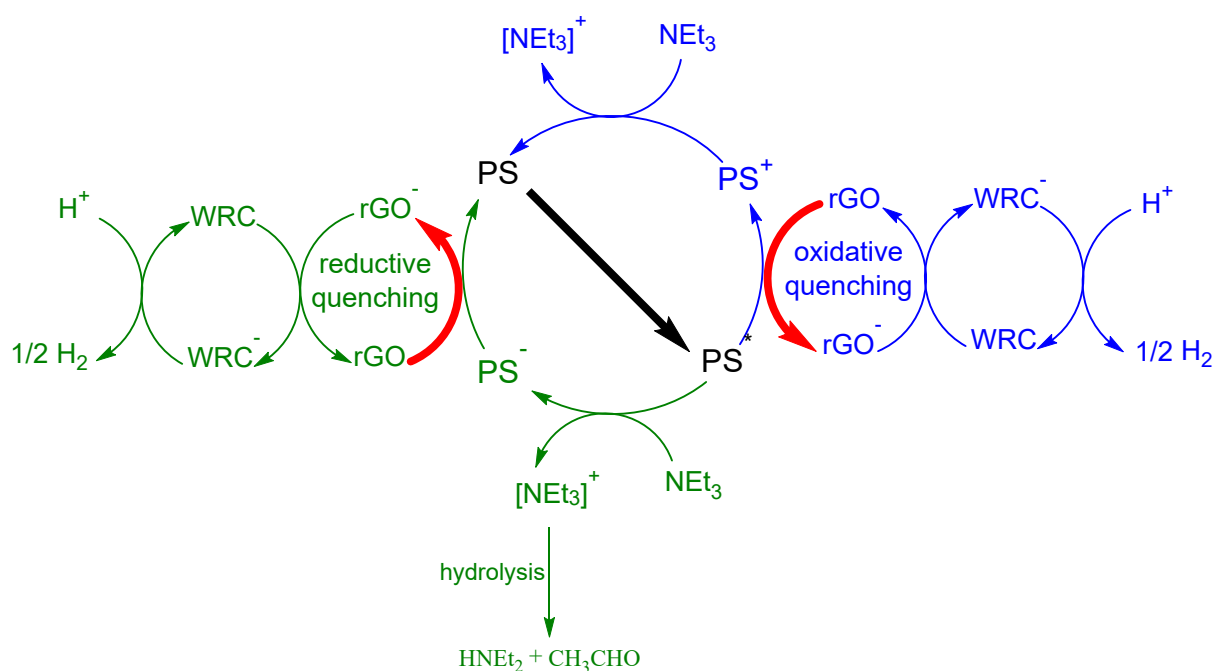


Figure 7: Photoluminescence lifetime of the Ir-PS in the presence of different components of the photocatalytic system.

Since the reduced graphene oxide has no influence on the luminescence lifetime of the excited Ir-PS it is evident that the excited Ir-PS is reduced by TEA (scheme 2, green cycle) and not by rGO (scheme 2, blue cycle). Moreover, the strong quenching by TEA indicates that reductive quenching is the active reaction path and oxidative quenching can be neglected (scheme 2).



Scheme 2. Photocatalytic mechanism for hydrogen generation in the presence of a photosensitizer (PS), reduced graphene oxide (rGO) and a water reduction catalyst (WRC) in case of a reductive or oxidative quenching of the PS.

Obviously, after irradiation the excited Ir-PS species is reduced by TEA and the reduced and probably labile Ir-PS quickly returns back to the initial state by transferring an electron to the conductive carbon. This quick oxidation of the labile Ir-PS intermediate explains the better stability of the Ir-PS and therefore the longer activity of the system in the presence of rGO(H₂) (Fig. 3a).

While TEM images of isolated materials from reactions with (Fig. 5c,d, S13) and without (Fig. 5g,h, S14) bpy showed no difference regarding the formed particles after 48 h, the photocatalytic

performance was significantly improved in the presence of bpy for the MCM-41 system (Fig. 3). Thus, the question arises what are the reasons for higher activity and stability of the CuI/Ir-PS/MCM-41/bpy system? On the one hand, bpy might stabilize the Ir-PS,⁴⁹ otherwise it functions as a radical scavenger preventing decomposition reactions⁵⁸. In order to investigate this in more detail, we performed several experiments trying to reactivate a bpy-free catalyst system (Fig. 8, red curve) by addition of (i) hydroquinone, (ii) paraquat, (iii) rGO and (iv) bpy after 40 h (Fig. 8). All these experiments were compared to the hydrogen evolution in the presence of the standard bpy-containing catalyst system (black curve).

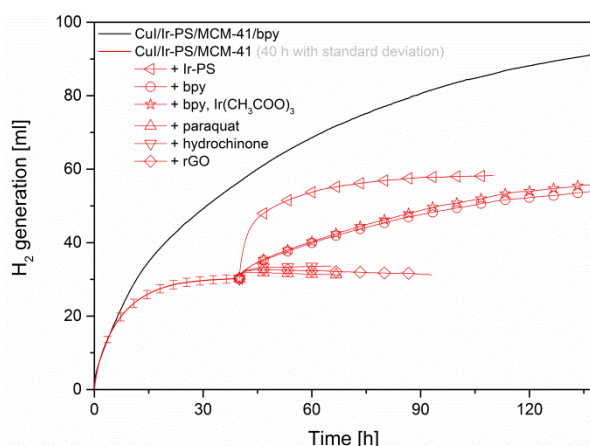


Figure 8. Photocatalytic experiments of CuI/Ir-PS/MCM-41 and the subsequent addition of several additives. For comparison the H₂ evolution curve of the CuI/Ir-PS/MCM-41/bpy system is also shown. Reaction conditions: 15 μ mol Ir-PS or Ir(CH₃COO)₃, 10 μ mol CuI, 11.4 mg MCM-41, 50 mL THF:TEA:H₂O=3:2:1 (volume based), 1.5 W Xe-light, ≥ 385 nm, subsequent addition of 20 μ mol bpy or paraquat and hydroquinone, respectively. Experiment with rGO: 12 mg.

Adding the radical scavenger hydroquinone, the non-coordinating bipyridinium derivative paraquat or rGO did not reactivate the original system. Thus, a role of bpy as radical scavenger or electron relay is very unlikely. Surprisingly, the addition of bpy renewed the activity to a significant part. Apparently, the lifetime of the photocatalyst determines the total amount of generated hydrogen under the present conditions. After 40 hours the original photocatalyst is fully deactivated; however, simply the addition of bpy regenerates the photocatalytic activity, although various UV-vis experiments revealed no regeneration of the initial photosensitizer (Fig. S16). Interestingly, the combined addition of bpy and an Ir source (Ir(CH₃COO)₃) could not further improve the restored catalyst performance; thus demonstrating that iridium is not the limiting factor for this step. Finally, the addition of fresh Ir-PS resulted in the most active system, however, this is again deactivated within relatively short time. While the presence of bpy seems to be beneficial for the stabilization of the photocatalyst and thus allowing for stable H₂ generation over a longer time, the role of the support (MCM-41 or rGO(H₂)) is the suppression of the growth of the copper oxo species leading to enhanced catalytic activities.

Conclusion

In situ generated copper particles constitute promising materials for photocatalytic proton reduction reactions. The stability of such nanoparticles can be significantly improved by adding nitrogen containing ligands such as bpy as well as by depositing them on appropriate supports. Interestingly, both insulating (SiO₂) and conducting (rGO) materials can be successfully used in the light driven hydrogen generation and revealed a 2-3 times higher activity compared to the non-supported system. The dominant role of the supporting material is the stabilization of the *in situ* generated small copper nanoparticles and the prevention of their growth. The addition of the ligand bpy

significantly increased the productivity and stability of the system by stabilizing the photo-catalyst. In agreement with this assumption photoluminescence measurements of rGO(H₂)-based material confirmed that the conductor does not influence the lifetime of the excited Ir-PS, which is only reduced by TEA, but on its stability.

The best WRC performance in hydrogen evolution was achieved for catalyst systems containing the support and bpy. Hence, in the presence of MCM-41 and bpy a fourfold increase of the hydrogen evolution was achieved and the WRC was still active after 160 h. STEM investigations showed no significant copper particle growth during this reaction. Besides its stable operation this catalyst material can be easily separated from the reaction mixture and proved to be active again in recycling experiments.

Conflicts of interest

There are no conflicts to declare.

Acknowledgements

The authors thank Petra Bartels for her work in the hydrogen generation measurements, Dr. Nils Rockstroh for his consultative support and Dr. Marga-Martina Pohl (TEM), Anja Simmula (ICP), Astrid Lehmann (EA) and Reinhard Eckelt (BET) for their analytical support. Financial support by the Deutsche Forschungsgemeinschaft via the priority program SPP 2102 (LO 714/11-1) is gratefully acknowledged.

References

1. J. Moore and B. Shabani, *Energies*, 2016, **9**, 674.
2. N. Armaroli and V. Balzani, *Angew. Chem. Int. Ed.*, 2007, **46**, 52-66.
3. A. Iulianelli, S. Liguori, J. Wilcox and A. Basile, *Catalysis Reviews*, 2016, **58**, 1-35.
4. J. P. Van Hook, *Catalysis Reviews*, 1980, **21**, 1-51.
5. S. A. Ghoneim, R. A. El-Salamony and S. A. El-Temtamy, *World Journal of Engineering and Technology*, 2016, 116-139.
6. M. Liszka, T. Malik and G. Manfrida, *Energy*, 2012, **45**, 142-150.
7. R. W. Breault, *Energies*, 2010, **3**, 216.
8. M. A. Salam, K. Ahmed, N. Akter, T. Hossain and B. Abdullah, *Int. J. Hydrogen Energy*, 2018, **43**, 14944-14973.
9. O. Schmidt, A. Gambhir, I. Staffell, A. Hawkes, J. Nelson and S. Few, *Int. J. Hydrogen Energy*, 2017, **42**, 30470-30492.
10. M. Carmo, D. L. Fritz, J. Mergel and D. Stolten, *Int. J. Hydrogen Energy*, 2013, **38**, 4901-4934.
11. D. B. Pal, R. Chand, S. N. Upadhyay and P. K. Mishra, *Renewable and Sustainable Energy Reviews*, 2018, **93**, 549-565.
12. T. L. LeValley, A. R. Richard and M. Fan, *Int. J. Hydrogen Energy*, 2014, **39**, 16983-17000.
13. T. Jafari, E. Moharreri, A. S. Amin, R. Miao, W. Song and S. L. Suib, *Molecules*, 2016, Medium: ED; Size: Article No. 900.
14. H. Ahmad, S. K. Kamarudin, L. J. Minggu and M. Kassim, *Renewable and Sustainable Energy Reviews*, 2015, **43**, 599-610.
15. P. Du and R. Eisenberg, *Energy Environ. Sci.*, 2012, **5**, 6012-6021.
16. K. L. Skubi, T. R. Blum and T. P. Yoon, *Chem. Rev.*, 2016, **116**, 10035-10074.
17. H. Junge, N. Rockstroh, S. Fischer, A. Brückner, R. Ludwig, S. Lochbrunner, O. Kühn and M. Beller, *Inorganics*, 2017, **5**, 14.
18. N. Fajrina and M. Tahir, *Int. J. Hydrogen Energy*, 2019, **44**, 540-577.

19. C. Acar, I. Dincer and C. Zamfirescu, *International Journal of Energy Research*, 2014, **38**, 1903-1920.
20. K. C. Christoforidis and P. Fornasiero, *ChemCatChem*, 2017, **9**, 1523-1544.
21. A. Kudo and Y. Miseki, *Chem. Soc. Rev.*, 2009, **38**, 253-278.
22. R. M. Navarro Yerga, M. C. Álvarez Galván, F. del Valle, J. A. Villoria de la Mano and J. L. G. Fierro, *ChemSusChem*, 2009, **2**, 471-485.
23. X. Chen, S. Shen, L. Guo and S. S. Mao, *Chem. Rev.*, 2010, **110**, 6503-6570.
24. S. Y. Tee, K. Y. Win, W. S. Teo, L.-D. Koh, S. Liu, C. P. Teng and M.-Y. Han, *Adv. Sci.*, 2017, **4**, 1600337.
25. T. Takayama, I. Tsuji, N. Aono, M. Harada, T. Okuda, A. Iwase, H. Kato and A. Kudo, *Chem. Lett.*, 2017, **46**, 616-619.
26. J. Bandara, C. P. K. Udawatta and C. S. K. Rajapakse, *Photochem. Photobio. Sci.*, 2005, **4**, 857-861.
27. T. Sreethawong and S. Yoshikawa, *Catal. Commun.*, 2005, **6**, 661-668.
28. V. Gombac, L. Sordelli, T. Montini, J. J. Delgado, A. Adamski, G. Adami, M. Cargnello, S. Bernal and P. Fornasiero, *J. Phys. Chem. A*, 2010, **114**, 3916-3925.
29. S. S. Lee, H. Bai, Z. Liu and D. D. Sun, *Appl. Catal. B*, 2013, **140-141**, 68-81.
30. Y. Wu, G. Lu and S. Li, *Catal. Lett.*, 2009, **133**, 97.
31. K. Lalitha, G. Sadanandam, V. D. Kumari, M. Subrahmanyam, B. Sreedhar and N. Y. Hebalkar, *J. Phys. Chem. C*, 2010, **114**, 22181-22189.
32. M. Jung, J. Scott, Y. H. Ng, Y. Jiang and R. Amal, *Int. J. Hydrogen Energy*, 2014, **39**, 12499-12506.
33. A. Wang, L. K. Che, R. Dong and G. Zhao, *Adv. Mat. Res.*, 2013, **724-725**, 740-743.
34. Z. Wang, Y. Liu, D. J. Martin, W. Wang, J. Tang and W. Huang, *PCCP*, 2013, **15**, 14956-14960.
35. Y.-H. Yu, Y.-P. Chen and Z. Cheng, *Int. J. Hydrogen Energy*, 2015, **40**, 15994-16000.
36. Q. Hu, J. Huang, G. Li, Y. Jiang, H. Lan, W. Guo and Y. Cao, *Appl. Surf. Sci.*, 2016, **382**, 170-177.
37. S. Xu and D. D. Sun, *Int. J. Hydrogen Energy*, 2009, **34**, 6096-6104.
38. Y. Sakata, T. Yamamoto, T. Okazaki, H. Imamura and S. Tsuchiya, *Chem. Lett.*, 1998, **27**, 1253-1254.
39. W. J. Foo, C. Zhang and G. W. Ho, *Nanoscale*, 2013, **5**, 759-764.
40. L. S. Yoong, F. K. Chong and B. K. Dutta, *Energy*, 2009, **34**, 1652-1661.
41. N.-L. Wu and M.-S. Lee, *Int. J. Hydrogen Energy*, 2004, **29**, 1601-1605.
42. Y. Liu, Z. Wang and W. Huang, *Appl. Surf. Sci.*, 2016, **389**, 760-767.
43. D. Praveen Kumar, M. V. Shankar, M. Mamatha Kumari, G. Sadanandam, B. Srinivas and V. Durgakumari, *Chem. Commun.*, 2013, **49**, 9443-9445.
44. I. Tamiolakis, I. T. Papadas, K. C. Spyridopoulos and G. S. Armatas, *RSC Adv.*, 2016, **6**, 54848-54855.
45. H.-J. Choi and M. Kang, *Int. J. Hydrogen Energy*, 2007, **32**, 3841-3848.
46. J. Yu and J. Ran, *Energy Environ. Sci.*, 2011, **4**, 1364-1371.
47. M. Jung, J. N. Hart, J. Scott, Y. H. Ng, Y. Jiang and R. Amal, *Appl. Catal., A*, 2016, **521**, 190-201.
48. Z. Jin, X. Zhang, Y. Li, S. Li and G. Lu, *Catal. Commun.*, 2007, **8**, 1267-1273.
49. H. Junge, Z. Codolà, A. Kammer, N. Rockstroh, M. Karnahl, S.-P. Luo, M.-M. Pohl, J. Radnik, S. Gatla, S. Wohlrab, J. Lloret, M. Costas and M. Beller, *J. Mol. Catal. A: Chem.*, 2014, **395**, 449-456.
50. S. Kreft, J. Radnik, J. Rabeah, G. Agostini, M.-M. Pohl, E. Gericke, A. Hoell, M. Beller, H. Junge and S. Wohlrab, *Int. J. Hydrogen Energy*, 2019, DOI: 10.1016/j.ijhydene.2019.1004.1006.
51. M. K. Gonce, E. Aslan, F. Ozel and I. Hatay Patir, *ChemSusChem*, 2016, **9**, 600-605.
52. P. Zhang, T. Wang and H. Zeng, *Appl. Surf. Sci.*, 2017, **391**, 404-414.
53. R. Cabriolu and T. Li, *Physical Review E*, 2015, **91**, 052402.
54. D. Wang, J. Huang, K. Li, C. Zhang, Y. Du and P. Yang, *RSC Adv.*, 2016, **6**, 34699-34707.
55. M. Zhu, Y. Dong, B. Xiao, Y. Du, P. Yang and X. Wang, *J. Mater. Chem.*, 2012, **22**, 23773-23779.

56. Z. Mou, Y. Dong, S. Li, Y. Du, X. Wang, P. Yang and S. Wang, *Int. J. Hydrogen Energy*, 2011, **36**, 8885-8893.
57. J. Huang, D. Wang, Z. Yue, X. Li, D. Chu and P. Yang, *J. Phys. Chem. C*, 2015, **119**, 27892-27899.
58. S. Park, H. Lee, S.-H. Shin, N. Kim, D. Shin and B. Bae, *ACS Omega*, 2018, **3**, 11262-11269.

Supporting Information

Light-Driven Proton Reduction with *in situ* Supported Copper Nanoparticles

*Stefanie Kreft^{‡, a}, Marcel Sonneck,^a Henrik Junge^{‡, a}, Ayla Pöpcke,^b Anja Kammer,^a Carsten
Kreyenschulte,^a Stefan Lochbrunner,^b Sebastian Wohlrab^{a*} and Matthias Beller^{a*}*

^a Leibniz Institute for Catalysis at the University of Rostock, Albert-Einstein-Straße 29a, 18059
Rostock, Germany

^b Institute of Physics and Department of Life, Light & Matter, University of Rostock, 18051
Rostock, Germany

* Corresponding Authors: Dr. Sebastian Wohlrab, E-mail: sebastian.wohlrab@catalysis.de;
Prof. Dr. Matthias Beller, E-mail: matthias.beller@catalysis.de;
FAX: (+49) 381 1281 5000

[‡] These authors contributed equally to this work.

Table S1: Results from literature for the photocatalytic proton reduction with CuO_x/TiO₂ catalysts and our own investigated copper systems.

No.	Active System	Amount of Cu	Irradiation	Activity [mmol·g _{catalyst} ⁻¹ ·h ⁻¹]	Conditions	Ref. in manuscript
1	CuO/TiO ₂ ^[a]	7 wt%	Hg lamp	4.2	5 vol% methanol in water	26
2	CuO/TiO ₂ ^[b]	1.5 wt%		1.8	10 vol% methanol in water	27
3	CuO/TiO ₂ ^[a]	2.5 wt%		1.3	50 vol% ethanol in 1 M aqueous glycerol	28
4	CuO _x /TiO ₂ ^[b]	6 mol%		10	10 vol% methanol in water	29
5	Cu ₂ O/TiO ₂	1 wt%		5	20 vol% ethanol in water	30
6	Cu ₂ O/TiO ₂	2 wt%		3	water	31
7	Cu ₂ O/TiO ₂	0.5 wt%		200	5 vol% glycerol in water	31
8	CuO _x /TiO ₂	0.5 wt%	Xe lamp	1.1	10 vol% methanol in water	32
9	CuO/TiO ₂ ^[b]	5 wt%		0.2	6 vol% methanol in water	33
10	Cu ₂ O-TiO ₂	42 wt%		0.1	20 vol% methanol in water	34
11	CuO/TiO ₂ ^[b]	1 wt%		3.5	20 vol% methanol in water	35
12	Cu ₂ O/TiO ₂	2.7 wt%		2.8 ^[c]	10 vol% methanol in water	36
13	CuO/TiO ₂ ^[a]	9 mol%		18.5	10 vol% methanol in water	37
14	Cu ₂ O/TiO ₂	1 wt%		5 · 10 ⁻³	50 vol% methanol in water	38
15	Cu-Cu ₂ O/TiO ₂	9 wt%		13	10 vol% methanol in water	39
16	CuO/TiO ₂ ^[b]	10 wt%	Halogen lamp	8.5	6 vol% methanol in water	40
17	Cu ₂ O/TiO ₂	1.2 wt%	UV-light	3	40 vol% methanol in water	41
18	Cu ₂ O/TiO ₂	1 wt%	> 300 nm	3.2	20 vol% methanol in water	42
19	CuO/TiO ₂ ^[b]	1.5 wt%		99.8	5 vol% glycerol in water	43
20	Cu ₂ O/TiO ₂	1.5 wt%	360-780 nm	36.1	20 vol% methanol in water	44
21	CuO/TiO ₂ ^[a]	10 mol%	365 nm	0.7	50 vol% methanol in water	45
22	Cu(OH) ₂ /TiO ₂ ^[a]	0.3 mol%		3.4	0.5 vol% ethylene glycol in water	46
23	Cu/TiO ₂	1 wt%	> 400 nm	5.8	10 vol% glycerol in water	47
24	CuO/TiO ₂ ^[d]	1 wt%	> 420 nm	0.5	15 vol% DEA in water ^[e]	48
25	CuI	10 μmol	385 nm	280 ^[f]	THF:TEA:H ₂ O = 3:2:1 ^[g]	49
26	CuO(0.1Cl)/SiO ₂	0.6 wt%		1702 ^[f]	THF:TEA:H ₂ O = 3:2:1 ^[g]	50
27	Cu ₂ NiSnS ₄ ^[d]	-	> 420 nm	2028	0.33 M TEOA in water ^[h]	51
28	Cu-Cu ₂ O/g-C ₃ N ₄ ^[i]	7 wt%		400	15 vol% TEOA in water ^[h]	52

^[a] Observation of a reduction of Cu(II) during the reaction.

^[b] active Cu-species was not analyzed.

^[c] unit: [μmol·cm⁻²·h⁻¹], catalyst: Cu incorporated TiO₂ thin films deposited on quartz glass.

^[d] Reaction was performed in the presence of a dye (Eosin Y).

^[e] DEA: Diethanolamine.

^[f] Activity = n(H₂)/(t·m(Cu)); unit: mmol·g_{Cu}⁻¹·h⁻¹.

^[g] TEA: Triethylamine.

^[h] TEOA: Triethanolamine.

^[i] Reaction was performed in the presence of a dye (Erythrosin B).

S2. Chemicals and Synthesis

S2a. Chemicals

Chemical	Provider	Purity [%]
CuI	Sigma-Aldrich	99.999% trace metals basis
(Synthesis Ir-PS)		
IrCl ₃ • xH ₂ O	Strem Chemicals	99.9 % Ir
2-Phenylpyridine	Sigma-Aldrich	98 %
2-Methoxyethanol	Sigma-Aldrich	≥99.9 %
2,2'-bipyridine	TCI	>99.0 %
Ethylene glycol	Alfa Aesar	99 %
Ammonium hexafluorophosphate	Sigma-Aldrich	≥95 %
Tetrahydrofuran (THF)	Fluka	>99.5 %
Triethylamine (TEA)	Roth	>99.5 %
MCM-41	Südchemie Berlin	>99 %
Nanoporous glass (39 nm)	VitraBio GmbH	>99 %
Graphite (3-4 nm)	IoLiTec	93%
Graphite (400nm)	IoLiTec	99.9%
Graphite (<20µm)	Sigma-Aldrich	synthetic
Activated carbon/Darco G60	Sigma-Aldrich	-
Activated carbon	Degussa Hüls	-
rGO (0.2-10 µm)	IoLiTec	>99 %
rGO (0.5-3 µm)	IoLiTec	>99 %

S2b. Synthesis SBA-15

The synthesis of the mesoporous silica SBA-15 was performed regarding the method described by Oden.¹ 2.4 g EO₂₀PO₇₀EO₂₀ (Pluronic, P123, M = 5800 g/mol, Sigma Aldrich, >99.5 %) and 0.028 g NH₄F were dissolved under stirring in 84 ml HCl solution (1.3 M) at 20 °C within 3 days. 5.5 ml tetraethyl orthosilicate (TEOS, Fluka, 98 %) were dissolved in 55.8 ml heptane and added to the obtained solution. The suspension was stirred for 20 h and transferred to a teflon-flask for hydrothermal treatment at 100 °C for 24 h. Afterwards, the product was filtered, washed with 600 ml distilled H₂O and dried at 80 °C for 12 h. To remove the template the solid was calcined at 550 °C for 6 h with a heating ramp of 1 K/min.

S2c. Synthesis graphene oxide (GO)

Graphene oxide was synthesized using Hummers' method.² 120 ml concentrated H₂SO₄ was added to a mixture of 5.0 g graphite flakes (Graphite (<20µm), Sigma Aldrich, synthetic) and 2.5 g NaNO₃. The suspension was cooled to 3 °C and 15 g KMnO₄ was added slowly in portions over a period of 2 h to keep the reaction temperature below 20 °C. The ice bath was removed and the reaction continued for 0.5 h. Subsequently the reaction was warmed to 40 °C and stirred for 1 h. After heating, 1 l water was added slowly, producing a large exothermic reaction. External heating was introduced to maintain the reaction temperature at 91 °C for 0.5 h. The reaction was cooled to room temperature and stirred over night. To the brownish suspension 35 ml H₂O₂ was added drop wise until gas evolution was completed. After stirring for further 3 h the obtained graphene oxide was removed by centrifugation and washed three times with 600 ml hydrochloric acid (3 M). Graphene oxid was further purified by repeated centrifugation und dispersion in water until the pH of the supernatant was neutral. At the end the graphene oxide was washed 2 times with diethyl ether and dried at room temperature in vacuum over four days. Elemental Analysis: C 55.53, H 1.49, N 0.06, S 1.05. Yield: 6.5 g.

S2d. Synthesis reduced graphene oxide – rGO (HI)

In a typical chemical reduction with hydriodic acid,³ 1.0 g of graphene oxide was dispersed in 0.375 l acetic acid and sonicated for 1.5 h. 20 ml HI (Applichem, 57 %, pure) was then added and the suspension was reacted at 40 °C for 45 h with constant stirring. The solid was isolated by filtration, washed four times with 100 ml saturated bicarbonate, five times with 100 ml water and finally two times with acetone. The product was vacuum dried overnight at room temperature to yield rGO (HI) (0.57 g). Elemental Analysis: C 75.28, H 0.45, N 0.13, I 12.41.

S2e. Synthesis reduced graphene oxide – rGO (N₂H₄)

In a typical chemical reduction with hydrazine hydrate,⁴ 0.4 g of graphene oxide was dispersed in 0.4 l water and sonicated for 1.5 h. 0.3 ml hydrazine monohydrate (Sigma Aldrich, 64-65 %, reagent grade, 98 %) was then added and the suspension was reacted under reflux for 4 h with constant stirring. After cooling to room temperature the suspension was further stirred for 18 h. The solid was isolated by filtration, washed four times with 100 ml water and finally two times with acetone. The product was vacuum dried overnight at room temperature to yield rGO (N₂H₄) (0.25 g). Elemental Analysis: C 73.29, H 0.26, N 3.25.

S2f. Synthesis reduced graphene oxide – rGO (H₂)⁵

The reduction of graphene oxide with hydrogen was divided into two parts. In the first one graphene oxide (GO) was thermally expanded by rapidly heating in a Loba 1100-30-220-1 (HTM REETS) tube furnace. Generally 0.5 g GO was first loaded in corundum tube of length 120 mm and diameter 10 mm, which was then inserted into a 400 mm long quartz tube with inner diameter of 22 mm and outer diameter of 25 mm. After the tube furnace was heated to 1050 °C and argon was flowed through the tube for 90 min, with a flow rate of 50 ml/min, the sample tube of GO placed in the quartz tube was rapidly moved into the middle heating zone and kept there for 30 s, before being quickly removed from the heating zone after expansion. In the second step the resulting exfoliated material (0.18 g) was placed in a quartz boat and insert in a Linn Elektro Therm tube furnace (FRHT-70-500-1100). After argon was flowed through the tube for 120 min, with a flow rate of 200 ml/min the exfoliated material was further reduced for 2 h at 450 °C in a gas flow of H₂ (30 ml/min) and argon(30 ml/min) to end up with 0.14 g reduced graphene oxid rGO (H₂). Elemental Analysis: C 87.58, H 0.93, N 0.35.

S2g. Materials Characterization

Scanning Transmission electron microscopy (STEM)

The STEM measurements were performed at 200 kV with a probe aberration-corrected JEM ARM200F (JEOL, Corrector: CEOS). The microscope is equipped with a JED-2300 (JEOL) energy-dispersive x-ray-spectrometer (EDXS) for chemical analysis. The samples were prepared from freshly prepared reaction mixtures. After certain hours of light irradiation a droplet of the reaction mixture was placed on a holey carbon supported Ni-grid mesh 300, dried and transferred to the microscope.

Atomic absorption spectroscopy

Atomic absorption spectroscopy (AAS) using a contra 800 D (Analytik Jena) was carried out, in order to quantify the amount of copper in the material.

Nitrogen sorption

Specific surface area and pore size distribution were determined from N₂-physisorption data obtained using a ASAP 2020 instrument (Micromeritics). As a pre-treatment, samples were outgassed and dried for 2 h at 220 °C at reduced pressure. Data analysis of isotherm data was carried out according to methods described by Brunauer, Emmett, Teller (BET)⁶ and Barrett, Joyner, Halenda (BJH)⁷.

X-ray photoelectron spectra (XPS)

The XPS measurements were performed on a VG ESCALAB220iXL with monochromated AlK α radiation (E = 1486.6 eV). The electron binding energies were obtained without charge compensation and referenced to the C1s peak assuming sp² carbon as main component at 284.0 eV. For quantitative analysis the peaks were

deconvoluted with Gaussian-Lorentzian curves, the peak areas were divided by a sensitivity factor obtained from the element specific Scofield factor and the transmission function of the spectrometer.

S3. General information about the experimental set up

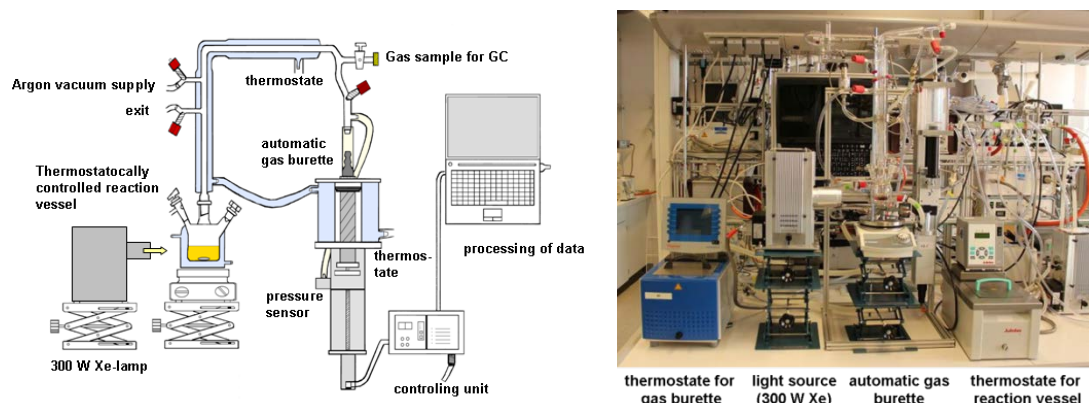


Figure S3a. Experimental set-up for automatic quantification of evolved gases (light source: output 1.5 W, ≥ 385 nm).

General principle of quantitative gas measurements:

A double walled thermostatically controlled reaction vessel (temperature kept constant at 25.0 °C during the reactions) is connected via a condenser to an automatic gas burette (temperature kept constant at 25 °C during measurements). The gas burette is equipped with a pressure sensor. The evolved gas causes a pressure increase in the closed system, which is compensated by volume increase of the burette syringe by an automatic controlling unit. The gas evolution curves are monitored by a PC.

Details on GC measurements:

A GC sample is taken from the collected gas in the burette after each reaction. The GC was calibrated with certified commercially available gas mixtures. GC measurements were carried out on one of two available systems:

GC a): HP Plot Q / FID – hydrocarbons, Carboxen / TCD - permanent gases, He carrier gas.

GC b): Carboxen / TCD / Methanizer / FID - permanent gases, He carrier gas.

The systems allow for the determination of H₂, Ar, CO, CH₄ and CO₂ within the ranges:

H₂ \geq 0.01 vol% - 100 vol%

CO \geq 10 ppm (system a), CO down to 1 ppm (system b)

CO₂ 1 - 100 vol%.

The measured gas volumes were corrected by a blank value (average 2.0 mL gas), which was measured in an experiment without catalysts present in the mixture.

S4. Further results for photocatalytic hydrogen generation in the presence of other materials

Table S4: Photocatalytic hydrogen generation from THF/TEA/H₂O mixture by adding further carbon supports to the system CuI/IrPS/bpy

Entry	Support	V (THF:TEA:H ₂ O) [ml]	V [ml] 3h	Activity [mmol·h ⁻¹ ·g ⁻¹] 3h	V [ml] 10h	activity [mmol·h ⁻¹ ·g ⁻¹] 10h	V [ml] 20h	activity [mmol·h ⁻¹ ·g ⁻¹] 20h
1 ^a	MCM-41	20	2.1	43.7	2.2	14.0	2.1	17.2
2 ^b	MCM-41	20	1.0	-	1.4	-	1.6	-
3 ^{a,c}	rGO(H ₂)	50	1.6	33.8	1.7	10.8	1.9	6.0
4 ^{b,c}	rGO(H ₂)	50	2.1	-	2.8	-	3.3	-
5 ^c	-	20	10.0	211.9	13.5	85.9	12.8	40.7
6 ^c	rGO(H ₂)	20	10.3	216.5	18.5	116.7	23.3	73.5
7 ^c	activated carbon ^d	50	9.6	202.9	17.7	112.2	21.1	66.9
8 ^c	graphite (400 nm)	50	7.3	154.3	16.5	104.6	24.6	78.1
9 ^c	graphite (<20 μm)	50	6.9	145.8	14.8	93.8	21.1	66.9

Experimental conditions: 10 μmol [Cu], 15 μmol Ir-PS, 20 μmol bpy, 12 mg support, THF:TEA:H₂O = 3:2:1, 1.5 W Xe-light irradiation with ≥ 385 nm, 25 °C, gas volumes determined by automatic gas burettes and corrected by blank volume (2 mL), gases analyzed by GC, Activity = n(H₂)/(t·m(Cu)).

^awithout Ir-PS

^bwithout CuI

^cmeasurements were performed without bpy.

^dDegussa-Hüls

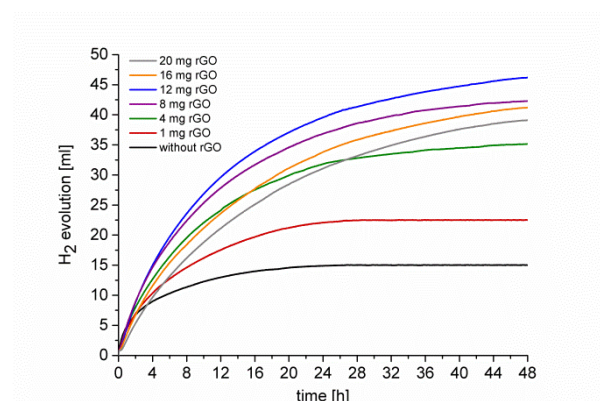


Figure S4. Optimization of the photocatalytic system regarding different amounts of rGO after 48 h in 50 mL solvent.

S5. Photocatalytic hydrogen generation in the presence of different rGOs

Tabelle S5: Photocatalytic hydrogen generation from THF/TEA/H₂O mixture by adding various rGO to the system CuI/IrPS/bpy in contrast to their surface area and conductivity.

Entry	Support	V [ml] 3h	Activity [mmol·h ⁻¹ ·g ⁻¹] 3h	V [ml] 10h	Activity [mmol·h ⁻¹ ·g ⁻¹] 10h	V [ml] 20h	Activity [mmol·h ⁻¹ ·g ⁻¹] 20h
1	rGO (H ₂) ^a	12.2	257.9	26.9	171.5	37.1	117.7
2	rGO (HI) ^b	9.6	202.9	20.4	130.0	27.0	85.7
3	rGO (N ₂ H ₄) ^c	8.4	177.5	16.4	104.5	21.8	69.2
4	rGO (0.2-10 μm)	10.9	230.4	22.6	144.0	30.8	97.7
5	rGO (0.5-3 μm)	11.9	251.5	25.4	161.9	34.4	109.1

Experimental conditions: 15 μmol Ir-PS, 10 μmol [Cu], 12 mg support, 50 ml THF:TEA:H₂O = 3:2:1, 1.5 W Xe-light irradiation, with 385 nm cut-off filter, 25 °C, gas volumes determined by automatic gas burettes and corrected by blank volume (2 mL), gases analyzed by GC, Activity = n(H₂)/(t·m(Cu)).

^areduced with H₂

^breduced with HI

^creduced with N₂H₄

S6. Long term H₂ evolution with CuI/MCM-41/bpy in 50 ml

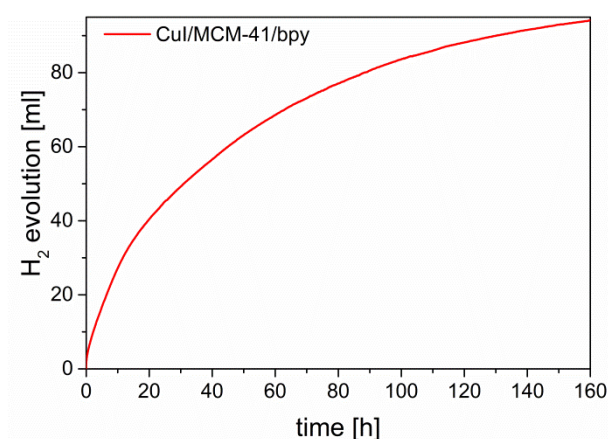


Figure S6. Reaction conditions: 15 μmol Ir-PS, 10 μmol CuI, 20 μmol bpy, 11.4 mg MCM-41, 50 mL THF:TEA:H₂O=3:2:1 (volume based), 1.5 W Xe-light, ≥ 385 nm.

S7. H₂ evolution curves of recycling curves

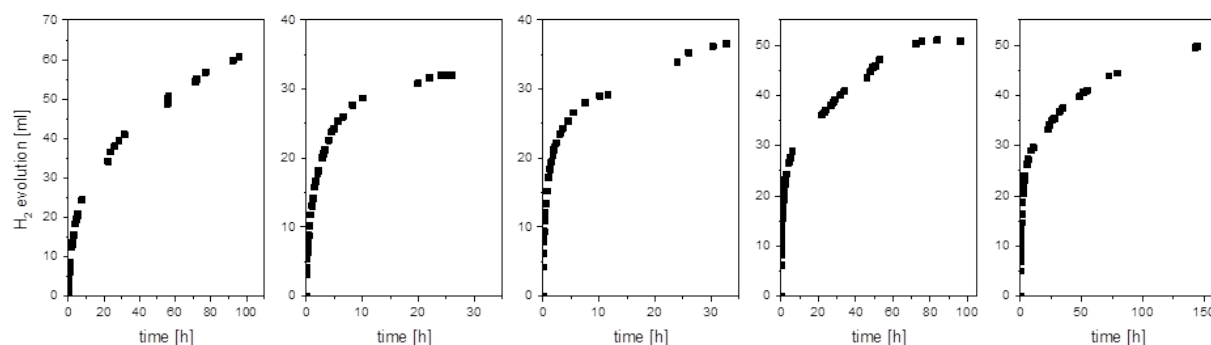


Figure S17. Recycling experiments: 10 μmol Cu from the prepared material; 15 μmol Ir-PS added after every run; 20 mL THF:TEA:H₂O (3:2:1, volume based); irradiation with 300 W Xe-lamp Lot Oriel 1.5W; ≥ 385 nm; manual burette. ICP analysis of investigated copper catalyst: 1.6 wt%.

S8. Characteristics structural properties of supports

Table S8 shows the surface area of the SiO₂ and rGO starting materials which were determined by N₂-physisorption or given by the manufacturer. For silica-based supports also the pore diameter and pore volume are given. The surface area of MCM-41 is the highest (1214 m²/g) and that of npG39 the smallest (199 m²/g) of the investigated SiO₂ supports. With respect to the photocatalytic results, the following conclusion can be established: Considering the significantly different material properties, the observed hydrogen generation is influenced only to a minor extent. As a general trend gas evolution is favored by increased surface area and decreased pore diameter of the support. This observation is in agreement with investigations for the photocatalytic water oxidation by supported IrO₂ which indicated a higher activity by lowering the pore diameter.⁸ In contrast to the results with SiO₂-based supports, the catalytic activity using different rGO materials is not related to size of the surface area.

Table S8. Material properties of the SiO₂ supports MCM-41, SBA-15 and npG39.

Support	A _o [m ² /g]	d _{pore} [nm]	V _{pore} [cm ³ /g]
MCM-41 ^a	1214	4.1	0.730
SBA-15 ^b	645	11	1.738
npG39 ^c	199	39	1.238
rGO (H ₂)	386	n.d. ^d	n.d. ^d
rGO (HI)	42	n.d. ^d	n.d. ^d
rGO (N ₂ H ₄)	159	n.d. ^d	n.d. ^d
rGO (0.2-10 μm)	185	n.d. ^d	n.d. ^d
rGO (0.5-3 μm)	529	n.d. ^d	n.d. ^d

^a purchased from Südchemie (Germany).

^b a description of the synthesis is provided in the Supporting Information (S3).

^c purchased from VitraBio (Germany).

^d rGO is not a porous material.

S9. Hydrogen generation measurements in 10 ml reaction media

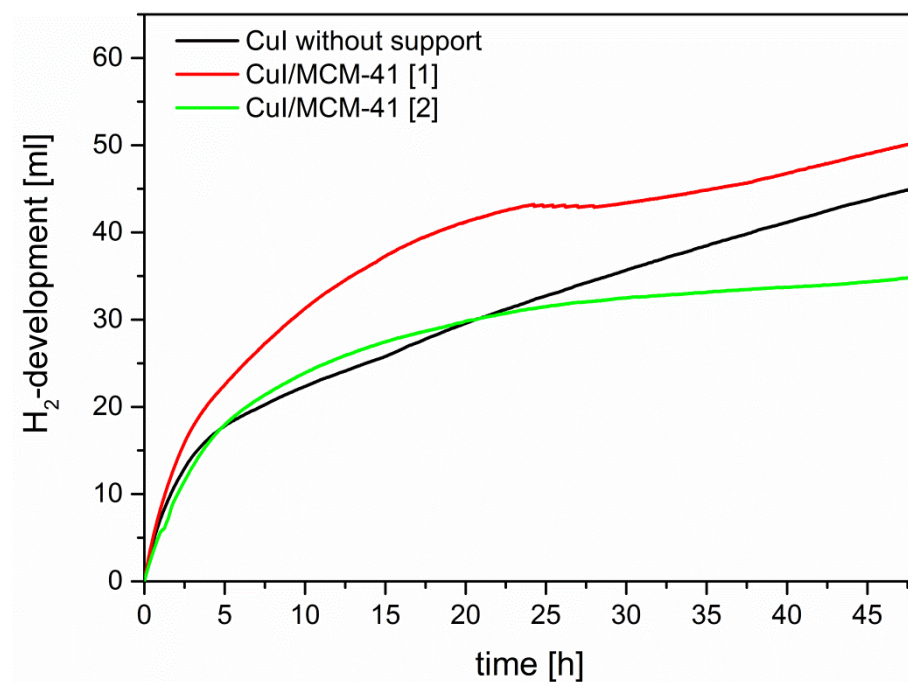


Figure S9. Reaction conditions: 15 μmol PS, 10 μmol CuI, 20 μmol bpy, 11.4 mg MCM-41, 10 mL THF:TEA:H₂O=3:2:1 (volume based), 1.5 W Xe-light, ≥ 385 nm.

S10. TEM analysis of reproduction reaction [2]

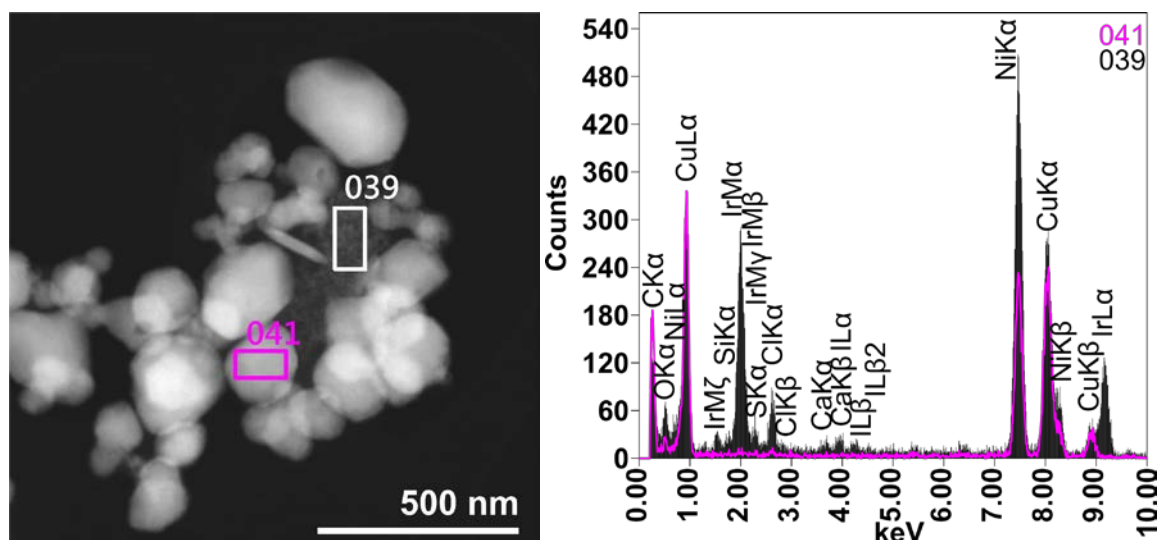


Figure S10a. HAADF-STEM image and EDX analysis of the Ir-PS/CuI/bpy system with MCM-41 (reaction Fig.S6 CuI/MCM-41 [2]) after a reaction of 48 h: Analysis of unsupported Cu-particles. Reaction conditions: 15 μmol PS, 10 μmol CuI, 20 μmol bpy, 11.4 mg MCM-41, 10 mL THF:TEA:H₂O=3:2:1 (volume based), 1.5 W Xe-light, ≥ 385 nm.

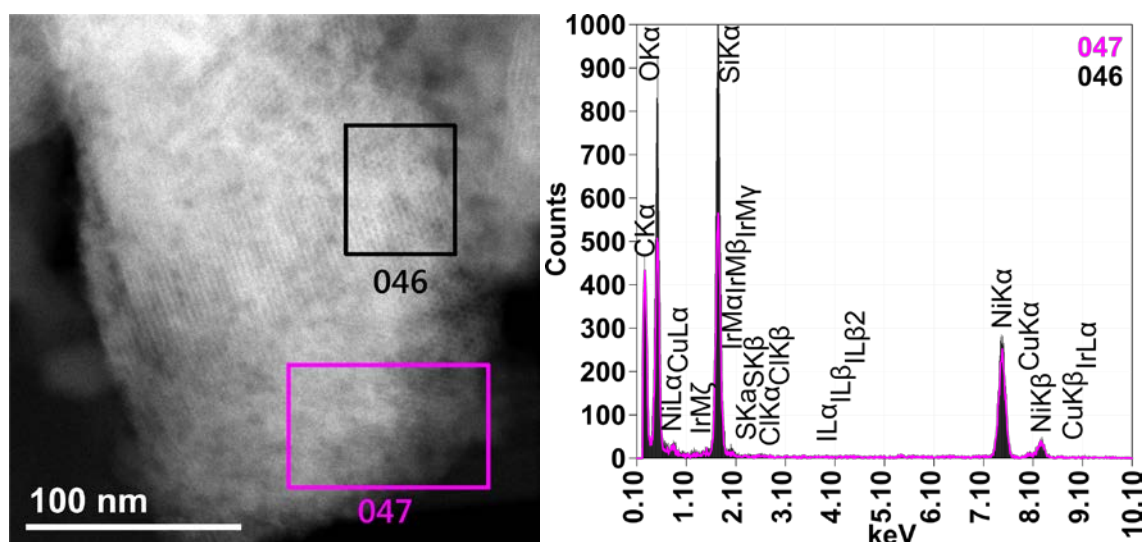


Figure S10b. HAADF-STEM image and EDX analysis of the Ir-PS/CuI/bpy system with MCM-41 (reaction Fig.S6 CuI/MCM-41 [2]) after a reaction of 48 h: Acquisition of the SiO₂ support without any Cu-particles. Reaction conditions: 15 μmol PS, 10 μmol CuI, 20 μmol bpy, 11.4 mg MCM-41, 10 mL THF:TEA:H₂O=3:2:1 (volume based), 1.5 W Xe-light, ≥ 385 nm.

S11. TEM analysis of reproduction reaction [1]

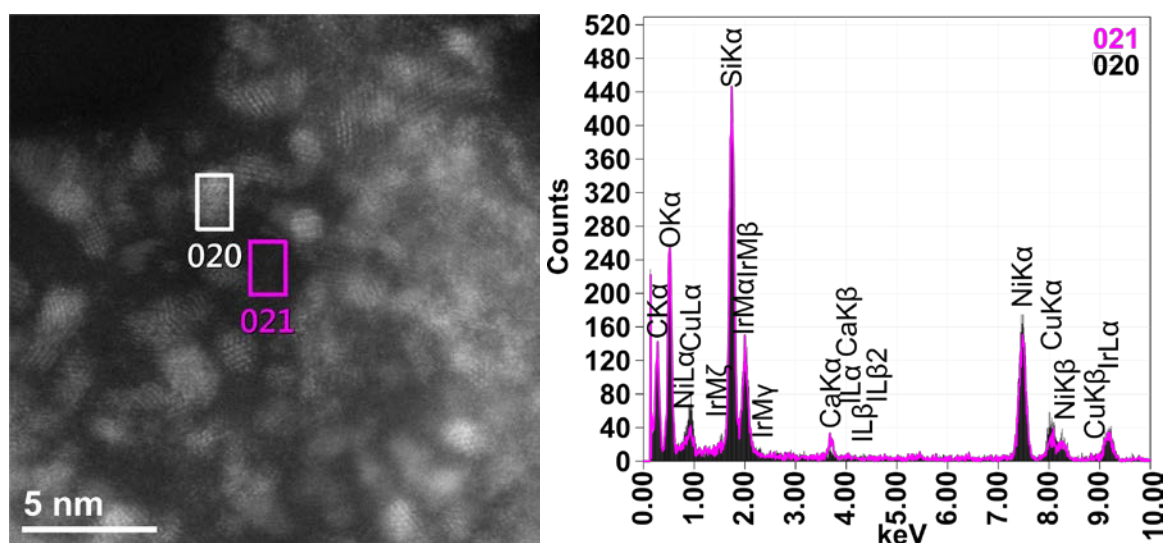


Figure S11a. HAADF-STEM image and EDX analysis of the Ir-PS/CuI/bpy system with MCM-41 (reaction Fig.S6 CuI/MCM-41 [1]) after a reaction of 48 h. Reaction conditions: 15 μmol PS, 10 μmol CuI, 20 μmol bpy, 11.4 mg MCM-41, 10 mL THF:TEA:H₂O=3:2:1 (volume based), 1.5 W Xe-light, ≥ 385 nm.

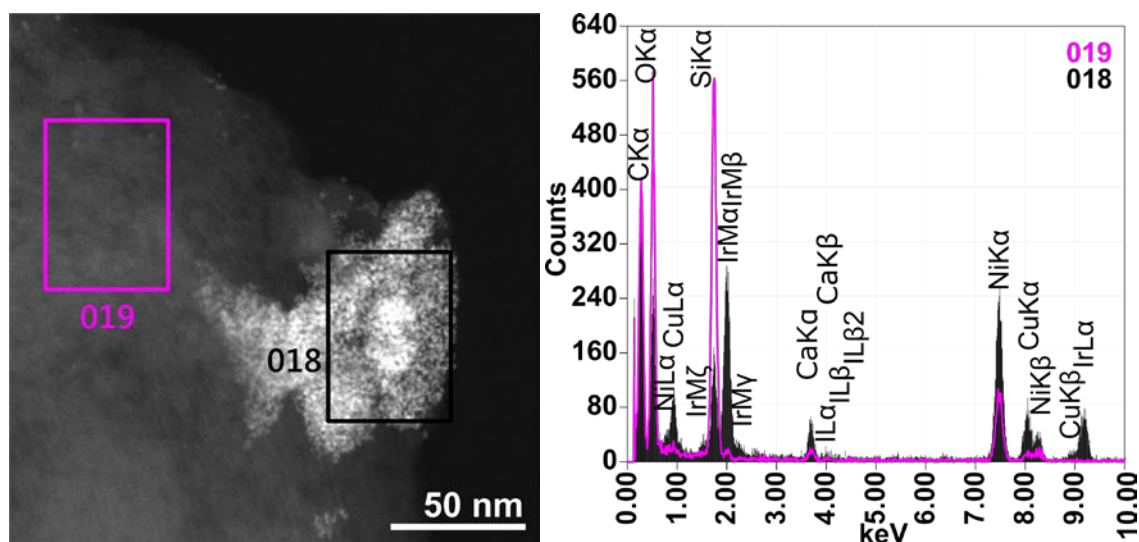


Figure S11b. HAADF-STEM image and EDX analysis of the Ir-PS/CuI/bpy system with MCM-41 (reaction Fig.S6 CuI/MCM-41 [1]) after a reaction of 48 h: Cu deposition surrounded by small Ir nanoparticles on outer surface of MCM-41. Reaction conditions: 15 μmol PS, 10 μmol CuI, 20 μmol bpy, 11.4 mg MCM-41, 10 mL THF:TEA:H₂O=3:2:1 (volume based), 1.5 W Xe-light, ≥ 385 nm.

S12. TEM analysis of the CuI/MCM-41 system in 20 ml reaction mixture

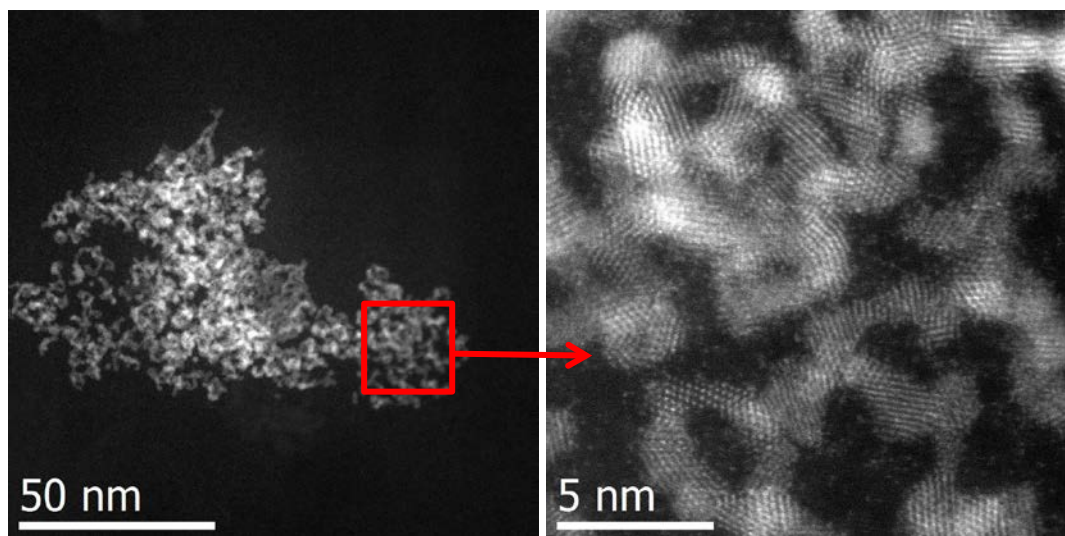


Figure S12a. HAADF-STEM images analysis of the Ir-PS/CuI/bpy system with MCM-41 after a reaction of 48 h in 20 ml solvent. Reaction conditions: 15 μmol PS, 10 μmol CuI, 20 μmol bpy, 11.4 mg MCM-41, 20 mL THF:TEA:H₂O=3:2:1 (volume based), 1.5 W Xe-light, ≥ 385 nm.

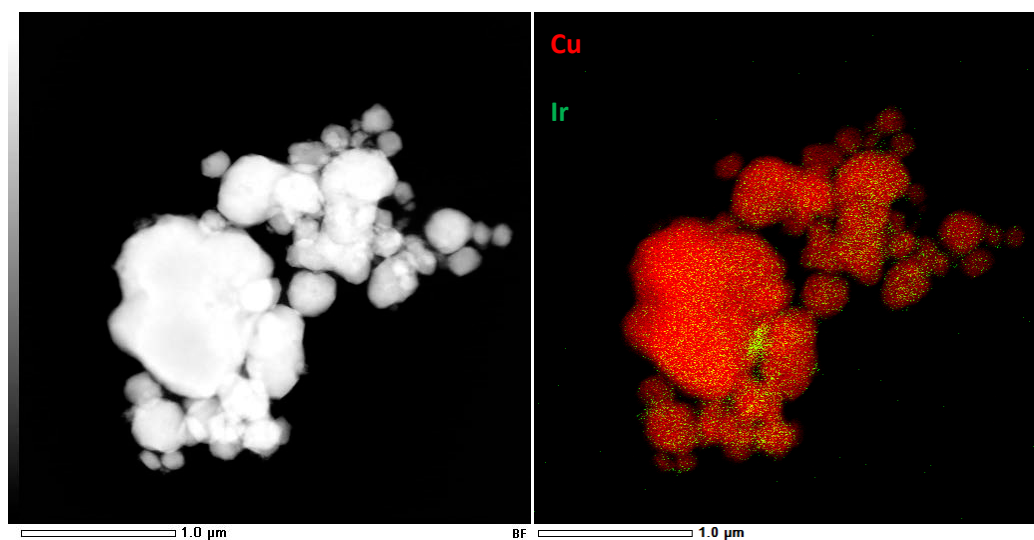


Figure S12b. HAADF-STEM images and overlay of EDX elemental maps of Cu (red) and Ir (green) of the Ir-PS/CuI/bpy system with MCM-41 after a reaction of 48 h in 20 ml solvent. Reaction conditions: 15 μmol PS, 10 μmol CuI, 20 μmol bpy, 11.4 mg MCM-41, 20 mL THF:TEA:H₂O=3:2:1 (volume based), 1.5 W Xe-light, ≥ 385 nm.

S13. TEM analysis of the CuI/MCM-41 system in 50 ml reaction mixture

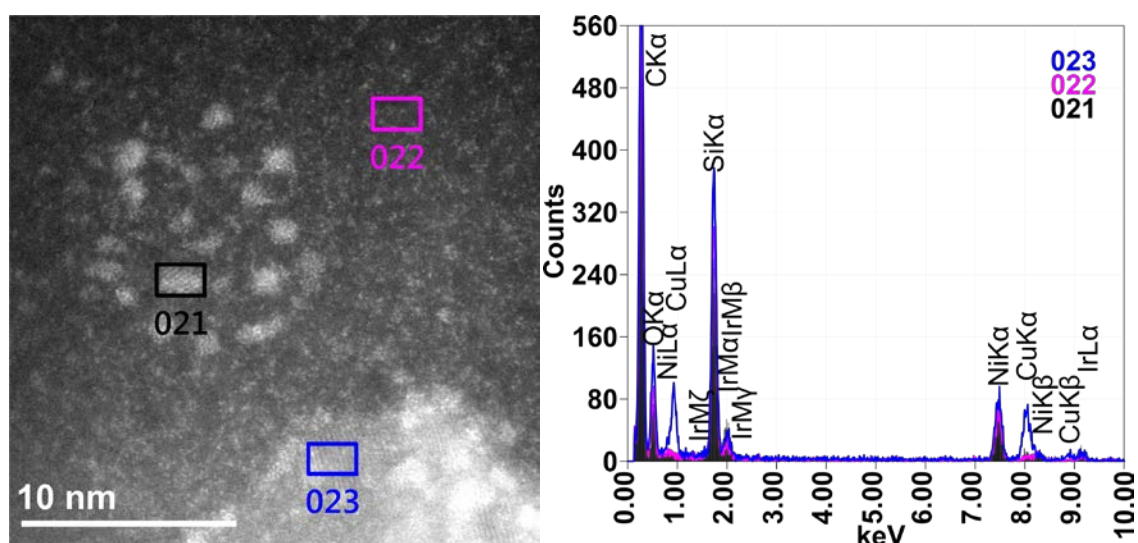


Figure S13a. HAADF-STEM image and EDX analysis of the Ir-PS/CuI system with MCM-41 after a reaction of 96 h in 50 ml solvent with the addition of bpy, showing small Ir nanoparticles (021), distributed Ir (022) and a larger Cu nanoparticle (023) decorated with Ir. Reaction conditions: 15 μmol PS, 10 μmol CuI, 20 μmol bpy, 11.4 mg MCM-41, 50 mL THF:TEA:H₂O=3:2:1 (volume based), 1.5 W Xe-light, ≥ 385 nm.

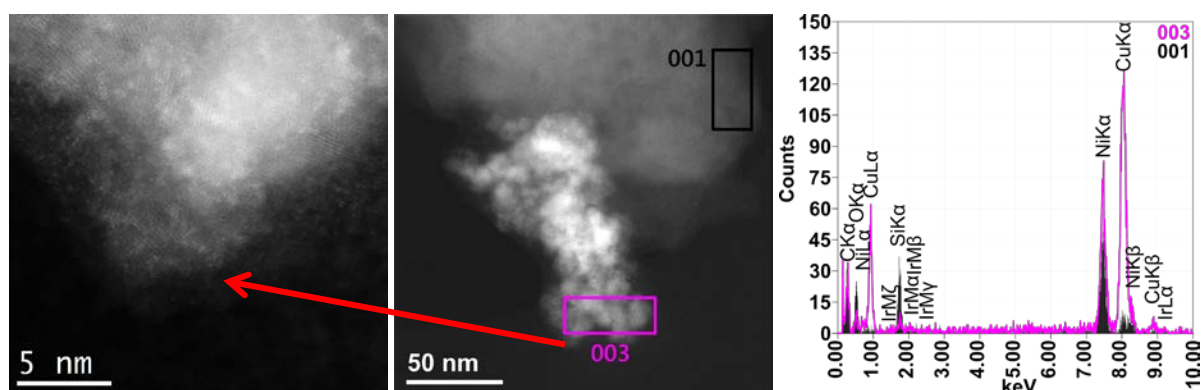


Figure S13b. HAADF-STEM images and EDX analysis of the Ir-PS/CuI system with MCM-41 after a reaction of 164 h in 50 ml with the addition of bpy showing an MCM-41 particle (001) with an attached Cu particle (003) decorated with Ir. Reaction conditions: 15 μmol PS, 10 μmol CuI, 20 μmol bpy, 11.4 mg MCM-41, 50 mL THF:TEA:H₂O=3:2:1 (volume based), 1.5 W Xe-light, ≥ 385 nm.

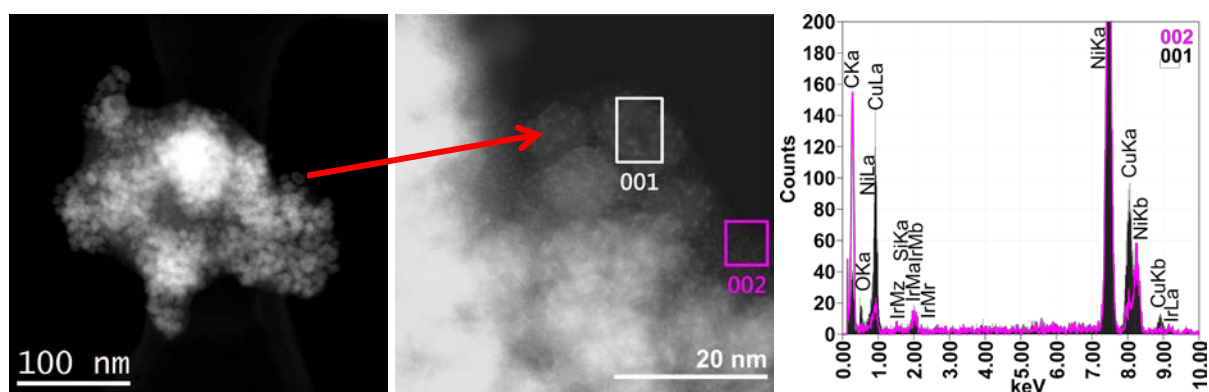


Figure S13c. HAADF-STEM images and EDX analysis of the Ir-PS/CuI system with MCM-41 after a reaction of 48 h in 50 ml without the addition of bpy. Reaction conditions: 15 μmol PS, 10 μmol CuI, 11.4 mg MCM-41, 50 mL THF:TEA:H₂O=3:2:1 (volume based), 1.5 W Xe-light, ≥ 385 nm.

S14. TEM analysis of the material without additive

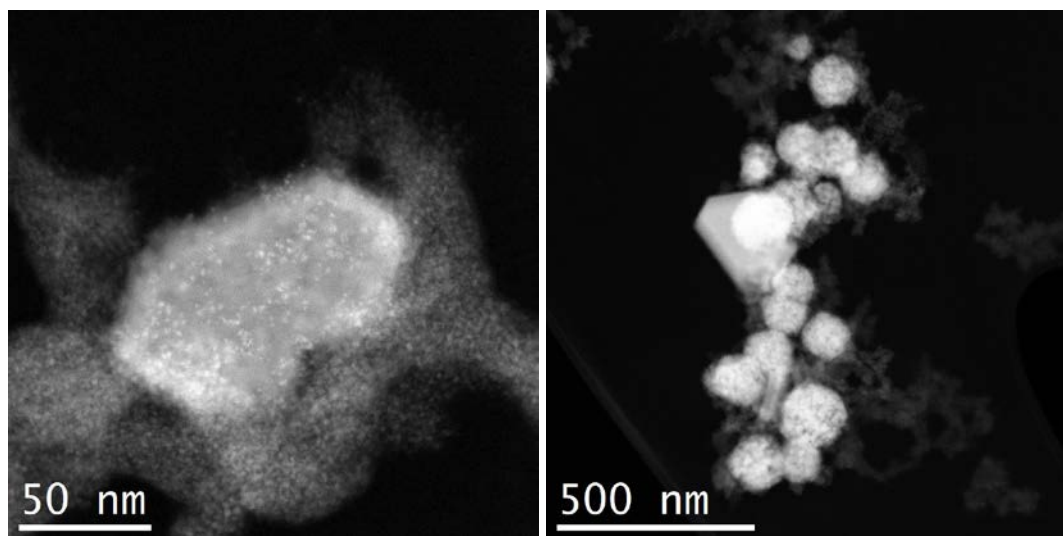


Figure S14. HAADF-STEM images and EDX analysis of the Ir-PS/CuI system without any additive after a reaction of 48 h in 50 ml and without the addition of bpy. Reaction conditions: 15 μmol PS, 10 μmol CuI, 50 mL THF:TEA:H₂O=3:2:1 (volume based), 1.5 W Xe-light, ≥ 385 nm.

S15. Time-resolved quenching experiments

Measurement procedure:

The samples were prepared and measured under Ar in 1 cm cuvettes. For the excitation ultrashort laser pulses at 388 nm were used which were obtained by second harmonic generation applied to the output of a Ti:sapphire laser system (CPA 2001, Clark MXR, Inc.). The luminescence lifetimes were determined by fitting a monoexponential decay to the data.

In table S15 the influence of different components on the luminescence lifetime of the Ir-PS is characterized. The luminescence lifetime of the Ir-PS in THF is 318 ns (Entry 1). By the addition of either reduced graphene oxide (Entry 6) or CuI (Entry 10) or both components (Entries 14 and 18) no change in the luminescence lifetime was observed. The addition of TEA with a ratio THF/TEA of 4:2 led to a strong quenching of the lifetime down to 6 to 14 ns (Entries 3, 7, 11, 15 and 19).

The addition of water decreases the lifetime by a factor of 1.5 to ca. 210 ns (Entries 4, 8, 12, 16 and 20). Maybe the coordination of water molecules accelerates the internal conversion pathway. But if water is added to a mixture of THF and TEA the quenching effect of TEA was weakened to ca. 24 ns (Entries 5, 9, 13, 17 and 21). This effect is probably due to water molecules hindering the TEA molecules to get in contact with the Ir-PS molecules.

To exclude that oxygen accidentally entering into the sample is responsible for the observed changes a control experiment was performed by adding 1 mL air to the sample. In this case the lifetime was quenched to 185 ns (Entry 2) showing that oxygen cannot be the reason for the lifetime changes obtained for the other solutions.

Table S15: Luminescence lifetimes of the Ir-PS with different components.

Entry	Solvent	Ratio	c (IrPS) / M	Addition	m respectively V (Addition)	Measurement range	lifetime / ns
1	THF	-	4.2E-05	-	-	5 μ s	318
2	THF	-	4.2E-05	O ₂	1 mL	5 μ s	185
3	THF/TEA	4:2	4.2E-05	-	-	200 ns	8.3
4	THF/H ₂ O	5:1	4.2E-05	-	-	2 μ s	204
5	THF/TEA/H ₂ O	3:2:1	4.2E-05	-	-	200 ns	24.2
6	THF	-	4.2E-05	rGO	0.36 mg / 3 mL	5 μ s	307
7	THF/TEA	4:2	4.2E-05	rGO	0.36 mg / 3 mL	200 / 100 ns	6.3 / 6.3
8	THF/H ₂ O	5:1	4.2E-05	rGO	0.36 mg / 3 mL	5 / 2 μ s	215 / 214
9	THF/TEA/H ₂ O	3:2:1	4.2E-05	rGO	0.36 mg / 3 mL	200 ns	25.0
10	THF	-	4.2E-05	CuI	0.0576 mg / 3 mL	5 μ s	315
11	THF/TEA	4:2	4.2E-05	CuI	0.0576 mg / 3 mL	100 ns	6.0
12	THF/H ₂ O	5:1	4.2E-05	CuI	0.0576 mg / 3 mL	5 / 2 μ s	211 / 208
13	THF/TEA/H ₂ O	3:2:1	4.2E-05	CuI	0.0576 mg / 3 mL	200 ns	25.1
14	THF	-	4.2E-05	CuI + rGO	(0.36 + 0.0576) mg	2 μ s	316
15	THF/TEA	4:2	4.2E-05	CuI + rGO	(0.36 + 0.0576) mg	100 ns	5.9
16	THF/H ₂ O	5:1	4.2E-05	CuI + rGO	(0.36 + 0.0576) mg	5 / 2 μ s	200 / 197
17	THF/TEA/H ₂ O	3:2:1	4.2E-05	CuI + rGO	(0.36 + 0.0576) mg	200 ns	22.1
18	THF	-	4.2E-05	CuI + rGO ^a	(0.36 + 0.0576) mg	2 μ s	303
19	THF/TEA	4:2	4.2E-05	CuI + rGO ^a	(0.36 + 0.0576) mg	200 / 100 ns	13.6 / 14.0
20	THF/H ₂ O	5:1	4.2E-05	CuI + rGO ^a	(0.36 + 0.0576) mg	2 μ s	211
21	THF/TEA/H ₂ O	3:2:1	4.2E-05	CuI + rGO ^a	(0.36 + 0.0576) mg	200 ns	24.0

^aafter catalysis so the catalyst had precipitated onto the reduced graphene oxide.

S16. UV-vis measurements

First, the UV-vis spectra of the initial Ir-PS (15 μ mol) dissolved in 10 ml of THF:TEA:H₂O = 3:2:1 was recorded. Afterwards, the reaction of S15 was performed under the following conditions: 15 μ mol Ir-PS, 10 μ mol CuI, 11.4 mg MCM-41, without bpy, 50 mL THF:TEA:H₂O = 3:2:1, 1.5 W Xe-light, \geq 385 nm, 40 h. 2 ml of the dispersion were separated from the reaction mixture to analyze the absorption spectra of the used Ir-PS (before bpy). Then, 20 μ mol bpy were added to the reaction mixture and stirred for 10 min. Another sample was taken to record an UV-vis spectra. The reaction mixture was irradiated and UV-vis analysis was carried out after several intervals

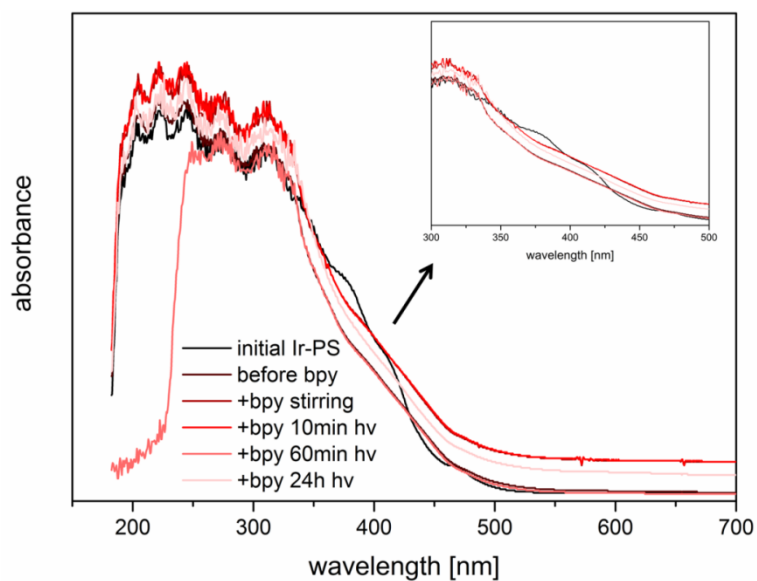


Figure S16. UV-vis spectra of the initial Ir-PS and the reaction mixture after the addition of bpy and different reaction times.

References

1. E. M. Johansson, J. M. Córdoba and M. Odén, *Materials Letters*, 2009, **63**, 2129-2131.
2. D. C. Marcano, D. V. Kosynkin, J. M. Berlin, A. Sinitskii, Z. Sun, A. Slesarev, L. B. Alemany, W. Lu and J. M. Tour, *ACS Nano*, 2010, **4**, 4806-4814.
3. I. K. Moon, J. Lee, R. S. Ruoff and H. Lee, *Nat. Commun.*, 2010, **1**, 73.
4. P. G. Ren, *Nanotechnology*, 2011, **22**, 055705.
5. Z.-S. Wu, W. Ren, L. Gao, B. Liu, C. Jiang and H.-M. Cheng, *Carbon*, 2009, **47**, 493-499.
6. S. Brunauer, P. H. Emmett and E. Teller, *J. Am. Chem. Soc.*, 1938, **60**, 309-319.
7. E. P. Barrett, L. G. Joyner and P. P. Halenda, *J. Am. Chem. Soc.*, 1951, **73**, 373-380.
8. H. Junge, N. Marquet, A. Kammer, S. Denurra, M. Bauer, S. Wohlrab, F. Gärtner, M.-M. Pohl, A. Spannenberg, S. Gladiali and M. Beller, *Chem. Eur. J.*, 2012, **18**, 12749-12758.

5.3 Improving Selectivity and Activity of CO₂ Reduction Photocatalysts with Oxygen

Stefanie Kreft, Roland Schoch, Jacob Schneidewind, Jabor Rabeah, Evgenii V. Kondratenko, Vita A. Kondratenko, Henrik Junge, Matthias Bauer, Sebastian Wohlrab, Matthias Beller

Chem, **2019**, DOI: 10.1016/j.chempr.2019.04.006.

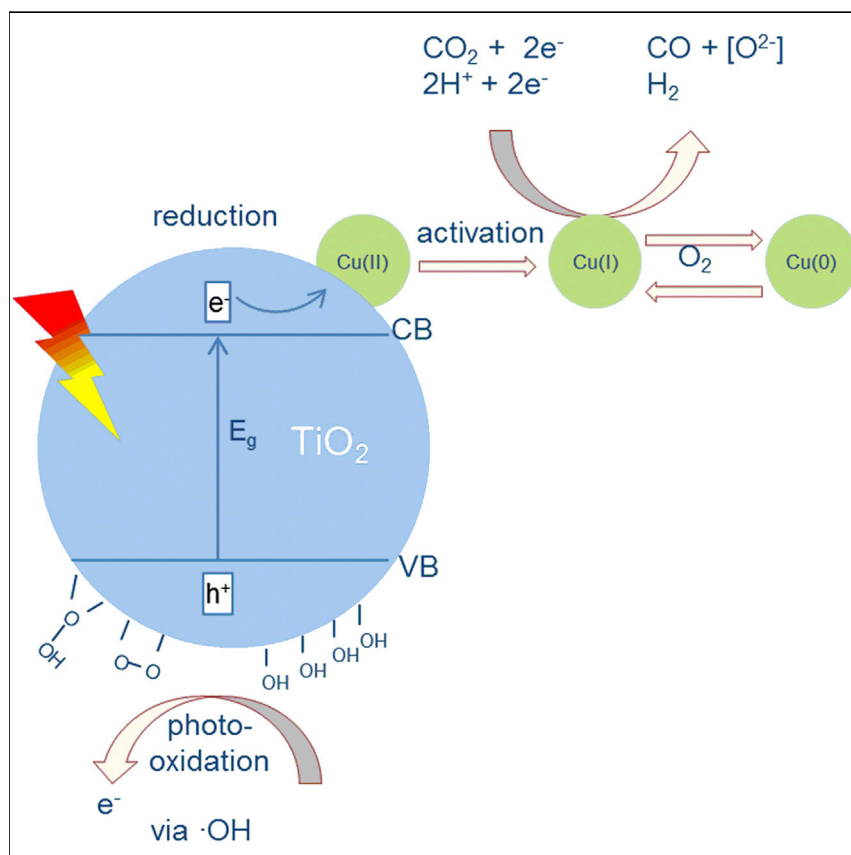
© 2019 Cell Press Subscriptions Office. Published by Elsevier Inc.

Electronic Supporting Information for this article is available under <https://doi.org/10.1016/j.chempr.2019.04.006>.

Contribution: S. K. found the activity of M/TiO₂ aerogel for the photocatalytic aqueous CO₂ reduction. She designed and synthesized all materials and performed all catalytic experiments and the *operando* UV-vis measurements and their evaluation. S. K. analyzed the data of the standard characteristic methods (XRD, TEM, XPS, N₂-sorption). In cooperation with R. S. she planned and carried out the *ex situ* and *in situ* XAS experiments at DESY. Furthermore, she designed the experiments for the oxidation half-reaction section with J. S. and planned and prepared the *in situ* EPR experiments with J. R. She wrote the main part of the manuscript, prepared the supporting information and has contributed significantly in the development and arrangement of the publications' concept. Her overall contribution is about 65 %.

Article

Improving Selectivity and Activity of CO₂ Reduction Photocatalysts with Oxygen



A highly porous copper-loaded titanium dioxide material has been developed to catalyze reduction of CO₂ to CO using light as the energy source. In this system, activity for CO production could be enhanced by addition of oxygen, which stabilizes the catalytically active Cu(I) oxidation state. The oxidation half-reaction has also been investigated, and the titanium dioxide itself was found to be the electron source.

Stefanie Kreft, Roland Schoch, Jacob Schneidewind, ..., Matthias Bauer, Sebastian Wohlrab, Matthias Beller

evgenii.kondratenko@catalysis.de (E.V.K.)
matthias.beller@catalysis.de (M.B.)

HIGHLIGHTS

Synthesized Cu/TiO₂ aerogel is active in CO₂ reduction compared to commonly used P25

Enhanced activity in the presence of small amounts of O₂

Photooxidation of surface hydroxyl groups provides electrons for CO₂ reduction

Various *in situ* investigations provide evidence of mechanism (e.g., EPR, XAS, UV-vis)

Article

Improving Selectivity and Activity of CO₂ Reduction Photocatalysts with Oxygen

Stefanie Kreft,¹ Roland Schoch,^{2,3} Jacob Schneidewind,^{1,3} Jabor Rabeah,¹ Evgenii V. Kondratenko,^{1,*} Vita A. Kondratenko,¹ Henrik Junge,¹ Matthias Bauer,² Sebastian Wohlrab,¹ and Matthias Beller^{1,4,*}

SUMMARY

A highly porous photocatalyst (copper on TiO₂ aerogel) was synthesized and applied in aqueous CO₂ reduction without using external sacrificial electron donors. For the first time, complete selectivity toward CO and improved catalyst productivity are observed in the presence of oxygen. The optimal activity is achieved in a feed containing 0.5 vol% O₂ in CO₂. *In situ* XAS, EPR, and UV-vis measurements suggest, among different Cu oxidation states, Cu(I) to be the most active species in photocatalytic CO₂ reduction. Oxygen sensing of the catalyst in the presence of O₂/CO₂ mixtures indicated an unexpected photoadsorption of oxygen on the titania surface. We propose photooxidation of surface hydroxyl groups to be the electron source for CO₂ reduction, which is supported by hydroxyl group consumption, detection of hydroxyl radicals using *in situ* EPR, and detection of surface peroxide species after the reaction.

INTRODUCTION

Usage of carbon dioxide (CO₂) under ambient conditions for the formation of organic matter is of fundamental importance in biology^{1,2} and is considered to be a key step for future artificial photosynthesis^{3,4} to convert this inexpensive and non-toxic C₁ building block into more valuable products.^{5,6} Since the beginning of the 20th century, CO₂ has been used on a large-scale in industry, particularly for the production of urea.^{7,8} More recently, the synthesis of various carbonates was also commercialized.^{9–11} In all these examples, the oxidation state of CO₂ remains unchanged. When CO₂ is involved in reduction reactions, the spectrum of the products generated can be significantly extended. For this purpose, hydrogen-rich chemicals such as CH₄ and lower alkanes are typically applied to convert CO₂ into syngas (a mixture of H₂ and CO).¹² In addition, direct hydrogenation to methanol or hydrocarbons^{13,14} continues to attract attention as alternative CO₂ valorizations. Recently, electrochemical,^{15,16} photochemical reductions,^{17,18} and combined approaches¹⁹ also became attractive from both fundamental and applied viewpoints. Undoubtedly, the direct photocatalytic conversion of CO₂ into methanol²⁰ or formic acid²¹ without additional reductants constitutes a benign and straightforward way to access these important building blocks. The selective deoxygenation of CO₂ to CO is also important because of the industrial use of the latter in large-scale Fischer-Tropsch synthesis, methanol synthesis, olefin hydroformylation, etc. Compared to the photocatalytic water-splitting process, fewer homogenous and heterogeneous systems are known for direct CO₂ conversion into CO without formation of other carbon-containing products. For example, molecular-defined systems consisting of a photosensitizer (PS) and a CO₂ reduction catalyst, e.g., Fe—^{22,23}, Ni—²⁴, Cu—,²⁵ Re—,²⁶ or Ru—²⁷ complexes, have been reported. Notably, in all these studies, external

The Bigger Picture

The consumption of fossil fuels for energy generation results in harmful CO₂ emissions, necessitating carbon-neutral energy sources for global environmental sustainability. Instead of releasing CO₂ into the atmosphere, using it as a renewable carbon feedstock for the synthesis of valuable chemicals and/or fuels is highly desirable. Photocatalytic CO₂ reduction to C₁ compounds combines the use of solar energy with CO₂ valorization and is of great interest in basic research. Semiconductors, especially TiO₂, are commonly used as photocatalysts. In this work, a highly porous TiO₂ aerogel was synthesized and applied in aqueous CO₂ reduction to CO. Thereby, improved catalyst productivity was observed in the presence of oxygen. Furthermore, progress in understanding the lesser known and challenging oxidation process has been achieved.

sacrificial reducing agents such as amines or alcohols are required, thus hampering potential applications. Complementary to the use of these molecular-defined systems, heterogeneous catalysts based on semiconductors like CdS,^{28,29} ZrO₂,³⁰ Ga₂O₃,³¹ graphene,³² and especially TiO₂^{14,17} were described for photocatalytic reduction of CO₂. In these materials, a photon with energy equal or higher than the band gap (E_g) of the semiconductor is absorbed and leads to the excitation of an electron from the valence band (VB) to the conduction band (CB). Thereby an electron-hole pair is generated. In order to make this process more efficient and to prevent a recombination of these charge carriers, co-catalysts that reduce CO₂ are deposited on the surface.^{17,33} However, such studies were mainly performed in the presence of sacrificial reductants such as alcohols^{34,35} or hole scavengers.^{36–38} In fact, only a small number of materials, such as TiO₂, Ga₂O₃,³⁹ N-doped ZnO,⁴⁰ and MTaO₃ (M = K, Na, Li),^{41,42} promote CO₂ conversion into CO without additional reagents.

Since the pioneering work of Honda and Fujishima in the early 70's,⁴³ TiO₂ has been among the best known semiconductors for photocatalysis owing to its abundance, semiconducting properties, low costs, and chemical stability.^{17,44,45} The primary crystal structures of titania are anatase and rutile, while the electrons of the former structure have a much longer lifetime (1 ms) of the excited state resulting in improved photocatalytic CO₂ reduction.⁴⁶ So far, titania-based catalysts with supported Pt,⁴⁷ Ag,⁴⁸ Au,^{49,50} Pd,⁵¹ Cu,^{52–65} Fe,⁶⁶ or Ni⁶⁷ species have been applied for photocatalytic CO₂ reduction. Among the known copper/titanium dioxide (Cu/TiO₂) materials (Table S1), active catalysts in batch or continuous-flow reactors required the presence of Cu(I) species.^{52,54,57,62–64} Thereby, the presence of Cu(0) decreased the activity.^{58,62,63} In gas-phase reactions, primarily, CH₄ and CO were generated upon light-driven CO₂ reduction.^{52,54,57–59,64,65} In contrast, CO₂ reduction in aqueous solutions toward oxygenates^{55,56,60–63} or methane^{53,55} competes with water reduction to form H₂ preferentially.

In addition to the supported co-catalyst, the crystallite size and specific surface area of TiO₂ are key parameters affecting overall performance of the material. For example, usage of TiO₂ crystallites larger than 20 nm led to a substantial decrease in photocatalytic activity.⁶⁸ On the basis of significantly smaller particles and mainly because of their high specific surface area, we speculated that metal-supported anatase aerogels may constitute promising catalytic materials.^{69–71} Surprisingly, apart from aerogels with supported platinum species,^{72,73} their counterparts with other supported metals have been scarcely investigated for the target reaction.

In this work, we describe the synthesis of composite materials like Cu/TiO₂-AG (AG: aerogel) possessing Cu(II)-nanoparticles on the surface of a highly porous TiO₂ aerogel (TiO₂-AG) and their application for room-temperature photocatalytic CO₂ reduction without any external sacrificial reagents. Remarkably, the presence of oxygen (O₂) improved the CO productivity and practically suppressed H₂ generation.

RESULTS AND DISCUSSION

Preparation and Characterization of Catalytic Materials

TiO₂-AG and Cu/TiO₂-AG were synthesized as previously described (Section S2).^{73–75} N₂-physisorption measurements revealed that these samples possess a specific surface area of 480 m²/g (Section S6). This value is almost 10 times higher than the specific surface area of commercially available TiO₂ (P25). The reasons for this difference are the larger particles and the random aggregation of the P25 powder in contrast to the defined wire-like structure⁷⁴ of the TiO₂-AG. The content of

¹Leibniz-Institut für Katalyse, an der Universität Rostock e.V., Albert-Einstein-Straße 29a, Rostock 18059, Germany

²Universität Paderborn, Department Chemie, Warburger Str. 100, Paderborn 33098, Germany

³These authors contributed equally

⁴Lead Contact

*Correspondence: evgenii.kondratenko@catalysis.de (E.V.K.), matthias.beller@catalysis.de (M.B.)

<https://doi.org/10.1016/j.chempr.2019.04.006>

copper (Cu) determined by inductively coupled plasma atomic emission spectroscopy (ICP-AES) is used in the abbreviations of the catalysts (see also [Section S5](#)).

Powder X-ray diffraction (XRD) analysis proved that the TiO₂-AG samples are composed of the anatase phase with nanosized crystallites as determined from the XRD reflection (101) ([Figure S7](#)). Transmission electron microscopy and high-angle annular dark field (TEM-HAADF) images revealed the preservation of the wire-like structure of the TiO₂-AG after addition of Cu-nanoparticles ([Figures S8 and S9](#)). Because of the low difference in molecular weights between Cu and titanium, it is difficult to distinguish between them in the TEM image. However, the three spectra recorded by energy dispersive x-ray spectroscopy (EDX) at different positions showed the same intensive Cu signal concluding a homogeneous dispersion of Cu. The calculated Ti:Cu ratio was about 9:1 in all three considered areas ([Figure S9B](#) EDX data), which corroborates the Cu/Ti ratio in 6.3_Cu/TiO₂-AG. Thereby, the Cu species seem to be finely dispersed on the surface of the support ([Figure S9](#)), which correlates with the XRD pattern without significant Cu reflections ([Figure S7](#)). As determined by x-ray photoelectron spectroscopy (XPS) ([Figure S10A](#)), the only weak Cu 2p_{3/2} peak was observed at 933.1 eV, which is characteristic for Cu(II) species.⁷⁶ The typical satellite peak in the area of around 941 eV can only be presumed because of the low signal intensity. This low-intensity signal at rather high Cu loading (6.3 wt %) supports the high Cu dispersion on the surface of the aerogel.

Reduction Half-Reaction

All catalytic experiments were performed in a batch reactor using a CO₂-saturated-catalyst dispersion in water at room temperature under UV-A/Vis (320–500 nm) irradiation ([Section S4](#)). In general, besides H₂ and CO, no CH₄ or any other gaseous or liquid products (formic acid, methanol) could be detected by gas chromatography equipped with a thermal conductivity detector (GC/TCD), gas chromatography/mass spectrometry (GC-MS), and capillary electrophoresis. Selected catalytic results are summarized in [Table 1](#). While common commercial TiO₂ samples showed neither CO nor H₂ production within the detection limit ([Table 1](#), entries 1 and 2), the synthesized TiO₂-AG displayed some activity, albeit mainly for water reduction ([Table 1](#), entry 3). Testing 6.3_Cu/TiO₂-AG, CO generation was 3 times higher than that with pristine TiO₂-AG; however, hydrogen evolution still dominated ([Table 1](#), entry 4). Unfortunately, the activity of Cu/TiO₂-AG decreased significantly over time ([Table 1](#), entries 4–7), which suggests a rapid catalyst deactivation (see “Improving Catalyst Activity and Selectivity” and “The Nature of Active Cu Species”). When Cu loading was reduced to 0.3 wt %, the activity toward CO increased strongly, while H₂ generation was slightly affected ([Table 1](#), entry 8). In agreement with previous observations, we believe that less Cu on the surface leads to higher dispersion and smaller particles, which prevents charge recombination and thereby promotes CO₂ photo reduction.^{59,63,65} Lowering the amount of the catalyst further increased catalytic activity ([Table 1](#), entry 9), apparently because of improved light absorption by the catalyst.

Although the highest activity was achieved with 0.3_Cu/TiO₂-AG, most of the analytical investigations were performed on the 6.3_Cu/TiO₂-AG because of clearer and easier interpretation of the recorded data. Regarding the analysis of the copper species (e.g. oxidation state), *in situ* measurements of 0.3_Cu/TiO₂-AG would not have been possible in an aqueous solution.

To demonstrate the importance of the aerogel support for CO₂ reduction, a reference Cu-containing catalyst on the basis of the TiO₂-P25 support was prepared

Table 1. Photocatalytic Reduction of CO₂ in H₂O with Various TiO₂ and Cu/TiO₂ Catalysts

Entry	Catalyst	Reaction Time (h)	Amount _{H₂} (μl) (Activity [μmol·g _{cat} ⁻¹ ·h ⁻¹])	Amount _{CO} (μl) (Activity [μmol·g _{cat} ⁻¹ ·h ⁻¹])
1	TiO ₂ -P25	4	n.d.	n.d.
2	TiO ₂ Anatase	4	n.d.	n.d.
3	TiO ₂ -AG	4	240 (200)	1.8 (1.5)
4	6.3_Cu/TiO ₂ -AG	4	530 (430)	6.2 (5.1)
5	6.3_Cu/TiO ₂ -AG	6	580 (320)	6.6 (3.6)
6	6.3_Cu/TiO ₂ -AG	20	750 (120)	7.5 (1.2)
7	6.3_Cu/TiO ₂ -AG	0.5	41 (290)	4.3 (28)
8	0.3_Cu/TiO ₂ -AG	4	600 (490)	13.2 (10.9)
9	0.3_Cu/TiO ₂ -AG ^a	4	80 (610)	3 (26)
10	0.5_Cu/TiO ₂ -P25 ^b	4	n.d.	n.d.
11	CuO NP	4	n.d.	n.d.
12	-	4	n.d.	n.d.
13	6.3_Cu/TiO ₂ -AG ^c	4	n.d.	n.d.
14	6.3_Cu/TiO ₂ -AG ^d	4	550 (450)	n.d.

All experiments have been performed at least twice and the averages are shown. Differences between the measurements are between 1% and 14%.

Experimental conditions: 12.6 mg catalyst, 7.5 mL H₂O, 60 min flushing with CO₂, 20°C, 4 h irradiation, Lumatec lamp: 2.5 W output, Filter 320–500 nm, gases analyzed by GC, Activity = n (gas)/(m(catalyst)*t). n.d., not detectable; detection limit see [Supplemental Information](#).

^aCatalyst amount: 1.2 mg.

^bPreparation method in Procedure S3.

^cwithout irradiation.

^dwithout CO₂.

(see [Section S3](#)). When this material was applied, no photochemical reduction was observed under standard reaction conditions ([Table 1](#), entry 10). This demonstrates that the application of the TiO₂-AG is an important prerequisite for successful CO₂ reduction. Similarly, commercially available CuO NP showed no formation of CO and H₂ ([Table 1](#), entry 11). Moreover, as expected, no conversion was detected without catalyst or light ([Table 1](#), entries 12–13). When the tests were performed in the absence of CO₂ with 6.3_Cu/TiO₂-AG, hydrogen was the only product ([Table 1](#), entry 14). Thus, CO₂ is the only carbon source for CO.

Furthermore, the influence of different salts in aqueous media was investigated using 1.3 mg of the 0.3_Cu/TiO₂-AG catalyst ([Figure S11](#)). Notably, generation of CO occurred in 1 M NaHCO₃ solution also, although the reduction of CO₂ under basic conditions is more difficult, which is also shown by our investigations. In CO₂-saturated 1 M NaHCO₃ and H₂O, respectively, nearly the same CO and H₂ evolution was observed. Also, using an NaHCO₃ solution resulted in nearly the same productivity. A severe deviation of the pH value above phosphate buffer, 0.1 M NaOH) led to decreased CO generation, and in the case of the phosphate buffer, the hydrogen generation also diminished significantly. Of course, by addition of

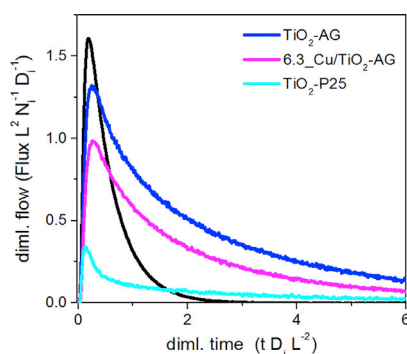


Figure 1. Dimensionless Responses of ¹³CO₂ (Colored Curves) and Ar (Black Line) after Pulsing of a ¹³CO₂:Ar = 1:1 Mixture over Different Catalysts at Room Temperature
L, N_i, and D_i stand for reactor length, number of molecules (Ar or ¹³CO₂), and diffusion coefficient of Ar or ¹³CO₂, respectively. See also Figure S12.

CO₂ to 0.1 M NaOH, the pH value is comparable to that of an NaHCO₃ solution (after establishment of equilibrium). This is the reason why the NaOH-CO₂ system shows higher activity compared to the phosphate buffer-CO₂ system, which stabilizes a more acidic pH.

CO₂ Adsorption and CO Formation – Why Cu and TiO₂ Are Essential

In order to understand the general mechanism of the aqueous CO₂ reduction and to get insights into the specific roles of Cu and the kind of TiO₂ support (TiO₂-P25 versus TiO₂-AG), we performed ¹³CO₂ (¹³CO₂:Ar=1:1) pulse experiments in a temporal analysis of products (TAP) reactor operating with about 10 μs time resolution in the absence of light. This technique enables near-to-molecular understanding of heterogeneously catalyzed reactions.^{77–79} The use of ¹³CO₂ unambiguously determines formation of CO from CO₂ by means of mass spectrometry. Before the pulse experiments, all materials were treated in high vacuum (about 10^{–5} Pa) at 80°C to remove water and CO₂ adsorbed from air while exposing the catalytic materials to ambient conditions. According to the profound mathematical procedure developed by Gleaves et al.,⁸⁰ the obtained transient responses of ¹³CO₂ and Ar were transformed into a dimensionless form. As seen in Figure 1, the response of ¹³CO₂ is situated under the Ar signal (black line) and crosses the latter. This is a “fingerprint”⁸⁰ for reversible adsorption of CO₂. Moreover, the position of the crossing point between the ¹³CO₂ and Ar responses is an indicator for the strength of CO₂ adsorption; the closer this point is to the x axis, the higher the ratio of the constant of adsorption to the constant of desorption is. On this basis, it can be concluded that TiO₂-P25 adsorbs CO₂ stronger than TiO₂-AG although the latter material has higher surface area (480 versus 56 m²·g^{–1}). Such difference may be related to the phase compositions of TiO₂-P25 and TiO₂-AG, being composed of rutile and anatase and pure anatase phases, respectively. An activity-improving factor is the presence of Cu species. Indeed, ¹³CO is detected as a product of ¹³CO₂ reduction only over 6.3_Cu/TiO₂-AG (Figure S12). EPR measurements also demonstrate the significance of Cu for the CO₂ reduction. *In situ* experiments in the presence of 5,5-dimethyl-1-pyrroline N-oxide (DMPO) as a spin trap showed that an organic radical intermediate ([•]CO₂[–]) was formed over 6.3_Cu/TiO₂-AG (Figure S13B), while only traces were observed over bare TiO₂-AG (Figure S13A). All these results together with the TAP data (Figure 1) support the importance of an active Cu species for CO₂ activation.

Oxidation Half-Reaction

Given that no external sacrificial oxidant is added to the system, one expects that water oxidation (forming O₂ or H₂O₂) provides the necessary electrons for CO₂ and/or proton reduction. Similar to other previous reports in TiO₂

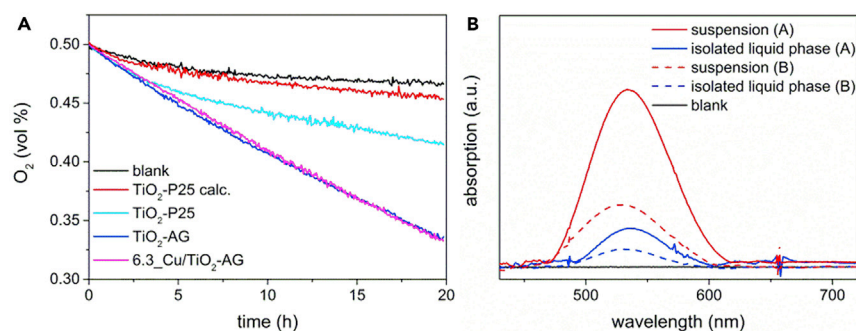


Figure 2. Photoadsorption of O₂ and Formation of Peroxo Species

(A) Following the O₂ concentration during the photocatalytic reduction of 0.5 vol % O₂/CO₂ mixture with Cu/TiO₂-AG and TiO₂-AG.

(B) Colorimetric detection of peroxide after long-term photoreaction under 0.5 vol % O₂/CO₂ (A) and after 20 h photoreaction under pure CO₂ (B). See also Figures S16 and S17.

photocatalysis,^{59,60} we were unable to detect O₂ formation in the gas phase using GC/TCD or an optical O₂ detection set-up (see Section S16). Furthermore, in TAP experiments where ¹³CO formation occurred, no O₂ was detected (Figure S12). As an alternative oxidation product, H₂O₂ could also not be identified by a typical H₂O₂ detection test (conversion of yellow chromate into dark blue chromium(VI) peroxide).⁸¹ Therefore, we concluded the TiO₂-AG material must be involved in the oxidation reaction(s). Notably, the involvement of Cu in a stoichiometric fashion can be excluded because of the small overall amount.

Interestingly, during optical O₂ detection studies in photoreactions with a 0.5 vol % O₂/CO₂ atmosphere, we observed light-induced O₂ uptake instead of evolution (Figure 2A). Studying photoadsorption of O₂ under CO₂ reduction conditions with different TiO₂ materials (Figure 2), we found that TiO₂-P25 (calcined at 500 °C) had the lowest uptake, while regular TiO₂-P25 showed a higher consumption. TiO₂-AG and 6.3_Cu/TiO₂-AG photoadsorbed the largest amount of O₂ and did not show significantly different behavior. It appears that the amount of O₂ consumed during Cu re-oxidation (vide infra) is too small to be detected in this configuration.

This observed trend of O₂ photoadsorption correlated with the number of surface hydroxyl groups on the different materials.⁸² Calcination of TiO₂ lowers the number of surface hydroxyl groups,⁸³ explaining the difference between calcinated and non-calcinated TiO₂-P25. Our TiO₂-AG was synthesized at low temperature (<100 °C), so a larger degree of surface hydroxylation is to be expected. The high surface area obtained should further enhance the total number of surface hydroxyl groups.

Indeed, when analyzing TiO₂-AG and TiO₂-P25 by FTIR spectroscopy (Figure S14), a significantly stronger absorption at 3,300 cm⁻¹ (stretching vibration of OH groups attached to titania)⁸⁴ was observed for TiO₂-AG, indicating a higher number of surface hydroxyl groups. This result was corroborated by XPS analysis: here the O1s peak at around 531.3 eV is assigned to OH groups on the TiO₂ surface.⁸⁵ Comparing TiO₂-AG and TiO₂-P25, it was found that the number of OH groups on the aerogel was around six times higher (rel. area 50% versus rel. area 8.1%, see Figure S15B).

It has been described that reductive photoadsorption of O₂ on TiO₂ can proceed to form (surface-bound) superoxo and peroxo species. Electrons for this process are provided by photooxidation of surface hydroxyl groups.^{82,86–89} Via

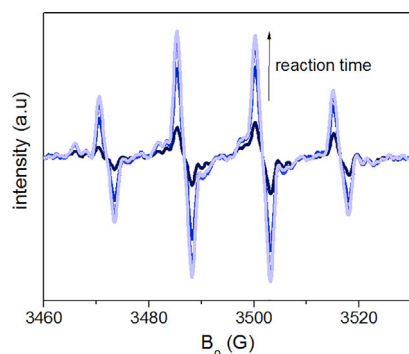


Figure 3. EPR Spectra of TiO₂-AG in CO₂-Saturated H₂O during the Photocatalytic CO₂ Reduction in the Presence of DMPO

See also Figure S13.

intermediate $\cdot\text{OH}$ radicals, this photooxidation has been reported to also result in surface-bound superoxo and peroxy species.^{88,90–92}

To investigate this possibility in our system, we have conducted a long-term photo-reaction (5 d reaction time, 6.3_Cu/TiO₂-AG, 0.5 vol % O₂/CO₂ atmosphere) and compared the number of surface hydroxyl groups before and after via titration (Section S15C).⁹³ Indeed, the number of surface hydroxyl groups was reduced by roughly one-half. Using *in situ* EPR spectroscopy and DMPO as a spin trap,⁹⁴ we detected $\cdot\text{OH}$ radicals during the irradiation of TiO₂-AG, as identified by the characteristic four-line signal at $g = 2.007$ ($a_N \approx a_H = 15.1$ G) due to the DMPO-OH spin adduct formation (Figure 3).⁹⁵ $\cdot\text{OH}$ radicals are presumed to be an intermediate in surface hydroxyl group photooxidation. Finally, analyzing the suspension after the long-term reaction, we detected peroxide via a coloring enzymatic reaction^{91,96} in the suspension, and, to a lesser degree, in the isolated liquid phase (Figures 2B and S17). This difference between the suspension and liquid phase shows that most peroxide species are bound to the TiO₂ surface.

Hence, the consumption of surface hydroxyl groups, detection of $\cdot\text{OH}$ radical intermediates by EPR, and formation of peroxide species after the reaction provide conclusive evidence for reductive O₂ photoadsorption via photooxidation of surface hydroxyl groups. The superior O₂ photoadsorption capability of TiO₂-AG can thus be explained by the higher number of surface hydroxyl groups in this material.

These observations led us to hypothesize that photooxidation of surface hydroxyl groups also provides the electrons for CO₂ and/or proton reduction. After a standard photoreaction with 6.3_Cu/TiO₂-AG under a pure CO₂ atmosphere, we thus applied the same coloring enzymatic reaction for peroxide detection. Indeed, peroxide species were detected in the suspension and to a lesser degree in the isolated liquid phase, again showing that most peroxide species are bound to the TiO₂ surface (Figure 2B). This demonstrates that surface hydroxyl group photooxidation is likely the oxidative process providing electrons for CO₂ and/or proton reduction.

We further investigated this theory via a final long-term experiment with 6.3_Cu/TiO₂-AG using a feed with 0.5 vol % O₂ in CO₂. If surface hydroxyl group photooxidation is indeed responsible for O₂ adsorption and CO₂ and/or proton reduction, O₂ adsorption should level off at some point and the material should lose its ability to reduce CO₂ and/or protons. O₂ adsorption does indeed level off after ca. 5 d (Figure S16), having consumed 0.33 vol % O₂, which corresponds to roughly 10 mol % O₂ with respect to TiO₂-AG. We conclude that O₂ consumption is stoichiometric with respect to the OH-groups of the TiO₂ surface and also that O-vacancies and/or

Ti³⁺ defects are not responsible for the photoadsorption since Ti³⁺ was not detectable using EPR. After the long-term reaction, the material was regenerated with air (vide infra) and again exposed to standard reaction conditions in a 0.5 vol % O₂/CO₂ atmosphere for 20 h. In this case, no CO or H₂ formation was observed; and the O₂ photoadsorption was significantly reduced (Figure S16B). These observations indicate that the material has been stripped of its ability to donate electrons because of the consumption of surface hydroxyl groups via surface oxidation (the fact that some O₂ photoadsorption was still observed can be attributed to a certain degree of reversibility).⁹⁷

Overall, we can conclude that electrons for CO₂ and/or proton reduction, photoadsorption of O₂, and likely also Cu(II) reduction (vide infra) result from photooxidation of surface hydroxyl groups. This oxidation process proceeds via ·OH radical intermediates and results in strongly surface-bound peroxide species, which have been detected colorimetrically. The high activity of TiO₂-AG supported materials in CO₂ and/or proton reduction can be explained by a high number of available surface hydroxyl groups. It is necessary to identify ways to release surface bound peroxides and to regenerate surface hydroxyl group to enable a truly catalytic process with respect to the TiO₂.

Improving Catalyst Activity and Selectivity

In order to check potential leaching of the metal, the 6.3_Cu/TiO₂-AG catalyst and the reaction solution were investigated after 4 h of reaction time. ICP analysis of the filtrate showed no detectable Cu in this phase. Remarkably, the spent Cu catalyst showed a change in color from pale blue to dark gray, although no color change was observed during the investigation of TiO₂-AG without Cu. If Ti³⁺ would have been formed, a light purple dispersion would have appeared. As indicated by *in situ* EPR, XAS, and UV-vis measurements the color change is due to reaction-induced reduction of the Cu(II) species (Figures S18, S20, and S21, section “The Nature of Active Cu Species”). To analyze if these reduced species can be reoxidized, the dark-colored catalyst suspension obtained after 4 h of photoreaction was flushed with air for 30 min. To our delight this treatment led to the original pale blue suspension. Moreover, the catalyst became active again and could be easily re-activated four times (Figure S19A). It is important to note that this oxidation led to a highly selective CO₂ reduction. After the first two runs, only CO was produced through CO₂ reduction and no H₂ was generated despite the aqueous media (Figure S19B). To address the question of the selectivity change and to characterize the Cu species before, during, and after each irradiation (hv) and reoxidation (redox) step, *in situ* XAS measurements were performed (Section S20). The results, shown below, clearly demonstrate that catalyst reoxidation affects its activity in CO formation; a certain degree of oxidation of the Cu species seems to be important for the target reaction. To verify this hypothesis, we performed CO₂ photoreduction tests in the presence of various amounts of O₂ added to the CO₂-containing reaction mixture (Figure 4). Clearly, CO₂ reduction in the presence of O₂ looks irrational at first site because the latter gas is far more easily reduced than the former one (E⁰ CO₂/CO = −0.53 V versus O₂/H₂O = 1.23 V).^{98,99} Moreover, it was shown by Strunk and co-workers that the presence of O₂ inhibits product formation of photocatalytic CO₂ reduction in the presence of TiO₂ (P25).¹⁰⁰ Nevertheless, adding 0.5 vol % O₂ to CO₂ in the presence of our Cu/TiO₂-AG catalyst improved CO formation after 20 h by nearly one order of magnitude. To the best of our knowledge this is the first time that such behavior has been observed. In the presence of O₂, we presume an *in situ* re-oxidation of less reactive Cu(0) species to Cu(II). Interestingly, hydrogen was also formed in this experiment but the ratio of CO/H₂ strongly increased in

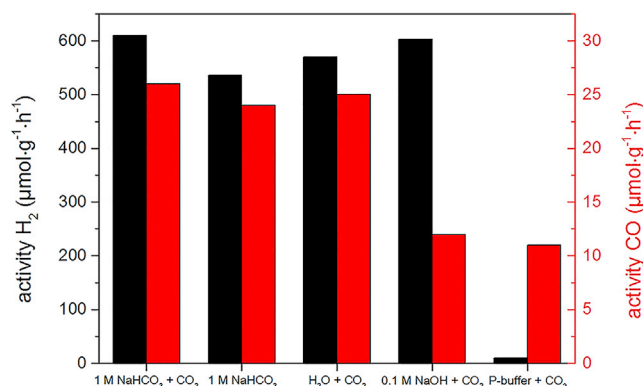


Figure 4. Photocatalytic CO₂ Reduction with 6.3_Cu/TiO₂-AG Catalyst by Using Different CO₂/O₂ Mixtures

Conditions: catalyst: 12.6 mg 6.3_Cu/TiO₂-AG, medium 7.5 mL H₂O, 20°C, 20 h, Lumatec lamp: 2.5 W output, Filter 320–500 nm. See also Table S22.

comparison to the corresponding O₂-free test. Consequently, applying 5 vol % of O₂ led to an excellent CO:H₂ ratio because even traces of hydrogen were not observed. The reason for the change in selectivity might be the re-oxidation of H₂ to H₂O by the addition of O₂. Further increasing the concentration of O₂ led to deactivation of the catalyst. To provide fundamental insights into the effect of O₂ on photocatalytic CO₂ reduction, *in situ* XAS and *operando* UV-vis measurements were performed (vide infra).

In order to show the influence of O₂ on the Cu sites during the reaction and the importance of the TiO₂-AG support, we performed the CO₂ reduction in 0.5 % O₂/CO₂ mixture also with TiO₂-AG and TiO₂-P25 (Table S22). As expected, TiO₂-P25 was also not active in this atmosphere (Table S22, entry 5). In comparison to 6.3_Cu/TiO₂-AG, the material TiO₂-AG was also less active with regard to H₂ and CO generation (Table S22, entry 3). Interestingly, the addition of O₂ not only led to a decrease in H₂ but also in CO generation (Table S22, entries 3 and 4), which is in contrast to the tests with 6.3_Cu/TiO₂-AG (Table S22, entries 1 and 2). This also shows the importance of the Cu co-catalyst and its reactivation for the CO₂ reduction by O₂.

The Nature of Active Cu Species

Operando UV-vis spectroscopy was applied to monitor changes in the oxidation state of Cu after different irradiation times upon CO₂ reduction in the presence and the absence of O₂. Figure 5 shows the UV-vis spectra expressed as the relative Kubelka-Munk function $F_{rel}(R)$ calculated according to Equation 1, while the absorption spectra are given in Figure S21. R_0 and R_i represent the reflectance of the catalyst before irradiation and after certain times of irradiation, respectively.

$$F_{rel}(R) = \frac{\left(1 - \frac{R_i}{R_0}\right)^2}{2 \frac{R_i}{R_0}} \quad (\text{Equation 1})$$

The absorption spectrum of fresh Cu/TiO₂-AG before irradiation (Figure S21A) is characterized by a strong band below 350 nm and by several less defined broad bands between 400 and 900 nm. According to the literature, absorption bands

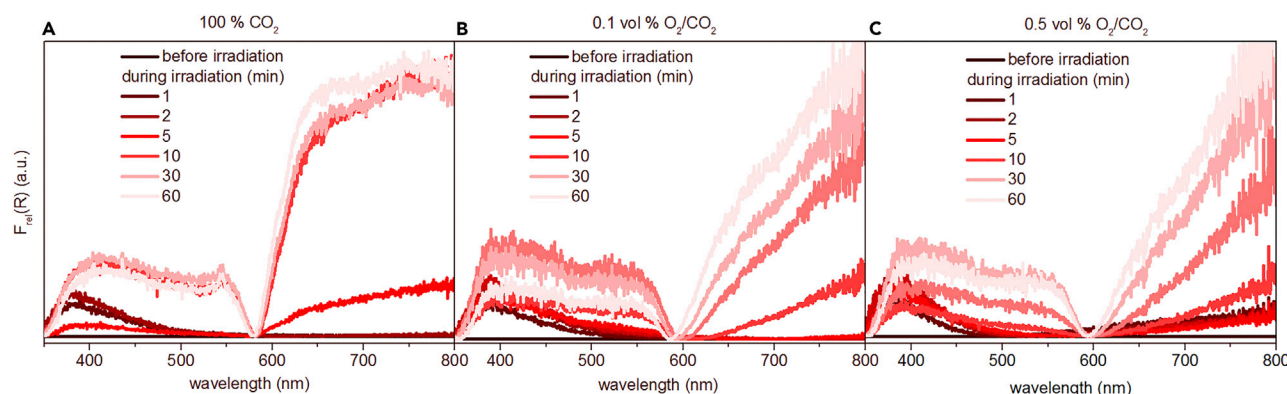


Figure 5. UV-vis Spectra (Relative Kubelka-Munk Calculated According to Equation 1) of Fresh Cu/TiO₂-AG and after Different Irradiation Times in Various Feeds of O₂/CO₂ Mixtures

(A–C) 100% CO₂ (A), 0.1 vol % O₂/CO₂ (B), and 0.5 vol % O₂/CO₂ (C) mixtures. See also Figure S21.

between 600 and 900 nm can be ascribed to transitions between d-d orbitals of Cu(II),^{85,91,96,101} while the bands below 450 nm are ascribed to charge transfer transitions in TiO₂⁹³ and CuO.⁹¹ Thus, Cu(II) is the main species in fresh Cu/TiO₂-AG. This conclusion is in agreement with the results of EPR (Figure S18) and XAS analysis (Figure 6).

For deriving insights into reaction-induced changes of the oxidation state of Cu, we analyzed the UV-vis spectra expressed as $F_{rel}(R)$. Such presentation directly illustrates how the spectrum of fresh Cu/TiO₂-AG changes. As seen in Figure 5A, a band with a maximum of 380 nm appeared after catalyst exposure to light for 1 min in the presence of CO₂ and in the absence of O₂ (Figure 5A). This band can be tentatively assigned to the presence of Cu(I) as concluded from the reference UV-vis spectrum of Cu₂O (Figure S21F).¹⁰¹ Its intensity increased within the first 2 min of irradiation, but decreased after 3 min of irradiation. This band was not apparent after longer catalyst exposure to light, while the intensity of $F_{rel}(R)$ between 350 and 580 nm continuously increased. Moreover, the intensity of $F_{rel}(R)$ above 580 nm also grew. Appearance of a sharp minimum in $F_{rel}(R)$ at around 580 nm can be caused by the formation of metallic Cu. The UV-vis spectrum of metallic Cu is characterized by the absorption edge at 580 nm,^{84,101} which is clearly seen in Figure S21.

When using a feed with a CO₂/O₂ ratio of 1, the absorption edge at 580 nm could hardly be observed, (Figure S21E) thus indicating that Cu(0) was not formed. Cu(I) species were also not identified under these reaction conditions. Thus, Cu(II) was the main oxidation state of copper in Cu/TiO₂-AG upon CO₂ irradiation in the presence of large amounts (33 vol %) of O₂. Importantly, both Cu(0) and Cu(I) species were formed during irradiation when O₂ concentration was lowered to 0.1 or 0.5 vol %. However, the kinetics of Cu(II) reduction and accordingly the fraction of different Cu species are affected by O₂ concentration. From a qualitative point of view, higher O₂ content leads to slower reduction of Cu(II) to Cu(I) and Cu(0) and to a lower Cu(0) fraction. Temporal changes in the UV-vis spectra in Figures 5A–5C suggest Cu(0) species dominate after 10 or 30 min of exposure to light in the absence of O₂ or in the presence of low (0.1 and 0.5 vol %) amounts of O₂.

Furthermore, the oxidation state of Cu was investigated by *in situ* X-ray absorption spectroscopy before, during, and after the reaction. Thereby, the measurements

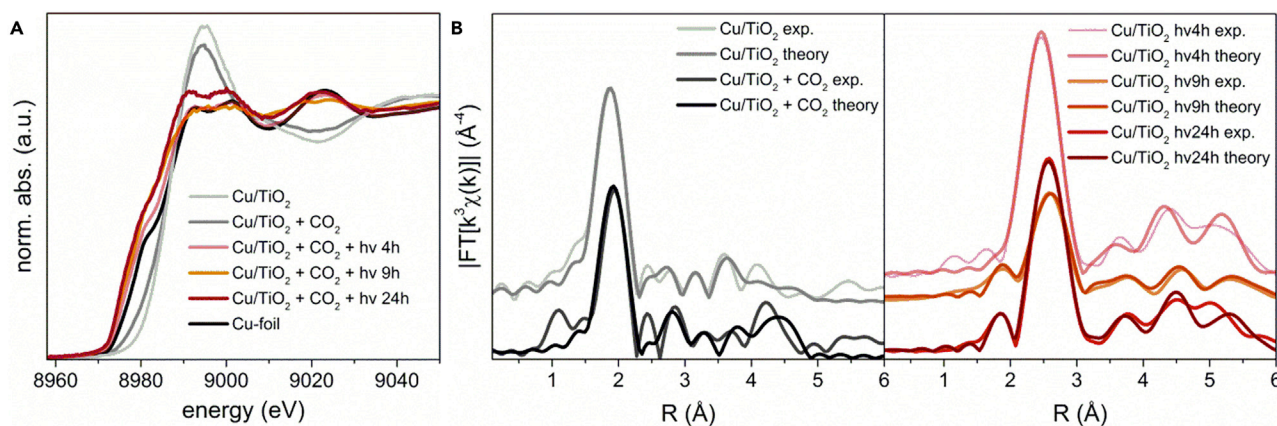


Figure 6. XAS Analysis before and after Various Reaction Times

(A and B) X-ray absorption spectra (A) and Fourier transformed EXAFS spectra (B) of the initial catalyst (6.3_Cu/TiO₂-AG) in a CO₂-saturated aqueous dispersion during illumination after 4 h, 9 h, and 24 h and of a Cu foil as reference. See also Procedure S20.

were carried out using a dedicated cell described in detail in the [Supplemental Information \(Section S20\)](#). XANES (X-ray absorption near edge structure) analysis enables beside the assignment of the oxidation state also the determination of a reference proportion to a certain sample spectrum.^{102,103} Therefore, the spectra of the initial catalyst (6.3_Cu/TiO₂-AG) and of a Cu-foil were applied as references to facilitate an investigation of the reduction degree during the reaction. Analysis of the EXAFS (extended X-ray absorption fine structure) part of an X-ray absorption spectrum allows the identification of neighboring atoms, their number, and their distance to the absorbing atom.¹⁰⁴ With this, the local structure of a Cu atom was determined. XANES analysis showed unambiguously a Cu(II) species with an absorption edge at 8,987.5 eV in the initial substance (Figure 6A). No changes are observed when the suspension is subjected to CO₂ atmosphere. Irradiation caused a reduction of Cu(II) and a Cu(0) species as concluded from the appearance of a signal with an edge energy of 8,979.5 eV. Comparison with a Cu-foil spectrum revealed a similar edge position and white line shape. The spectra of the reaction mixture illuminated for 4 h, 9 h, and 24 h uninterruptedly revealed a similar trend.

To obtain a more detailed insight into the local geometric structure around the Cu centers, thorough analysis of the EXAFS spectra was carried out.¹⁰⁵ The structural parameters obtained are shown in the supplementary information (Table S20B), while the corresponding spectra are given in Figure 6B. In the case of the initial 6.3_Cu/TiO₂-AG catalyst, the typical backscattering and distances of CuO were adjusted.¹⁰⁶ To optimize the fitting error, a Ti shell in a characteristic distance of a Cu-Ti mixed oxide (Cu_{0.25}Ti_{0.75}O₂) was added to the model.¹⁰⁷ Because of the small number of Cu backscatterer and the significant contribution of Ti neighboring atoms, very small Cu oxide particles finely distributed on the titanium oxide support can be deduced, which is in perfect agreement with the results of XRD and TEM analysis.

For the analysis of the spectra measured during the photoinduced reaction, exclusively Cu backscatter in distances similar to metallic Cu were adjusted, since through the LC-XANES fits (Table S20A), metallic Cu was identified as the major component. The high amount of Cu backscatterers and the absence of Ti contributions led to the conclusion that larger metallic Cu-domains are formed during the reaction in comparison to the initial catalyst. Illumination of the sample for 9 h and 24 h led to the

Table 2. Results of CO Formation after 10 min, 30 min, and 20 h in Various O₂/CO₂ Mixtures

Amount of O ₂ in CO ₂ Atmosphere	Amount _{10min} [μmol _{CO} /g _{cat}]	Amount _{30min} [μmol _{CO} /g _{cat}]	Amount _{20h} [μmol _{CO} /g _{cat}]
0 vol %	11.4	14.1	24.7
0.1 vol %	13.8	16.9	30.5
0.5 vol %	8.9	15.5	74.2

formation of even smaller metallic Cu domains, since the number of backscatterers became significantly smaller.

Summarizing the results of UV-vis and XAS tests of CO₂ photoreduction in the absence of added O₂, it can be concluded that during photocatalytic CO₂ reduction over Cu/TiO₂-AG, Cu(II) is initially reduced to Cu(I) followed by further reduction to Cu(0).

Finally, the below discussion is aimed at identifying factors affecting catalyst activity for CO₂ reduction to CO. Table 2 shows the amount of CO formed after 10 min, 30 min, and 20 h using feeds with different O₂/CO₂ ratios. After 10 min of reaction, the highest amount of CO was obtained in the presence of 0.1 vol % O₂, while operating with 0.5 vol % O₂ resulted in the lowest amount. The difference between the feeds became significantly smaller after 30 min of reaction. When irradiating for 20 h, the amount of CO strongly increased in the presence of 0.5 vol % O₂, while the increase in the absence of O₂ or in the presence of 0.1 vol % was significantly lower and only marginally compared to the CO generation after 30 min. These results reveal that the duration of efficient CO₂ reduction to CO depends on the O₂ content. This effect can be explained by considering the changes in the oxidation state of Cu under reaction conditions. Cu(0) is the main species after 30 min of CO₂ reduction without added O₂. In the absence of O₂, as well as in the presence of just 0.1 vol % O₂, the amount of CO formed between 30 min and 20 h is lower than the amount of CO formed between 0 and 30 min. Thus, we conclude that metallic Cu(0) species have low intrinsic activity for the target reaction. Regardless of O₂ content, the highest rate of CO formation was achieved at the beginning of the photocatalytic process, i.e., within the first 30 min. On the basis of the UV-vis spectra, Cu(I) is present during this time and thus can be assigned as an active species for CO₂ photoreduction. This statement is supported by the fact that the rate of Cu(I) reduction to Cu(0) is suppressed in the presence of O₂ thus resulting in stabilization of Cu(I) for longer reaction time. The amount of CO initially increased with rising O₂ content and passed a maximum at 0.5 vol % (Figure 4). According to UV-vis analysis (Figure S21), Cu(II) is not reduced in large amounts to Cu(I) or Cu(0) at higher O₂ concentration. Thus, Cu(I) is proposed to be the active species for CO₂ photoreduction to CO.

In conclusion, the first highly selective photocatalytic reduction of CO₂ to CO in aqueous solution is described. Key to success was the use of a specific Cu(II)-supported TiO₂-AG catalyst system, which shows high activity for CO generation (28.2 μmol·g_{cat}⁻¹·h⁻¹) in UV-A/Vis light (320–500 nm). The rate for CO₂ reduction decreases with time but can be improved when performing the reaction in the presence of O₂. To the best of our knowledge such behavior is observed for the first time and may lead to completely new CO₂ reduction catalysts. UV-vis measurements in the presence of O₂ suggest photogenerated Cu(I) as the active species. Regarding the mechanism, we found that the electrons for CO₂/proton reduction in the active catalyst can be provided by photooxidation of the TiO₂ surface hydroxyl groups. The regeneration of these surface hydroxyl groups has to be solved in the future to develop truly catalytic reductions. This opens up a new research field for

photocatalysis without sacrificial electron donors, which should be addressed in upcoming studies.

SUPPLEMENTAL INFORMATION

Supplemental Information can be found online at <https://doi.org/10.1016/j.chempr.2019.04.006>.

ACKNOWLEDGMENTS

This work has been supported by the BMBF within the project “Kopernikus projects for the Energiewende: P2X concepts” (03SFK2B) and the Danish National Research Foundation within the project “CADIAC.” Financial support by Fonds der Chemischen Industrie (Kekulé-Stipendium n. 102151 for J.S.) is gratefully acknowledged. The authors thank Dr. Rafael daSilva for his contribution in material synthesis and also Dr. S. Bartling, Dr. H. Lund, Dr. C. Kreyenschulte, Dr. J. Radnik, and A. Simmula for their analytical support.

AUTHOR CONTRIBUTIONS

S.K. performed the catalyst synthesis, the analysis of the standard material characteristic data, the experiments for analyzing the surface species, the photocatalytic experiments and the *operando* UV-vis measurements. R.S. and S.K. planned and carried out the XAS experiments. R.S. and M. Bauer designed the used liquid cell and analyzed the related data. J.S. carried out the experiments with the optical oxygen meter set-up for the O₂ detection and performed data analysis and interpretation; designed the experiments for the oxidation half-reaction section together with S.K. and wrote the oxidation half-reaction section. J.R. and S.K. prepared the *in situ* EPR measurements and J.R. evaluated the obtained results. V.A.K. performed the ¹³CO₂ pulse experiments in the temporal analysis of products (TAP) reactor and analyzed together with E.V.K. the experimental data. E.V.K. and S.K. planned UV-vis tests and analyzed the UV-vis data. S.W. was involved in the material development and the interpretation of the analytical results. S.K., S.W., E.V.K., H.J., and M. Beller developed the concept and arranged the whole data for the publication. All authors were involved in the discussion of the results and commented on the manuscript.

DECLARATION OF INTERESTS

The authors declare no competing interests.

Received: August 22, 2018

Revised: September 25, 2018

Accepted: April 12, 2019

Published: May 6, 2019

REFERENCES AND NOTES

1. Asmatulu, E. (2016). Biological Systems for Carbon Dioxide Reductions and Biofuel Production (The Royal Society of Chemistry), pp. 274–293.
2. Becklin, K.M., Walker, S.M., Way, D.A., and Ward, J.K. (2017). CO₂ studies remain key to understanding a future world. *New Phytol.* 214, 34–40.
3. Tu, W., Zhou, Y., and Zou, Z. (2014). Photocatalytic conversion of CO₂ into renewable hydrocarbon fuels: state-of-the-art accomplishment, challenges, and prospects. *Adv. Mater.* 26, 4607–4626.
4. Zhou, H., Yan, R., Zhang, D., and Fan, T. (2016). Challenges and perspectives in designing artificial photosynthetic systems. *Chemistry* 22, 9870–9885.
5. Mikkelsen, M., Jørgensen, M., and Krebs, F.C. (2010). The teraton challenge. A review of fixation and transformation of carbon dioxide. *Energy Environ. Sci.* 3, 43–81.
6. Yuan, L., and Xu, Y.-J. (2015). Photocatalytic conversion of CO₂ into value-added and renewable fuels. *Appl. Surf. Sci.* 342, 154–167.
7. Bosch, C., and Meiser, W. (1922). Process of manufacturing urea. US patent US1429483 A.
8. Glibert, P.M., Harrison, J., Heil, C., and Seitzinger, S. (2006). Escalating worldwide use of urea – a global change contributing to coastal eutrophication. *Biogeochemistry* 77, 441–463.

9. Büttner, H., Longwitz, L., Steinbauer, J., Wulf, C., and Werner, T. (2017). Recent developments in the synthesis of cyclic carbonates from epoxides and CO₂. *Top. Curr. Chem.* 375, 50.
10. Sakakura, T., and Kohno, K. (2009). The synthesis of organic carbonates from carbon dioxide. *Chem. Commun.* 1312–1330.
11. Pescarmona, P.P., and Taherimehr, M. (2012). Challenges in the catalytic synthesis of cyclic and polymeric carbonates from epoxides and CO₂. *Catal. Sci. Technol.* 2, 2169–2187.
12. Mette, K., Kühl, S., Düdder, H., Kähler, K., Tarasov, A., Muhler, M., and Behrens, M. (2014). Stable performance of Ni catalysts in the dry reforming of methane at high temperatures for the efficient conversion of CO₂ into syngas. *ChemCatChem* 6, 100–104.
13. Moret, S., Dyson, P.J., and Laurenczy, G. (2014). Direct synthesis of formic acid from carbon dioxide by hydrogenation in acidic media. *Nat. Commun.* 5.
14. Kondratenko, E.V., Mul, G., Baltrusaitis, J., Larrazábal, G.O., and Pérez-Ramírez, J. (2013). Status and perspectives of CO₂ conversion into fuels and chemicals by catalytic, photocatalytic and electrocatalytic processes. *Energy Environ. Sci.* 6, 3112–3135.
15. Jones, J.-P., Prakash, G.K.S., and Olah, G.A. (2014). Electrochemical CO₂ reduction: recent advances and current trends. *Isr. J. Chem.* 54, 1451–1466.
16. Zhang, L., Zhao, Z.J., and Gong, J. (2017). Nanostructured materials for heterogeneous electrocatalytic CO₂ reduction and their related reaction mechanisms. *Angew. Chem. Int. Ed.* 56, 11326–11353.
17. Habisreutinger, S.N., Schmidt-Mende, L., and Stolarczyk, J.K. (2013). Photocatalytic reduction of CO₂ on TiO₂ and other semiconductors. *Angew. Chem. Int. Ed.* 52, 7372–7408.
18. Nikakavoura, A., and Trapalis, C. (2017). Alternative photocatalysts to TiO₂ for the photocatalytic reduction of CO₂. *Appl. Surf. Sci.* 391, 149–174.
19. León, A., Reuquen, P., Garín, C., Segura, R., Vargas, P., Zapata, P.A., and Orihuela, P. (2017). FTIR and Raman characterization of TiO₂ nanoparticles coated with polyethylene glycol as carrier for 2-methoxyestradiol. *Appl. Sci.* 7, 49.
20. Hou, J., Cheng, H., Takeda, O., and Zhu, H. (2015). Three-dimensional bimetal-graphene-semiconductor coaxial nanowire arrays to harness charge flow for the photochemical reduction of carbon dioxide. *Angew. Chem. Int. Ed.* 54, 8480–8484.
21. Stock, M., and Dunn, S. (2011). LiNbO₃ - A polar material for solid-gas artificial photosynthesis. *Ferroelectrics* 419, 9–13.
22. Rosas-Hernández, A., Alsabeh, P.G., Barsch, E., Junge, H., Ludwig, R., and Beller, M. (2016). Highly active and selective photochemical reduction of CO₂ to CO using molecular-defined cyclopentadienone iron complexes. *Chem. Commun.* 52, 8393–8396.
23. Takeda, H., Ohashi, K., Sekine, A., and Ishitani, O. (2016). Photocatalytic CO₂ reduction using Cu(I) photosensitizers with a Fe(II) catalyst. *J. Am. Chem. Soc.* 138, 4354–4357.
24. Thoi, V.S., Kornienko, N., Margarit, C.G., Yang, P., and Chang, C.J. (2013). Visible-light photoredox catalysis: selective reduction of carbon dioxide to carbon monoxide by a nickel N-heterocyclic carbene–isoquinoline complex. *J. Am. Chem. Soc.* 135, 14413–14424.
25. Guo, Z., Yu, F., Yang, Y., Leung, C.F., Ng, S.M., Ko, C.C., Cometto, C., Lau, T.C., and Robert, M. (2017). Photocatalytic conversion of CO₂ to CO by a copper(II) Quaterpyridine complex. *ChemSusChem* 10, 4009–4013.
26. Takeda, H., Koike, K., Inoue, H., and Ishitani, O. (2008). Development of an efficient photocatalytic system for CO₂ reduction using rhenium(I) complexes based on mechanistic studies. *J. Am. Chem. Soc.* 130, 2023–2031.
27. Rosas-Hernández, A., Junge, H., and Beller, M. (2015). Photochemical reduction of carbon dioxide to formic acid using ruthenium(II)-based catalysts and visible light. *ChemCatChem* 7, 3316–3321.
28. Liu, B.-J., Torimoto, T., and Yoneyama, H. (1998). Photocatalytic reduction of CO₂ using surface-modified CdS photocatalysts in organic solvents. *J. Photochem. Photobiol. A* 113, 93–97.
29. Kanemoto, M., Ishihara, K., Wada, Y., Sakata, T., Mori, H., and Yanagida, S. (1992). Visible-light induced effective photoreduction of CO₂ to CO catalyzed by colloidal CdS microcrystallites. *Chem. Lett.* 21, 835–836.
30. Sayama, K., and Arakawa, H. (1993). Photocatalytic decomposition of water and photocatalytic reduction of carbon dioxide over zirconia catalyst. *J. Phys. Chem.* 97, 531–533.
31. Park, H.-A., Choi, J.H., Choi, K.M., Lee, D.K., and Kang, J.K. (2012). Highly porous gallium oxide with a high CO₂ affinity for the photocatalytic conversion of carbon dioxide into methane. *J. Mater. Chem.* 22, 5304–5307.
32. Yang, M.-Q., and Xu, Y.-J. (2016). Photocatalytic conversion of CO₂ over graphene-based composites: current status and future perspective. *Nanoscale Horiz.* 1, 185–200.
33. Li, K., Peng, B., and Peng, T. (2016). Recent advances in heterogeneous photocatalytic CO₂ conversion to solar fuels. *ACS Catal.* 6, 7485–7527.
34. Ulagappan, N., and Frei, H. (2000). Mechanistic study of CO₂ photoreduction in Ti silicalite molecular sieve by FT-IR spectroscopy. *J. Phys. Chem. A* 104, 7834–7839.
35. Bahnemann, D.W., Hilgendorff, M., and Memming, R. (1997). Charge carrier dynamics at TiO₂ particles: reactivity of free and trapped holes. *J. Phys. Chem. B* 101, 4265–4275.
36. Liu, S., Zhao, Z., and Wang, Z. (2007). Photocatalytic reduction of carbon dioxide using sol-gel derived titania-supported CoPc catalysts. *Photochem. Photobiol. Sci.* 6, 695–700.
37. Handoko, A.D., and Tang, J. (2013). Controllable proton and CO₂ photoreduction over Cu₂O with various morphologies. *Int. J. Hydr. Energ.* 38, 13017–13022.
38. Sasirekha, N., Basha, S.J.S., and Shanthi, K. (2006). Photocatalytic performance of Ru doped anatase mounted on silica for reduction of carbon dioxide. *Appl. Catal. B* 62, 169–180.
39. Yamamoto, M., Yoshida, T., Yamamoto, N., Nomoto, T., Yamamoto, Y., Yagi, S., and Yoshida, H. (2015). Photocatalytic reduction of CO₂ with water promoted by Ag clusters in Ag/Ga₂O₃ photocatalysts. *J. Mater. Chem. A* 3, 16810–16816.
40. Núñez, J., de la Peña O'Shea, V.A., Jana, P., Coronado, J.M., and Serrano, D.P. (2013). Effect of copper on the performance of ZnO and ZnO_{1-x}N_x oxides as CO₂ photoreduction catalysts. *Catal. Today* 209, 21–27.
41. Zhou, H., Li, P., Guo, J., Yan, R., Fan, T., Zhang, D., and Ye, J. (2015). Artificial photosynthesis on tree trunk derived alkaline tantalates with hierarchical anatomy: towards CO₂ photo-fixation into CO and CH₄. *Nanoscale* 7, 113–120.
42. Li, K., Handoko, A.D., Khraisheh, M., and Tang, J. (2014). Photocatalytic reduction of CO₂ and protons using water as an electron donor over potassium tantalate nanoflakes. *Nanoscale* 6, 9767–9773.
43. Fujishima, A., and Honda, K. (1972). Electrochemical photolysis of water at a semiconductor electrode. *Nature* 238, 37–38.
44. Schneider, J., Matsuoka, M., Takeuchi, M., Zhang, J., Horiuchi, Y., Anpo, M., and Bahnemann, D.W. (2014). Understanding TiO₂ photocatalysis: mechanisms and materials. *Chem. Rev.* 114, 9919–9986.
45. Li, X., Yu, J., and Jaroniec, M. (2016). Hierarchical photocatalysts. *Chem. Soc. Rev.* 45, 2603–2636.
46. Yamakata, A., Vequizo, J.J.M., and Matsunaga, H. (2015). Distinctive behavior of photogenerated electrons and holes in anatase and rutile TiO₂ powders. *J. Phys. Chem. C* 119, 24538–24545.
47. Xiong, Z., Wang, H., Xu, N., Li, H., Fang, B., Zhao, Y., Zhang, J., and Zheng, C. (2015). Photocatalytic reduction of CO₂ on Pt²⁺-Pt⁰/TiO₂ nanoparticles under UV/vis light irradiation: a combination of Pt²⁺ doping and Pt nanoparticles deposition. *Int. J. Hydr. Energ.* 40, 10049–10062.
48. Li, K., Peng, T., Ying, Z., Song, S., and Zhang, J. (2016). Ag-loading on brookite TiO₂ quasi nanocubes with exposed {210} and {001} facets: activity and selectivity of CO₂ photoreduction to CO/CH₄. *Appl. Catal. B* 180, 130–138.
49. Rossetti, I., Villa, A., Compagnoni, M., Prati, L., Ramis, G., Pirola, C., Bianchi, C.L., Wang, W., and Wang, D. (2015). CO₂ photoconversion to fuels under high pressure: effect of TiO₂ phase and of unconventional reaction conditions. *Catal. Sci. Technol.* 5, 4481–4487.

50. Collado, L., Reynal, A., Coronado, J.M., Serrano, D.P., Durrant, J.R., and de la Peña O'Shea, V.A. (2015). Effect of Au surface plasmon nanoparticles on the selective CO₂ photoreduction to CH₄. *Appl. Catal. B* 178, 177–185.
51. Vaiano, V., Sannino, D., and Ciambelli, P. (2015). Steam reduction of CO₂ on Pd/TiO₂ catalysts: a comparison between thermal and photocatalytic reactions. *Photochem. Photobiol. Sci.* 14, 550–555.
52. Aguirre, M.E., Zhou, R., Eugene, A.J., Guzman, M.I., and Grela, M.A. (2017). Cu₂O/TiO₂ heterostructures for CO₂ reduction through a direct Z-scheme: Protecting Cu₂O from photocorrosion. *Appl. Catal. B* 217, 485–493.
53. Zhang, T., Low, J., Huang, X., Al-Sharab, J.F., Yu, J., and Asefa, T. (2017). Copper-decorated micro-sized nanoporous titanium dioxide photocatalysts for carbon dioxide reduction by water. *ChemCatChem* 9, 3054–3062.
54. Liu, L., Zhao, C., Miller, J.T., and Li, Y. (2017). Mechanistic study of CO₂ photoreduction with H₂O on Cu/TiO₂ nanocomposites by in situ X-ray absorption and infrared spectroscopies. *J. Phys. Chem. C* 121, 490–499.
55. Fang, B., Xing, Y., Bonakdarpour, A., Zhang, S., and Wilkinson, D.P. (2015). Hierarchical CuO–TiO₂ hollow microspheres for highly efficient photodriven reduction of CO₂ to CH₄. *ACS Sustain. Chem. Eng.* 3, 2381–2388.
56. Gonell, F., Puga, A.V., Julián-López, B., García, H., and Corma, A. (2016). Copper-doped titania photocatalysts for simultaneous reduction of CO₂ and production of H₂ from aqueous sulfide. *Appl. Catal. B* 180, 263–270.
57. Jeong, S., Kim, W.D., Lee, S., Lee, K., Lee, S., Lee, D., and Lee, D.C. (2016). Bi₂O₃ as a promoter for Cu/TiO₂ photocatalysts for the selective conversion of carbon dioxide into methane. *ChemCatChem* 8, 1641–1645.
58. Li, Y., Wang, W.-N., Zhan, Z., Woo, M.-H., Wu, C.-Y., and Biswas, P. (2010). Photocatalytic reduction of CO₂ with H₂O on mesoporous silica supported Cu/TiO₂ catalysts. *Appl. Catal. B* 100, 386–392.
59. Liu, L., Gao, F., Zhao, H., and Li, Y. (2013). Tailoring Cu valence and oxygen vacancy in Cu/TiO₂ catalysts for enhanced CO₂ photoreduction efficiency. *Appl. Catal. B* 134–135, 349–358.
60. Slamet, Nasution, H., Purnama, E., Riyani, K., and Gunlazuardi, J. (2009). Effect of copper species in a photocatalytic synthesis of methanol from carbon dioxide over copper-doped titania catalysts world appl. Sci. J. 6, 112–122.
61. Nasution, H., Purnama, E., Kosela, S., and Gunlazuardi, J. (2005). Photocatalytic reduction of CO₂ on copper-doped Titania catalysts prepared by improved-impregnation method. *Catal. Commun.* 6, 313–319.
62. Tseng, I.H., and Wu, J.C.-S. (2004). Chemical states of metal-loaded titania in the photoreduction of CO₂. *Catal. Today* 97, 113–119.
63. Tseng, I.H., Wu, J.C.S., and Chou, H.-Y. (2004). Effects of sol–gel procedures on the photocatalysis of Cu/TiO₂ in CO₂ photoreduction. *J. Catal.* 221, 432–440.
64. Zhang, Q., Gao, T., Andino, J.M., and Li, Y. (2012). Copper and iodine co-modified TiO₂ nanoparticles for improved activity of CO₂ photoreduction with water vapor. *Appl. Catal. B* 123–124, 257–264.
65. Singhal, N., Ali, A., Vorontsov, A., Pendem, C., and Kumar, U. (2016). Efficient approach for simultaneous CO and H₂ production via photoreduction of CO₂ with water over copper nanoparticles loaded TiO₂. *Appl. Catal. A* 523, 107–117.
66. Do, J.Y., Im, Y., Kwak, B.S., Kim, J.-Y., and Kang, M. (2015). Dramatic CO₂ photoreduction with H₂O vapors for CH₄ production using the TiO₂/Fe–TiO₂ double-layered films. *Chem. Eng. J.* 275, 288–297.
67. Kwak, B.S., Vignesh, K., Park, N.-K., Ryu, H.-J., Baek, J.-I., and Kang, M. (2015). Methane formation from photoreduction of CO₂ with water using TiO₂ including Ni ingredient. *Fuel* 143, 570–576.
68. Zhygotsky, A., Rynda, E., Kochkodan, V., Zagorny, M., Lobunets, T., Kuzmenko, L., and Ragulya, A. (2013). Effect of dispersity and porous structure of TiO₂ nanopowders on photocatalytic destruction of azo dyes in aqueous solutions. *J. Chem. Chem. Eng.* 7, 949–957.
69. Gesser, H.D., and Goswami, P.C. (1989). Aerogels and related porous materials. *Chem. Rev.* 89, 765–788.
70. Pajonk, G.M. (1991). Aerogel catalysts. *Appl. Catal.* 72, 217–266.
71. Pietron, J.J., Stroud, R.M., and Rolison, D.R. (2002). Using three dimensions in catalytic mesoporous nanoarchitectures. *Nano Lett.* 2, 545–549.
72. Puskelova, J., Baia, L., Vulpoi, A., Baia, M., Antoniadou, M., Dracopoulos, V., Stathatos, E., Gabor, K., Pap, Z., Danciu, V., et al. (2014). Photocatalytic hydrogen production using TiO₂–Pt aerogels. *Chem. Eng. J.* 242, 96–101.
73. da Silva, R.O., Heiligt, F.J., Karnahl, M., Junge, H., Niederberger, M., and Wohlrab, S. (2015). Design of multicomponent aerogels and their performance in photocatalytic hydrogen production. *Catal. Today* 246, 101–107.
74. Heiligt, F.J., Rossell, M.D., Süess, M.J., and Niederberger, M. (2011). Template-free co-assembly of preformed Au and TiO₂ nanoparticles into multicomponent 3D aerogels. *J. Mater. Chem.* 21, 16893–16899.
75. Heiligt, F.J., Kränzlin, N., Süess, M.J., and Niederberger, M. (2014). Anatase–silica composite aerogels: a nanoparticle-based approach. *J. Solgel Sci. Technol.* 70, 300–306.
76. Ghijsen, J., Tjeng, L.H., van Elp, J., Eskes, H., Westerink, J., Sawatzky, G.A., and Czyzyk, M.T. (1988). Electronic structure of Cu₂O and CuO. *Phys. Rev. B* 38, 11322–11330.
77. Perez-Ramirez, J., and Kondratenko, E.V. (2007). Evolution, achievements, and perspectives of the TAP technique. *Catal. Today* 121, 160–169.
78. Morgan, K., Maguire, N., Fushimi, R., Gleaves, J.T., Goguet, A., Harold, M.P., Kondratenko, E.V., Menon, U., Schuurman, Y., and Yablonsky, G.S. (2017). Forty years of temporal analysis of products. *Catal. Sci. Technol.* 7, 2416–2439.
79. Gleaves, J.T., Yablonsky, G., Zheng, X., Fushimi, R., and Mills, P.L. (2010). Temporal analysis of products (TAP)—recent advances in technology for kinetic analysis of multi-component catalysts. *J. Mol. Catal. A* 315, 108–134.
80. Gleaves, J.T., Yablonskii, G.S., Phanawadee, P., and Schuurman, Y. (1997). TAP-2: an interrogative kinetics approach. *Appl. Catal. A* 160, 55–88.
81. Buchera, G., Kampe, M., and Roelcke, J.F. (2005). Peroxides and chromium compounds - The ether test for identity. *Z. Naturforsch. B.* 60, 1–6.
82. Boonstra, A.H., and Mutsaers, C.A.H.A. (1975). Relation between the photoadsorption of oxygen and the number of hydroxyl groups on a titanium dioxide surface. *J. Phys. Chem.* 79, 1694–1698.
83. Yu, J.C., Lin, J., Lo, D., and Lam, S.K. (2000). Influence of thermal treatment on the adsorption of oxygen and photocatalytic activity of TiO₂. *Langmuir* 16, 7304–7308.
84. Lv, K., Zuo, H., Sun, J., Deng, K., Liu, S., Li, X., and Wang, D. (2009). (Bi, C and N) codoped TiO₂ nanoparticles. *J. Hazard. Mater.* 161, 396–401.
85. Bharti, B., Kumar, S., Lee, H.N., and Kumar, R. (2016). Formation of oxygen vacancies and Ti³⁺ state in TiO₂ thin film and enhanced optical properties by air plasma treatment. *Sci. Rep.* 6, 32355.
86. Harbour, J.R., Tromp, J., and Hair, M.L. (1985). Photogeneration hydrogen peroxide aqueous TiO₂ dispersions. *Can. J. Chem.* 63, 204–208.
87. González-Elipe, A.R., Soria, J., and Munuera, G. (1978). EPR study of oxygen adsorption on X-ray irradiated anatase. *Chem. Phys. Lett.* 57, 265–268.
88. Munuera, G., Gonzalez-Elipe, A.R., Soria, J., and Sanz, J. (1980). Photo-adsorption and photo-desorption of oxygen on highly hydroxylated TiO₂ surfaces. part 3. Role of H₂O₂ in photo-desorption of O₂. *J. Chem. Soc. Farad. Trans.* 1 76, 1535–1546.
89. Berger, T., Sterrer, M., Diwald, O., and Knözinger, E. (2005). Charge trapping and photoadsorption of O₂ on dehydroxylated TiO₂ nanocrystals—An electron paramagnetic resonance study. *ChemPhysChem* 6, 2104–2112.
90. Jaeger, C.D., and Bard, A.J. (1979). Spin trapping and electron spin resonance detection of radical intermediates in the photodecomposition of water at titanium dioxide particulate systems. *J. Phys. Chem.* 83, 3146–3152.
91. Daskalaki, V.M., Panagiotopoulou, P., and Kondarides, D.I. (2011). Production of

- peroxide species in Pt/TiO₂ suspensions under conditions of photocatalytic water splitting and glycerol photoreforming. *Chem. Eng. J.* **170**, 433–439.
92. Kiwi, J., and Graetzel, M. (1987). Specific analysis of surface-bound peroxides formed during photoinduced water cleavage in titanium dioxide-based microheterogeneous systems. *J. Mol. Catal.* **39**, 63–70.
93. Oosawa, Y., and Grätzel, M. (1988). Effect of surface hydroxyl density on photocatalytic oxygen generation in aqueous TiO₂ suspensions. *J. Chem. Soc. Faraday Trans. 1* **84**, 197–205.
94. Rosen, G.M., and Rauckman, E.J. (1984). Spin trapping of superoxide and hydroxyl radicals. *Methods Enzymol.* **105**, 198–209.
95. Makino, K., Hagiwara, T., and Murakami, A. (1991). A mini review: fundamental aspects of spin trapping with DMPO. *Radiat. Phys. Chem.* **37**, 657–665.
96. Shiraishi, F., Nakasako, T., and Hua, Z. (2003). Formation of hydrogen peroxide in photocatalytic reactions. *J. Phys. Chem. A* **107**, 11072–11081.
97. Stradella, L. (1984). Energetics of the adsorption-desorption cycles of oxygen on a titania-based catalyst. *J. Mol. Catal.* **26**, 105–115.
98. Bratsch, S.G. (1989). Standard electrode potentials and temperature coefficients in water at 298.15 K. *J. Phys. Chem. Ref. Data* **18**, 1–21.
99. Jitaru, M. (2007). Electrochemical carbon dioxide reduction - Fundamental and applied topics. *J. Univ. Chem. Technol. Metall.* **42**, 333–344.
100. Dilla, M., Schlögl, R., and Strunk, J. (2017). Photocatalytic CO₂ reduction under continuous flow high-purity conditions: quantitative evaluation of CH₄ formation in the steady-state. *ChemCatChem* **9**, 696–704.
101. Praliaud, H., Mikhailenko, S., Chajar, Z., and Primet, M. (1998). Surface and bulk properties of Cu-ZSM-5 and Cu/Al₂O₃ solids during redox treatments. Correlation with the selective reduction of nitric oxide by hydrocarbons. *Appl. Catal. B* **16**, 359–374.
102. Gotthardt, M.A., Schoch, R., Wolf, S., Bauer, M., and Kleist, W. (2015). Synthesis and characterization of bimetallic metal-organic framework Cu-Ru-BTC with HKUST-1 structure. *Dalton Trans.* **44**, 2052–2056.
103. Kau, L.S., Hodgson, K.O., and Solomon, E.I. (1989). X-ray absorption edge and EXAFS study of the copper sites in zinc oxide methanol synthesis catalysts. *J. Am. Chem. Soc.* **111**, 7103–7109.
104. Ene, A.B., Bauer, M., Archipov, T., and Roduner, E. (2010). Adsorption of oxygen on copper in Cu/HZSM5 zeolites. *Phys. Chem. Chem. Phys.* **12**, 6520–6531.
105. Okemoto, A., Ueyama, K., Taniya, K., Ichihashi, Y., and Nishiyama, S. (2017). Direct oxidation of benzene with molecular oxygen in liquid phase catalysed by heterogeneous copper complexes encapsulated in Y-Type zeolite. *Catal. Commun.* **100**, 29–32.
106. Yamada, H., Soejima, Y., Zheng, X.G., and Kawaminami, M. (2000). Structural study of CuO at low temperatures. *Trans. Mat. Res. Soc. Japan* **25**, 1199–1202.
107. Xueping, H., Zhanchang, P., Xiao, Z., Chumin, X., Shirong, C., Yu, X., and Zhigang, W. (2009). First-principles studies of Cu(II) doped anatase titanium dioxide. *J. Mater. Sci. Eng.* **27**, 613–616.

Supporting Information

Improving Selectivity and Activity of CO₂ Reduction Photocatalysts with Oxygen

Stefanie Kreft,¹ Roland Schoch,² Jacob Schneidewind,¹ Jabor Rabeah,¹ Evgenii V. Kondratenko,^{1,} Vita A. Kondratenko,¹ Henrik Junge,¹ Matthias Bauer,² Sebastian Wohlrab,¹ and Matthias Beller^{1,*}*

¹Leibniz-Institut für Katalyse an der Universität Rostock e.V., Albert-Einstein-Straße 29a, 18059 Rostock (Germany)

²Universität Paderborn, Department Chemie, Warburger Str. 100, 33098 Paderborn (Germany)

*Correspondence: matthias.beller@catalysis.de

Table of Contents

S1: Results for aqueous CO ₂ reduction known from literature	2
S2: Synthesis of Cu/TiO ₂ -AG	2
S3: Synthesis of Cu/TiO ₂ -P25	3
S4: Procedure of photocatalytic aqueous CO ₂ reduction and product calculation	3
S5: Methods for the material characterization	4
S6: Pore size distribution (BJH) of TiO ₂ -AG	5
S7: XRD patterns of TiO ₂ -AG and Cu/TiO ₂ -AG	5
S8: TEM images of TiO ₂ -AG	5
S9: TEM images of 6.3_Cu/TiO ₂ -AG	6
S10: XPS images of 6.3_Cu/TiO ₂ -AG and 0.3_Cu/TiO ₂ -AG	7
S11: Influence of different aqueous media for the photocatalytic CO ₂ reduction	8
S12: Effect of catalyst composition on ¹³ CO formation from ¹³ CO ₂	9
S13: EPR measurement regarding the generation of ·OH and ·CO ₂ · radicals	9
S14: Analysis of hydroxyl groups on TiO ₂ -AG and TiO ₂ -P25 via FT-IR spectroscopy	10
S15: XPS analysis of hydroxyl groups on TiO ₂ -AG and TiO ₂ -P25, procedure of titration experiments	10
S16: Oxygen detection using an optical oxygen sensor and long-term experiment	11
S17: Analysis of peroxo species on the TiO ₂ -AG surface	12
S18: <i>In situ</i> EPR measurement of 6.3_Cu/TiO ₂ -AG regarding the copper species	12
S19: Recycling experiments with 6.3_Cu/TiO ₂ -AG	13
S20: X-ray absorption spectroscopy	13
S21: UV-vis measurements in various O ₂ /CO ₂ mixtures	17
S22: Photocatalytic CO ₂ reduction with TiO ₂ -AG and TiO ₂ -P25 in various O ₂ /CO ₂ mixtures	18

S1: Results of various studies for aqueous CO₂ reduction with Cu/TiO₂ catalysts.

System	Media	Irradiation	Main product	Activity [$\mu\text{mol}\cdot\text{g}^{-1}\cdot\text{h}^{-1}$]	Conditions	Comment	Ref. in manuscript
Cu₂O/TiO₂ (0.95:0.05)	CO ₂ /H ₂ O	305-665 nm	CO	2.1	Flow, 20 °C	OH radicals, no chance of Cu(I) during reaction	50 ¹
0.4 % Cu(0)/TiO₂	NaHCO ₃ /H ₂ SO ₄	Xe lamp without filter	CH ₄	8	Batch	25 °C, 1 atm	51 ²
1% Cu₂O/TiO₂	CO ₂ /H ₂ O	< 390 nm	CO CH ₄	7.5 0.4	Flow, 150 °C, 1 atm		52 ³
3% CuO/TiO₂	H ₂ O/CO ₂	254 nm	CO CH ₄ H ₂	14.5 2.1 2.7	Batch, temp. not given	Cu ₂ O/TiO ₂ 28% higher CH ₄ generation	53 ⁴
1% Cu₂O/TiO₂	CO ₂ /H ₂ O	320-780 nm	CH ₄ CO	1 10	Flow, 25 °C, 1 atm		54 ⁵
0.5% Cu₂O/TiO₂-SiO₂	CO ₂ /H ₂ O	250-400 nm	CO CH ₄	60 10	flow	T not given	55 ⁶
1% Cu/TiO₂	CO ₂ /H ₂ O	200-1000 nm	CO CH ₄	3.8 0.7	flow	Mixture of Cu(0) and Cu(I)	56 ⁷
3% CuO/TiO₂	1 M KHCO ₃	UV	CH ₃ OH	450	Batch	60 °C	57, 58 ⁸
2% Cu₂O/TiO₂	0.2 N NaOH	254 nm	CH ₃ OH	20	Batch	50 °C	59,60 ^{9,10}
1% Cu₂O/TiO₂	CO ₂ /H ₂ O	400 nm	CO	2.0	flow	Addition of I-, traces of CH ₄	61 ¹¹
0.1% Cu₂O/TiO₂	CO ₂ /H ₂ O	254 nm	CO	3.4	flow	Addition of I-, traces of CH ₄	61 ¹¹
1% Cu₂O/TiO₂	CO ₂ /H ₂ O	254 nm	CO H ₂	334 452	flow		62 ¹²
1% Cu₂O/TiO₂	CO ₂ /H ₂ O	350 nm	CO H ₂	50 70	flow		62 ¹²

S2: Synthesis of Cu/TiO₂-AG

Synthesis of trizma-functionalized TiO₂¹³: 6.49 mmol (786 mg) 2-amino-2-(hydroxymethyl)-1,3-propanediol (trizma, >99 %, Sigma Aldrich), was dissolved in 170 ml benzyl alcohol (99 %, Alfa Aesar) by heating to 50 °C for 30 min. After cooling to room temperature 77.5 mmol (8.5 ml) TiCl₄ 99.9 %, Sigma Aldrich) was added dropwise under stirring in Ar atmosphere. The reaction solution was stirred for 24 h at 80 °C. Afterwards, the solution was cooled to room temperature and the obtained anatase nanoparticles were separated from the solvent by centrifugation. The yellowish supernatant was decanted away; the white precipitate was washed with chloroform (99 %, Acros), re-dispersed in chloroform and centrifuged again. These steps were repeated at least three times. Finally, the precipitate was dried in ambient air.

Synthesis of CuO nanoparticles: 1.2 g Cu(OAc)₂·H₂O (99.9 %, Acros) were dissolved in 900 ml distilled H₂O. 3 ml acetic acid (>99 %, Walter CMP) were added under stirring and heated under reflux. Afterwards, the addition of 2.4 g NaOH (>99 %, Baker) led to black precipitate (pH-value of 6-7) which was centrifuged and washed one time with water and three times with ethanol. Finally, the drying step was carried out under ambient conditions.

Preparation of particle mixtures and gelation of the nanoparticle dispersion: For the preparation of a mixture of CuO and TiO₂ nanoparticles (material: 6.3_Cu/TiO₂-AG), 100 mg of the CuO nanoparticles were dispersed in 8.5 ml distilled water. Furthermore, 1 g trizma-functionalized TiO₂ was added under vigorous stirring. After pouring the dispersions in a Teflon container, the container was sealed and the gelation was induced by heating to 90 °C for 30 min in an oven. The final gels can be removed from the container after cooling to room temperature. For the material 0.3_Cu/TiO₂-AG 10 mg CuO-NP were used.

Supercritical drying: The liquid water in the pores of the gels was stepwise exchanged by acetone for 24 h respectively, in steps of: 30 vol%, 50 vol%, 75 vol%, 90 vol%, and 100 vol% acetone/H₂O mixtures. CO₂ supercritical drying was performed in a 50 ml autoclave. The obtained gels were transferred in the autoclave filled with acetone. At first the chamber was pre-cooled to 5 °C and purged with liquid CO₂. Then the sample was left to soak in CO₂ for 30 minutes and after this period the gas was released and another purging step was repeated (in general this procedure was performed for 8-10 h by checking with a filter paper at the outlet of exhaust of the equipment for damp patch indicating solvent exchange conditions).

After the solvent exchange was completed the autoclave was heated to at least 40 °C reaching a pressure of >80 bar. Normally, the supercritical drying condition is achieved at around 31 °C and 74 bar. Finally, the gas was released slowly and the aerogel was obtained.

S3: Synthesis of 0.5_Cu/TiO₂-P25

1 g of commercial available TiO₂ (P25, Evonik) was used as received and impregnated with 0.5 ml of 1.66 M aqueous Cu(NO₃)₂ (>99 %, Sigma Aldrich) to achieve complete incipient wetness impregnation. After drying at 80 °C for 3 h, the material was calcined at 400 °C at a heating ramp of 5 K/min for 2 h under air (0.5_Cu/TiO₂-P25). The amount of copper was analysed by ICE-OES.

S4: Photocatalytic reduction of aqueous CO₂

A double-walled temperature-controlled 85-mL reaction vessel was evacuated and refilled with Ar three times followed by an additional three cycles using CO₂ (purity 4.8, Linde) or O₂/CO₂ mixture. In general, 12.6 mg catalysts and 7.5 mL of doubly distilled water were then added. Prior to irradiation, the reaction mixture was bubbled with CO₂ (or O₂/CO₂ mixture) for 60 min. The temperature was maintained at 20 °C using a thermostat. The solution was irradiated through a plain borosilicate-glass wall in the reaction vessel using a Hg-lamp (Lumatec Superlite 400, output 2.5 W), equipped with a 320-500 nm filter. The gaseous reaction products were analyzed using a calibrated GC and the liquid phase was analyzed by the use of HPLC and capillary electrophoresis techniques.

Gas content was determined by gas-phase GC. A GC sample was taken from the reaction system and was analyzed by the following system:

GC: Carboxen / TCD / Methanizer / FID - permanent gases, He carrier gas.

The gas integration was calibrated using certified gas mixtures from commercial suppliers (Linde and Air Liquide) with the following gas vol%:

H₂: 2500 ppm, 5000 ppm, 1 %, 5 %

CO: 1 ppm, 10 ppm, 75 ppm, 250 ppm, 1 %, 5 %

CH₄: 10 ppm, 75 ppm, 250 ppm, 1%, 5 %

CO₂: 10 ppm, 75 ppm, 250 ppm, 1%, 5 %, 10 %, 25 %, 50 %, 100 %

The system allows for the determination of H₂, Ar, CH₄, CO and CO₂ within the ranges:

H₂ ≥ 0.25 vol% - 100 vol%

CO ≥ 1 ppm

CH₄ ≥ 1 ppm

CO₂ ≥ 1 ppm - 100 vol%

GC analysis provides the relative composition of the different components of the collected gas. H₂, CO and CO₂ amounts were determined and their ratios established.

Calculation of gas production rate

The gas production rate was calculated by equation (S1):

$$\text{Gas production rate} = \frac{n_{\text{gas}}}{m_{\text{cat}} \times t} \quad (\text{S1})$$

where n_{gas} was calculated by the quotient of the related gas volume measured in the catalytic reaction and the related molar volume (S2):

$$n_{\text{gas}} = \frac{V_{\text{gas}}}{V_{m,\text{gas}}} \quad (\text{S2})$$

The calculation of $V_{m,\text{H}_2,20^\circ\text{C}}$ was carried out using the Van der Waals equation (equation (S3)):

$$V_{m,\text{H}_2,20^\circ\text{C}} = \frac{RT}{p} + b - \frac{a}{RT} = 24.07 \frac{\text{L}}{\text{mol}} \quad (\text{S3})$$

Where:

R: 8.3145 m³·Pa·mol⁻¹·K⁻¹;

T: 293.15 K;
P: 101325 Pa;
a: $24.7 \cdot 10^{-3} \text{ Pa} \cdot \text{m}^6 \cdot \text{mol}^{-2}$;
b: $26.6 \cdot 10^{-6} \text{ m}^3 \cdot \text{mol}^{-1}$

The calculation of $V_{m,CO,20^\circ C}$ was carried out using the Van der Waals equation (equation (S4)):

$$V_{m,CO,20^\circ C} = \frac{RT}{p} + b - \frac{a}{RT} = 24.03 \frac{L}{mol} \quad (S4)$$

Where:

R: $8.3145 \text{ m}^3 \cdot \text{Pa} \cdot \text{mol}^{-1} \cdot \text{K}^{-1}$;
T: 293.15 K;
P: 101325 Pa;
a: $14.6 \cdot 10^{-2} \text{ Pa} \cdot \text{m}^6 \cdot \text{mol}^{-2}$;
b: $39.3 \cdot 10^{-6} \text{ m}^3 \cdot \text{mol}^{-1}$

S5: Methods for the material Characterization

Nitrogen sorption

Specific surface area and pore size distribution were determined from N₂-physisorption data obtained using a NOVA 4200e instrument (Quantachrome). As a pre-treatment, samples were outgassed and dried for 4 h at 80 °C at reduced pressure. Data analysis of isotherm data was carried out according to methods described by Brunauer, Emmett, Teller (BET)¹⁴ and Barrett, Joyner, Halenda (BJH)¹⁵.

Powder X-ray diffraction

Powder X-ray diffraction (XRD) was carried out on a STADI P automated transmission diffractometer from STOE (Darmstadt, Germany) with an incident beam curved germanium monochromator selecting CuKα₁ radiation ($\lambda = 1.5406 \text{ \AA}$, 40 kV, 40 mA) and a 6° linear position sensitive detector (PSD). The alignment was checked by use of a silicon standard. The data were collected in the 2 Theta range from 5 – 60 ° with a step size of 0.5 ° and a measurement time of 50 seconds per step.

Transmission electron microscopy

The TEM measurements were performed at 200 kV with an aberration-corrected JEMARM200F (JEOL, Corrector: CEOS). The microscope is equipped with a JED-2300 (JEOL) energy-dispersive x-ray-spectrometer (EDXS) for chemical analysis. The samples were measured on a Au-Grid.

X-Ray Photoelectron Spectroscopy

The XPS measurements were performed with a VG ESCALAB 220 iXL with monochromated AlK_α radiation (E = 1486.6 eV). The electron binding energies EB were obtained without charge compensation.

Electron paramagnetic resonance

EPR spectra were recorded at RT on a Bruker cw spectrometers EMX CW-micro and ELEXSYS 500-10/12 (X-band, $\nu \approx 9.7 \text{ GHz}$) with a microwave power of 6.3 mW, a modulation frequency of 100 kHz and modulation amplitude up to 5 G. For spin-trap experiments, 5,5-dimethyl-1-pyrroline N-oxide (DMPO, Enzo Life Sciences GmbH) was used after a purification with activated charcoal as adsorbent.¹⁶

Spin trapping experiments: a reaction suspension (6 mg Cu/TiO₂ in 3.5 ml H₂O) was mixed and loaded into the flat cell placed in the EPR cavity. CO₂ (0.5 ml/min) was fed into the catalyst suspension through a fused silica capillary under visible-light irradiation. 50 μL of DMPO (600 mM) were dosed into the suspension via a self-modified syringe. EPR spectra were recorded before and after DMPO feeding. Signal fitting were carried out by using the SpinFit program (Bruker) or EasySpin.¹⁷

Note: the relative number of DMPO-OOH and DMPO-OH adducts were interpreted from the double integral of the fitted spectrum multiplied by the relative percentage of each component given by EasySpin.

Inductively coupled plasma optical emission spectrometry

Inductively coupled plasma optical emission spectrometry (ICP-OES) using a Varian 715-ES ICP-emission spectrometer was carried out, in order to quantify the amount of copper in the material.

S6: Pore size distribution (BJH) of TiO₂ aerogel

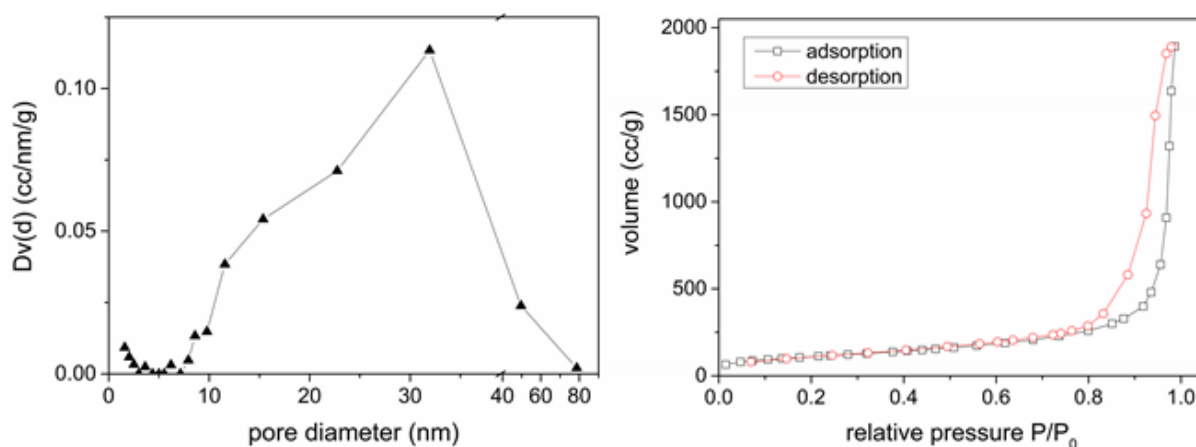


Figure S6. Pore size distribution of TiO₂-AG by using N₂ adsorption measurements.

Table S6. Results of N₂-physisorption measurements of TiO₂-AG.

Surface area	482.387 m ² /g
Pore volume	2.968 cc/g
Pore diameter $Dv(d)$	319.404 Å

S7: XRD patterns of TiO₂-AG and Cu/TiO₂-AGs

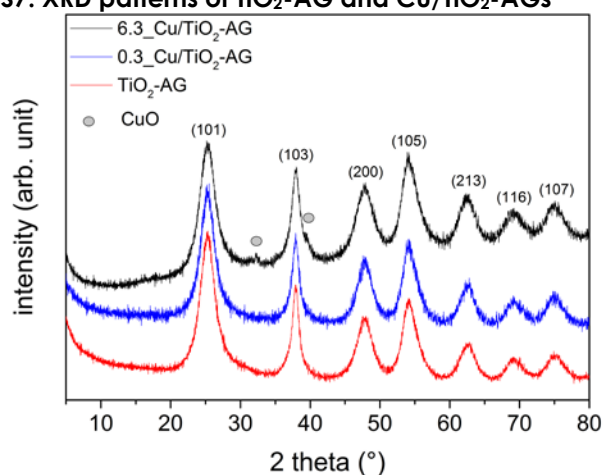


Figure S7. XRD patterns of TiO₂ and Cu/TiO₂ aerogels marked with reflection of Cu(II)-species (grey dots) compared to PDF 80-1268¹⁸. TiO₂ phase is identified to be Anatase compared to PDF C1-562.

S8: TEM images of TiO₂-AG

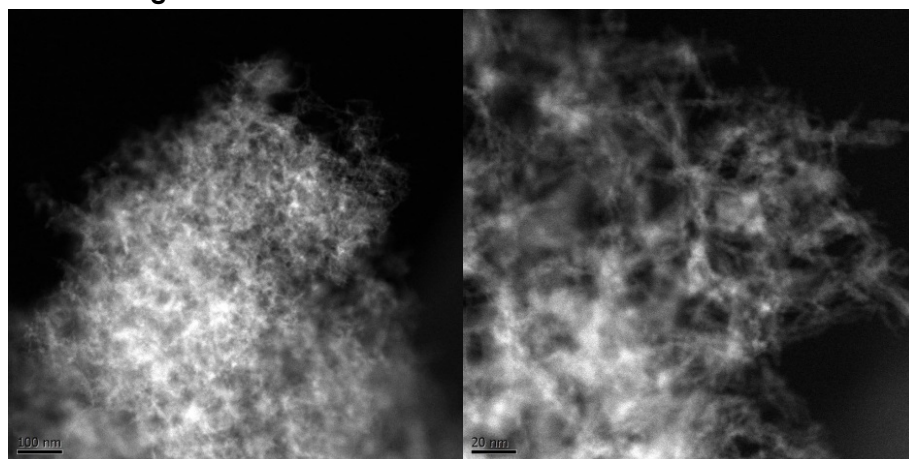


Figure S8. HAADF-TEM images of TiO₂-AG.

S9a: TEM images of 6.3_Cu/TiO₂-AG

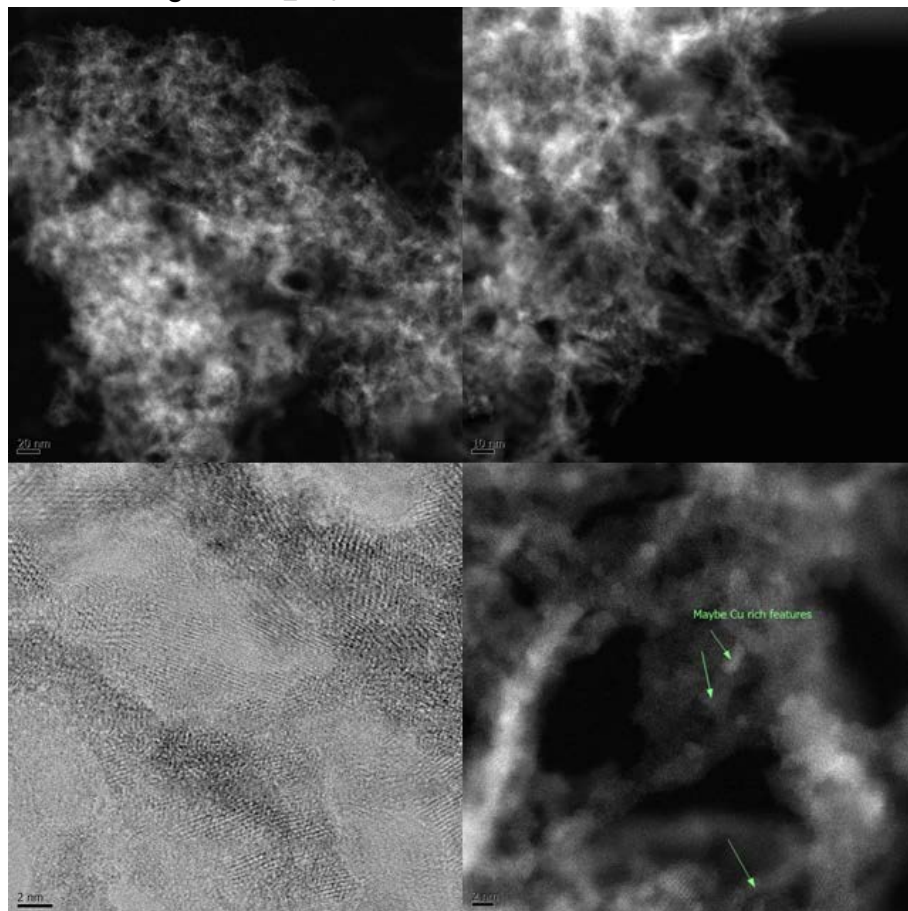


Figure S9a. HAADF-TEM images 6.3_Cu/TiO₂-AG.

S9b: TEM and EDX images of 6.3_Cu/TiO₂-AG

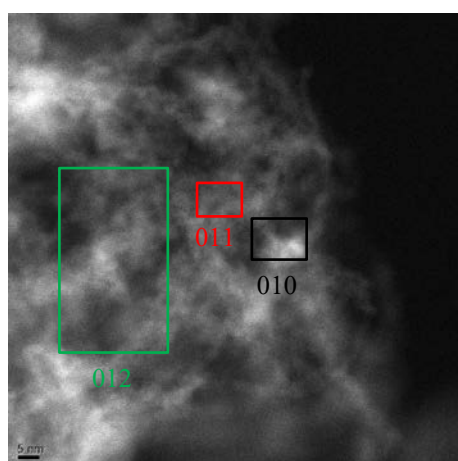


Figure S9b. TEM images 6.3_Cu/TiO₂-AG, EDX data see below.

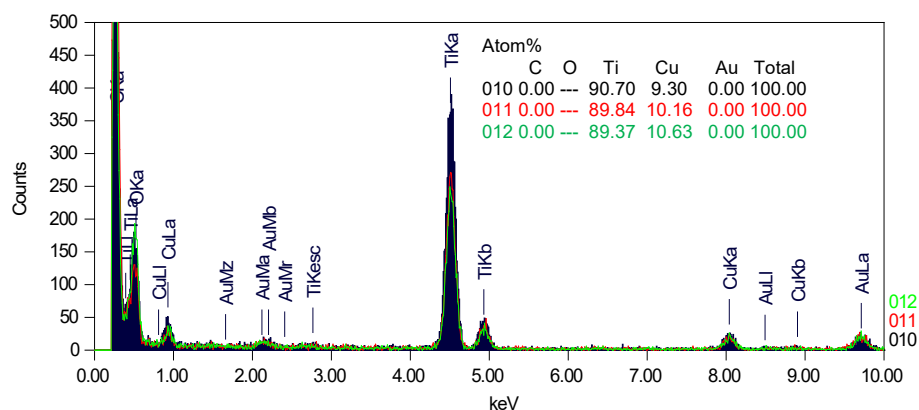


Figure S9b. EDX analysis for TEM images seen above.

S10: XPS of 6.3_Cu/TiO₂-AG (a) and 0.3_Cu/TiO₂-AG (b)

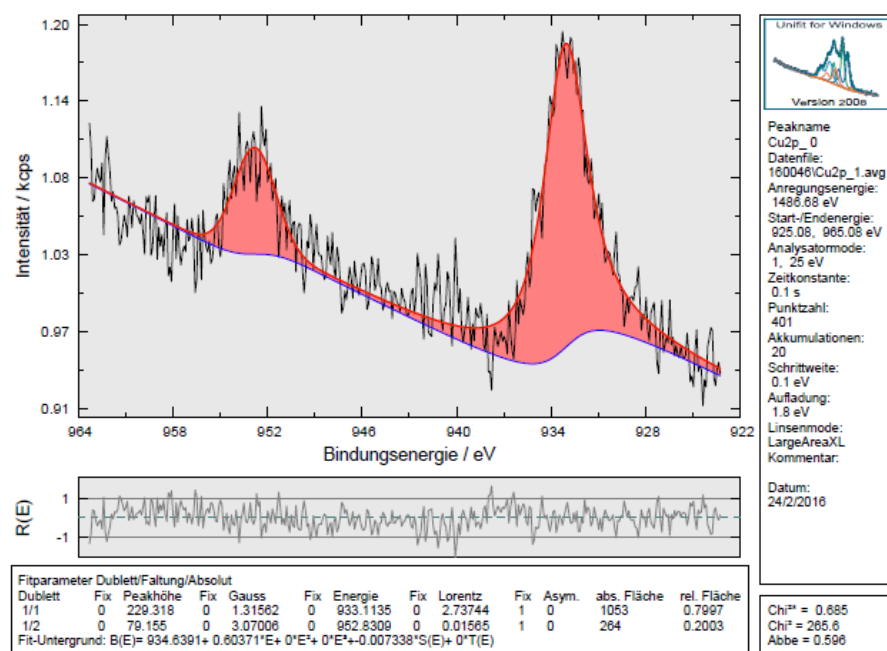


Figure S10a. XPS on 6.3_Cu/TiO₂-AG showing Cu(II) signals.

XPS analysis of the Cu/TiO₂-AG after the photocatalytic reaction was done but showed instability of the material under the measurement conditions.

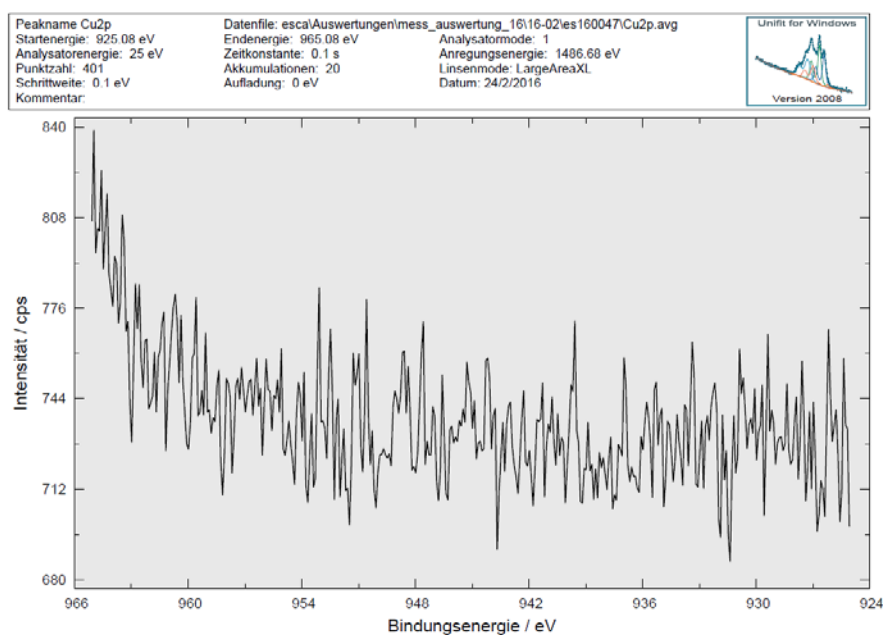


Figure S10b. XPS on 0.3% Cu/TiO₂-AG showing no Cu(II) signals.

S11: Influence of using different aqueous media for photocatalytic CO₂ reduction

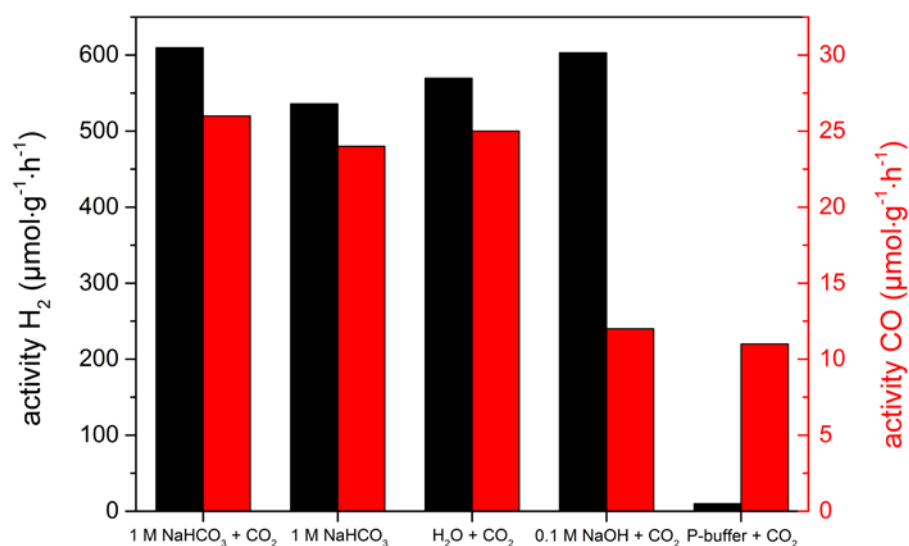


Figure S11. Influence of different reaction media. Reaction conditions: catalyst: 1.2 mg 0.3 wt% Cu/TiO₂, medium 7.5 ml, 60 min flushing with CO₂, 20 °C, 4 h irradiation, Lumatec lamp: 2.5 W output, Filter 320-500 nm. P-Puffer: phosphate buffered aqueous solution (pH of approximately 5).

S12: Effect of catalyst composition on ^{13}CO formation from $^{13}\text{CO}_2$

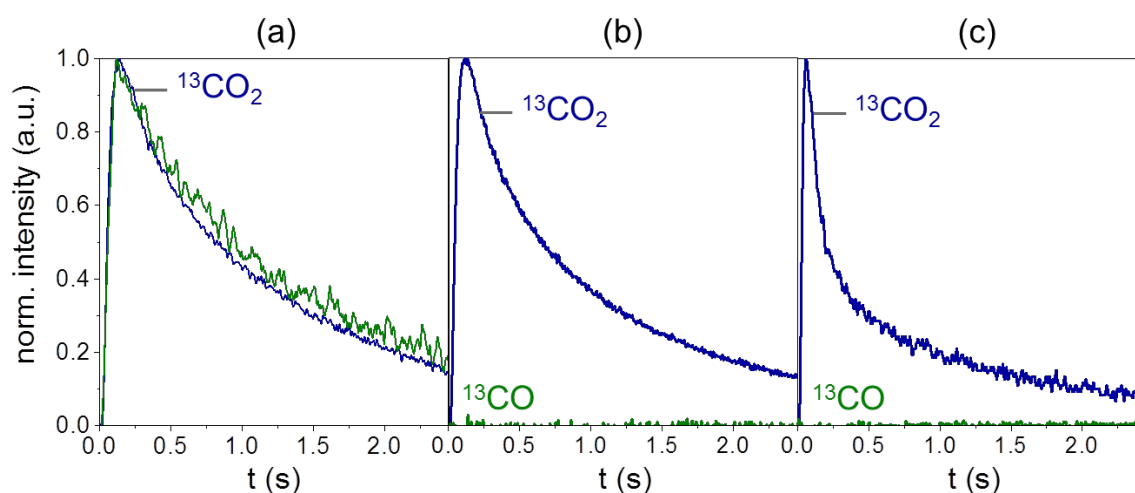


Figure S12. Height-normalized transient responses of $^{13}\text{CO}_2$ and ^{13}CO recorded upon pulsing of a $^{13}\text{CO}_2$:Ar = 1:1 mixture over 6.3-Cu/TiO₂-AG (a), TiO₂-AG (b), and TiO₂-P25 (c) at room temperature.

S13: EPR measurement regarding the generation of $\cdot\text{OH}$ and $\cdot\text{CO}_2$ radicals

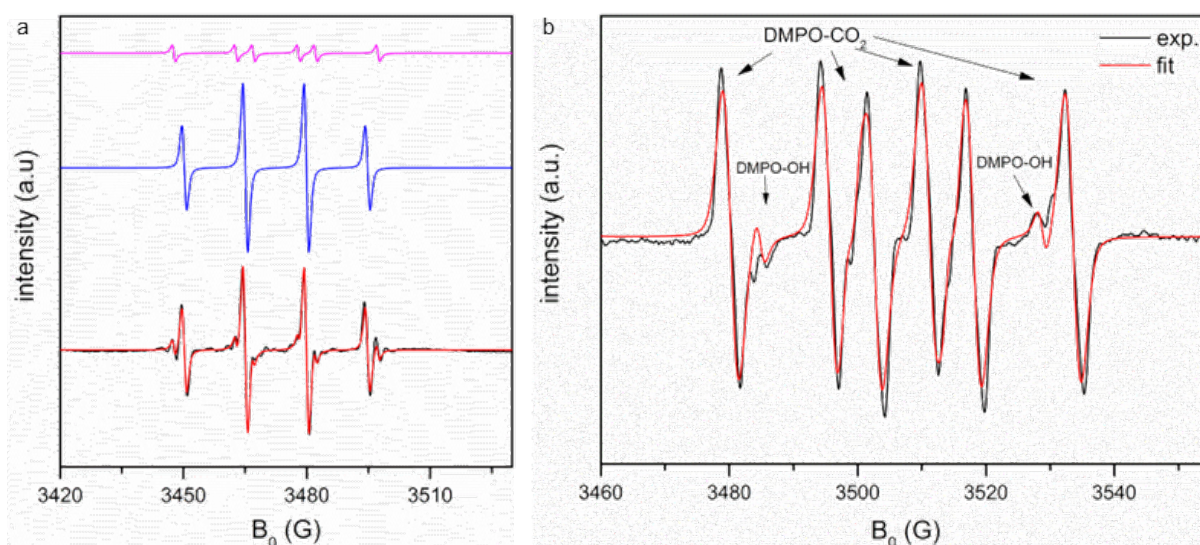


Figure S13. a) Normalized EPR spectra (black: experimental, red: calculated) of TiO₂-AG in aqueous CO₂ in the presence of DMPO after irradiation. The hyperfine splitting values obtained by spectra simulation were: $A_N \approx A_H = 14.9$ G for DMPO-OH (blue signal) and $A_N = 15.2$, $A_H = 19.4$ for DMPO- CO_2 (pink signal) spin adducts. b) EPR spectra of the generation of primary $\cdot\text{CO}_2$ radicals during the photocatalytic CO₂ reduction using 6.3-Cu/TiO₂-AG catalyst.

S14: Analysis of hydroxyl groups on TiO₂-AG and TiO₂-P25 via FT-IR spectroscopy

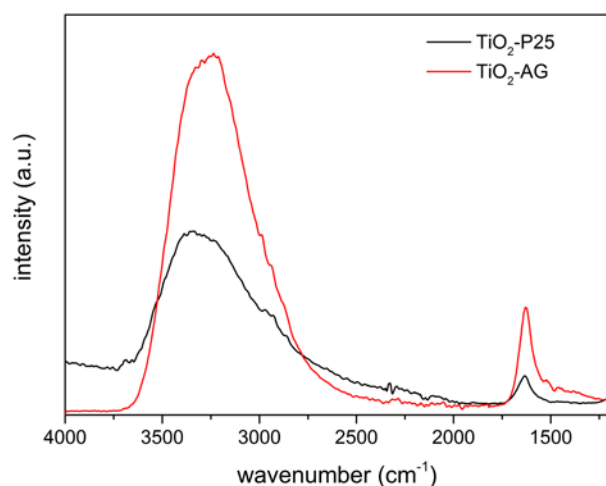


Figure S14: FT-IR spectra of TiO₂-AG and TiO₂-P25 measured via ATR technique (attenuated total reflection).

S15: XPS analysis of hydroxyl groups on TiO₂-AG, TiO₂-P25 and Analysis of 6.3_Cu/TiO₂-AG before and after reaction by titration of hydroxyl groups

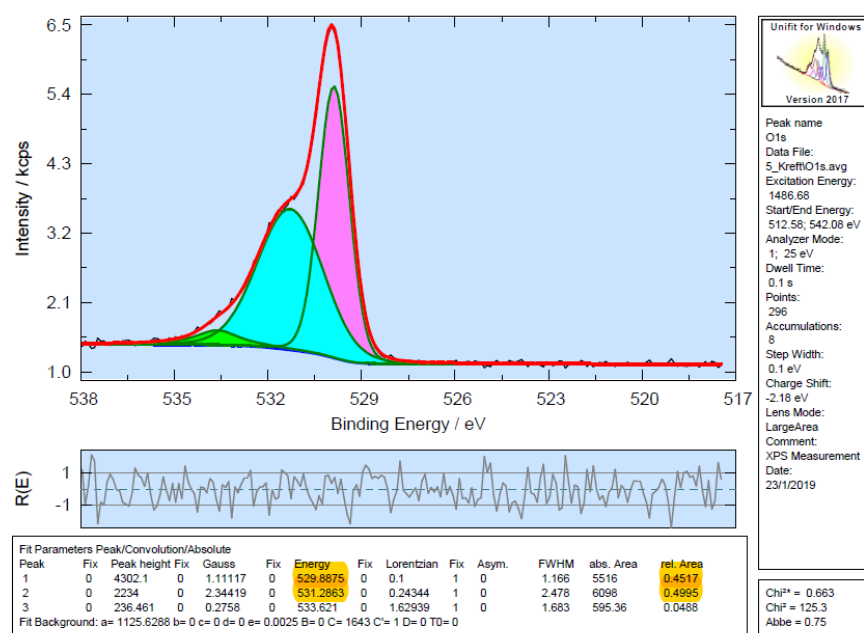


Figure S15a XPS on TiO₂-AG showing O1s signal for the analysis of OH-groups on the surface.

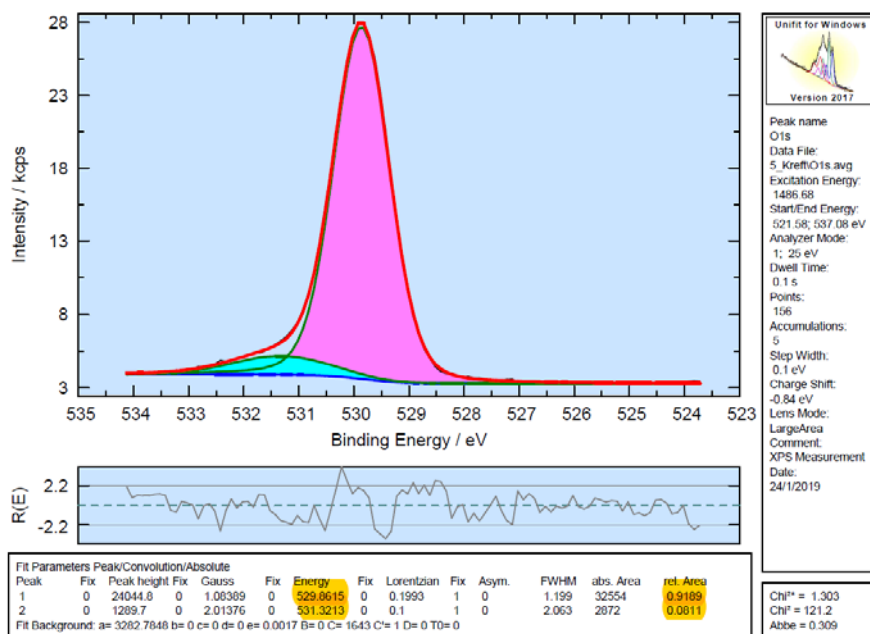


Figure S15b XPS on TiO₂-P25 showing O 1s signal for the analysis of OH-groups on the surface.

S15c Procedure of titration experiments

The amount of surface hydroxyl groups can be titrated by the following procedure:¹⁹

10 mg of 6.3-Cu/TiO₂-AG (before and after photoreaction reaction for 5 d under 0.5 vol% O₂/CO₂) were added to 10 ml of a NaOH solution (2 mmol/l) and stirred for 15 h. The dispersion was centrifuged and the supernatant liquid was titrated with HCl_(aq) (10mmol/l). Bromothymol blue was used as indicator. The investigation of the initial material showed a two times higher consumption compared to the material after the reaction (1.55 ml HCl_(aq) compared to 0.8 ml HCl_(aq)).

S16: Oxygen detection using an optical oxygen sensor

Oxygen detection was achieved by mounting a fiber-optic oxygen sensor (PyroScience, robust probe, normal range) in the gas phase of the photo-reactor. The sensor was attached to a FireStingO2 optical oxygen meter (PyroScience). Along with the oxygen sensor, a PT100 (Therma Thermofühler GmbH) was mounted in the reactor's gas phase for temperature compensation of the oxygen reading. The sensor was calibrated by a separate 2-point calibration in purified argon (> 99.9%) and air. In a typical experiment, the reactor was flushed with 0.5 vol% O₂/CO₂ for 30 min and then sealed. The oxygen baseline was measured for 1.5 – 2h in the dark and usually showed a slight, linear increase in oxygen content (on the order of 6-8 × 10⁻⁷ vol% O₂ s⁻¹). To compensate for this, a linear regression was calculated in each experiment modelling the baseline in the dark. This linear regression was then subtracted from the subsequent O₂ readings obtained during irradiation. Since the actual initial O₂ content at the beginning of irradiation varied slightly (between 0.39 – 0.46 vol% O₂), all data sets were normalized to 0.5 vol% O₂ during processing. In case of the long-term experiment, no baseline correction was applied, the light was turned on at 8250 s.

Long term and long term recycling experiment

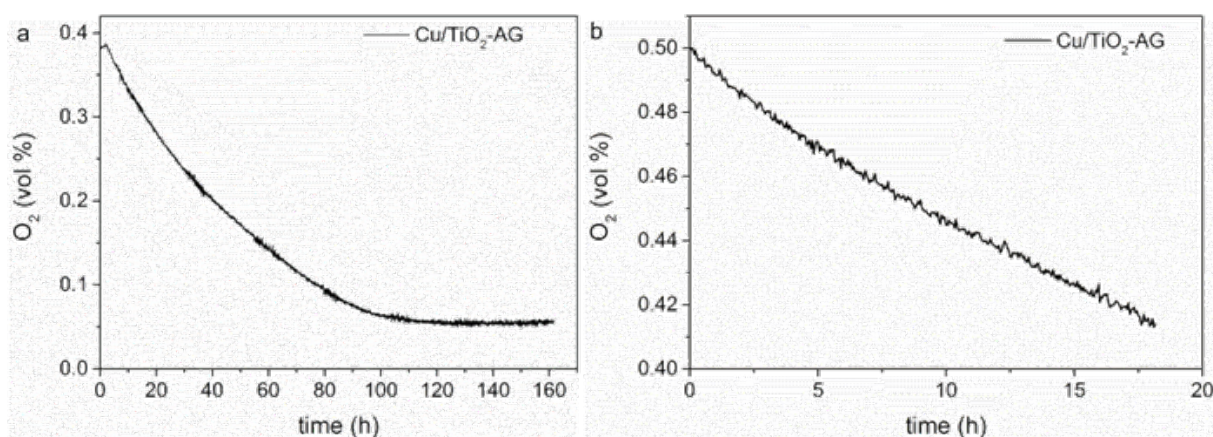


Figure S16: a) Long term experiment using 6.3_Cu/TiO₂-AG in 0.4 vol% O₂/CO₂ atmosphere and b) recycling experiment (after long term reaction (a)) of 6.3_Cu/TiO₂-AG in a 0.4 vol% O₂/CO₂ atmosphere under standard reaction conditions (catalyst material was regenerated using air in between experiments).

S17: Analysis of peroxo species on the TiO₂-AG surface

The analysis for the detection of peroxo was the following: After a long-term photoreaction using 6.3_Cu/TiO₂-AG under 0.5 % O₂/CO₂ atmosphere (5 d, solid line) and after a standard reaction using 6.3_Cu/TiO₂-AG in 100 % CO₂ atmosphere (20h, dotted line), respectively, the whole volume of the suspension was collected. Part of it was analyzed directly, in order to determine the total amount of peroxide species in dispersion (dispersion with catalyst). Another part was filtered with the use of a 0.45 μ m syringe filter to remove the photocatalyst powder. The solution was then analyzed to determine the amount of peroxide species in the liquid phase (separated solution). In each case 3 ml of a solution of LabAssay™ Glucose (Wako) were added to 3 ml of the sample and stirred for 10 min at 30 °C. After that the dispersion with catalyst was filtered and the colored solution was analyzed. The same procedure was done with the separated solution.

S18: *in situ* EPR measurement of 6.3_Cu/TiO₂-AG regarding the copper species

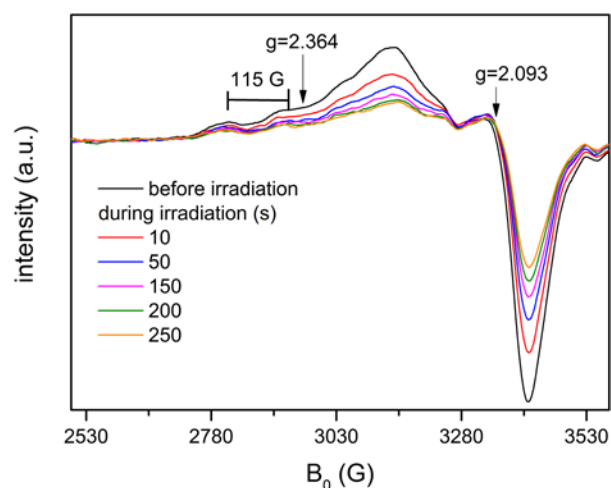


Figure S18. EPR spectra of 6.3_Cu/TiO₂-AG in CO₂-saturated H₂O during the photocatalytic CO₂ reduction regarding the copper species.

The EPR spectrum of the aqueous suspension of 6.3 wt%_Cu/TiO₂-AG catalyst showed an axial signal at $g_{||}=2.364$ and $g_{\perp}=2.093$ characteristic of isolated Cu^{II} sites. The perpendicular component of the g tensor displayed no hyperfine structure (hfs) splitting while the parallel component showed splitting with a hfs constant of $A_{||}=115$ G due to the coupling of the unpaired electron spin of Cu^{II} ion (d^9 , $S=1/2$) with its nuclear spin ($^{63,65}\text{Cu}$, $I=3/2$). *In situ* bubbling of CO₂ (or using NaHCO₃ solution) into the suspension of the catalyst and H₂O did not change the Cu^{II} EPR signal. However, irradiation of the sample resulted in a decrease in the EPR

signal intensity of Cu^{II} due to its reduction as evidenced from *in situ* XAS investigation (see S18: X-ray absorption spectroscopy).

S19: Recycling experiments for the photocatalytic CO₂ reduction with 6.3_Cu/TiO₂-AG

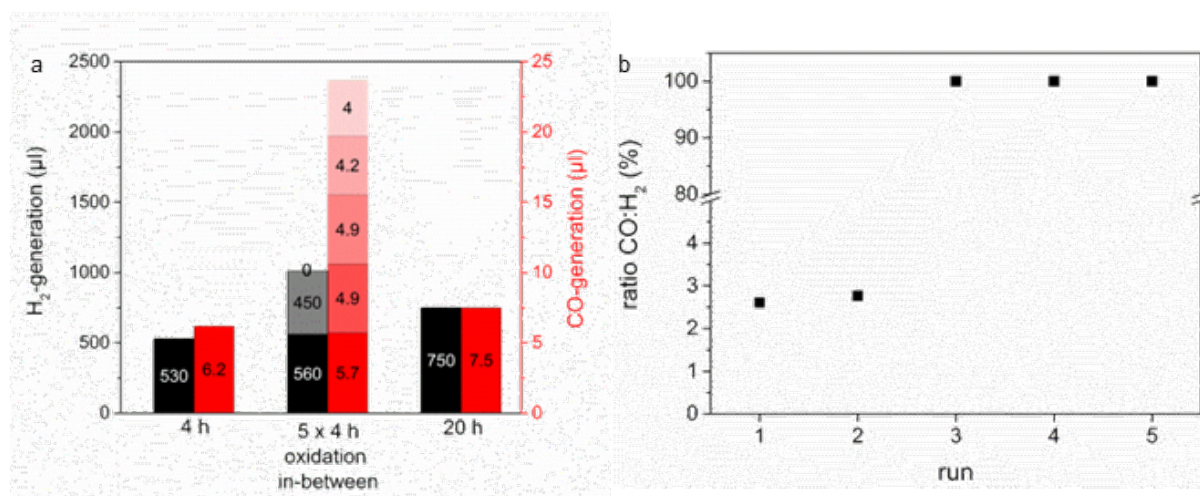


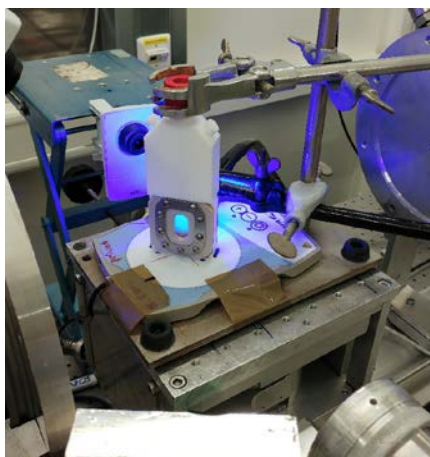
Figure S19. a) Recycling experiments for the photocatalytic CO₂ reduction with 6.3_Cu/TiO₂-AG catalyst (in 100% CO₂ atmosphere) in comparison to the reaction with 4 and 20 h irradiation time. Between every recycling step the suspension was flushed with air for 30 min and with CO₂ for 60 min afterwards. Catalyst: 12.6 mg 6.3_Cu/TiO₂-AG, medium 7.5 ml H₂O, 20 °C, Lumatec lamp: 2.5 W output, Filter 320-500 nm. b) Calculated CO:H₂ ratio of the recycling experiment 5 x 4 h oxidation in-between.

S 20: X-ray absorption spectroscopy

Experimental details:

X-ray absorption experiments (XAS) were carried out at PETRA III beamline P65 at Deutsches Elektronensynchrotron (DESY) in Hamburg, Germany. The measurements at the copper K-edge (8979 eV) were performed using a Si(111) double-crystal monochromator and a maximum synchrotron beam current of 100 mA. Spectra of the catalysts were recorded as a stirred suspension in water in a special designed liquid cell in fluorescence mode. Furthermore, this liquid cell enables the exchange of the atmosphere above the reaction mixture. To enable the illumination during the reaction, the Kapton® window of the back side of the cell was replaced by a polystyrene foil. For energy calibration, a copper foil was used.

After measurements of the catalyst (6.3_Cu/TiO₂-AG) as a suspension in water and under CO₂-atmosphere to exclude changes even without the presence of light, the reaction mixture was investigated under reaction conditions. After 4h, the catalyst was reactivated using oxygen, afterwards the atmosphere was exchanged by CO₂ and the light-driven reaction was started again. The catalyst was applied in three runs. In addition, a second initial solution was irradiated for 9 h without regeneration and after measurement even further to reach 24 h without reoxidation.



X-ray absorption measurements for the declaration of the change in selectivity during the reactivation of the initial 6.3_Cu/TiO₂-AG catalyst

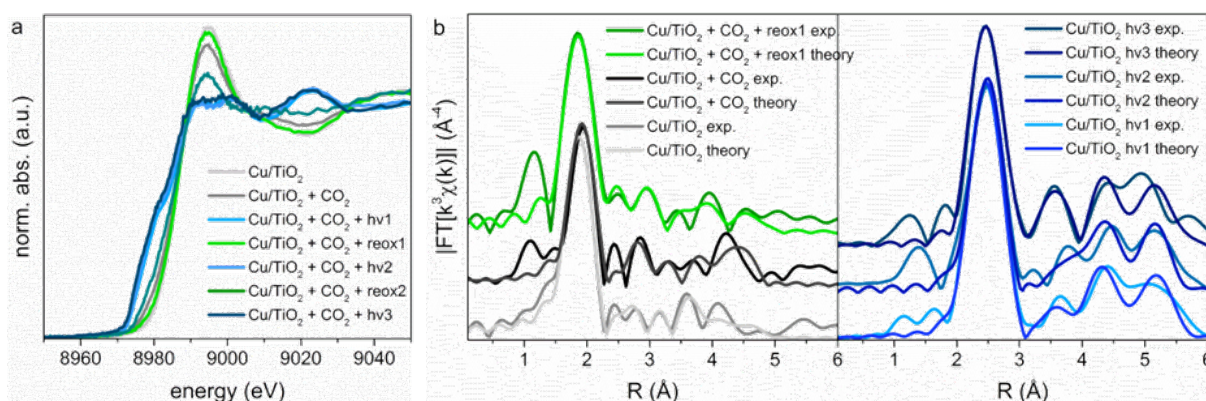


Figure S20a. a) X-ray absorption spectra and b) Fourier transformed EXAFS spectra of the initial catalyst (6.3_Cu/TiO₂-AG), in a CO₂ saturated aqueous dispersion during illumination after 4 h, 9 h, 24 h and of a copper foil as reference.

XANES analysis shows clearly a Cu(II) species with an absorption edge at 8987.5 eV in the initial Cu/TiO₂-AG catalyst (Fig. S18a). No changes are observed when the suspension is subjected to CO₂ atmosphere (Cu/TiO₂ + CO₂). Irradiation causes a reduction of Cu(II) and a Cu(0)-species as concluded from the appearance a signal with an edge energy of 8979.5 eV (Cu/TiO₂ + CO₂ + hv1). Comparison with a Cu-foil spectrum reveals a similar edge position and whiteline shape. After reactivation of the catalyst using oxygen, metallic Cu was transformed to Cu(II) species (Cu/TiO₂ + CO₂ + reox1). This procedure was reproducibly repeated for three times. Although the spectrum after the second reactivation reveals also a complete oxidation to Cu(II) (Cu/TiO₂ + CO₂ + reox2), the reduced whiteline intensity and the slightly different shape of the post-edge line indicate structural changes. Due to the low signal-to-noise ratio of this spectrum, an EXAFS-analysis was not possible to clarify these changes.

To determine the character of the illuminated and the reactivated samples during the catalysis cycles a linear combination fit of the XANES spectra using the spectra of the initial sample and of a Cu-foil was carried out.^{20,21} The resulting LC-XANES fits are shown below (Table S18a, Fig. S18). The illuminated spectra of all three runs exhibit nearly a full agreement with a Cu(0) spectrum, while after the oxidation in the reactivation process resulted mainly in the initial substance. Furthermore, the spectra of the uninterrupted illuminated sample show a very large fraction of Cu(0).

In case of the reactivated (6.3_Cu/TiO₂-AG reox) catalysts typical backscatterer and distances of CuO were adjusted by the analysis of the EXAFS spectra.²² As mentioned in the manuscript, larger metallic Cu-domains are formed during the photocatalytic reaction in comparison to the initial catalyst elucidated by the high amount of Cu backscatterer. After the second reactivation of the catalyst the formation of this large domains appears to be inhibited, which is reflected in smaller amounts of backscattering atoms in all fitted shells in the third run. These structural changes can be correlated with the observed changes in selectivity.

Larger domains of Cu-species seem to catalyze both, the generation of hydrogen and of carbon monoxide, while the smaller Cu domains seem to catalyze the generation of CO exclusively.

Data analysis:

In the first step of data analysis, the background of the spectrum was removed by subtracting a Victoreen-type polynomial²³⁻²⁶. Due to the very differing shapes of the absorption edges of the samples and the used references, the first inflection point of the first derivative of the corresponding spectrum was defined as energy E_0 . Afterwards a piecewise polynomial was used to determine the smooth part of the spectrum and was adjusted in a way that the low- R components of the resulting Fourier transform were minimal. The background subtracted spectrum was divided by its smoothed part and the photon energy was converted to photoelectron wave number k . For evaluation of the EXAFS spectra the resulting functions were weighted with k^3 and calculated with EXCURVE98, which works based on the EXAFS function and according to a formulation in terms of radial distribution functions²⁷:

$$\chi(k) = \sum_j S_0^2(k) F_j(k) \int P_j(r_j) \frac{e^{\frac{-2r_j}{\lambda}}}{kr_j^2} \sin[2kr_j + \delta_j(k)] dr_j$$

The number of independent points N_{ind} was calculated according to information theory to determine the degree of overdeterminacy²⁷:

$$N_{ind} = \frac{2\Delta k \Delta R}{\pi}$$

Here, Δk describes the range in k -space used for data analysis and ΔR corresponds to the distance range in the Fourier filtering process. For the analysis a Δk -range of 8 and a ΔR -range of 4 was used, which yielded a number of independent points of 20.3. The quality of a fit was determined using two methods. The reduced χ_{red}^2 considers the degree of overdeterminacy of the system and the number of fitted parameters p . It therefore allows a direct comparison of different models²⁸:

$$\chi_{red}^2 = \frac{(N_{ind}/N)}{N_{ind} - p} \sum_i \left(\frac{k_i^n}{\sum_j k_j^n |\chi_j^{exp}(k_j)|} \right)^2 (\chi^{exp}(k_i) - \chi^{theo}(k_i))^2$$

The R-factor, which represents the percentage disagreement between experiment and adjusted function and takes into account both systematic and random errors according to the equation²⁸:

$$R = \sum_i \frac{k_i^n}{\sum_j k_j^n |\chi_j^{exp}(k_j)|} |\chi^{exp}(k_i) - \chi^{theo}(k_i)| \cdot 100\%$$

The accuracy of the determined distances is 1 %, of the Debye-Waller-like factor 10 %²⁹ and of the coordination numbers depending of the distance 5-15 %. Initial values for coordination numbers and distances were adopted from Rietveld-analysis and afterwards iterated free in every fit as well as the Debye-Waller-like factor and the amplitude reducing factor.

LC-XANES Fits

As restriction of the fitting procedure, E_0 of the references were not fitted since the E_0 -shifts obtained in some cases were unrealistically large. Furthermore, the sum of the reference weightings was forced to equal one.

Table S20a: Standards, fitting parameter and errors of the carried out LC-XANES fits.

Sample	Standards	Weight	E_0 -shift	R-factor
				χ^2_{red}
6.3_Cu/TiO ₂ -AG/CO ₂ hv1	6.3_Cu/TiO ₂ -AG/CO ₂	0,035 (0,032)	0	0,0151587
	Cu-foil	0,965(0,032)	0	0,0026427
6.3_Cu/TiO ₂ -AG/CO ₂ hv2	6.3_Cu/TiO ₂ -AG/CO ₂	0,000 (0,032)	0	0,0162867
	Cu-foil	1,000 (0,032)	0	0,0026088
6.3_Cu/TiO ₂ -AG/CO ₂ hv3	6.3_Cu/TiO ₂ -AG/CO ₂	0,103 (0,065)	0	0,0881401
	Cu-foil	0,897 (0,065)	0	0,0111874
6.3_Cu/TiO ₂ -AG/CO ₂ reox1	6.3_Cu/TiO ₂ -AG/CO ₂	1,000 (0,000)	0	0,0057380
	Cu-foil	0,000 (0,000)	0	0,0012683
6.3_Cu/TiO ₂ -AG/CO ₂ reox2	6.3_Cu/TiO ₂ -AG/CO ₂	1,000 (0,000)	0	0,2567725
	Cu-foil	0,000 (0,000)	0	0,0287988
6.3_Cu/TiO ₂ -AG/CO ₂ hv 9h	6.3_Cu/TiO ₂ -AG/CO ₂	0,000 (0,058)	0	0,0526010
	Cu-foil	1,000 (0,058)	0	0,0089625
6.3_Cu/TiO ₂ -AG/CO ₂ hv 24h	6.3_Cu/TiO ₂ -AG/CO ₂	0,000 (0,050)	0	0,0371588
	Cu-foil	1,000 (0,050)	0	0,0064700

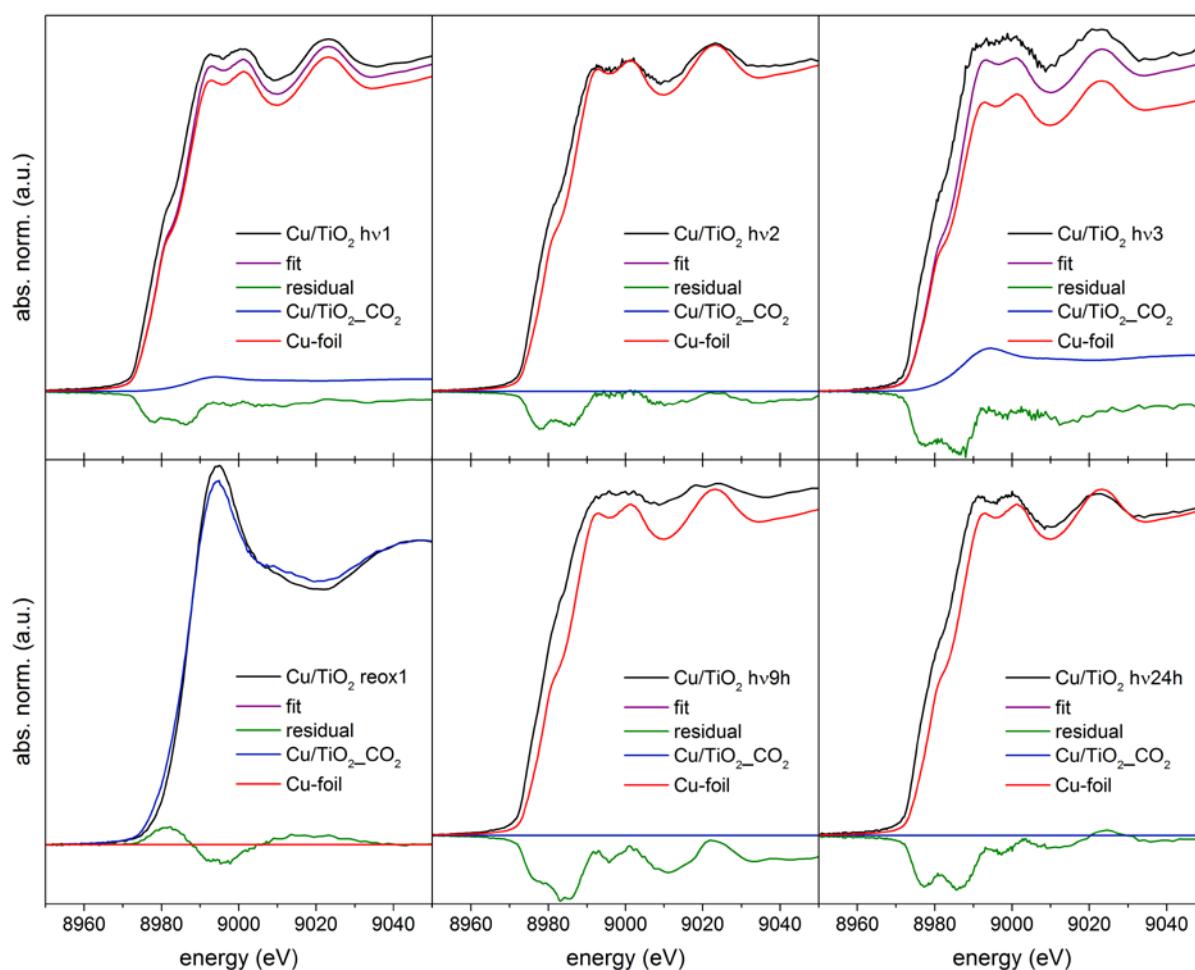


Figure S20b: Linear combination XANES fits of the illuminated samples of the three runs, the first reactivation, after 9 h and 24 h with the spectrum of the initial catalyst and of a Cu-foil as references.

Table S20b: EXAFS analysis fitting parameter, results and fitting errors of the investigated samples.

Sample	Abs- Bs ^[a]	N(Bs) ^[b]	R(Abs-Bs) [Å] ^[c]	σ [Å ⁻¹] ^[d]	R [%] ^[e] χ^2_{red} ^[f] E_f ^[g] Afac ^[h]
6.3_Cu/TiO ₂ -AG	O	3.9 ± 0.19	1.934 ± 0.019	0.071 ± 0.007	34.27
	O	3.0 ± 0.30	2.727 ± 0.027	0.112 ± 0.011	2.12E-05
	Ti	0.8 ± 0.08	3.050 ± 0.030	0.112 ± 0.011	8.269
	Cu	0.5 ± 0.05	3.625 ± 0.036	0.032 ± 0.003	0.800
	Cu	2.0 ± 0.26	4.302 ± 0.043	0.110 ± 0.011	
6.3_Cu/TiO ₂ -AG CO ₂	O	2.6 ± 0.13	1.975 ± 0.019	0.055 ± 0.005	47.93
	O	2.9 ± 0.29	2.803 ± 0.028	0.112 ± 0.011	3.64E-05
	Ti	0.3 ± 0.03	3.183 ± 0.031	0.032 ± 0.003	5.817
	Cu	0.4 ± 0.04	3.737 ± 0.037	0.045 ± 0.004	0.800
	Cu	0.8 ± 0.49	4.347 ± 0.043	0.032 ± 0.003	
6.3_Cu/TiO ₂ -AG hv1	Cu	12 ± 0.24	2.534 ± 0.025	0.095 ± 0.009	23.65
	Cu	5.2 ± 0.52	3.562 ± 0.035	0.112 ± 0.011	5.00E-06
	Cu	22 ± 2.20	4.416 ± 0.044	0.112 ± 0.011	-3.775
	Cu	28 ± 4.20	5.263 ± 0.052	0.112 ± 0.011	0.8492
6.3_Cu/TiO ₂ -AG reox1	O	3.5 ± 0.17	1.92 ± 0.019	0.067 ± 0.006	35.11
	O	3.1 ± 0.31	2.572 ± 0.025	0.112 ± 0.011	2.67E-05
	Ti	1.1 ± 0.11	2.857 ± 0.028	0.100 ± 0.010	-2.972
	Cu	0.6 ± 0.06	3.817 ± 0.038	0.032 ± 0.003	0.8325
6.3_Cu/TiO ₂ -AG hv2	Cu	12 ± 1.20	2.527 ± 0.025	0.095 ± 0.009	39.42
	Cu	3.7 ± 0.37	3.570 ± 0.035	0.112 ± 0.011	1.90E-05
	Cu	18 ± 2.70	4.393 ± 0.043	0.112 ± 0.011	-2.3151
	Cu	19 ± 2.85	5.244 ± 0.052	0.097 ± 0.009	0.8513
6.3_Cu/TiO ₂ -AG hv3	Cu	10 ± 1.00	2.537 ± 0.025	0.095 ± 0.009	38.51
	Cu	1.7 ± 0.17	3.541 ± 0.035	0.032 ± 0.003	1.87E-05
	Cu	18 ± 2.70	4.434 ± 0.044	0.112 ± 0.011	-2.972
	Cu	26 ± 3.90	5.241 ± 0.052	0.112 ± 0.011	0.8325
6.3_Cu/TiO ₂ -AG hv 9h	Cu	4.4 ± 0.44	2.543 ± 0.025	0.084 ± 0.008	47.62
	Cu	2.0 ± 0.20	3.548 ± 0.035	0.077 ± 0.007	2.69E-05
	Cu	8.9 ± 1.33	4.430 ± 0.044	0.112 ± 0.011	-6.714
	Cu	12 ± 1.80	5.338 ± 0.053	0.112 ± 0.011	0.7742
6.3_Cu/TiO ₂ -AG hv 24h	Cu	7.9 ± 0.79	2.535 ± 0.025	0.084 ± 0.008	28.68
	Cu	4.5 ± 0.45	3.556 ± 0.035	0.102 ± 0.010	1.04E-05
	Cu	18 ± 2.70	4.405 ± 0.044	0.112 ± 0.011	-3.537
	Cu	19 ± 2.85	5.248 ± 0.052	0.112 ± 0.011	0.7845

[a] Abs: X-ray absorbing atom, Bs: backscattering atom; [b] Number of backscattering atoms; [c] Distance of absorbing atom to backscattering atom; [d] Debye-Waller like factor; [e] Fit index; [f] Reduced χ^2 ; [g] Fermi energy, which accounts for the shift between theory and experiment; [h] Amplitude reducing factor.

S21: UV-vis measurements in various O₂/CO₂ mixtures

Experimental:

Following the general procedure of the photocatalytic reduction experiment a double-walled temperature-controlled 85-mL reaction vessel was evacuated and refilled with Ar three times followed by an additional three cycles using CO₂ (or O₂/CO₂ mixture). In general, 12.6 mg of the 6.3_Cu/TiO₂-AG catalysts and 7.5 mL of doubly distilled water were then added. Prior to irradiation, the reaction mixture was bubbled with CO₂ (or O₂/CO₂ mixture) for 60 min. The temperature was maintained at 20 °C using a thermostat. In addition, the UV-vis probe was inserted to the vessel kept during the reaction. The solution was irradiated through a plain borosilicate-glass wall in the reaction vessel using a Hg-lamp (Lumatec Superlite 400, output 2.5 W), equipped with a 320-500 nm filter.

UV-vis spectra were recorded in the range of $\lambda = 250\text{--}1100\text{ nm}$ by using an AVASPEC fibre optical spectrometer (Avantes) equipped with aDH-2000 deuterium-halogen light source and a charge coupled device (CCD) array detector. As dark and reference measurement a spectrum of a BaSO_4 suspension (12.6 mg in 7.5 ml H_2O) was taken with and without light, respectively.

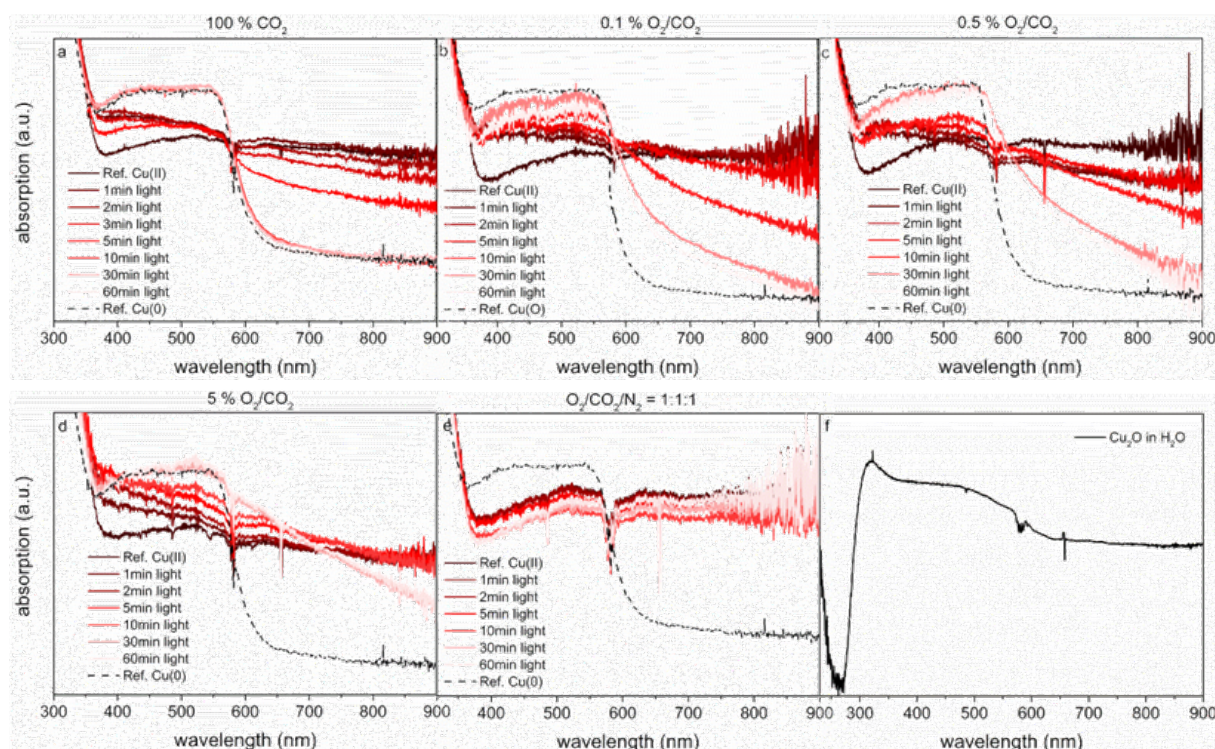


Figure S21: Absorption spectra of UV-vis measurements during the photocatalytic reduction of aqueous CO_2 in various O_2/CO_2 mixtures (a-e) and of the reference Cu_2O in H_2O .

S22: Photocatalytic CO_2 reduction with 6.3_Cu/TiO₂-AG, TiO₂-AG and TiO₂-P25 in various O_2/CO_2 mixtures

Table S22: Photocatalytic CO_2 reduction in various O_2/CO_2 mixtures

Entry	Catalyst	O_2/CO_2 mixture	VH_2 [μl]	VCO [μl]
1	6.3_Cu/TiO ₂ -AG	0.5% O_2 in CO_2	260	22.5
2	6.3_Cu/TiO ₂ -AG	100% CO_2	750	7.5
3	TiO ₂ -AG	0.5% O_2 in CO_2	108	9.4
4	TiO ₂ -AG	100% CO_2	244	12
5	TiO ₂ -P25	0.5% O_2 in CO_2	n. d.	n. d.
6	TiO ₂ -P25	100% CO_2	n. d.	n. d.

Conditions: catalyst: 12.6 mg catalyst, medium 7.5 ml H_2O , 20 °C, **20 h**, Lumatec lamp: 2.5 W output, Filter 320-500 nm.

References

- 1 Aguirre, M. E., Zhou, R., Eugene, A. J., Guzman, M. I. & Grela, M. A. Cu₂O/TiO₂ heterostructures for CO₂ reduction through a direct Z-scheme: Protecting Cu₂O from photocorrosion. *Appl. Catal. B* **217**, 485-493, doi:https://doi.org/10.1016/j.apcatb.2017.05.058 (2017).
- 2 Zhang, T. *et al.* Copper-Decorated Microsized Nanoporous Titanium Dioxide Photocatalysts for Carbon Dioxide Reduction by Water. *ChemCatChem* **9**, 3054-3062, doi:10.1002/cctc.201700512 (2017).
- 3 Liu, L., Zhao, C., Miller, J. T. & Li, Y. Mechanistic Study of CO₂ Photoreduction with H₂O on Cu/TiO₂ Nanocomposites by in Situ X-ray Absorption and Infrared Spectroscopies. *J. Phys. Chem. C* **121**, 490-499, doi:10.1021/acs.jpcc.6b10835 (2017).
- 4 Fang, B., Xing, Y., Bonakdarpour, A., Zhang, S. & Wilkinson, D. P. Hierarchical CuO–TiO₂ Hollow Microspheres for Highly Efficient Photodriven Reduction of CO₂ to CH₄. *ACS Sustain. Chem. Eng.* **3**, 2381-2388, doi:10.1021/acssuschemeng.5b00724 (2015).
- 5 Jeong, S. *et al.* Bi₂O₃ as a Promoter for Cu/TiO₂ Photocatalysts for the Selective Conversion of Carbon Dioxide into Methane. *ChemCatChem* **8**, 1641-1645, doi:10.1002/cctc.201600099 (2016).
- 6 Li, Y. *et al.* Photocatalytic reduction of CO₂ with H₂O on mesoporous silica supported Cu/TiO₂ catalysts. *Appl. Catal. B* **100**, 386-392, doi:http://dx.doi.org/10.1016/j.apcatb.2010.08.015 (2010).
- 7 Liu, L., Gao, F., Zhao, H. & Li, Y. Tailoring Cu valence and oxygen vacancy in Cu/TiO₂ catalysts for enhanced CO₂ photoreduction efficiency. *Appl. Catal. B* **134–135**, 349-358, doi:http://dx.doi.org/10.1016/j.apcatb.2013.01.040 (2013).
- 8 Slamet, Nasution, H. W., Purnama, E., Kosela, S. & Gunlazuardi, J. Photocatalytic reduction of CO₂ on copper-doped Titania catalysts prepared by improved-impregnation method. *Catal. Commun.* **6**, 313-319, doi:http://dx.doi.org/10.1016/j.catcom.2005.01.011 (2005).
- 9 Tseng, I. H. & Wu, J. C. S. Chemical states of metal-loaded titania in the photoreduction of CO₂. *Catal. Today* **97**, 113-119, doi:http://dx.doi.org/10.1016/j.cattod.2004.03.063 (2004).
- 10 Tseng, I. H., Wu, J. C. S. & Chou, H.-Y. Effects of sol–gel procedures on the photocatalysis of Cu/TiO₂ in CO₂ photoreduction. *J. Catal.* **221**, 432-440, doi:http://dx.doi.org/10.1016/j.jcat.2003.09.002 (2004).
- 11 Zhang, Q., Gao, T., Andino, J. M. & Li, Y. Copper and iodine co-modified TiO₂ nanoparticles for improved activity of CO₂ photoreduction with water vapor. *Appl. Catal. B* **123–124**, 257-264, doi:http://dx.doi.org/10.1016/j.apcatb.2012.04.035 (2012).
- 12 Singhal, N., Ali, A., Vorontsov, A., Pendem, C. & Kumar, U. Efficient approach for simultaneous CO and H₂ production via photoreduction of CO₂ with water over copper nanoparticles loaded TiO₂. *Appl. Catal., A* **523**, 107-117, doi:http://dx.doi.org/10.1016/j.apcata.2016.05.027 (2016).
- 13 Polleux, J. *et al.* Ligand functionality as a versatile tool to control the assembly behavior of preformed titania nanocrystals. *Chem.-Eur. J.* **11**, 3541-3551, doi:10.1002/chem.200401050 (2005).
- 14 Brunauer, S., Emmett, P. H. & Teller, E. Adsorption of Gases in Multimolecular Layers. *J. Am. Chem. Soc.* **60**, 309-319, doi:10.1021/ja01269a023 (1938).
- 15 Barrett, E. P., Joyner, L. G. & Halenda, P. P. The Determination of Pore Volume and Area Distributions in Porous Substances. I. Computations from Nitrogen Isotherms. *J. Am. Chem. Soc.* **73**, 373-380, doi:10.1021/ja01145a126 (1951).
- 16 Buettner, G. R. & Oberley, L. W. Considerations in the spin trapping of superoxide and hydroxyl radical in aqueous systems using 5,5-dimethyl-1-pyrroline-1-oxide. *Biochem. Biophys. Res. Commun.* **83**, 69-74, doi:https://doi.org/10.1016/0006-291X(78)90398-4 (1978).
- 17 Stoll, S. & Schweiger, A. EasySpin, a comprehensive software package for spectral simulation and analysis in EPR. *J. Magn. Reson.* **178**, 42-55, doi:https://doi.org/10.1016/j.jmr.2005.08.013 (2006).
- 18 Fleet, M. The crystal structure of paratacamite, Cu₂(OH)₃Cl. *Acta Crystallogr. Sect. B* **31**, 183-187, doi:doi:10.1107/S0567740875002324 (1975).
- 19 Oosawa, Y. & Grätzel, M. Effect of surface hydroxyl density on photocatalytic oxygen generation in aqueous TiO₂ suspensions. *J. Chem. Soc. Farad. T 1* **84**, 197-205, doi:10.1039/F19888400197 (1988).
- 20 Busser, G. W. *et al.* Cocatalyst Designing: A Regenerable Molybdenum-Containing Ternary Cocatalyst System for Efficient Photocatalytic Water Splitting. *ACS Catal.* **5**, 5530-5539, doi:10.1021/acscatal.5b01428 (2015).
- 21 Bauer, M., Heusel, G., Mangold, S. & Bertagnolli, H. Spectroscopic set-up for simultaneous UV-Vis/(Q)EXAFS in situ and in operando studies of homogeneous reactions under laboratory conditions. *J. Synchrotron Radiat.* **17**, 273-279, doi:doi:10.1107/S0909049509054910 (2010).
- 22 Yamada, H., Soejima, Y., Zheng, X. G. & Kawaminami, M. Structural Study of CuO at Low Temperatures. *T. Mrs. Jap.* **25**, 1199-1202 (2000).
- 23 Ravel, B. & Newville, M. ATHENA, ARTEMIS, HEPHAESTUS: data analysis for X-ray absorption spectroscopy using IFEFFIT. *J. Synchrotron Radiat.* **12**, 537-541, doi:10.1107/s0909049505012719 (2005).
- 24 Newville, M. IFEFFIT : interactive XAFS analysis and FEFF fitting. *J. Synchrotron Radiat.* **8**, 322-324, doi:doi:10.1107/S0909049500016964 (2001).
- 25 Newville, M., Līviņš, P., Yacoby, Y., Rehr, J. J. & Stern, E. A. Near-edge x-ray-absorption fine structure of Pb: A comparison of theory and experiment. *Phys. Rev. B* **47**, 14126-14131, doi:10.1103/PhysRevB.47.14126 (1993).
- 26 Ertel, T. S., Bertagnolli, H., Hückmann, S., Kolb, U. & Peter, D. XAFS Spectroscopy of Liquid and Amorphous Systems: Presentation and Verification of a Newly Developed Program Package. *Appl. Spectrosc.* **46**, 690-698 (1992).
- 27 Binsted, N. & Hasnain, S. S. State-of-the-Art Analysis of Whole X-ray Absorption Spectra. *J. Synchrotron Radiat.* **3**, 185-196, doi:doi:10.1107/S0909049596005651 (1996).
- 28 Bauer, M. & Bertagnolli, H. The Amplitude Reduction Factor and the Cumulant Expansion Method: Crucial Factors in the Structural Analysis of Alkoxide Precursors in Solution. *J. Phys. Chem. B* **111**, 13756-13764, doi:10.1021/jp076386i (2007).
- 29 Koningsberger, D. C., Mojet, B. L., van Dorssen, G. E. & Ramaker, D. E. XAFS spectroscopy; fundamental principles and data analysis. *Top. Catal.* **10**, 143-155, doi:10.1023/a:1019105310221 (2000).

6 Appendix

6.1 Results for the photocatalytic CO₂ reduction reaction since 2015

Table A1 Overview of the photocatalytic CO₂ reduction on different TiO₂ without any co-catalyst.

Entry	Material	Product	Activity [$\mu\text{mol}\cdot\text{g}^{-1}\cdot\text{h}^{-1}$]	Conditions	Comments	Ref. (year)
1	TiO ₂	CH ₄	7	Gas phase, flow, UV light	Ref. to entry 1 table 2	¹⁶³ (2015)
		CO	10			
		H ₂	27			
		O ₂	n.d.			
2	1 wt% Ce- TiO ₂	CH ₃ OH	24	Liquid phase, 254 nm, NaOH, 50 °C	No hint for oxidation, higher Ce amount decreases activity, Blank measurements	¹⁶¹ (2015)
		HCHO	11			
		CH ₄	1.2			
		CO	b.d.l.			
		H ₂	b.d.l.			
		O ₂	n.d.			
3	N-doped TiO ₂ anatase	CH ₃ OH	0.13	Gas phase, batch, > 400 nm		²¹⁸ (2016)
		H ₂	n.d.			
		O ₂	n.d.			
4	3 wt% N/TiO ₂	CO	45	Gas phase, flow, 254 nm, addition of H ₂	Blank measurements, oxidation: back reaction, •H	¹⁶⁶ (2016)
		CH ₄	2			
		H ₂	n.d.			
		O ₂	n.d.			
5	TiO ₂	CH ₄	3	Gas phase, batch, Xe light	Ref. to entry 3,4 table 2	¹⁶⁴ (2016)
		CO	9			
		H ₂	n.d.			
		O ₂	n.d.			
6	TiO ₂ hollow microspheres	CH ₄	0.4	Liquid phase, 254 nm	Ref. to entry 1 table 3	¹¹⁴ (2015)
		CO	5.6			
		H ₂	1.8			
		O ₂	n.d.			
7	TiO ₂ nano flower films	CH ₃ OH	0.3 $\mu\text{mol}/\text{cm}^2/\text{h}$	Liquid phase, > 420 nm	Ref. to entry 2 table 3	¹⁶⁵ (2015)
		H ₂	n.d.			
		O ₂	n.d.			
8	TiO ₂ nanosheets	CH ₄	3.3	Gas phase, batch, > 400 nm	Blank exp., Surface treated with H ₂ SO ₄ , Increased O ₂ /N ₂ ratio	²⁰³ (2016)
		H ₂	b.d.l.			
		O ₂	n.d.			
9	TiO ₂ flakes	HCOO ⁻	1.9	Liquid phase, Hg lamp, 0 °C	No hint to oxidation reaction, no blank exp.	¹⁹⁰ (2016)
		H ₂	n.d.			
		O ₂	n.d.			
10	Ti ³⁺ -TiO ₂ brookite	CH ₄	12	Gas phase, flow, > 420 nm	No hint to oxidation reaction, no blank exp.	²¹⁹ (2016)
		CO	23			
		H ₂	n.d.			
		O ₂	n.d.			
11	TiO ₂ nanoparticles	CH ₄	3	Gas phase, flow, UV light	Oxidation process: proposed back reaction	²⁰⁵ (2015)
		CO	6			
		H ₂	200			
		O ₂	n.d.			

12	TiO ₂ P25	HCOOH	660	Liquid phase, 7 bar, 80 °C, 254 – 364 nm, pH 14, Na ₂ SO ₃ as h.s.	After 20 h, at the beginning only HCOOH, HCHO; blank measurements	¹⁶² (2017)
		HCHO	1400			
		CO	3.6			
		H ₂	24			
13	TiO ₂ anatase- brookite	CH ₄	1	Liquid phase, NaOH, 254 nm	Proposed oxidation to •OH radicals	²²⁰ (2017)
		H ₂	10			
		O ₂				

Table A2 Overview of the photocatalytic CO₂ reduction on different TiO₂ with noble metals as co-catalyst.

Entry	Material	Product	Activity [μmol·g ⁻¹ ·h ⁻¹]	Conditions	Comments	Ref. (year)
1	0.3 wt% Pt ²⁺ -Pt ⁰ /TiO ₂ (P25)	CH ₄	38	Gas phase, flow, 320 – 420 nm	Higher amount Pt ²⁺ decreases activity	¹⁶³ (2015)
		CO	8			
		H ₂	395			
		O ₂	290			
2	1 wt% Pt/Ti ³⁺ -TiO ₂ (P25)	CH ₄	1.7	Gas phase, batch, > 405 nm	Addition of H ₂ , oxidation: proposed •H+H ⁺	¹⁷³ (2017)
		CO	Traces			
		C ₂ H ₆	Traces			
		H ₂	n.d.			
		O ₂	n.d.			
3	0.4 wt% Pt/Ti ³⁺ -TiO ₂ (P25)	CH ₄	80	Gas phase, flow, Xe lamp	Generation of ¹³ CH ₄ , no hint for oxidation	¹⁷⁰ (2017)
		H ₂	n.d.			
		O ₂	n.d.			
4	1 wt% Pt/TiO ₂ nanocrystals	CH ₄	4.6	Gas phase, flow, 300 – 420 nm	Blank measurements	¹⁷² (2017)
		H ₂	10			
		O ₂	n.d.			
5	Pt/TiO ₂ photonic crystals	CH ₄	3.2	Gas phase, batch, 320 – 780 nm	Blank measurements	¹⁶⁹ (2017)
		CO	0.2			
		H ₂	34			
		O ₂	28			
6	0.9 wt % Pt on 0.2 wt% MgO/TiO ₂ (anatase)	CH ₄	1.9	Gas phase, batch, Xe lamp	Blank measurements, No hint to oxidation reaction	¹⁷¹ (2016)
		H ₂	n.d.			
		O ₂	n.d.			
7	0.5 wt% Ag/TiO ₂ (brookite)	CH ₄	4	Gas phase, batch, Xe lamp	Higher amount Ag decreases CO, increases CH ₄ up to 2 wt% Ag (entry 3), blank measurement	¹⁶⁴ (2016)
		CO	41			
		H ₂	n.d.			
		O ₂	n.d.			
8	2 wt% Ag/TiO ₂ (brookite)	CH ₄	10	Gas phase, batch, Xe lamp	Higher amount Ag decreases CO and CH ₄	¹⁶⁴ (2016)
		CO	24			
		H ₂	n.d.			
		O ₂	n.d.			
9	1.5 wt% Ag/TiO ₂ (P25)	CH ₄	1.4	Gas phase, batch, Xe lamp	Higher amount Ag decreases CH ₄ , detection ¹³ CH ₄ , oxidation: generation of •H	¹⁷⁴ (2016)
		H ₂	n.d.			
		O ₂	n.d.			

10	1.5 wt% Ag/TiO ₂ (P25)	CH ₃ OH	4	liquid phase,	Nearly same amount with 1, 1.5 and 2 wt% Ag	¹⁷⁴ (2016)
		H ₂	n.d.	batch, Xe		
		O ₂	n.d.	lamp, NaHCO ₃		
11	2 wt% Ag 0.5 wt% Au/TiO ₂	CO	1800	Gas Phase,	Blank measurements, oxidation: proposed generation of •H	²²¹ (2017)
		CH ₄	33	batch, Xe		
		CH ₃ OH	20	lamp, addition		
		H ₂	n.d.	of H ₂		
		O ₂	n.d.			
12	0.1 wt% Au/TiO ₂ (P25)	CH ₄	11	Liquid phase,	¹⁷⁵ (2015)	
		H ₂	3	254 – 364 nm,		
		Liquid products (MeOH, EtOH, FA, FAI.)	67	Na ₂ SO ₃ (h. sc.), 6 bar, 65 °C, pH 11		
13	0.1 wt% Au/TiO ₂ (Rutile)	CH ₄	7	Liquid phase,	¹⁷⁵ (2015)	
		H ₂	2	254 – 364 nm,		
		Liquid products (MeOH, EtOH, FA)	87	Na ₂ SO ₃ (h. sc.), 6 bar, 65 °C, pH 11		
14	Au/TiO ₂ nanosheets	CH ₄	0.65	Gas phase,	Blank measurements, Only vis range: activity significantly decreased, additional CO formation, no hint to oxidation	¹⁷⁶ (2016)
		CO	-	flow, Xe lamp		
		H ₂	n.d.			
		O ₂	n.d.			
15	Au/TiO ₂ nanosheets	CH ₃ OH	3.5	Liquid phase,	Blank measurements	¹⁷⁶ (2016)
		H ₂	n.d.	Xe lamp		
		O ₂	n.d.			
16	1 wt % Au ₆ Pd ₁ /TiO ₂	CH ₄	13	Gas phase,	Blank measurements, detection of ¹³ CH ₄	²²² (2019)
		CO	11	UV light		
		C ₂ H ₆	1			
		C ₂ H ₄	1			
		H ₂	n.d.			
		O ₂	35			
17	5 wt% Pd/TiO ₂ nanosheets	CH ₄	3	Liquid phase,	Blank measurements, detection of O ₂ but showed no results	¹⁷⁷ (2017)
		CO	12	< 400 nm		
		H ₂	21			
		O ₂	n.d.			
18	5 wt% Pd/TiO ₂ nanosheets	CH ₄	-	Liquid phase,	Blank measurements	¹⁷⁷ (2017)
		CO	0.3	400 – 780 nm		
		H ₂	0.2			
		O ₂	n.d.			
19	Pd/TiO ₂ nanosheets	CO	17	Liquid phase,	Blank measurements, detection of O ₂ but showed no results	¹⁷⁸ (2017)
		C ₂ H ₅ OH	13	< 400 nm		
		CH ₄	4			
		H ₂	20			
		O ₂	n.d.			

20	Rh/TiO ₂ nanosheets	CO	14	Liquid phase, < 400 nm	Blank measurements, detection of O ₂ but showed no results	¹⁷⁸ (2017)
		C ₂ H ₅ OH	12			
		CH ₄	4.5			
		H ₂	10			
		O ₂	n.d.			
21	1 wt% Co/TiO ₂	CH ₃ OH	25	Gas phase, batch, > 380 nm	Blank measurements, No hint to oxidation reaction	¹⁸² (2015)
		CH ₃ CHO	20			
		C ₂ H ₅ OH	19			
		H ₂	62			
		O ₂	n.d.			
22	0.9 wt % Pt on 0.2 wt% MgO/TiO ₂ (anatase)	CH ₄	1.9	Gas phase, batch, Xe lamp	Blank measurements, No hint to oxidation reaction	¹⁷¹ (2016)
		H ₂	n.d.			
		O ₂	n.d.			

Table A3 Overview of the photocatalytic CO₂ reduction on semiconductors with copper species as co-catalyst.

Entry	Material	Product	Activity [μmol·g ⁻¹ ·h ⁻¹]	Conditions	Comments	Ref. (year)
1	3 wt% CuO/TiO ₂ (P25)	CH ₄	2.1	Liquid phase, 254 nm	Treatment in H ₂ led to Cu ₂ O/TiO ₂ , 6 % higher activity for CH ₄ ; blank measurement	¹¹⁴ (2015)
		CO	14			
		H ₂	2.8			
		O ₂	n.d.			
2	0.5 wt% Cu/TiO ₂ nano flower films	MeOH	1.8 μmol/cm ² /h	Liquid phase, > 420 nm	Blank measurement	¹⁶⁵ (2015)
		H ₂	n.d.			
		O ₂	n.d.			
3	0.0005 wt% Cu _x O/SrTiO ₃ film	CO	0.015 μmol/cm ² /h	Liquid phase, pH 12, 240 – 300 nm	¹³ CO ₂ , H ₂ ¹⁸ O; ¹³ CO, ¹⁸ O ₂ verified	¹⁸⁴ (2016)
		H ₂	0.003 μmol/cm ² /h			
		O ₂	Value n.d.			
4	10 wt% Cu(II)/Nb ₃ O ₈ ⁻ nanosteets	CO	0.7	Liquid phase, pH 12, 240 – 300 nm	¹³ CO ₂ , H ₂ ¹⁸ O; ¹³ CO, ¹⁸ O ₂ verified; red. of Cu(II) to Cu(I) during reaction	¹⁹³ (2015)
		H ₂	n.d.			
		O ₂	Value n.d.			
5	1 wt% CuCo ₂ O ₄ /CdS	CO	1100	Liquid phase, 420 nm, Ru(bpy) ₃ ²⁺ as PS, TEOA as SR	Blank measurement, ¹³ CO verified	²²³ (2016)
		H ₂	300			
6	TiO ₂ /Ti ₄ O ₉ /Cu ₂ O	CH ₃ OH	0.6	Gas phase, batch, solar light, 70 °C	Blank measurement	¹⁸⁵ (2016)
		H ₂	n.d.			
		O ₂	n.d.			
7	1 wt% Cu ₂ O/TiO ₂ nanosheets	CH ₄	8.7	Gas phase, batch, Xe lamp	Higher amount Cu decreases activity; proposed oxidized species on surface	¹⁶⁸ (2015)
		H ₂	n.d.			
		O ₂	n.d.			
8	1 wt%	CO	140	Gas phase,	Blank	¹⁶⁷ (2016)

	Cu ₂ O/TiO ₂	H ₂ O ₂	450 n.d.	flow, 254 nm	measurements, oxidation: proposed HCOOH formation during reaction & ox. to CO ₂	
9	3 wt% Cu/TiO ₂	CO CH ₄ H ₂ O ₂	500 10 n.d. n.d.	Gas phase, flow, 254 nm, addition of H ₂	Blank measurements, oxidation: back reaction, •H	¹⁶⁶ (2016)
10	2 wt% Cu(I)/TiO ₂	CH ₄ CO H ₂ O ₂	2 1.5 70 n.d.	Liquid phase, NaOH, 254 nm	Blank measurements, no hint for oxidation	¹⁸⁶ (2018)
11	0.4 wt% Cu(0)/TiO ₂ (anatase/rutile)	CH ₄ H ₂ O ₂	8 n.d. n.d.	Gas phase, batch, Xe lamp	Blank measurements, no hint for oxidation	¹⁸⁷ (2017)
12	TiO ₂ 1 wt% Cu/C	CO CH ₄ H ₂ O ₂	20 2.5 n.d. n.d.	Liquid phase, NaOH, 254 nm	Blank measurements, no hint for oxidation	¹⁹⁴ (2016)
13	g-C ₃ N ₄ /(3 wt% CuO/TiO ₂) 30:70	HCOOH CH ₃ OH H ₂ O ₂	950 470 n.d. n.d.	Liquid phase, NaOH, 254 nm	Blank measurements, proposed photo- oxidation reactions in g- C ₃ N ₄ , selectivity depends on ratio g-C ₃ N ₄ :(3 wt% CuO/TiO ₂)	¹⁹¹ (2017)
14	CuS _x /TiO ₂ film	CH ₄ H ₂ O ₂	6.6 n.d. n.d.	Gas phase, batch, 385 nm	Blank measurements, proposed oxidation to •OH	¹⁸⁸ (2017)
15	Pt-Cu ₂ O/TiO ₂ nanocrystals	CH ₄ CO H ₂ O ₂	1.4 0.05 0 3	Gas phase, batch, 300 – 400 nm,	Blank measurements, change in selectivity by Pt- Cu ₂ O instead of Cu or Pt	¹⁸⁹ (2017)
16	CuPt/TiO ₂	CH ₄ H ₂ O ₂	19 n.d. n.d.	Gas phase, batch, Xe lamp, 40 °C	Blank measurements	²²⁴ (2016)

Table A4 Overview of the photocatalytic CO₂ reduction on semiconductors with co-catalysts for the reduction and oxidation in one system.

Entry	Material	Product	Activity [$\mu\text{mol}\cdot\text{g}^{-1}\cdot\text{h}^{-1}$]	Conditions	Comments	Ref. (year)
1	Au/BiOI/MnO _x	CO	10	Gas phase, batch, > 420 nm		²²⁵ (2016)
		CH ₄	0.2			
		H ₂	traces			
		O ₂	traces			
2	Ag-Mn/N-doped TiO ₂ anatase	CH ₃ OH	0.26	Gas phase, batch, > 400 nm	Blank	²¹⁸ (2016)
		H ₂	n.d.		measurements,	
		O ₂	n.d.		No hint to oxidation reaction	
3	Cu(I)/Pd/Ti ³⁺ - TiO ₂	CH ₄	1	Gas phase, batch, > 400 nm	Blank	²²⁶ (2015)
		H ₂	n.d.		measurement	
		O ₂	n.d.			

6.2 List of publications

1. Light-Driven Proton Reduction with *in situ* Supported Copper Nanoparticles

S. Kreft, M. Sonneck, H. Junge, A. Pöpke, A. Kammer, C. Kreyenschulte, S. Lochbrunner, S. Wohlrab, M. Beller; *Int. J. Hydrogen Energ.* **2019**, submitted.

2. Dye Activation of Heterogeneous Copper(II)-Species for Visible Light Driven Hydrogen Generation

S. Kreft, J. Radnik, J. Rabeah, G. Agostini, M. M. Pohl, E. Gericke, A. Hoell, M. Beller, H. Junge, S. Wohlrab; *Int. J. Hydrogen Energ.* **2019**, DOI: 10.1016/j.ijhydene.2019.04.006.

3. Improving Selectivity and Activity of CO₂ Reduction Photocatalysts with Oxygen

S. Kreft, R. Schoch, J. Schneidewind, J. Rabeah, E. V. Kondratenko, V. A. Kondratenko, H. Junge, M. Bauer, S. Wohlrab, M. Beller; *Chem*, **2019**, DOI: 10.1016/j.chempr.2019.04.006.

4. Rice Husk Derived Porous Silica as Support for Pd and CeO₂ for Low Temperature Catalytic Methane Combustion

D. Liu, D. Seeburg, S. Kreft, R. Binding, I. Hartmann, D. Schneider, D. Enke, S. Wohlrab; *Catalysts*, **2019**, 9 (1), 26-34.

5. Low-Temperature Steam Reforming of Natural Gas after LPG-Enrichment with MFI Membranes

D. Seeburg, D. Liu, R. Dragomirova, H. Atia, M. M. Pohl, H. Amani, G. Georgi, S. Kreft, S. Wohlrab; *Processes*, **2018**, 6 (12), 263-275.

6. Synthesis of N-Lauroyl Sarcosine by Amidocarbonylation: Comparing Homogeneous and Heterogeneous Palladium Catalysts

S. Hancker, S. Kreft, H. Neumann, M. Beller; *Org. Process Res. Dev.*, **2017**, 21 (12), 2045-2051.

7. Routes for deactivation of different autothermal reforming catalysts

J. Pasel, S. Wohlrab, S. Kreft, M. Rotov, K. Löhken, R. Peters, D. Stolten; *J. Power Sources*, **2016**, 325, 51-63.

6.3 Conference participations

6.3.1 Talks

1. Energy-Symposium „Nutzung regenerativer Energiequellen und Wasserstofftechnik“, Stralsund, 2016. *Production of Sun Fuels by photo- and electro-catalytic CO₂ Reduction*.
2. 50. Jahrestreffen Deutscher Katalytiker, Weimar, 2017. *Application of Copper Compounds in Photocatalytic Sun Fuel Generation*.
3. 11th International conference on Advanced Nanomaterials, Aveiro, Portugal, 2018. *Photocatalytic CO₂ Reduction Using Cu/TiO₂ Aerogel – The Mystery of Oxygen*.

6.3.2 Poster contributions

1. DGMK Challenges for Petrochemicals and Fuels, Dresden, 2017. *Generation of Solar Fuels based on H₂O and CO₂ using Copper Catalysts*.
2. 51. Jahrestreffen Deutscher Katalytiker Weimar, 2018. *Selective Photocatalytic Reduction of Aqueous CO₂ in the Presence of Oxygen*.
3. 4th Symposium on Chemistry for Energy Conversion, Berlin, 2018. *Photocatalytic Reduction of Aqueous CO₂ Using Cu/TiO₂ Aerogel and the Mystery of Oxygen*. (Poster award)
4. 52. Jahrestreffen Deutscher Katalytiker Weimar, 2019. *Photocatalytic CO₂ Reduction Using Highly Porous Cu/TiO₂ Aerogels in the Presence of Oxygen*. (Poster workshop presentation).

Lebenslauf

Persönliche Daten

Name	Stefanie Kreft
Anschrift	Gellertstraße 8, 18057 Rostock
Email	stefanie.kreft@catalysis.de
Geburtsdatum	29.08.1985
Staatsangehörigkeit	Deutsch
Familienstand	ledig

Studium

Seit 10/2015	Beginn der Promotion am Leibniz-Institut für Katalyse e.V. an der Universität Rostock im Arbeitskreis von Prof. M. Beller Thema: Photokatalytische CO ₂ Reduktion mittels heterogener Katalysatoren
10/2013 - 09/2015	Masterstudium der Chemie, Universität Rostock Schwerpunkt: heterogene Katalyse Abschluss: Master of Science Titel der Masterarbeit: „Zwischen homogener und heterogener Photokatalyse: Die kupferkatalysierte Wasserspaltung“
10/2010 - 09/2013	Bachelorstudium der Chemie, Universität Rostock Abschluss: Bachelor of Science Titel der Abschlussarbeit: „Einfluss der Präparation von kupferfunktionalisierten porösen Materialien auf die photokatalytische Wasserspaltung“
09/1996 - 06/2005	Gymnasium Carolinum in Neustrelitz Abschluss: Allgemeine Hochschulreife

Berufliche Erfahrung

Seit 10/2015	Wissenschaftliche Mitarbeiterin Leibniz-Institut für Katalyse e.V. Thema: Katalyse für Energietechnologien
11/2018 - 12/2018	Auslandsaufenthalt Aarhus, Dänemark University of Aarhus, Denmark Thema: Elektrokatalyse (Prof. Kim Daasbjerg)
10/2010 - 09/2015	Studentische Hilfskraft Leibniz-Institut für Katalyse e.V. Thema: anorganische Funktionsmaterialien
02/2009 - 09/2010	Chemielaborantin Leibniz-Institut für Katalyse e.V. Thema: anorganische Funktionsmaterialien
09/2005 – 01/2009	Ausbildung zur Chemielaborantin Ernst-Moritz-Arndt-Universität Greifswald Abteilung: Analytische Chemie und Umweltchemie Abschluss: Facharbeiter mit Auszeichnung (IHK sowie Berufsschule)

Konferenz- und Tagungsbeiträge

13. – 15.03.2019	52. Jahrestreffen Deutscher Katalytiker in Weimar <u>Posterbeitrag:</u> <i>Photocatalytic CO₂ Reduction Using Highly Porous Cu/TiO₂ Aerogels in the Presence of Oxygen.</i> (Poster Workshop Präsentation)
15. – 16.01.2019	Klausurtagung BMBF Kopernikus Projekt „P2X“ in Frankfurt am Main <u>Posterbeitrag:</u> <i>Development and Investigation of non-Ag-based Heterogeneous Catalysts for the Electrocatalytic CO₂ Reduction to CO.</i>
19. – 20.11.2018	3rd Meeting of the Carbon Dioxide Activation Center (CADIAC) in Arrhus, Dänemark <u>Vortrag:</u> <i>Utilization of CO₂ using highly porous aerogels.</i>

18. – 20.07.2018 **11th International conference on Advanced Nanomaterials** in Aveiro, Portugal
Vortrag: *Photocatalytic CO₂ Reduction Using Cu/TiO₂ Aerogel – The Mystery of Oxygen.*
14. – 16.03.2018 **51. Jahrestreffen Deutscher Katalytiker** in Weimar
Posterbeitrag: *Selective Photocatalytic Reduction of Aqueous CO₂ in the Presence of Oxygen.*
28. – 31.01.2018 **4th Symposium on Chemistry for Energy Conversion** in Berlin
Posterbeitrag: *Photocatalytic Reduction of Aqueous CO₂ Using Cu/TiO₂ Aerogel and the Mystery of Oxygen.* (Posterpreis)
22. – 24.01.2018 **Klausurtagung BMBF Kopernikus Projekt „P2X“** in Frankfurt am Main
Posterbeitrag: *Development and Investigation of non-Ag-based Heterogeneous Catalysts for the Electrocatalytic CO₂ Reduction to CO.*
22. – 23.11.2017 **2nd Meeting of the Carbon Dioxide Activation Center (CADIAC)** in Arrhus, Dänemark
Vortrag: *Photocatalytic Reduction of Aqueous CO₂ with Cu/TiO₂ Aerogel.*
09. – 11.10.2017 **DGMK Challenges for Petrochemicals and Fuels** in Dresden
Posterbeitrag: *Generation of Solar Fuels based on H₂O and CO₂ using Copper Catalysts.*
- 12.07.2017 **LIKAT Institutsseminar zum Thema Photokatalyse** in Rostock
Vortrag: *Application of heterogeneous copper catalysts in photocatalytic H₂O and CO₂ reduction.*
15. – 17.03.2017 **50. Jahrestreffen Deutscher Katalytiker** in Weimar
Vortrag: *Application of Copper Compounds in Photocatalytic Sun Fuel Generation.*
16. – 18.11.2016 **1st Meeting of the Carbon Dioxide Activation Center (CADIAC)** in Arrhus, Dänemark
Vortrag: *Selective Photocatalytic Reduction of CO₂ in aqueous media using highly porous M/TiO₂ Aerogel.*

03.11.2016

23. Energy-Symposium „Nutzung regenerativer Energiequellen und Wasserstofftechnik“ in Stralsund

Vortrag: *Production of Sun Fuels by photo- and electro-catalytic CO₂ Reduction.*

Publikationen

Light-Driven Proton Reduction with *in situ* Generated and Supported Copper Nanoparticles

S. Kreft, M. Sonneck, H. Junge, A. Pöpke, A. Kammer, C. Kreyenschulte, S. Lochbrunner, S. Wohlrab, M. Beller; *Int. J. Hydrogen Energ.*, eingereicht.

Dye Activation of Heterogeneous Copper(II)-Species for Visible Light Driven Hydrogen Generation

S. Kreft, J. Radnik, J. Rabeah, G. Agostini, M. M. Pohl, E. Gericke, A. Hoell, M. Beller, H. Junge, S. Wohlrab; *Int. J. Hydrogen Energ.* **2019**, DOI: 10.1016/j.ijhydene.2019.04.006.

Improving Selectivity and Activity of CO₂ Reduction Photocatalysts with Oxygen

S. Kreft, R. Schoch, J. Schneidewind, J. Rabeah, E. V. Kondratenko, V. A. Kondratenko, H. Junge, M. Bauer, S. Wohlrab, M. Beller; *Chem*, **2019**, DOI: 10.1016/j.chempr.2019.04.006.

Rice Husk Derived Porous Silica as Support for Pd and CeO₂ for Low Temperature Catalytic Methane Combustion

D. Liu, D. Seeburg, S. Kreft, R. Binding, I. Hartmann, D. Schneider, D. Enke, S. Wohlrab; *Catalysts*, **2019**, 9 (1), 26-34.

Low-Temperature Steam Reforming of Natural Gas after LPG-Enrichment with MFI Membranes

D. Seeburg, D. Liu, R. Dragomirova, H. Atia, M. M. Pohl, H. Amani, G. Georgi, S. Kreft, S. Wohlrab; *Processes*, **2018**, 6 (12), 263-275.

Synthesis of N-Lauroyl Sarcosine by Amidocarbonylation: Comparing Homogeneous and Heterogeneous Palladium Catalysts

S. Hancker, S. Kreft, H. Neumann, M. Beller; *Org. Process Res. Dev.*, **2017**, 21 (12), 2045-2051.

Routes for deactivation of different autothermal reforming catalysts

J. Pasel, S. Wohlrab, S. Kreft, M. Rotov, K. Löhken, R. Peters, D. Stolten; *J. Power Sources*, **2016**, 325, 51-63.

Improved catalytic methane combustion of Pd/CeO₂ catalysts via porous glass integration

M. Hoffmann, S. Kreft, C. Berger-Karin, S. Wohlrab; *Appl. Catal. B*, **2015**, 179, 313-320.

Inverse replica of porous glass as catalyst support

S. Wohlrab, A. Janz, M.-M. Pohl, S. Kreft, D. Enke, A. Köckritz, A. Martin, B. Luecke; *Stud Surf Sci Catal*, **2010**, 175, 315-319.